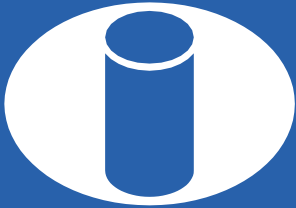


ISSN 1983-4195



IBRACON

IBRACON Structures and Materials Journal
Revista IBRACON de Estruturas e Materiais

Volume 14, Number 6
December 2021



IBRACON Structures and Materials Journal

Revista IBRACON de Estruturas e Materiais

Contents

- Evaluation of different fly ash samples on the production of alkali-activated materials* 14601
A. G. S. AZEVEDO, L. F. T. DOMINGOS and K. STRECKER
- Analysis of mortar coating with different types and proportions of chemical admixtures that have water retentivity properties*..... 14602
A. T. SOUZA, C. A. CARVALHAIS and W. J. SANTOS
- A review on the evolution of Portland cement and chemical admixtures in Brazil* 14603
J. F. NATALLI, E. C. S. THOMAZ, J. C. MENDES and R. A. F. PEIXOTO
- Numerical analyses of two-pile caps considering lateral friction between the piles and soil* 14604
R. G. DELALIBERA and G. F. SOUSA
- Properties of recycled aggregates from different composition and its influence on concrete strength* 14605
F. A. SALGADO and F. A. SILVA
- Influence of internal sulfate attack on cement paste properties: contamination by pyrite*..... 14606
A. P. B. CAPRARO, J. H. FILHO and M. H. MEDEIROS
- Analysis of structural masonry buildings taking into account the construction sequence loads and soil-structure interaction* 14607
A. C. S. LOPES, J. A. NASCIMENTO NETO and R. BARROS
- Study of red ceramic residues as pigments in matrices based on white Portland cement*..... 14608
L. A. DIAS, F. B. BIRCK, L. KAEFER, D. C. M. ARNOLD and A. S. VARGAS
- Probabilistic analysis of slab-column connections subjected to punching shear according to the ABNT NBR 6118 (2014) recommendations considering the model error measure*..... 14609
N. L. A. MARQUE and C. G. NOGUEIRA
- Optimization of slender reinforced concrete columns subjected to biaxial bending using genetic algorithms* 14610
S. L. PIRES and M. C. A. T. SILVA
- Numerical and parametric study of the yield stress limits of reinforcement bars in clay block masonry structures*..... 14611
O. S. IZQUIERDO, M. R. S. CORRÊA, I. S. IZQUIERDO and I. G. ARAÚJO
- Load transfer on instrumented prestressed ground anchors in sandy soil*..... 14612
A. M. D. SOUSA, Y. D. J. COSTA, L. A. S. FLORÊNCIO and C. M. L. COSTA
- Erratum* 14613



Cover: Parametric Tower

Courtesy: Marcela Noronha P. de O. e Sousa



IBRACON

IBRACON Structures and Materials Journal is published bimonthly (February, April, June, August, October, and December) by IBRACON.

IBRACON

Instituto Brasileiro do Concreto Founded in 1972

Av. Queiroz Filho, nº 1700 — sala 407/408
Torre D — Villa Lobos Office Park
CEP 05319-000 — São Paulo, SP — Brazil
Phone: +55 11 3735-0202
Fax: +55 11 3733-2190
E-mail: riem@ibracon.org.br
Website: <http://www.ibracon.org.br>

Cover design & Layout: Editora Cubo
www.editoracubo.com.br

Aims and Scope

Aims and Scope

The IBRACON Structures and Materials Journal (in Portuguese: Revista IBRACON de Estruturas e Materiais) is a technical and scientific divulgation vehicle of IBRACON (Brazilian Concrete Institute), published every two months. Each issue has 12 to 15 articles and, possibly, a technical note and/or a technical discussion regarding a previously published paper. All contributions are reviewed and approved by professionals with recognized scientific competence in the area. The IBRACON Structures and Materials Journal is an open access Journal, free of charges for authors and readers.

Objectives

The IBRACON Structures and Materials Journal's main objectives are:

- Present current developments and advances in concrete structures and materials.
- Make possible the better understanding of structural concrete behavior, supplying subsidies for a continuous interaction among researchers, producers, and users.
- Stimulate the development of scientific and technological research in the areas of concrete structures and materials, through papers peer-reviewed by a qualified Editorial Board.
- Promote the interaction among researchers, constructors and users of concrete structures and materials and the development of Civil Construction.
- Provide a vehicle of communication of high technical level for researchers and designers in the areas of concrete structures and materials.

Submission Procedure

The procedure to submit and revise the contributions, as well as the formats, are detailed in the Journal Website (ismj.org).

The papers and the technical notes are revised by at least two reviewers indicated by the editors. Discussions and replies are accepted for publication after a review by the editors and at least one member of the Editorial Board. In case of disagreement between the reviewer and the authors, the contribution will be sent to a specialist in the area, not necessarily linked to the Editorial Board. Conflict of interests is carefully handled by the Editors.

Contribution Types

The Journal will publish original papers, short technical notes, and paper discussions. Original papers will be accepted if they are in accordance with the objectives of the Journal and present quality of information and presentation. A technical note is a brief manuscript. It may present a new feature of research, development, or technological application in the areas of Concrete Structures and Materials, and Civil Construction. This is an opportunity to be used by industries, companies, universities, institutions of research, researchers, and professionals willing to promote their works and products under development.

A discussion is received no later than 3 months after the publication of the paper or technical note. The discussion must be limited to the topic addressed in the published paper and must not be offensive. The right of reply is granted to the Authors. The discussions and the replies are published in the subsequent issues of the Journal.

The submission file should be in accordance with the paper template available at the Journal Website. It is recommended that the length of the papers does not exceed 25 pages. Where available, URLs for the references should be provided.

The IBRACON Structures and Materials Journal will conduct the review process for manuscripts submitted in English. Titles, abstracts, and keywords are presented in English, and in Portuguese or Spanish. Articles and technical notes are peer-reviewed and only published after approval of the reviewers and the Editorial Board.

Once accepted, an article is typeset according to the journal layout. The author will be required to review and approve the galleys before publishing. At this stage only typesetting errors will be considered.

Internet Access

The IBRACON Structures and Materials Journal Webpage is available at <http://ismj.org>.

Sponsors

The funds for the maintenance of the Journal are currently obtained from the IBRACON. The Journal is not supposed to be maintained with funds from private sponsorship, which could diminish the credit of the publications.

Photocopying

Photocopying in Brazil. Brazilian Copyright Law is applicable to users in Brazil. IBRACON holds the copyright of contributions in the journal unless stated otherwise at the bottom of the first page of any contribution. Where IBRACON holds the copyright, authorization to photocopy items for internal or personal use, or the internal or personal use of specific clients, is granted for libraries and other users registered at IBRACON.

Copyright

All rights, including translation, reserved. Under the Brazilian Copyright Law No. 9610 of 19th February 1998, apart from any fair dealing for the purpose of research or private study, or criticism or review, no part of this publication may be reproduced, stored in a retrieval system, or transmitted in any form or by any means, electronic, mechanical, photocopying, recording or otherwise, without the prior written permission of IBRACON. Requests should be directed to IBRACON:

IBRACON

Av. Queiroz Filho, 1700 – sala 407/408 – Torre D
Villa Lobos Office Park
05319-000 – Vila Hamburguesa
São Paulo – SP
Phone: +55 (11) 3735-0202
E-mail: riem@ibracon.org.br

Disclaimer

Papers and other contributions and the statements made, or opinions expressed therein are published on the understanding that the authors of the contribution are the only responsible for the opinions expressed in them and that their publication does not necessarily reflect the views of IBRACON or of the Journal Editorial Board.

Editorial Board

Editor-in-chief emeritus

José Luiz Antunes de Oliveira e Sousa, Universidade Estadual de Campinas - UNICAMP, Campinas, SP, Brazil, jls@fec.unicamp.br

Editor-in-chief

Guilherme Aris Parsekian, Universidade Federal de São Carlos – UFSCAR, São Carlos, SP, Brazil, parsekian@ufscar.br

Associate Editors

Antônio Carlos dos Santos, Universidade Federal de Uberlândia – UFU, Uberlândia, MG, Brazil
Bernardo Horowitz, Universidade Federal de Pernambuco - UFPE, Recife, PE, Brazil
Bernardo Tutikian, Universidade do Vale do Rio dos Sinos – UNISINOS, São Leopoldo, RS, Brazil
Bruno Briseghella, Fuzhou University, Fujian, China
David Oliveira, Jacobs Engineering, Sydney, Australia
Edgar Bacarji, Universidade Federal de Goiás - UFG, Goiânia, GO, Brazil
Edna Possan, Universidade Federal da Integração Latino Americana – UNILA, Foz do Iguaçu, PR, Brazil
Fernando Pelisser, Universidade Federal de Santa Catarina – UFSC, Florianópolis, SC, Brazil
Fernando Soares Fonseca, Brigham Young University – BYU, Provo, UT, USA
José Marcio Fonseca Calixto, Universidade Federal de Minas Gerais – UFMG, Belo Horizonte, MG, Brazil
José Tadeu Balbo Universidade de São -Paulo, São Paulo, SP, Brazil
Leandro Mouta Trautwein, Universidade Estadual de Campinas - UNICAMP, Campinas, SP, Brazil
Leandro F. M. Sanchez, University of Ottawa, Ottawa, Canada
Lia Lorena Pimentel, Pontifícia Universidade Católica de Campinas – PUCCAMP, Campinas, SP, Brazil
Luís Oliveira Santos, Laboratório Nacional de Engenharia Civil, Lisboa, Portugal
Mark G Alexander, University of Cape Town, Cape Town, South Africa
Marco Di Prisco, Politecnico di Milano, Milan, Italy
Mário Jorge de Seixas Pimentel, Universidade do Porto - FEUP, Porto, Portugal
Maurício de Pina Ferreira, Universidade Federal do Pará - UFPA, Belém, PA, Brazil
Mauro de Vasconcellos Real, Universidade Federal do Rio Grande – FURG, Rio Grande, RS, Brazil
Nigel G. Shrive, University of Calgary, Calgary, Canada
Osvaldo Luís Manzoli, Universidade Estadual Paulista “Júlio de Mesquita Filho” - UNESP, Bauru, SP, Brazil
Rebecca Gravina, RMIT University, Melbourne, Australia
Ricardo Carrazedo, Universidade de São Paulo - USP, São Carlos, SP, Brazil
Samir Maghous, Universidade Federal do Rio Grande do Sul - UFRGS, Porto Alegre, RS, Brazil
Sérgio Hampshire de Carvalho Santos, Universidade Federal do Rio de Janeiro - UFRJ, Rio de Janeiro, RJ, Brazil
Túlio Nogueira Bittencourt, Universidade de São -Paulo, São Paulo, SP, Brazil
Vladimir Guilherme Haach, Universidade de São Paulo - USP, São Carlos, SP, Brazil
Yury Villagrán Zaccardi, Universidad Tecnológica Nacional Facultad Regional La Plata, Buenos Aires, Argentina

Editorial Comission

Antônio Carlos R. Laranjeiras, ACR Laranjeiras, Salvador, BA, Brazil
Emil de Souza Sánchez Filho, Universidade Federal Fluminense, UFF, Rio de Janeiro, RJ, Brazil
Geraldo Cechella Isaia, Universidade Federal de Santa Maria, UFSM, Santa Maria, RS, Brazil
Gonzalo Ruiz, Universidad de Castilla-La Mancha - UCLM, Ciudad Real, Spain
Ivo José Padaratz, Universidade Federal de Santa Catarina - UFSC, Florianópolis, SC, Brazil
Joaquim de Azevedo Figueiras, Faculdade de Engenharia da Universidade do Porto - FEUP, Porto, Portugal
Paulo Monteiro, University of California Berkeley, Berkeley, CA, USA
Pedro Castro Borges, CINVESTAV, Mérida, Yuc., México
Vladimir Antônio Paulon, Universidade Estadual de Campinas - UNICAMP, Campinas, SP, Brazil

Former Editors

Américo Campos Filho, Universidade Federal do Rio Grande do Sul - UFRGS, Porto Alegre, RS, Brazil
Denise C. C. Dal Molin Universidade Federal do Rio Grande do Sul - UFRGS, Porto Alegre, RS, Brazil
Eduardo Nuno Brito Santos Júlio, Instituto Superior Técnico - IST, Lisboa, Portugal
Guilherme Sales Melo, Universidade de Brasília, UnB, Brasília, DF, Brazil
Luiz Carlos Pinto da Silva Filho, Universidade Federal do Rio Grande do Sul - UFRGS, Porto Alegre, RS, Brazil
Mounir Khalil El Debs, Universidade de São Paulo - USP, São Carlos, SP, Brazil
Nicole Pagan Hasparyk, Eletrobras Furnas, Aparecida de Goiânia, GO, Brazil
Paulo Helene, Universidade de São Paulo - USP, São Paulo, SP, Brazil
Roberto Caldas de Andrade Pinto, Universidade Federal de Santa Catarina - UFSC, Florianópolis, SC, Brazil
Ronaldo Barros Gomes, Universidade Federal de Goiás - UFG, Goiânia, GO, Brazil
Romilde Almeida de Oliveira, Universidade Católica de Pernambuco - UNICAP, Recife, PE, Brazil
Romildo Dias Toledo Filho, Universidade Federal do Rio de Janeiro - UFRJ, Rio de Janeiro, RJ, Brazil
Rubens Machado Bittencourt, Eletrobras Furnas, Aparecida de Goiânia, GO, Brazil



Board of Direction 2019/2021 Biennium

President

Paulo Helene

1st Vice-President Director

Júlio Timerman

2nd Vice-President Director

Enio José Pazini Figueiredo

Presidency Advisors

Antônio Domingues de Figueiredo

Iria Lícia Oliva Doniak

Jairo Abud

Jorge Batlouni Neto

Luís Aurélio Fortes da Silva

Mario William Esper

Maurice Antoine Traboulsi

Paula Baillet

Simão Priskulnik

1st Director-Secretary

Cláudio Sbrighi Neto

2nd Director-Secretary

Carlos José Massucato

1st Treasurer Director

Júlio Timerman

2nd Treasurer Director

Hugo S. Armelin

Marketing Director

Jéssika Pacheco

Marketing Director Advisor

Guilherme Covas

Publications Director

Guilherme Parsekian

Publications Director Advisor

Túlio Nogueira Bittencourt

Event Director

Rafael Timerman

Event Director Advisor

Luis César De Luca

Technical Director

José Tadeu Balbo

Technical Director Advisor

Selmo Chapira Kuperman

Institutional Relations Director

César Henrique Daher

Institutional Relations Director Advisor

José Vanderley de Abreu

Course Director

Leandro Moura Trautwein

Course Director Advisor

Antônio Carlos dos Santos

Student Activities Director

Jéssica Andrade Dantas

Student Activities Director Advisor

Sandra Regina Bertocini

Personnel Certification Director

Adriano Damásio Soterio

Personnel Certification Director Advisor

Gilberto Antônio Giuzio

Research and Development Director

Bernardo Tutikian

Research and Development Director Advisor

Roberto Christ

Council 2019/2021 Biennium

Individual Members

Antônio Carlos dos Santos

Antônio Domingues de Figueiredo

Arnaldo Forti Battagin

Bernardo Fonseca Tutikian

Carlos José Massucato

César Henrique Sato Daher

Cláudio Sbrighi Neto

Enio José Pazini Figueiredo

Hugo da Costa Rodrigues Filho

Inês Laranjeira da Silva Battagin

Iria Lícia Oliva Doniak

Jéssika Mariana Pacheco

José Tadeu Balbo

Leandro Moura Trautwein

Luiz Carlos de Almeida

Luiz Prado Vieira Júnior

Mário William Esper

Maurice Antoine Traboulsi

Rafael Timerman

Vladimir Antônio Paulon

Past President Members

Eduardo Antônio Serrano

José Marques Filho

Júlio Timerman

Paulo Helene

Ronaldo Tartuce

Rubens Machado Bittencourt

Selmo Chapira Kuperman

Simão Priskulnik

Túlio Nogueira Bittencourt

Corporate Members

ABCIC - Associação Brasileira da
Construção Industrializada de Concreto –
Iria Lícia Oliva Doniak

ABCP - Associação Brasileira de Cimento
Portland – Paulo Camilo Penna

ABECE - Associação Brasileira de
Engenharia e Consultoria Estrutural –
João Alberto de Abreu Vendramini

ABESC - Associação Brasileira das
Empresas de Serviços de Concretagem –
Jairo Abud

EPUSP - Escola Politécnica da
Universidade de São Paulo – Túlio
Nogueira Bittencourt

FURNAS Centrais Elétricas S/A – Flávio
de Lima Vieira

IPT - Instituto de Pesquisas Tecnológicas
do Estado de São Paulo – José Maria de
Camargo Barros

L. A. FALCÃO BAUER Centro
Tecnológico – Patrícia Bauer

PhD Engenharia Ltda – Douglas de
Andreza Couto

TQS Informática Ltda – Nelson Covas

VOTORANTIM Cimentos S/A –
Maurício Bianchini

Reviewers List 2020-2021

Acchar, Wilson
Afrughasabet, Vahid
Aguado, Antonio
Aguilar, Maria Teresa
Ajith, Julian Thamboo
Akil, Hazizan Md
Akiyama, Mitsuyoshi
Albuquerque, Arthur
Almeida Filho, Fernando
Almeida, Fernando do Couto Rosa
Almeida, João A. P. P.
Almeida, Luiz
Almeida, Saulo José Castro
Almeida, Sylvia Regina Mesquita de
Almeida, Valério
Alva, Gerson Moacyr Sisniegas
Alves, Elcio
Ameri, Farshad
Amorim Júnior, Nilson
Amorim, David
Andrade, Daniel
Andrade, Jairo Jose de Oliveira
Andrade, Rodolfo Mendes de
Ângulo, Sérgio
Aoki, Nelson
Arantes, João
Araujo, Daniel Lima de
Araújo, Gregório Luis Silva
Assis, Andre
Azenha, Miguel
Azevedo, Crysthian Purcino
Azhari, Fae
Balbo, Jose
Baldassino, Nadia
Bandeira, Alex
Barbosa, Andre R.
Barbosa, Maria
Barbosa, Normando Perazzo
Barboza, Aline da Silva
Barros, Joaquim A. O.
Barros, Rodrigo
Baságliá, Cilmar
Batista, Eduardo de Miranda
Batiston, Eduardo
Bauer, Elton
Beck, André
Beeldens, Anne
Bentz, Evan C.
Beraldo, Antonio
Bernard, Stefan
Berto, Filippo
Betoli, Andrea
Bhattacharya, Subhamoy
Bittencourt Junior, Luis
Bittencourt, Túlio
Bonaldo, Everaldo
Bonnet, Stephanie
Borges, Paulo Henrique
Bounassar Filho, Jorge
Brás, Ana
Brito, Jorge de
Brunesi, Emanuele
Buratto, Caroline
Buttignol, Thomaz
Cabral, Kleber
Calado, Luís
Calixto, José Marcio
Calmon, Joao Luiz
Camões, Aires
Campelo, Henrique
Campos Filho, Américo
Caprani, Colin
Capuzzo, Valdirene Maria Silva
Cardoso, Fabio
Carneiro, Arnaldo Manoel Pereira
Carrazedo, Ricardo
Carrazedo, Rogério
Carvalho, David
Carvalho, Hermes
Carvalho, Roberto Chust
Castro, Alessandra Lorenzetti de
Cavalaro, Sergio
Ceroni, Francesca
Cerqueira, Niander
Chaallal, Omar
Chen, Airong
Cheng, Min-Yuan
Christoforo, André
Cincotto, Maria
Cladera, Antoni
Climent, Miguel Ángel
Coelho, Antonio Carlos Vieira
Cordeiro, Liciana
Cornish, Katrina
Corrêa, Marcio
Correia, João R.
Correia, José
Costa, Carla Neves
Cyr, Martin
Dalfré, Gláucia
D'Andrea, Renata
De Nardim, Silvana
Delalibera, Rodrigo
Deng, Yaohua
Di Mascio, Paola
Dias, Salvador J. E.
Diaz, Ernani
Diógenes, Hidelbrando
Dourado, João Carlos
El Debs, Mounir Khalil
Eslami, Javad
Espinosa, Ana
Esquivel, Edmundo
Etchegaray, Augusto
Etman, Emad
Fakury, Ricardo
Faria, Obede Borges
Feldman, Lisa
Felipe, Túlio
Felix, Emerson
Ferrari, Vladimir
Ferreira, Felipe
Ferreira, Luiz Eduardo Teixeira
Ferreira, Maurício de Pina
Ferreira, Régis de C.
Fioriti, Cesar
Firmo, Joao P.
Fonseca, Joao
Freitas, Osvaldo
Furtado, Andre
Futai, Marcos
Gachet, Luisa
Galal, Khaled
Garcez, Monica Regina
Gavilan, Sergio
Genikomsou, Aikaterini S.
Ghorbel, Elhem
Giannini, Eric R.
Gleize, Philippe
Gomes, Carlos Marmorato
Gomes, Herbert
Gomes, João Paulo Castro
Gomes, Ronaldo
Gomes, Wellison
Gonçalves, Paulo J. P.
Greco, Marcelo
Hadi, Muhammad
Hanai, João Bento de
Haselbach, Liv
Holanda, Jose Nilson Franca de
Hooton, Doug
Hoppe Filho, Juarez
Horgnies, Matthieu
Horowitz, Bernardo
Houben, Lambert
Houmard, Manuel
Jacintho, Ana
Jiménez, José Ramón
John, Vanderley
Gonilha, José A.
Joshaghani, Alireza
Juenger, Maria
Justino Filho, Manoel Rodrigues
Kang, Zhan
Karray, Mourad
Kataoka, Marcela
Kazmi, Syed
Kenai, S.
Khoshnazar, Rahil
Kirchheim, Ana Paula
Kotynia, R.
Kowalski, Robert
Krahl, Pablo Augusto
Kroetz, Henrique Machado
Ladeira, Luiz Orlando
Laim, Luis
Lameiras, Rodrigo de Melo
Landesmann, Alexandre
Langelaar, Matthijs
Lantsoght, Eva O. L.
Lautenschläger, Carlos
lazzari, Bruna
Leite, Mônica Batista
Lemes, Igor
Lenart, Malgorzata
Leonel, Edson
Liang, Qing Quan
Lima, Flávio
Lima, Maria Cristina Vidigal de
Lima, Maryangela
Lima, Paulo
Lima, Paulo Roberto
Lima, Silvio Souza
Lintz, Rosa Cristina
Liu, Faqi
Longhi, Marlon
Lopez, Rafael Holdorf
Loredo-Souza, Acir
Lothenbach, Barbara
Lu, Jian Xin
Luo, Quantian
Luz, Caroline Angulski da
Magalhães, Aldo de
Maia, Wanderson

Reviewers List 2020-2021

Manickam, Ramesh
Mansur, Alexandra
Manzoli, Osvaldo
Mappa, Paulo César
Marangon, Ederli
Mari, Antonio R.
Marques Filho, Jose
Marques, Severino
Marreiros, Rui
Martins, Carlos Humberto
Masia, Mark
Mata, Rodrigo da
Mateos, Angel
Mateus, Ricardo
Matos, Paulo de
Mazzilli, Carlos Eduardo Nigro
Medeiros, Arthur
Medeiros, Marcelo
Medeiros, Marcelo Henrique
Meira, Gibson Rocha
Melges, José Luiz Pinheiro
Melo, Carlos Eduardo Luna de
Mendes, Rafael Farinassi
Menegoto, Mauro
Menon, Nara Villanova
Miguel, Leandro Fleck Fadel
Milani, Ana Paula da Silva
Mohamad, Gihad
Moita, Gray
Monte, Renata
Montes-Garcia, Pedro
Montserrat, Tai Ikumi
Moraes, Poliana Dias de
Morsch, Inácio
Mota, Neusa
Nallim, Liz
Nascimento, Aderson
Nematzadeh, Mahdi
Noaman, Ahmed Tareq
Nóbrega, Petrus
Nogueira, Caio
Nogueira, Fernando
Novais, Rui
Oliveira, Andrielli Morais de
Oliveira, Carlos
Oliveira, Dênio
Oliveira, Leonardo Henrique
Oliveira, Marcos
Ortega, Jose Marcos
Oudah, Fadi
Ozbakkaloglu, Togay
Pacheco, Fernanda
Padaratz, Ivo José
Paes, José Luiz
Pais, Jorge C.
Panzer, Tulio
Parente Junior, Evandro
Patel, Vipul
Paula, Júnia de
Pauletti, Ruy Marcelo de Oliveira
Paulino, Glaucio
Pavanello, Renato
Pavic, Aleksandar
Paya, Jorge
Pecce, Marisa
Peixoto, Ricardo André Fiorotti
Pelisser, Fernando
Pereira, Eduardo
Pereira, Sebastião Salvador Real
Perlingeiro, Mayra
Pfeil, Michèle
Piancastelli, Elvio
Picelli, Renato
Pileggi, Rafael
Pimenta, Roberval
Pimentel, Roberto
Pinheiro, Ivone
Pipa, Manuel
Pituba, Júlio
Poon, Chi Sun
Pravia, Z. M. C.
Prudencio, Roberto
Quaranta, Giuseppe
Quinino, Uziel
Racic, Vitomir
Radlinska, Aleksandra
Rajabipour, Farshad
Ramos, José Luís
Ranzi, Gianluca
Real, Mauro
Rêgo, João da Silva
Resende, Thomás Lima de
Ribeiro, António Bettencourt
Rizzatti, Eduardo
Rocha, Janaide Cavalcante
Robles, Desiree Rodriguez
Rodrigues, Conrado
Rodrigues, João Paulo
Rodrigues, José de Anchieta
Rodrigues, Roger
Rodriguez, Erich D.
Rodriguez, Jose Maria Fernandez
Roehl, Deane
Roesler, Jeffery
Roman, Humberto Ramos
Romano, Roberto Cesar Oliveira
Romero, Manuel L.
Rossi, Alexandre
Rossi, Rodrigo
Rovere, Henriette
Ruan, Xin
Saez, Paola Villoria
Sahoo, Dipti Ranjan
Salvador Filho, José Américo Alves
Sanchez, Emil
Sanchez, Leandro
Sanjuan, Miguel Angel
Santos, Ana Carolina Parapinski dos
Santos, António Carlos dos
Santos, Daniel
Santos, Sérgio Hampshire C.
Santos, White
Sarker, Prabir K.
Savija, Branko
Schaumann, Peter
Schulz, Mauro
Sciarretta, Francesca
Scott, Allan
Seara-Paz, Gumersinda
Segantini, Antonio Anderson
Sennah, Khaled
Serrano-Gonzalez, Javier
Shafigh, Payam
Sheehan, Therese
Shehata, Lidia
Shi, Jinjie
Shrive, Nigel
Siacara, Adrian Torrico
Silva Filho, Luiz Carlos
Silva Junior, Francisco
Silva, Amilton Rodrigues da
Silva, André da
Silva, Bruno do Vale
Silva, Emilio
Silva, Flávio de Andrade
Silva, Jefferson Lins da
Silva, José Guilherme da
Silva, Marcelo Araujo da
Silva, Renata Gomes Lanna da
Silva, Ricardo
Silva, Wellington Andrade da
Siqueira, Gustavo
Snoeck, Didier
Somja, Hugues
Soto, Orieta
Sousa, Adla
Sousa-Coutinho, Joana
Soutsos, Marios
Souza, Alex Sander
Souza, Regina
Stefanidou, Maria
Strauss, Alfred
Taerwe, Luc
Taha, Mahmoud
Tamayo, Jorge
Tang, W. C.
Tarabia, Ahmed
Tavares, Lisiane
Thanaraj, Daniel Paul
Thomas, Carlos
Thomé, Antônio
Titotto, Silvia Lenyra Meirelles Campos
Toledo Filho, Romildo
Troncone, Antonello
Tsuha, Cristina H. C.
Van Coile, Ruben
Vandenbossche, Julie
Vargas, Alexandre
Verissimo, Gustavo de Souza
Vieira, Manuel
Vitek, Jan
Vizotto, Isaías
Wahrhaftig, Alexandre de Macêdo
Wally, Gustavo
Wang, Xiao-Yong
Xie, Tianyu (Anson)
Yalcin, Omer
Yang, Shangtong
Yang, You-fu
Yassin, Ahmed
Yusuf, Moruf Olalekan
Zaccardi, Yury Andrés Villagrán
Zedan, Cristian Maluk
Zhu, X. X.
Zuchetti, Lais



ORIGINAL ARTICLE

Evaluation of different fly ash samples on the production of alkali-activated materials

Avaliação de diferentes amostras de cinza volante na produção de materiais álcali-ativados

Adriano Galvão Souza Azevedo^a Luis Fernando Tonholo Domingos^a Kurt Strecker^a ^a Universidade Federal de São João del-Rei, Departamento de Engenharia Mecânica, São João del-Rei, MG, Brasil

Received 22 April 2020

Accepted 11 January 2021

Abstract: In this work, different samples of fly ash (FA-A and FA-B) classified as type F as used to produce the AAM samples. The FA-A presented a higher Fe_2O_3 content than FA-B, 6.1 to 3.8 wt.%, and a slightly higher $\text{SiO}_2/\text{Al}_2\text{O}_3$ ratio of 3.52 in comparison to 3.34 of FA-B. The average particle size (D50) of fly ash A was 19.7 μm and of fly ash B 30.8 μm , while the specific mass of the ashes A and B were 2.38 and 2.21 g/cm^3 , respectively. The results revealed that the mechanical strength of the AAM produced with fly ash A was higher than fly ash B, close to 80 and 44 MPa, respectively. The variation of the strength has been attributed to the different $\text{SiO}_2/\text{Al}_2\text{O}_3$ ratios and different particle sizes. The mechanical strength decreased with increasing curing time, which is attributed to excess alkali in the system. Only very small differences in porosity and density have been found.

Keywords: alkali-activated materials, fly ash, alkali activation, mechanical strength.

Resumo: Neste trabalho, diferentes amostras de cinza volante (CV-A e CV-B) classificadas como tipo F foram usadas para a produção dos AAM. A amostra CV-A apresentou uma maior concentração de Fe_2O_3 (6,1%) em comparação a amostra CV-B (3,8%). A razão $\text{SiO}_2/\text{Al}_2\text{O}_3$ foi de 3,52 e 3,34 para as amostras CV-A e CV-B, respectivamente. O tamanho médio das partículas (D50) foi de 19,7 μm (CV-A) e 30,8 μm (CV-B), enquanto a massa específica foram 2,38 e 2,21 g/cm^3 , respectivamente. A resistência mecânica das amostras produzidas com a CV-A foi de 80 MPa enquanto valores próximos de 44 MPa foram obtidos com a CV-B. Essa variação foi relacionada com os diferentes tamanhos médios das partículas da cinza. A diminuição da resistência foi relacionada com o álcali em excesso no sistema. Pequenas variações nos valores de porosidade e densidade foram observadas nas amostras produzidas.

Palavras-chave: materiais álcali-ativados, cinza volante, álcali-ativação, resistência mecânica.

How to cite: A. G. S. Azevedo, L. F. T. Domingos, and K. Strecker, "Evaluation of different fly ash samples on the production of alkali-activated materials," *Rev. IBRACON Estrut. Mater.*, vol. 14, no. 6, e14601, 2021, <https://doi.org/10.1590/S1983-41952021000600001>

1. INTRODUCTION

Ordinary Portland cement (OPC) is the most used binding material in the construction industry worldwide. However, the production of cement releases large quantities of CO_2 , the main greenhouse gas, which may contribute to drastic climate changes [1], [2]. According to Pedrosa (2008), it is predicted that in 2030, maintaining the annual growth rate of cement production of 2008, the cement production industry will be responsible for the emission of 2820 million tons of carbon dioxide [3]. Therefore, because of the possible environmental problems, the search for new types of binders with similar properties to OPC is necessary. These alternative binding materials must be able of replacing

Corresponding author: Adriano Azevedo. E-mail: adrianoagalvao26@yahoo.com.br

Financial support: Coordenação de Aperfeiçoamento de Pessoal de Nível Superior (CAPES).

Conflict of interest: Nothing to declare.



This is an Open Access article distributed under the terms of the Creative Commons Attribution License, which permits unrestricted use, distribution, and reproduction in any medium, provided the original work is properly cited.

traditional cement, ensuring high mechanical strength, chemical inertia, acquiring resistance in short curing periods, resistance to acid, and sulfate attacks, besides presenting low cost [4]–[6].

A new class of binders, which is also known as inorganic polymers or geopolymers, is obtained by the polycondensation or inorganic polymerization of aluminosilicate minerals in a highly alkaline environment. The term geopolymer was first described by Glukhovskiy in 1959 and widely spread in the 1970s by Joseph Davidovits [7]. The nomenclature to name geopolymers is based on the term polysialate, an abbreviation for silico-oxo-aluminate, of composition $M_n[-(Si-O)_z-Al-O]_n \cdot wH_2O$ [8], wherein M is a cation such as potassium, sodium, or calcium, n is the degree of polycondensation, z is 1, 2, or 3, indicating the Si/Al ratio in the basic silico-aluminate unit of the polysialate [6], and w corresponds to the degree of hydration. The variation of “z” automatically causes a variation in the SiO_2/Al_2O_3 ratio, which allows the formation of different types of geopolymers, such as poly(sialate) which are based on the sialate unit $[-Si-Al-Si-O]$, with a Si/Al ratio of 1:1, poly(sialate-siloxy) that have the sialate-siloxy $[-Si-O-Al-O-Si-O-]$ as the basic unit and a Si/Al ratio equal to 2:1 and poly(sialate-disiloxy) with the sialate disiloxy $[Si-O-Al-O-Si-O-Si-O-]$ as the basic unit and a Si/Al ratio of 3:1. The production of the alkali-activated materials is also known to form a short-range atomic array, an aluminosilicate gel which may be referred to as an N-A-S-H type gel (with $N=Na_2O$, $A=Al_2O_3$, $S=SiO_2$, $H=H_2O$). This general formula for the product of the geopolymerization shows that even after polycondensation reactions, water molecules remain in the system, promoting gel stability, and favoring the obtention of high mechanical strength materials with denser structures [9]–[12].

The geopolymer production process may become complex due to large variations in the chemical and mineralogical composition of the starting materials, which may alter the characteristics of the final product [12], [13]. Andini et al. [14] conducted a study using various types of fly ashes with different SiO_2 to Al_2O_3 ratios, thus forming different types of geopolymeric structures, such as poly(sialate-siloxy) and poly(sialate-disiloxy). They used calcium hydroxide (NaOH) and potassium hydroxide (KOH) as alkaline activators, and for the thermal curing, the materials were submitted to different temperatures and times of exposure. It was concluded that the geopolymer materials obtained from fly ash with a SiO_2/Al_2O_3 ratio equal to 3 resulted in materials of higher strength, lower porosity, and higher apparent density. However, the authors emphasized that the most satisfactory results were obtained when using KOH as an alkaline activator and curing temperature of 25 and 80°C, but without stating the reasons for the improved performance [14]. Similar work was done by van Jaarsveld et al. [15] and they concluded that the origin of the industrial byproducts plays a fundamental role in determining the final properties of the geopolymer matrix, which may be associated with the origin of the mineral coal used and the burning process used in the thermoelectric plant.

This work presents the production of geopolymer materials using fly ash from the same thermoelectric complex obtained in different years, 2013 and 2020. This type of investigation is important to demonstrate how different fly ash samples can promote different properties for the AAM produced under the same conditions. In the work of Jahromy et al. [16], the authors demonstrated how six fly ash samples obtained in different ways have high changes in the final properties. The study of the different mineralogical characteristics of the starting material is of great interest to ascertain the modification of the physical and mechanical properties of the geopolymer matrix, as well as to give an ecologically more attractive application.

2. JUSTIFICATION

Correlate the chemical composition of the different fly ash samples with the mechanical and physical properties of the hardened alkali-activated materials after different curing times.

3. MATERIALS AND EXPERIMENTAL PROGRAM

3.1 Materials

3.1.1 Fly Ash (FA)

Two samples of fly ash from the Jorge Lacerda/SC thermoelectric complex, commercialized by Pozo-Fly industry, Lima® ash trade, were used to produce the pastes. The ashes were benefited by separation of coarse residues and ball milling. The fly ash A (FA-A) originated from the burning of coal in the thermoelectric plant in the years 2013 and 2014, while fly ash B (FA-B) was obtained in the period between 2019 and 2020. The intent of using fly ash from the same plant is to establish a relationship between the chemical composition of the ashes and the mechanical, physical,

and chemical properties of the slurries produced by alkaline activation and how ashes from the same thermal plant can promote the obtainment of materials with different properties

3.1.2 Sodium hydroxide (NaOH)

The alkaline solutions were prepared using sodium hydroxide pellets provided by Sulfal Química LTDA, type P.A, with a purity of 98%.

3.2 Experimental program

The activating solutions (alkaline solutions) were prepared by dissolving the NaOH in water to obtain a final concentration of 16 mol.L^{-1} , equivalent to about 17 wt.-% of Na_2O . Due to the exothermic nature of the NaOH dissolution, the solutions prepared were allowed to cool down to room temperature for at least 24h before their use.

The geopolymer mixtures were produced by mixing the fly ashes with the 16 mol.L^{-1} NaOH solution at room temperature in a mechanical mixer for 5 min with a maximum capacity of 5 liters. The ratio of fly ash to the activator solution was maintained constant close to 0.5 for both mixtures. The pastes prepared were then filled into plastic molds of 50 mm diameter and 25 mm height and vibrated for 60 seconds on a vibrating table to ensure accommodation within the molds. The molds were sealed using PVC film to prevent water loss by evaporation. After 24 hours, the plastic film was removed, and the samples were cured at 90°C for 24 h. The hardened specimens were removed from the molds and further cured at room temperature for 1, 7, and 28 days [16]. The samples produced with fly ash A (FA-A) and B (FA-B) are denominated GP-A and GP-B, respectively, further adding the time of curing. For example, sample GP- A- 7 corresponds to a sample prepared with fly ash of type A (FA-A) cured for 7 days.

3.3 Characterization of precursor materials and the geopolymer pastes

The FA samples were characterized using a Shimadzu Energy Dispersive X-Ray Fluorescence, model EDX 8000 to determine the chemical composition. The particle size distribution of the fly ashes was measured by laser diffraction analysis, Malvern Mastersizer 2000 (0.02 - 2000 μm), and the specific mass of the fly ashes was obtained with a Helium pycnometer, Micromeritics, model AccuPyc 1340 [17]. The morphology of the FA and the geopolymer samples were analyzed using scanning electron microscopy, Hitachi, model TM 300 with coupled EDS, Bruker, model X-Flash. The physical properties of the geopolymers were determined following the recommendations of the British standard BS EN ISO 10545-3 [18]. Infrared spectroscopy was carried out using a PerkinElmer Spectrometer, model Spectrum 1000. The analysis was done by mixing inorganic binder samples in powder form with KBr (1:300), compacting pellets, and analyzing the sample in the range of 400 to 4000 cm^{-1} with a resolution of 4cm^{-1} .

A total of 10 specimens for each preparation condition were used for the measurement of the compressive strength and physical analysis. The samples were characterized by uniaxial compression as described in standard NBR - 5739 [19], using a universal testing machine, Shimadzu model AG - X Plus, under a crosshead speed of 2 mm/min.

Present the physical, chemical and mechanical characterization of the materials used in the experimental program. Describe the laboratory investigations and procedures.

4. RESULTS AND DISCUSSIONS

4.1 Characterization of Fly Ash Samples

The particle size distribution of fly ash samples A and B are presented in Figure 1. The two ashes used in the process of geopolymer production exhibit different particle size distributions. The samples presented the particle size D10, D50, and D90, listed in Table 1, which correspond to the sizes of 10, 50, and 90% of the accumulated mass of the fly ash powders, respectively. The specific mass of the two FA samples is also presented in Table 1.

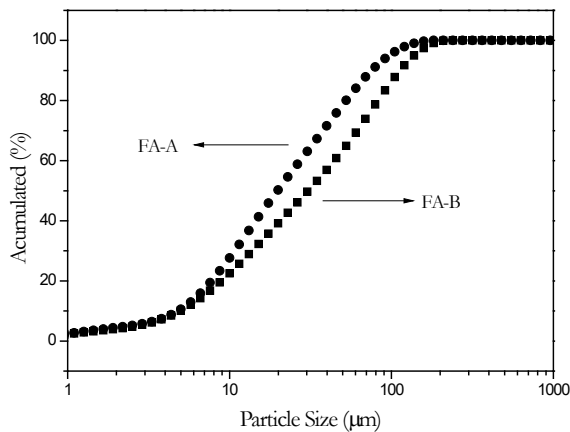


Figure 1. Particle size distribution of the fly ash samples FA-A and FA-B.

Table 1. D10, D50 and D90 equivalent sizes and specific mass of fly ash samples.

Sample	D10 (µm)	D50 (µm)	D90 (µm)	Specific mass (g/cm ³)
FA-A	4.81	19.70	75.44	2.38
FA-B	4.97	30.82	112.87	2.21

The chemical compositions of fly ash samples A and B are shown in Table 2. It is possible to see that the ashes consist basically of SiO₂, Al₂O₃, and Fe₂O₃. It was observed similar composition of the FA in the work of Azevedo et al. [17], that the authors studied the production of fly ash-based alkali-activated materials with simple and compound solutions of NaOH and Na₂SiO₃. Other chemical elements are also present in lower concentrations. According to the chemical composition, both fly ashes can be classified as type F, in which the sum of the SiO₂, Al₂O₃, and Fe₂O₃ concentrations is higher than 70% and the CaO concentration lower than 10%, according to ASTM C 618 [20]. The high concentration of Si and Al in the samples is mainly due to the mineral origin of these ashes which originate from the burning of coal. The organic matter present in the coal is decomposed at high temperatures while the inorganic material is entrained and collected by the electrostatic precipitators installed in the chimneys. This material retained is the fly ash, presenting elevated amounts of amorphous aluminosilicates, which turns the ashes susceptible to an alkaline attack to produce the AAM. The molar ratio SiO₂/Al₂O₃ is higher for fly ash A, 3.52, compared to 3.34 of fly ash B. A high SiO₂/Al₂O₃ molar ratio is desirable to promote more Si released during the dissolution process of the raw material and consequently a larger amount of N-A-S-H gel formed (AAM) [17].

Table 2. The chemical composition of fly ash samples used in the production of the alkali-activated materials.

Sample	SiO ₂ (wt.-%)	Al ₂ O ₃ (wt.-%)	Fe ₂ O ₃ (wt.-%)	Other Oxides* (wt.-%)	SiO ₂ /Al ₂ O ₃ **
FA-A	61.025	29.406	6.155	3.414	3.52
FA-B	61.546	31.234	3.884	3.336	3.34

*(ZnO, CaO, Na₂O, K₂O, MnO, Cr₂O₃, SrO, CuO, Rb₂O, Y₂O₃, PbO, Ga₂O₃, GeO₂, NiO e NbO) **Molar ratio.

Figure 2 shows SEM images of particles of FA-A and FA-B used in the production of the alkali-activated materials. Both fly ash powders present spherical particles, with sizes ranging from approximately 5 to 200 µm, consistent with the results of particle size analysis by laser diffraction analysis, see Figure 1 and Table 1.

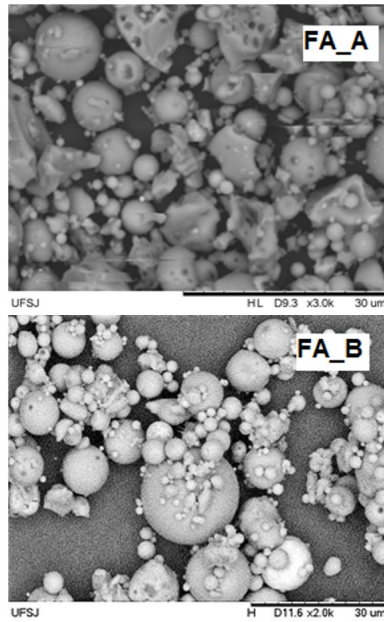


Figure 2. Scanning electron microscopy of FA-A, and FA-B.

The particles of FA-A are less homogeneous than the particles of FA-B and some non-spherical fragments are also observed, which may be produced during the milling process of the residue before its distribution by the company. The chemical composition of the fly ash samples and the EDS spectra related to the Si, Al, and Fe elements are shown in Table 3 and Figure 3. The chemical composition is similar to that found in the FRX results showed in Table 2.

Table 3. EDS analysis of FA-A and FA-B.

	Element	[at. %]
FA-A	Si	72.09
	Al	25.50
	Fe	2.41
FA-B	Si	66.56
	Al	29.62
	Fe	3.82

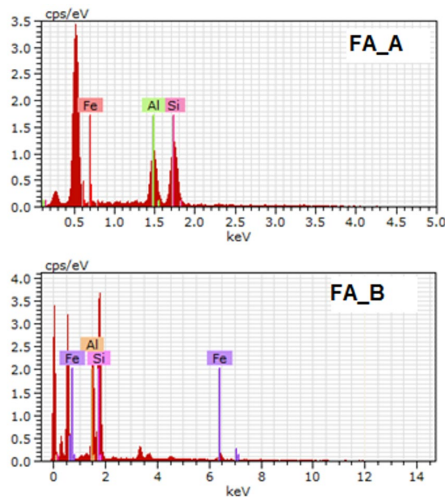


Figure 3. EDS spectra of the elements present on the surface of fly ash particles of FA-A and FA-B.

4.2 Characterization of the alkali-activated materials

4.2.1 Water absorption, porosity, and density

The results of water absorption, apparent porosity, and density of the AAM produced with fly ash samples A and B are shown in Table 4. It is possible to observe that the geopolymer matrices produced with FA-A presented higher water absorption than the materials synthesized with FA-B. The apparent porosity of the matrices GP-A and GP-B were close to 20%; the highest porosity value (21.1%) was observed for the sample GP-A-1, produced with FA-A after 1 day of curing, and the lowest (19.2%) was found when the sample was synthesized with FA-B after 7 days of curing. The density of the hardened matrices varied between 1.6 and 1.8 g/cm³, demonstrating that the new structure formed after the geopolymerisation and formation of the N-A-S-H gel presents a lower density than that observed for the original fly ash, see Table 4.

Table 4. Water absorption, apparent porosity and density of the alkali-activated materials produced with FA-A and FA-B after 1, 7 and 28 days of cure.

Sample	Water absorption (%)	Apparent porosity (%)	Density (g/cm ³)
GP-A - 1	13.2 ± 0.5	21.1 ± 0.9	1.6 ± 0.1
GP-A - 7	13.5 ± 0.5	20.7 ± 0.7	1.6 ± 0.1
GP-A - 28	12.4 ± 0.1	20.0 ± 0.2	1.6 ± 0.2
GP-B - 1	12.3 ± 0.4	20.6 ± 0.5	1.7 ± 0.1
GP-B - 7	6.4 ± 0.5	19.2 ± 0.5	1.8 ± 0.1
GP-B - 28	9.7 ± 0.3	20.2 ± 1.5	1.7 ± 0.2

4.2.2 Microstructural analysis

The scanning electron microscopy images of the AAM samples produced with fly ashes A and B are presented in Figure 4. It is possible to observe that the samples synthesized with FA-A presented a more homogeneous surface without the presence of unreacted spheres. The absence of unreacted FA particles can be related to the greater effectiveness of the dissolution of the particles found in this fly ash. The increase in the dissolution rate is linked to the improvement in the mechanical strength of the samples, as discussed below. With an increased dissolution of the fly ash particles, higher amounts of Si and Al-rich species will be released into the system, which, after the polycondensation reactions, results in a high amount of the N-A-S-H gel, which is responsible for the increase in compressive strength [21]–[24].

In the samples produced with FA-B, it is possible still to observe some spherical particles after contact with the alkaline solution. The presence of these particles may be associated with the lower dissolution of this material in the alkaline environment promoted by the 16 mol. L⁻¹ NaOH solution. The presence of the spherical particle after the contact the fly ash with the activator solution was observed in the work of Morsy et al. [25], that the authors founded fly ash particles embedded in a continuous matrix rich in Si, Al, and Na (N-A-S-H gel). The spheres present in the system are embedded in the aluminosilicate gel formed. The surface of these particles is intact, and it is possible to observe that their interior was dissolved by the alkaline activator. This fact, according to Provis et al. [5], is due to the difference in the cooling rate of these particles during the burning of mineral coal in the furnaces. According to the authors, the ash particles may have different chemical compositions even if they are next to each other. This variation is associated with the composition of the coal used in the electrical power plant and the cooling rate of the melting mass after the burning process of the coal. The rate of cooling can promote the formation of different ordered structures (long-range and short-range atomic ordering) that have different dissolution rates in the alkaline environment.

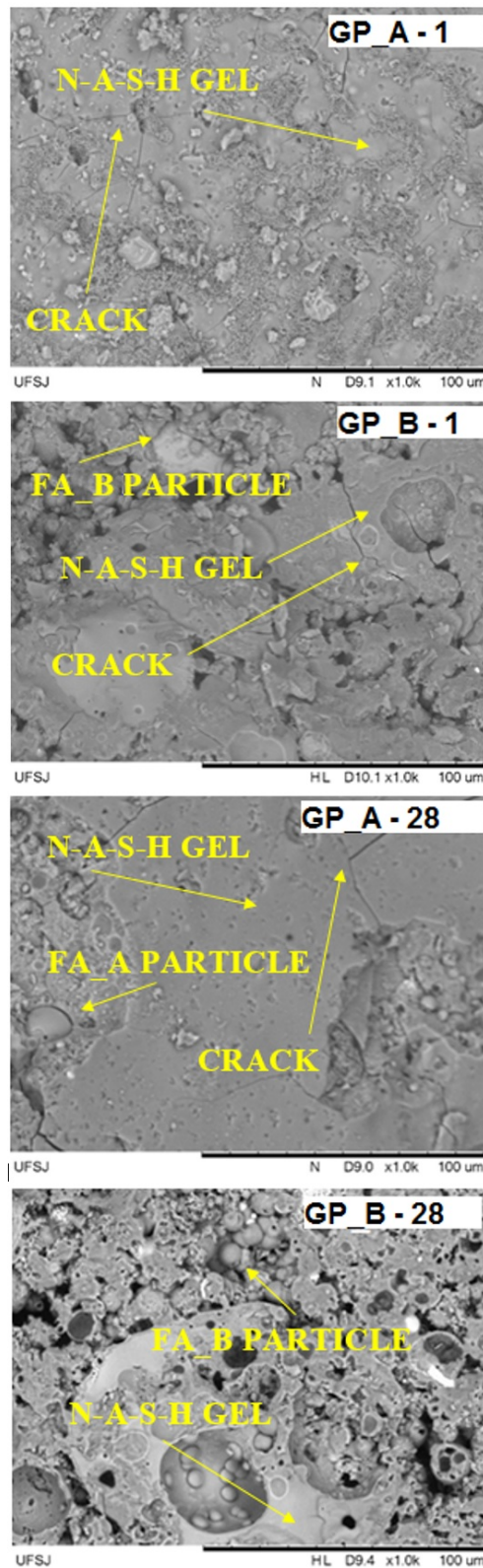


Figure 4. SEM images of the alkali-activated samples produced with the different fly ash samples after 1 (GP-A – 1 and GP-B – 1), and 28 days (GP-A – 28 and GP-B – 28), respectively.

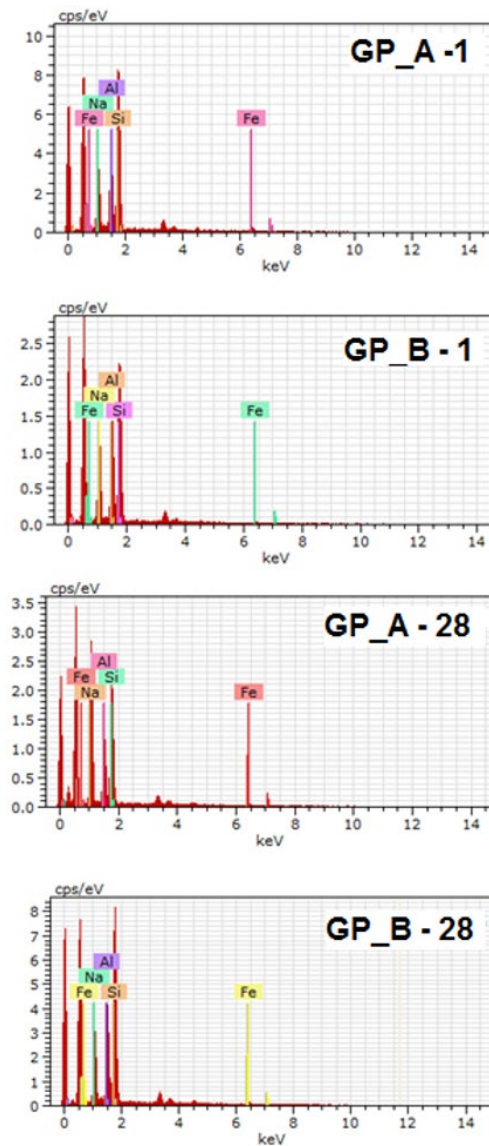


Figure 5. Spectra of the elements present on the surface of the alkali-activated samples produced with the different fly ash samples after 1 (GP-A – 1 and GP-B – 1), and 28 days (GP-A – 28 and GP-B – 28), respectively.

The use of FA samples with different chemical compositions may have favored the appearance of some particles with different atomic compositions and arrangements. This can modify the rate of dissolution, the geopolymerization reaction and, consequently, the final properties of the hardened material. After 28 days of curing, the morphology of the samples produced with both fly ashes is presented in Figure 4. The spectra of the surface elements and the chemical composition are shown in Figures 5 and Table 5, respectively. It is possible to observe a more homogeneous surface for the sample produced with FA-A, after curing for 28 days. The presence of some cracks may be associated with the polycondensation reactions that occur during the geopolymerization, characterized by the release of water molecules. The presence of a small number of unreacted FA-A particles on the surface of the sample corroborates the results observed in the samples after 24h of curing, showing that the dissolution rate was higher for the geopolymers produced with this fly ash.

In the samples produced with FA-B, some spheres of the original fly ash powder particles were observed on the surface even after curing for 28 days. This observation may be associated with a lower amount of N-A-S-H gel formed which is the main responsible for the decrease of the mechanical strength of the specimens when compared to samples produced with FA-A.

The analysis of different points on the surface of the samples after the different curing days demonstrates that a Si-Al-Na system was present in the hardened material. As shown in Table 5, the presence of Fe may be associated with unreacted fly ash

particles that remain embedded in the aluminum silicate gel. It is known that the presence of fly ash in contact with the highly alkaline environment produced by the solution promotes the dissolution of species and subsequent reorganization (geopolymer reaction). The modification of the Si/Al ratio is associated with changes in the structure of the new material produced after the geopolymerization reactions. EDS analysis showed that the Si/Al ratios present on the surfaces of the materials produced with fly ash A and B are close to 2.02 and 2.47, respectively. Considering the Si/Al ratio, it is concluded that the geopolymers formed (after the geopolymerization reactions) by FA-A have the structure of the poly(sialate-siloxo), Si/Al = 2, and the matrices produced with FA-B, a variation between poly(sialate-siloxo), Si/Al = 2 and poly(sialate-disiloxo), Si/Al = 3, respectively [21]. However, the EDS analysis shows that the amount of Na (from the NaOH solution) has its concentration increased and varies when different fly ash samples were used. During the synthesis of the geopolymers, the replacement of SiO₄ species by AlO₄ favors the appearance of a negative charge due to the coordination IV in which the Al³⁺ ion is found. The electroneutrality of the polymer network is obtained by the approximation of Na⁺ ions to the Al present in AlO₄⁻. Thus, a Na/Al ratio close to 1 corresponds to a structure in which the amount of Na and Al atoms are in the ideal proportion to obtain a stable structure after the hardening process of the pastes (electrically stable).

The Na/Al ratio of the matrices after 24 hours of curing is close to 1.0 for both samples produced with FA-A and FA-B. However, after 28 days of curing, samples produced with FA-A showed an increased Na/Al surface concentration for 2.07, as showed in Table 5. Such excess sodium on the surface of the matrices may be associated with the decrease of the mechanical strength of the specimens of GP-A after 28 days of curing. Excess Na⁺ ion in the matrices can cause deterioration of the formed polymer structure, which is reflected by the decrease of the maximum strength of the matrices. On the other hand, FA-B produced a geopolymeric matrix with a Na/Al ratio of 0.99 after 28 days of curing, demonstrates that this matrix produced with a Na and Al concentration close to the ideal and without Na⁺ in excess maintained good mechanical strength exhibiting a strength decrease of only 3.8% after 28 days of cure. Otherwise, the matrices produced with FA-A showed a decrease of strength close to 19% after the same curing period. These results show that the increase of the Na/Al ratio in the system produced with FA-A resulted in a reduction of the compressive strength near to 5 times higher when compared to the materials produced by the alkaline activation of FA-B. This increase in the amount of Na on the surface and the consequent decrease in the mechanical strength of the material can be observed by spectroscopy analysis that shows the formation of new sodium-rich phases on the material surface after 28 days of curing.

Table 5. Chemical composition of the alkali-activated materials produced with the different fly ash samples.

Sample - Curing time (days)	Element	[at.- %]	Si/Al ratio	Na/Al ratio
FA-A - 1	Si	49.77±0.1	2.02±0.2	0.99±0.3
	Al	24.61±0.2		
	Na	24.30±0.2		
	Fe	1.32±0.4		
FA-A - 28	Si	38.97±0.2	2.01±0.3	2.07±0.4
	Al	19.37±0.4		
	Na	40.24±0.5		
	Fe	1.43±0.4		
FA-B - 1	Si	52.76±0.1	2.47±0.3	1.05±0.1
	Al	21.39±0.5		
	Na	22.42±0.2		
	Fe	3.43±0.1		
FA-B - 28	Si	55.57±0.1	2.62±0.2	0.99±0.2
	Al	21.18±0.1		
	Na	21.17±0.5		
	Fe	2.08±0.4		

4.2.3 Infrared Spectroscopy (FTIR)

Figure 6 presents the infrared spectra of the original FA samples and the AAM produced with alkaline activation after 28 days of curing. The absorption bands of the fly ash and AAM at 3667 and 1641 cm⁻¹ are due to the stretching and deformation of H-O-H and O-H groups, respectively. These bands are related to weakly bound water molecules, adsorbed on the surface or trapped in the cavities of the inorganic binder [26]. Bands at 1090 and 458 cm⁻¹ are associated with the stretching and bending of Si-O or Al-O bands, respectively [27].

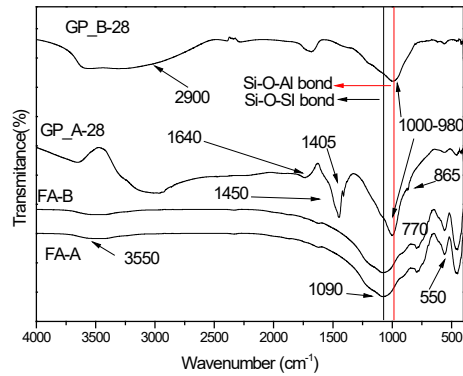


Figure 6. FTIR spectra of hardened samples produced with different fly ash samples after 28 days.

The band observed close to 1090 cm^{-1} is shifted to wavenumbers close to $1000\text{--}990\text{ cm}^{-1}$. This shift is related to the formation of N-A-S-H gel after contact with NaOH solution and presents the formation of a three-dimensional structure with cementing properties [20]. Changing the Si-O absorption band to shorter wavelengths indicates the incorporation of Al^{3+} into Si^{4+} sites. This shift was associated with the geopolymerization process and is titled as the digital inorganic polymer production process (AAM production). This is responsible for the aluminum IV-coordination formation and the necessity of metals cations to promote the electrical balance of the system, as previously mentioned [28]. The carbonation products can be associated to the band close to 1445 and 1405 cm^{-1} , and represent, according to Temujin, et. al. (2014), to the sodium carbonate (Na_2CO_3) formation [29], as represented by Equation 1. The excess sodium present in the system after the high alkaline solution mixture can reach the surface through diffusion processes and reacting with atmospheric CO_2 . The presence of this absorption band can be related to the excess of Na^+ ions previously mentioned as responsible for the decrease in the mechanical resistance of the hardened material after 28 days [30], [31].



4.2.4 Compressive strength and Young’s modulus

The mechanical strength and Young’s modulus of the AAM specimens after different curing times are presented in Table 6 and Figures 7 and 8. It is possible to observe that the different fly ash samples produced materials with different mechanical strengths. The mechanical strength value close to 88 MPa was measured for samples fabricated with FA-A after 24 hours of curing, while samples fabricated with FA-B exhibited a strength of only 44 MPa , representing a difference of approximately 50%.

Table 6. Compressive strength and elastic modulus of fly ash-based alkali-activated materials after 1, 7 and 28 days of curing.

Sample	Compressive strength (MPa)	Elastic modulus (GPa)
GP-A - 1	88.5 ± 1.1	9.0 ± 0.6
GP-A - 7	82.3 ± 1.1	8.4 ± 0.5
GP-A - 28	71.1 ± 2.1	6.9 ± 0.2
GP-B - 1	44.2 ± 4.5	4.6 ± 0.3
GP-B - 7	32.5 ± 5.0	3.6 ± 0.5
GP-B - 28	42.5 ± 1.7	4.2 ± 0.7

The same tendency has been observed for the elastic modulus of the alkali-activated samples. Samples produced with FA-A presented values close to 9.0 GPa , while samples produced using FA-B achieved only 4.6 GPa after 1 day of cure. An increase in curing time promoted changes in the values of the compressive strength and, consequently, in the elastic modulus of the samples. The increase of the ratio Si/Al in the hardened matrices is related to produce the alkali-activated material with higher mechanical strength. This can be associated with the formation of the

geopolymeric framework with more Al atoms presents in the of the silicon atoms [20]. When the curing time of the samples increased, decreasing strengths were observed, which is attributed to an excess of Na^+ and OH^- ions from the NaOH solutions that promote the deterioration of the gel N-A-S-H gel of the structure ($\text{N} = \text{Na}_2\text{O}$, $\text{A} = \text{Al}_2\text{O}_3$, $\text{S} = \text{SiO}_2$, $\text{H} = \text{H}_2\text{O}$), responsible for the mechanical strength. According to Somna et al. [21], an excess of OH^- ions in the system causes the precipitation of aluminosilicates at early stages that promote the decrease of the polymer chains formed. This precipitation is responsible for the decrease in the mechanical strength with increasing curing time, corresponding to a strength loss of about 19%, as shown in Figure 7 [17], [21].

The higher compressive strength of samples produced with FA-A can be related to two main factors:

- I. To the higher dissolution rate of FA-A particles in comparison to FA-B, as can be verified by the presence of residual original fly ash particles on the surface of the specimens GP-B, while no unreacted FA-A particles were observed in the GP-A hardened specimens, see Figure 4. From this image, it is possible to observe a homogeneous surface produced by fly ash A (GP-A), which may also be associated with a higher compressive strength due to higher formation of the N-A-S-H gel when more silicon and aluminum-rich species are released to the system due to a higher amount of FA dissolution [22].
- II. Another important factor is the $\text{SiO}_2/\text{Al}_2\text{O}_3$ ratio of the original fly ash, close to 3.52 and 3.34, for FA-A and FA-B, respectively, see Table 2. This modification in the molar ratio of $\text{SiO}_2/\text{Al}_2\text{O}_3$ may be responsible for the inferior mechanical strength observed in the samples prepared with FA-B [24]. This decrease observed in the alkali-activated products can be associated to lower silicon amount in the FA-B compared to the FA-A. The presence of more rich-silicon species during the dissolution can be responsible to form the complex structures and cyclic trimers and species with a large ring with high $\text{SiO}_2/\text{Al}_2\text{O}_3$ (Si/Al) molar ration in the hardened specimens.

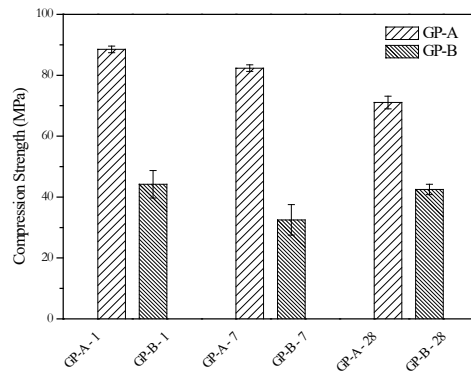


Figure 7. Compressive strength of the alkali-activated materials produced with different fly-ash samples after 1, 7 and 28 days.

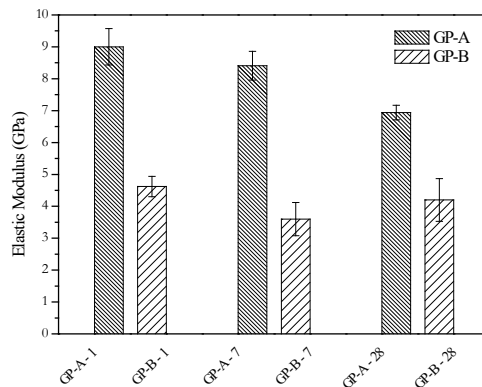


Figure 8. Elastic modulus of the alkali-activated materials produced with different fly-ash samples after 1, 7 and 28 days.

5. CONCLUSIONS

From the results obtained, it can be concluded that both fly ash samples can be used as precursor material in obtaining high mechanical strength alkali-activated materials. The different ashes used as raw material presented different chemical composition, different elemental compositions, different particle size distributions of the spherical particles, and similar surface areas. It was possible to obtain matrices with compressive strength close to 88 MPa after 24 hours of cure at room temperature. The increase in the curing time of the hardened matrices up to 28 days promoted a reduction of the mechanical strength of the GP-A matrices, which was associated with the excess of alkali present in the system after the hardening of the pastes. This alkali excess was observed by carbonation reaction products formed on the surface of samples and observed by the absorption bands in the IRFT. It was observed that the different fly ash samples resulted in materials with different mechanical strength, which has been associated with the dissolution process of the fly ash particles and the subsequent formation of the N-A-S-H gel. It was observed that the increase of Si/Al molar ration of the hardened specimens promoted the formation of the high mechanical strength due to the formation of a geopolymeric framework.

The matrices exhibited decreasing water absorption, porosity, and increasing density with increasing of the curing time. The morphology of the inorganic materials after different curing times showed a densified matrix with the presence of some fly ash particles embedded in the aluminosilicate gel. The GP-A matrices showed smaller amounts of unreacted particles, which was related to an increase in the dissolution of the particles, and a larger amount of N-A-S-H gel formed. On the other hand, the matrices produced using FA-A showed an increase in the amount of alkali on the surface after 28 days of curing, which caused a decrease in the compressive strength close to 19%. These results demonstrate that the modification of the ash produced during the production of energy in thermoelectric plants provides different characteristics in the alkali active materials produced. These variations of composition, particle size distribution, and particle morphology must be considered in the fabrication of alkali-activated binders. Alkali activation technology represents an option to replace ordinary Portland cement in some sectors of the construction industry.

ACKNOWLEDGEMENTS

The authors are grateful for the financial support from the Coordenação de Aperfeiçoamento de Pessoal de Nível Superior (CAPES).

6. CITATIONS

- [1] A. Ali, T. Job, and P. B. Nidhin, "Geopolymer as repair material," *Int. J. Innov. Res. Adv. Eng.*, vol. 3, no. 9, pp. 2349–2763, 2016.
- [2] Sindicato Nacional da Indústria do Cimento, *Relatório Anual*, Rio de Janeiro: SNIC, 2013.
- [3] F. L. Pedroso, "Concreto e construções," *IBRACON Brasil*, vol. 52, pp. 37–46, 2008.
- [4] R. Davidovits and C. James, "Proceedings of the World Congress Geopolymer," in *Géopolymère '99, 2nd Intern. Conf.*, France, Saint-Quentin, France, 1999.
- [5] J. L. Provis and J. S. J. van Deventer, *Geopolymers: Structures, Processing, Properties and Industrial Applications*, USA: Woodhead Publishing, 2009. <https://doi.org/10.1533/9781845696382>.
- [6] J. L. Provis and S. A. Bernal, "Geopolymers and related alkali-activated materials," *Annu. Rev. Mater. Res.*, vol. 44, pp. 299–327, 2014, <http://dx.doi.org/10.1146/annurev-matsci-070813-113515>.
- [7] J. Davidovits and D. Comrie, "Long term durability of hazardous toxic and nuclear waste disposals," in *Proc. 1st European Conf. Soft Miner.*, Compiègne, France, 1988, pp. 125–134.
- [8] J. Davidovits, "Geopolymer '88," in *Proc. 1st European Conf. Soft Miner.*, Compiègne, France, 1988, pp. 25–48.
- [9] A. G. S. Azevedo and K. Strecker, "Influência da Composição Química das Soluções Alcalinas Ativadoras na Produção de Geopolímeros a Base de Cinza Volante," *Rev. Eletr. Mater. Process.*, vol. 12, pp. 39–46, 2017.
- [10] M. Soutsos, A. P. Boyle, R. Vinai, A. Hadjierakleous, and S. J. Barnett, "Factors influencing the compressive strength of fly ash based geopolymers," *Constr. Build. Mater.*, vol. 110, pp. 355–368, 2016, <http://dx.doi.org/10.1016/j.conbuildmat.2015.11.045>.
- [11] W. K. Part, M. Ramli, and C. B. Cheah, "An overview on the influence of various factors on the properties of geopolymer concrete derived from industrial by-products," *Constr. Build. Mater.*, vol. 77, pp. 370–395, 2015, <http://dx.doi.org/10.1016/j.conbuildmat.2014.12.065>.
- [12] A. Fernández-Jiménez and A. Palomo, "Composition and microstructure of alkali activated fly ash binder: Effect of the activator," *Cement Concr. Res.*, vol. 35, pp. 1984–1992, 2005, <http://dx.doi.org/10.1016/j.cemconres.2005.03.003>.

- [13] M. Zhang, T. El-Korchi, G. Zhang, J. Liang, and M. Tao, "Synthesis factors affecting mechanical properties, microstructure, and chemical composition of red mud-fly ash based geopolymers," *Fuel*, vol. 134, pp. 315–325, 2014, <http://dx.doi.org/10.1016/j.fuel.2014.05.058>.
- [14] S. Andini, R. Cioffi, F. Colangelo, T. Grieco, F. Montagnaro, and L. Santoro, "Coal fly ash as raw material for the manufacture of geopolymer-based products," *Waste Manag.*, vol. 28, pp. 416–423, 2008, <http://dx.doi.org/10.1016/j.wasman.2007.02.001>.
- [15] J.G.S. van Jaarsveld, J.S.J. van Deventer, and G.C. Lukey, "The characterization of source materials in fly ash-based geopolymers," *Mater. Lett.*, vol. 57, no. 7, pp. 1272–1280, 2003, [https://doi.org/10.1016/S0167-577X\(02\)00971-0](https://doi.org/10.1016/S0167-577X(02)00971-0).
- [16] S. S. Jahromy et al., "Comparing fly ash samples from different types of incinerators for their potential as storage materials for thermochemical energy and CO₂," *Materials (Basel)*, vol. 12, pp. 3358, 2019., <http://dx.doi.org/10.3390/ma12203358>.
- [17] A. G. S. Azevedo, K. Strecker, A. G. Araújo Jr., and C. A. Silva, "Produção de geopolímeros à base de cinza volante usando soluções ativadoras com diferentes composições de Na₂O e Na₂SiO₃," *Cerâmica*, vol. 63, pp. 143–151, 2017, <http://dx.doi.org/10.1590/0366-69132017633662078>.
- [18] International Organization for Standardization, *Ceramic Tiles - Part 3 - Determination of Water Absorption, Apparent Porosity, Apparent Relative Density and Bulk Density*, EN ISO 10545-3:1998, 1998.
- [19] Associação Brasileira de Normas Técnicas, *Concreto - Ensaio de Compressão de Corpos-de-prova cilíndricos*, ABNT NBR5739:2007, 2007.
- [20] ASTM International, *Standard Specification for Coal Fly Ash and Raw or Calcined Natural Pozzolan for Use as a Mineral Admixture in Concrete*, ASTM-C 618:2001, 2001.
- [21] K. Somna, C. Jaturapitakkul, P. Kajitvichyanukul, and P. Chindapasirt, "NaOH-activated ground fly ash geopolymer cured at ambient temperature," *Fuel*, vol. 90, pp. 2118–2124, 2011, <http://dx.doi.org/10.1016/j.fuel.2011.01.018>.
- [22] A. G. S. Azevedo and K. Strecker, "Brazilian fly ash based inorganic polymers production using different alkali activator solutions," *Ceram. Int.*, vol. 43, pp. 9012–9018, 2017, <http://dx.doi.org/10.1016/j.ceramint.2017.04.044>.
- [23] P. Duxson et al., "Geopolymer technology: the current state of the art," *J. Mater. Sci.*, vol. 42, pp. 2917–2933, 2007, <http://dx.doi.org/10.1007/s10853-006-0637>.
- [24] G. Kovalchuk, A. Fernández-Jiménez, and A. Palomo, "Alkali-activated fly ash: Effect of thermal curing conditions on mechanical and microstructural development-Part II," *Fuel*, vol. 86, pp. 315–322, 2007, <http://dx.doi.org/10.1016/j.fuel.2006.07.010>.
- [25] M. S. Morsy, S. H. Alsayed, Y. Al-Salloum, and T. Almusallam, "Effect of sodium silicate to sodium hydroxide ratios on strength and microstructure of fly ash geopolymer binder," *Arab. J. Sci. Eng.*, vol. 39, pp. 4333–4339, 2014, <http://dx.doi.org/10.1007/s13369-014-1093-8>.
- [26] A. G. S. Azevedo, K. Strecker, L. A. Barros, L. F. Tonholo, and C. T. Lombardi, "Effect of curing temperature, activator solution composition and particle size in Brazilian fly-ash based geopolymer production," *Mater. Res.*, vol. 22, pp. 1–12, 2019, <http://dx.doi.org/10.1590/1980-5373-MR-2018-0842>.
- [27] A. Palomo, M. W. Grutzeck, and M. T. Blanco, "Alkali-activated fly ashes - A cement for the future," *Cement Concr. Res.*, vol. 29, pp. 1323–1329, 1999.
- [28] A. Fernández-Jiménez and A. Palomo, "Mid-infrared spectroscopic studies of alkali-activated fly ash structure," *Microporous Mesoporous Mater.*, vol. 86, pp. 207–214, 2005, <http://dx.doi.org/10.1016/j.micromeso.2005.05.057>.
- [29] J. Temuujin et al., "Utilization of radioactive high-calcium Mongolian fly ash for the preparation of alkali-activated geopolymers for safe use as construction materials," *Ceram. Int.*, vol. 40, pp. 16475–16483, 2014, <http://dx.doi.org/10.1016/j.ceramint.2014.07.157>.
- [30] W. Mozgawa and J. Deja, "Spectroscopic studies of alkaline activated slag geopolymers," *Mol. Struct.*, vol. 924–926, pp. 434–441, 2009, <http://dx.doi.org/10.1016/j.molstruc.2008.12.026>.
- [31] S. F. A. Shah, B. Chen, S. Y. Oderji, M. A. Haque, and M. R. Ahmad, "Improvement of early strength of fly ash-slag based one-part alkali activated mortar," *Constr. Build. Mater.*, vol. 246, pp. 118533, 2020, <http://dx.doi.org/10.1016/j.conbuildmat.2020.118533>.

Author contributions: AGSA, LFTD and KS: conceptualization, formal analysis, methodology, writing; AGSA and LFTD: data curation.

Editors: Edna Possan, Guilherme Aris Parsekian.



ORIGINAL ARTICLE

Analysis of mortar coating with different types and proportions of chemical admixtures that have water retentivity properties

Análise de argamassas de revestimento com variação do tipo e concentração de aditivos com propriedades retentoras de água

Alessandra Tolentino Souza^a Catharina de Almeida Carvalhais^a White José dos Santos^a ^aUniversidade Federal de Minas Gerais – UFMG, Departamento de Engenharia de Materiais e Construção, Belo Horizonte, MG, Brasil

Received 7 May 2020

Accepted 15 January 2021

Abstract: Water retaining agents are the main admixtures used to retain water against evaporation and substrate suction, and there are several chemical compounds for this purpose. To deepen the knowledge of mortar admixtures, several concentrations (0%, 1.5%, 5%, 10% and 15%) of three different types of admixtures were studied: an acrylic polymer, a cellulosic and ethylene vinyl acetate. Fresh properties (consistency, water retention, density and incorporated air), physical indexes (density and porosity) and compressive strength at 28 days were analyzed. It has been found that admixtures can act in different ways on mortars depending on the type of chemical agent used and can significantly affect the mechanical and durability characteristics in the fresh and hardened state. With this work it was verified the importance of searching references about the influence of chemical compounds before using it.

Keywords: coating mortar, water retaining, admixture proportion, performance.

Resumo: Os retentores de água são os principais aditivos utilizados para reter água frente a evaporação e a sucção do substrato, existindo diversos compostos químicos para essa finalidade. Com o intuito de aprofundar os conhecimentos dos aditivos nas argamassas, estudou-se várias concentrações (0%, 1.5%, 5%, 10% e 15%) de três tipos diferentes de aditivos: um polímero acrílico, um celulósico e um polímero de acetato vinil etileno. Foram analisadas propriedades no estado fresco (consistência, retenção de água, densidade e ar incorporado), índices físicos (densidade endurecida e porosidade) e a resistência à compressão com 28 dias. Verificou-se que os aditivos podem atuar de diversas formas nas argamassas dependendo do tipo de agente químico utilizado, podendo afetar significativamente as características mecânicas e de durabilidade no estado fresco e endurecido. Com o trabalho, verificou-se a importância de buscar referências sobre a influência dos compostos químicos antes da utilização.

Palavras-chave: argamassa, retentor de água, proporção dos aditivos, performance.

How to cite: A. T. Souza, C. A. Carvalhais, and W. J. Santos, “Analysis of mortar coating with different types and proportions of chemical admixtures that have water retentivity properties,” *Rev. IBRACON Estrut. Mater.*, vol. 14, no. 6, e14602, 2021, <https://doi.org/10.1590/S1983-41952021000600002>

1 INTRODUCTION

Water retaining agents are widely used on coating mortars, mainly, to retain water during the dehydration process caused by substrate suction or caused by evaporation into the atmosphere due to climate agents [1], [2]. These phenomena may result in an inefficient hydration of cementitious compounds, decreasing mechanical and durability properties of mortars [3]–[5].

Corresponding author: White José dos Santos. E-mail: white.santos@denc.ufmg.br

Financial support: None.

Conflict of interest: Nothing to declare.



This is an Open Access article distributed under the terms of the Creative Commons Attribution License, which permits unrestricted use, distribution, and reproduction in any medium, provided the original work is properly cited.

The best known and most used water retaining admixture are cellulose ethers: Hydroxypropyl methyl cellulose (HPMC/MHPC), hydroxyethyl methyl cellulose (HEMC/MHEC), hydroxyethyl cellulose (HEC), hydroxypropyl cellulose (HPC), methyl cellulose (MC) [2], [5]–[7]. However, there are other types of compounds used for this function, such as Superabsorbent polymers (SAP), a polymeric group capable of retaining part of the kneading water, which is gradually released during the hydration process [6]; guar ether; starch ether [8]; natural gums, silica fume and bentonite.

Current research indicates that depending on the type of admixture used, there may be great variability in their properties' results [9], [10], even with compounds with the same chemical name [11]. Viscosity, molar mass and/or nature and quantity of chemical substitution groups can be responsible for these variations [12]. For example, the increase in the molar mass of an additive can directly affect the increase in mortar viscosity [13]. It is important to note that water retainers can act differently in cement mortars (cement: sand: water) and mixed mortars (cement: hydraulic lime: sand: water) [8]. On mixed mortars, the excessive water or trapped water can prevent CO₂ from penetrating the mortar, slowing carbonation process [13]–[15]. Studies showed that the same type of cellulosic (HPMC) can present different percentages of water retention, according to the length of the molecular chain of the additive used and the dosage [16], [17]. This variation could reach up to 14% when comparing different types of cellulosic products [13]. The more water retaining added to the mixture, greater the ability to incorporate air of mortar [8]. With the incorporated air increase, density [17] and mechanical resistance of the mortar decrease since pores are weakening points of the material. The lower elastic modulus is also related with the increase in the air incorporation [8] and it can be favorable in reducing pathologies due to structural deformations or land settlement [16]. The water retainer also affects, secondarily, by slowing the setting of the cement, because, inorganic compounds, such as cellulose ether, added to cement paste demonstrate affinity to cement hydration products [18].

Due to the exposed facts, it is important to know the chemical additive which will be added to the mortar, or even carry out a previous analysis of the influence of it on mortar's properties to achieve the desired results of designed properties [9]. This study intended to research the properties of three different types of admixtures with potential to act as a water retainer: hydroxyethyl methyl cellulose (HEMC), vinyl acetate and ethylene polymer (pAVE) and acrylic polymer (pA), varying their content (including over dosage). HEMC is a hydroxyethyl methyl cellulosic commonly used in mortars for its excellent water retention at low dosage [19]. It could also be used in fiber cement, fine mortars (adhesive) and adhesives for cement-based tiles. pAVE is a copolymer of vinyl acetate and ethylene [20] dispersible in water and it has good resistance to saponification. Its main activities are in improving adhesion, flexural strength, deformability, abrasion resistance, maximizing its use in adhesive mortars, grouts and plasterboards glues. However, studies [21], [22] showed the potential of this admixture for use as water retainer.

pA is a polymeric adhesive based on acrylic for stabilized and productive mortars [23] generally used in plastering and masonry laying, stabilized light mortars, smoothing and filling layers, and mortars for underlay. It tends to improve the adherence of the mortar on the substrate, the workability, the water retention, the cohesion and thereby reduce the shrinkage cracks [23].

These three admixtures are marketed as water retainers, however, though previous research [9], [10] it was identified that some did not have enough retention. It is also important to note that the dosages are variable in the research [2], [5]–[8], [13], [18], [21], [22], and because of this it can generate different influences on mortars. Therefore, it was decided to carry out this research to investigate the dosage and efficiency of each admixture exposed. Most studies of admixtures are in concrete or micro concrete for structural purposes, there are few references with typical situations of coating mortars (thin layer subjected to substrate suction and insolation), so it is essential to verify how each admixture behaves in coating mortar as regards properties in fresh and hardened state, so more suitable coating mortars can be used. Therefore, this study tended to establish a comparison between the admixtures, highlighting the differences and similarities between each one in properties in the fresh state: consistency, fresh state density and water retention; physical indexes: density in the hardened state, theoretical incorporated air and theoretical porosity; and compressive strength at 28 days. It was also proposed, when it was possible, equations for approximating the behavior of each mortar.

2 MATERIALS AND EXPERIMENTAL PROGRAM

The cement used was CP II-F 32 (Brazilian ordinary Portland cement with 10% addition of limestone powder), of chemical and physical composition expressed in Table 1, with specific gravity of 3100 kg/m³ and bulk density of 1700 kg/m³.

Table 1. Chemical and Physical characteristics of cement and hydraulic lime

Material	SiO ₂ (%)	Al ₂ O ₃ (%)	Fe ₂ O ₃ (%)	CaO (%)	MgO (%)	LOI (%)	D ₁₀ (µm)	D ₅₀ (µm)	D ₉₀ (µm)
Cement	18.97	4.21	2.81	64.52	2.01	5.21	5.3	22	63
Hydraulic Lime	1.88	0,26	0.22	49.35	26.45	21.74	0.47	4.28	30.84

This type of cement was chosen because it does not have potentially reactive mineral additions that can affect the behavior of admixtures. The hydraulic lime was used to assess whether the retention measurement time influenced this parameter. Was used Brazilian CH I, with physical and chemical composition expressed in Table 1, with specific mass of 2800 kg/m³ and bulk density of 800 kg/m³. This hydraulic lime has certification of 0% of non-hydrated oxides in its composition, according to the supplier. The sand used was natural quartz sand from the riverbed: well graded, its main characteristics are shown in Table 2 and Figure 1.

The chemical composition was determined by X-ray fluorescence (XRF) and loss on ignition was determined by calcination of the sample at 405 °C and/or 1000 °C, using the method PHY01E: LOI (Loss on ignition). To determine the particle size distribution of the material a laser diffraction granulometer (Sympatec Helos 12LA) was used along with a 50 mm lens and 0.05% sodium hexametaphosphate dispersant. In addition, a helium gas pycnometer (Quantachrome SPY-3) was used to determine the specific mass of the material.

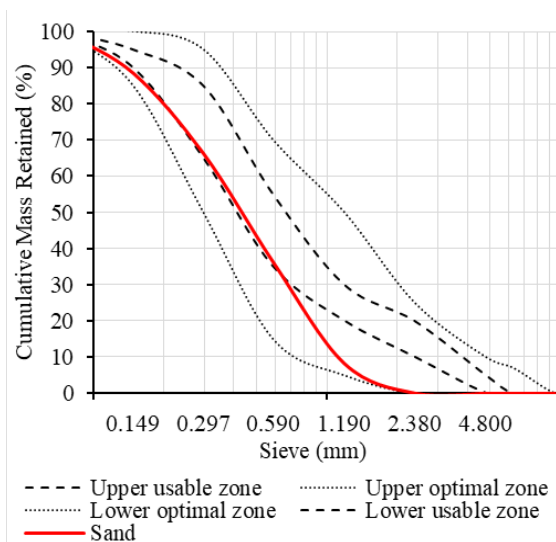


Figure 1. Fine aggregate particle size distribution.

Table 2. Fine aggregate characteristics

Fine aggregate	
Specific gravity (kg/m ³)	2584
Bulk density (kg/m ³)	1283
Fineness Modulus	1.995
Maximum diameter (mm)	2.4

The mix proportion adopted for the analyzed mixtures was 1:5:1.83 (cement: sand: water by volume), according to the prescriptions established in Santos’ methodology [24] which considered the amount of binder according to the voids between the aggregate particles, established through the characteristic’s distribution of cement and sand. The proportions of admixtures used were 0% (reference, without admixture), 1.5%, 5%, 10% and 15% in relation to the cement mass for each type of admixture: acrylic polymer (pA), vinyl acetate polymer and ethylene (pAVE) and hydroxyethyl methyl cellulose (HEMC). The proportions adopted were chosen due to the correlations established with the proportions found in the literature and through manufactures’ specifications for the studied admixtures [19], [20], [23], [25]. The main characteristics of admixtures

are shown in Table 3, the density of cellulosic ether is not specified in the product's technical sheet. The amount of water used was 15.26% of the total dry material, and came from public supply, which is acceptable for use in the dosage of cementitious materials without requiring prior analysis, according to NBR 15900-1 [26].

Table 3. Admixture's characteristics

Name	Density (Kg/m ³)	Type	Chemical base
pA	1000	Liquid	Acrylic polymer
pAVE	540	Powder	Vinyl acetate and ethylene polymer
HEMC	-	Powder	Hydroxyethyl methyl cellulose

Two of the three admixtures used were in powder form and therefore must be previously added with dry materials (cement and sand). So, they were mixed for 30 seconds and then water was added, continuing the mixing process for another 3 minutes. For mixing the acrylic polymer, as it is in liquid form, it must be diluted in part of the mixing water. Therefore, first the cement and sand were added and mixed for 30 seconds, then the water and the diluted admixture were added, and the mixing procedure continues for more 3 minutes. All mixing processes occurred for 3 minutes and 30 seconds in total.

After the mixing process, the mortars were tested on the Flow-Table [27] to obtain consistency. And water retention was obtained through NBR 13277 [28], measuring the capacity of the mortar to retain water under the action of suctioning paper filters under the pressure of a standardized weight of 2 kg. Mortar and paper filters were weighed with the aid of a 0.001g precision balance. For each of the three polymers proportion were molded 3 samples of the same mortar-mix to obtain the results variability.

Regarding water retention, it was also analyzed whether the test measurement time can influence the results, so that the most appropriate retention value for the method used can be measured. For this comparison, a mixed mortar was used with proportion of 1.00:1.08:4.41:1.82 (cement: hydraulic lime: sand: water by volume), proportion from Souza's [29] previous research, which considered particle size of cement, sand and hydraulic lime. This proportion was compared with a cement mortar with 1.5% of acrylic polymer. The cement mortar was made using the same process as for powder admixtures [29], which considered characteristics of cement, sand and water, by same mix designer method of mortar without lime. It was water retention measures were made per time in 0, 15, 30 and 60 minutes.

The physical indexes analyzed were: density in the fresh and hardened state [30], theoretical incorporated air and theoretical porosity. The theoretical parameters were obtained through the relationship between the density of the materials used, without considering the voids, with the density in the fresh state (to obtain the theoretical incorporated air) and, to obtain the theoretical porosity, with density in the hardened state. The hardened specific mass method used four cylindrical samples (5x10) cm, for each mixture, which were kept for 24 hours in an electric oven at (100 ± 5) °C to remove any loose water, when the stability of the mass was verified. A precision balance weight of 0.01 g was used to measure the samples. The theoretical specific mass was acquired by the ratio of materials, cement (m_c), sand (m_s), admixture (m_a) and water (m_w), of a given volume of specimen (v_c). The theoretical porosity was obtained through Equation 1, through the relation of hardened state density (μ_h) and theoretical specific mass.

$$P_t = 100 \times \left\{ 1 - \left\{ \mu_h / \left[(m_c + m_s + m_a + m_w) / v_c \right] \right\} \right\} \quad (1)$$

Compressive strength was evaluated according to NBR 7215 [31] with a loading rate of (500 ± 10) N/s in the EMIC DL 30000 N universal machine. The cylindrical samples to measure specific mass and compressive strength are 10cm height and 5 cm diameter. Mortars were molded in two layers with 12 strokes in each one for a proper densification. After 48 hours of molding, the samples were unmolded and remained in laboratory environment, with an average temperature of 24 °C and relative humidity of 60% for more 26 days before testing density in the hardened state and compressive strength.

3 RESULTS AND DISCUSSIONS

3.1 Consistency

All tested mixtures (0%, 1.5%, 5%, 10% and 15%) were submitted to the consistency experiment by the Flow- Table [27]. According to Figure 2, it is possible to see the behavior of HEMC, pA and pAVE admixtures in mortar consistency. All samples have a reference consistency of 216 mm (0% admixture).

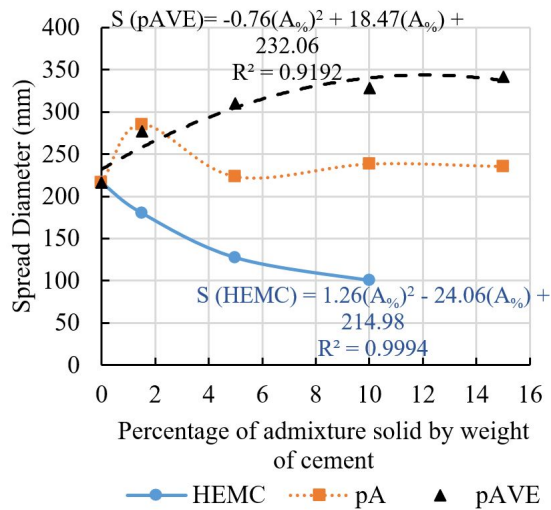


Figure 2. Flow-Table results.

First, it is possible to observe in Figure 2 that cellulosic (HEMC) was responsible for a representative drop (50%) in consistency. Higher the concentration of this admixture, drier the mixture was found [2], [32], [33]. So, it was impossible to carry out the experiment for 15% dosage of HEMC, as the mortar was extremely dry and had a stick aspect, the mechanical mixer used was unable to complete the mixing procedure proposed in item 2. The spread diameter for 10% of HEMC was the same of the cone (100 mm), as the mixture did not spread with the 30 falls of the table (Figure 3).



Figure 3. Spread Diameter HEMC – 10% (a), pAve – 10% (b).

Cellulose ethers can act through three mechanisms: adsorption, association and entanglement [34]. However, it is noticeable that the most significant effect of this admixture is the association with water molecules, generating a mortar gel, and significantly increasing the consistency and cohesion of coating mortars as found in the bibliography [5], [6], [35], [36]. This mechanism was verified in the mixing process, in which the mortar had a sticky aspect (high cohesion), and it was difficult to mix in high dosages of HEMC.

Through the results of the mixtures with pAVE (Figure 2) it was possible to see that the spreading diameter increases considerably (36.48%) with the increase of the concentration of the admixture, reaching up to 342 mm with 15% dosage, being its behavior contrary to HEMC admixture, which can be seen in Figure 3, where both have the same concentration.

Such behavior justifies the use indicated in the bibliography [6], [21], [22], [35], demonstrating performance also as a plasticizer, increasing the consistency. It is noticed that this admixture acts through the entanglement of polymeric molecules, which in high concentrations, and suffering the stresses of the spreading table, fluidized the material [37], explaining the increase in the spreading diameter with the higher dosage of the admixture. It presented a more pronounced increase of spread diameter (22%) up to 1.5% of admixture, decreasing its rate of fluidization after this concentration. The behavior of this type of admixture is associated with entanglement with water molecules, increasing the initial apparent viscosity that tends to disappear when subject to stresses, fluidizing the material and increasing its consistency [6], [35].

The admixture pA did not significantly influence the consistency of mortars. Disregarding the outliers' values, it is possible to observe a linear behavior close do 240 mm, as seen in Figure 2. It appears that despite the supplier [23] disclosing improvements in workability it was not observed in the results, not showing a significant variation. The acrylic polymer (pA) is classified as a Superabsorbent polymer (SAP), which has the association retention mechanism, by trapping surrounding water in its structure, which is gradually released during the curing process. This association leads to the formation of a gel and increase the viscosity of the mixture [6], [37]. Despite these characteristics, this behavior was not observed in this study, and the consistency remained practically unchanged, similar to the mixture without admixture, as observed by João [38].

The consistencies showed great variability among the admixtures and dosages used considering the amount of water fixed in the mixture. According to Bauer et al. [39] *Flow-Table* method has great variability, and therefore mortars with spreading diameter between 190 mm and 290 mm by this method would be within a range suitable for use as coating mortar. Analyzing the results by this interval [39], it is observed that for concentrations below about 1% of HEMC, 3.5% of pAVE and all pA concentrations the mortar would be suitable for use as a coating. The adequate consistency for external coating mortars according to Santos et al. [24], must have spread diameter of 260 ± 10 mm. The consistencies that reached closest to this range is up to 1.5% of pAVE, and for the cellulosic, the value of 1.5% still has a low spread diameter (180 mm) generating dry mortars. For this reason, it is recommended to study lower dosages of HEMC to verify this behavior. Thus, to achieve the desired consistency for external coating proposed, the lowest dosages of all polymers used are the most suitable.

3.2 Water retention

Figure 4 shows the behavior of each admixture tested relating to water retention measured according to NBR 13277 [28]. The water retention property in mortars is particularly important due to the suction of water by the substrate because the coating mortar that loses a lot of water will not have enough water to react with the cement, compromising the adherence [40] due to the high retraction and the promotion of a powdery coating.

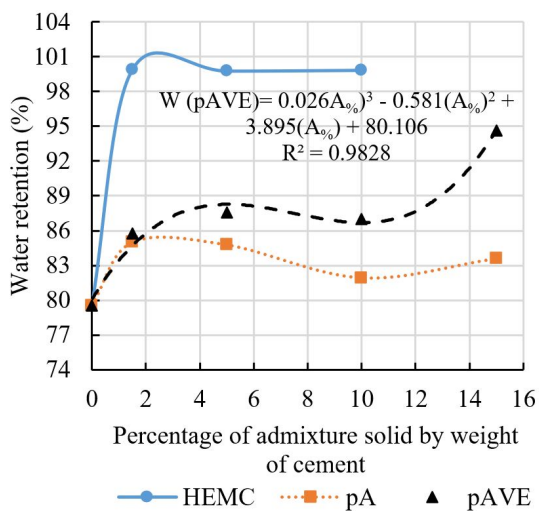


Figure 4. Water retention results

It is observed that all mortars obtained a result higher than the reference (79.5% of retention). HEMC cellulosic obtained the highest water retention results in comparison to the other compounds, samples already showed high water retention (99.9%) with 1.5% of this admixture, and the highest concentrations 5%, 10% and 15% maintained the standard presented with 1.5%. It is noteworthy that the sample with 10% of admixture were extremely dry, due to the formation of a gel that significantly increased the consistency and cohesion of the coating mortar as verified in bibliography [5], [6], [35], [36]. Thus, the result presented 100% retention due to dry consistency, and this property could not be measured by the Flow-Table, as it did not present any spread with table drops. However, it is important to emphasize that extremely high-water retentions must be studied with caution, case of HEMC, as values above 96% may be unsuitable for the mechanical adherence of the mortar, since the substrate will not be able to absorb the necessary water for anchoring reactions [41], as the retention mechanism would be predominant over the absorption of the substrate. Thus, for a complete analysis of the influence of the cellulose ether retention, an analysis is recommended between results of tensile bond strength versus water retention, varying the type of admixture used and its concentration (less than that tested in this work).

PAVE was the second compound with the highest retention results, this behavior was associated with the interlacing mechanism of water retention, even with the fluidity presented on Flow-Table. It was observed an increase in water retention from 0% to 1.5%, where the results stabilize at approximately 86.5%, then continue to grow at 15% concentration, reaching 94.6% of water retention. As seen in Figure 3, the sample was fluid and even so presented high water retention. This demonstrates that the increase in the concentration of pAVE is directly related to the increase in the water retention and consistency, due to the plasticizer effect of the admixture.

With the water retention of acrylic polymer, it is possible to see that this admixture did not presented a similar behavior with any of the other samples, being its highest result 85% at 1.5% concentration, presenting a little loss of water retention with the increase of concentration of pA. Lower water retention is associated with non-variation of spread diameter in Flow-Table. Despite being a superabsorbent polymer (SAP), the effective action of its mechanism by the increase of viscosity of the sample was not observed. This affected the water retention as this mixture did not trapped such water as the other mixtures. However, despite this, it is observed that pA obtained greater retention compared with the reference mortar, without admixture.

Thus, this study observed that the results of retention using various compounds can vary from 100% to 85%. Due to the older methodology used and the great variability of results, the question about the validity of the method arose. Do Ó and Bauer [42] established that with the methodology used in NBR 13277 [28], there is the confinement and gravitational weight of the sample preventing water loss, and thus this method would present higher water retention results. The authors also established that the water retention analysis should not be made punctual on time, right after dosing it, but performed over time until the stabilization is verified. Thus, water retention, using the method adopted, was measured again for mixtures of 1.5% pA (lowest results) and a mixed mortar, mixture was measured at times 0, 15, 30 and 60 minutes with the intention of verifying the variation of the results over time (Figure 5).

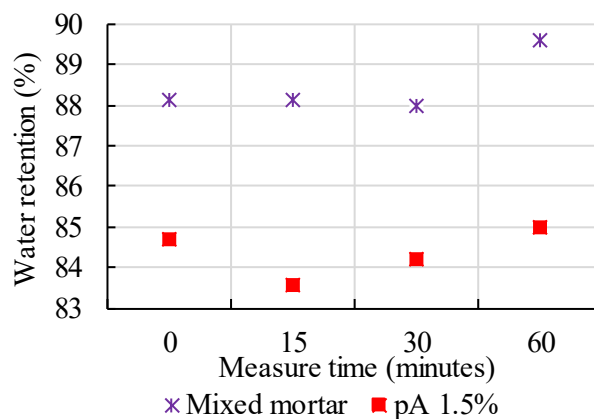


Figure 5. Water retention: mixed mortar x pA 1.5%, measured through time.

Figure 5 showed that results did not present a large variation of water retentions through time. The results, in both studied samples, only obtained a slight increase when they were measured after 1 hour of placement at the mold, which means that the mortar was already drying, and because of that the filter was not able to suck the water, inducing the test to indicate greater water retention. Since, if the 60 minutes result was removed, it is feasible to approach the results on a straight line. Thus, from the results obtained, it is concluded that time does not influence the measures taken and that they could be done right after the mortars were dosed, without compromising the results.

Due to the questioning of the method used presents inferior results compared with the retention of the suction method of NBR 13277 [28] revision of 2005. Through bibliographic review it was verified that Forti [43] and Hermann and Rocha [44] obtained inferior results for mixed mortar (78.05%) and mortar with admixture (52.2%) than those obtained by the old study standard (Figure 5). Therefore, the results presented are adequate according to the method, and to establish a comparison with other studies, it is important that they have been carried out by a similar method to the one employed in this research [45].

With all the questions exposed and the results obtained, it can be seen that the studied admixtures can have high retention depending on the chemical type used [13], [16], and they can have great variability of results between them, varying according to the chemical used and its characteristics.

3.3 Fresh state density and air entrained

Figure 6 presented the results of fresh density of the studied samples. It is observed that the results of HEMC showed the greatest drop in density in relation to the 0% reference (1950 kg/m³), approximately 35% decrease, density rise a little and established around 1554 kg/m³. Mortars with cellulosic are known for their low density [17], similar to that obtained in comparison to other samples. In this property (Figure 6), it was not possible to establish a behavior equation of HEMC, since all proposed equations had different behavior from that presented by data. In addition, Santos [46] established that a mortar suitable for application at external coatings must have a density in fresh state greater than 1600 kg/m³, so that all results presented are below the proposed limit of suitability.

PAVE, unlike HEMC, presented the highest densities among the three admixtures studied. It is observed through the consistency presented by the mixture that the fluidization of the mortar resulted in a better particle packing, favoring a better densification and a higher fresh density. It presented similar result to the 0% reference sample (1950 kg/m³). The results are close to 1900 kg/m³, only at 1.5% concentration of pAVE that this behavior is not seen, obtaining 1700 kg/m³. Similar to HEMC, it was not possible to approach the results with a tendency curve.

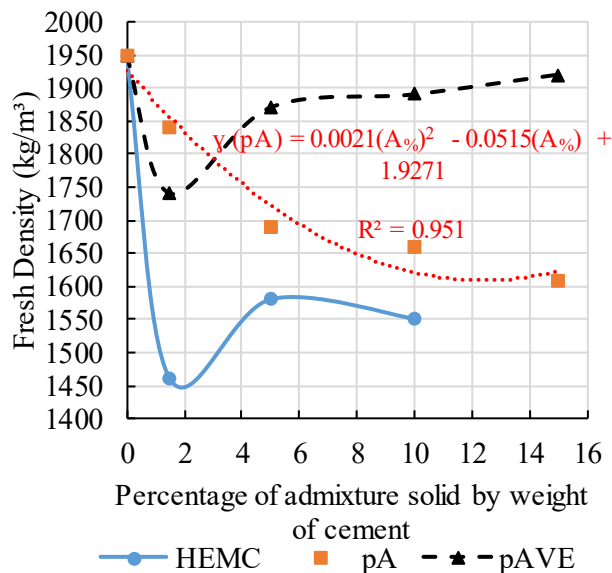


Figure 6. Fresh density results.

PAVE tends to incorporate more air, as seen in Figure 7, at lower concentrations reducing density, while at higher concentrations the plasticity gain tends to maintain density. PA admixture obtained intermediary results when compared with the other polymers used, and it also has a more pronounced density decrease between 0% and 5%, and the decay rate begins to decrease above 5% of its concentration. This decrease is linked to the greater air incorporation promoted by pA, which, by releasing the water associated in the polymeric chain, generates spherical pores [6]. However, when an equilibrium at consistency is observed, above 5%, it is also observed that density stabilizes, as consistency was not strongly influenced, density followed the same behavior.

Making a parallel between density in the fresh state, Figure 6, and consistency, Figure 2, it is possible to note that the mixture with the lowest spread diameter (HEMC), and the mixture with the greatest spread diameter (pAVE) were those that obtained the lowest density and the highest density respectively. And pA, as there was no great variation in spread diameter, the consistency remained with an intermediate result compared with others samples. This behavior is associated with the facility of sample densification in the molds, when the mixture is dry, with low spread diameter, it will be more difficult to densify it, and because of this more voids could appear, thus decreasing sample density.

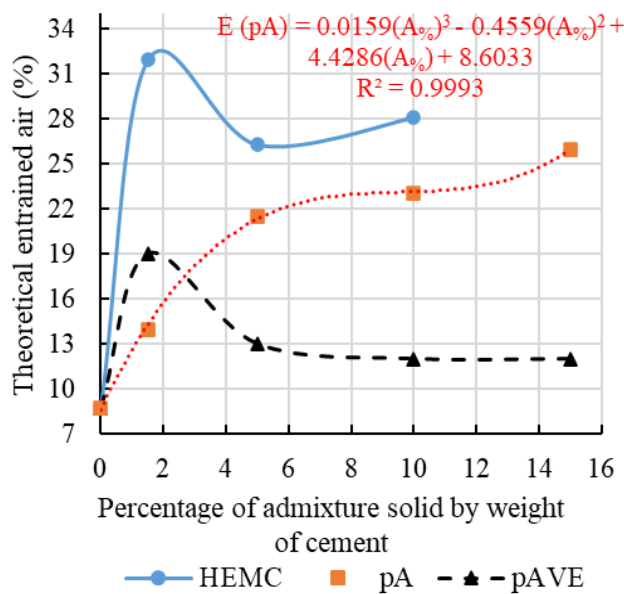


Figure 7. Theoretical entrained air results.

The incorporated air, as mentioned in item 2, was obtained theoretically through the relationship between the density in the fresh state and the proportion of the materials versus the specific mass of the materials used (cement, sand, admixture and water), with this procedure the results presented in Figure 7 were obtained.

As expected, due to the results obtained in fresh state density (Figure 6), HEMC cellulosic was the one that incorporated more air into the mixture, reaching an expressive result of 32% at 1.5% dosage, around 350% higher than reference (9% of incorporated air). However, with the increase in concentration, there is a slight drop in the incorporated air to 26%. In 10% concentration, the result start to increase again. This variation may be associated with the difficult in molding its samples, because the mixture was extremely dry and with high cohesion because of forming a Strong gel and/or strengthening gel formed by the mineral particles presented in the mortar [8]. Cellulose ethers are well known for incorporating air into the mixture [2], and due to this it obtained higher air incorporation compared with the other compounds. HEMC did not possess a trend behavior it was not possible so establish a curve for its air incorporation. However, it is possible to see a correlation between the results of HEMC in water retention, Figure 4, with theoretical air incorporation, Figure 7 as, more the mixture incorporates air, greater the water retention capacity [8], obtaining high water retention (above 94%) with the air incorporation above 25%. However, the behavior relating the highest retention to the highest theoretical incorporated air is not valid for pAVE or pA. So, even the action mechanisms were similar, they act differently in each sample.

Admixture pAVE incorporated more air with 1.5% concentration (19%), as seen in HEMC, but the incorporated air decreased with the increase of its concentration, above 5%, stabilizing the result by around 12% of incorporated air. Even with a 15% concentration of the admixture, which achieved a retention peak of 95%, the incorporated air remained at 12%. Analysing the theoretical incorporated air, it is observed a similar behaviour to fresh state density, however inverse, since this result is obtained through this parameter. It is also possible to associate the incorporated air with the consistency increase of pAVE, its highest content of incorporated air was obtained when the data had a more accentuated growth (1.5%), after this value it is noticed a stabilization of incorporated air and consistency. As already explained the higher content of incorporated air in HEMC, despite the mixture being dry, it was due this reason and the difficult of densification.

pA admixture, despite not having influenced the consistency, was responsible for the greater incorporation of air in the mixture, explaining the decrease in density. For mixtures with a higher content of incorporated air, the Flow-Table method may not evaluate the consistency adequately, as the air is able to absorb the impacts generated by the table, presenting the same consistency for a better workability [39], explaining the equilibrium of consistency presented by pA. From the pA behaviour, it is observed that it was the only compound that presented a more uniform growth with the variation of concentration of the Polymer. The air incorporation increases more sharply up to 5% of utilization (22% of incorporated air), and continues to increase, with a lower rate, up to 15% (26% of air incorporated). Presenting, between the three polymers studied, an intermediate air incorporation. These being a more significant effect of air incorporation of this Polymer, this being a basic condition to reduce density, however without affecting the consistency and water retention, by the evaluated methods.

3.4 Hardened state density and porosity

Figure 8 presents the results of hardened state density of the samples, being the reference 1800 kg/m³. In general, the results presented are similar to those presented in the fresh state density (Figure 6), as the two properties are linked, the difference between them being characterized by matrix stiffening and evaporation of water, which favours density decrease of the samples. It is also noted that the density decrease in the hardened state compared with the fresh state is a behaviour presented by all samples, presenting little differences of behaviour, associated with the secondary effect of air incorporation (Figure 7), generating greater porosity (Figure 9) and thus reducing the density of the samples.

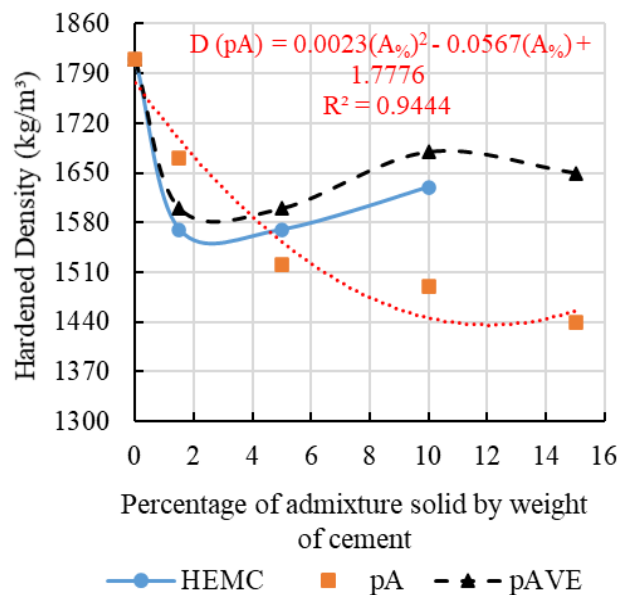


Figure 8. Hardened Density results

HEMC results showed a variation of its behaviour compared with density in the fresh state, sample had decrease of 13.33% of its density, less accentuated until 1.5% concentration, and subsequently, the results increase, except in the last concentration studied (10%). Until 5% concentration of HEMC, it is responsible for the lowest sample densities,

after this interval pA obtained the lowest results. It is believed that HEMC associated with the water, reducing consistency (Figure 2) due to the formation of a gel that traps the water, generating isolated pores, and due to the difficult of densification because of the drier consistency of mortars. This trapped water evaporated after a while, being responsible for the decrease of this property. Polymer pAVE presented similar behaviour with HEMC until 5% of its concentration, presenting intermediary results of density in the hardened state when compared with the other polymers, and above this percentage it presented the highest hardened densities among all the samples. It is observed that, as well as the fresh state density of pAVE, the hardened state density presented a considerable decrease between 0% and 1.5% and above this concentration the results fluctuates between 1600 kg/m³ and 1700 kg/m³ (in other words, it remained constant), 11% below the result of fresh state density. This result is justified due to the greater air incorporation (Figure 7) at lower concentrations of this Polymer, reducing density, while at higher concentration the gain in plasticity tended to maintain density due to the better densification and less demand for kneading water. Polymer pA maintained the same behaviour for density in the hardened state (Figure 8), which it presented in the fresh state density (Figure 6). There was observed a density decrease of 11%, at 15% concentration of the Polymer, when density in the fresh state and hardened state are compared. Whit up to 5% of this polymer, it is responsible for the highest results of density in the hardened state, and with concentration above 5% it presented the lowest results of hardened density. The effect of incorporating air promoted by the admixture pA becomes more evident in this property and in the porosity, generating proportional decrease of density with the increase in its content.

The behaviour of the samples in density in the hardened state follows the same behaviour presented in density in the fresh state, only HEMC admixture that presented a smaller variation between the fresh and the hardened density than the other admixtures, this is due to the samples already presented low density because of the voids left by densification, as it was dry, because of this there was less variation in density in the hardened state.

All the results found for density in the hardened state characterized mortars suitable for use as external coating, as they have hardened density greater than 1400 kg/m³ [24].

Theoretical porosity, as well as the air incorporated, were obtained through the relation between density in the hardened state and the specific mass of materials used. In Figure 9, the results of porosity for HEMC, pA and pAVE are presented.

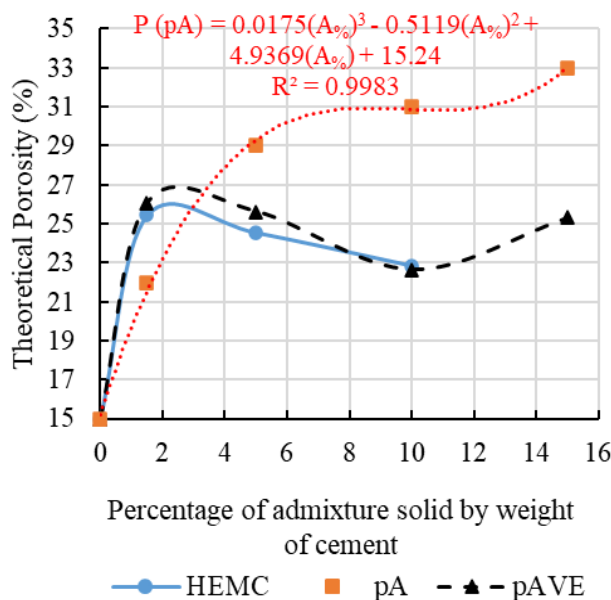


Figure 9. Theoretical Porosity results.

Firstly, when analysing Figure 9, in the HEMC curve all porosities were inferior to the results presented by the theoretical incorporated air, despite the curve maintaining a similar pattern. The porosity had an accentuated increase compared to the reference 0%, and after 1.5% of its concentration, the results slowly decay. This decay in porosity in relation to the incorporation of air may be associated with a better use of the kneading water retained by the Polymer

in the hydration of cement compounds, which filled the previously empty voids. Due to the exposed, the samples with HEMC admixture, in general, obtained the reduction of theoretical porosity.

Mortars with pAVE obtained similar porosity with HEMC, being pAVE responsible for a greater porosity when compared to HEMC, reaching 26% of porosity with 1.5% of its concentration. Afterwards, the results decrease up to 10% of polymer. In other words, the results above 5% of its concentration, varied between 23% and 26% of porosity, not having a data stabilization, similarly to that presented in the incorporation of air property.

Both pAVE and pA showed an increase in porosity compared to the theoretical incorporated air, these results are associated with the exit of the water from the sample in the fresh state, increasing the porosity in the hardened state. However pAVE and HEMC stabilize the porosity around 25%, pA shows a density increase with the increase of admixture content, as well as the theoretical incorporated air, it is noticed again that despite the incorporated air is responsible for the improvement of workability [32], [47], [48], these improvement was not measured by the Flow- Table method. Comparing pA with HEMC and pAVE, it is possible to notice that pA is the only one with porosity increase, indicating excessive water in the mixture, which did not occur with the other samples. It is important to highlight that mixtures with excessive porosity may have their mechanical and durability properties affected and therefore should be used with caution.

Due to the large variations in the results, it was not possible to establish a prediction equation of the theoretical porosity for HEMC and pAVE. However, it is possible to establish a prediction curve for pA, with r^2 of 0.99. Where, it is possible to see a less pronounced increase in porosity up to 5% of its utilization, compared to the other polymers. After this concentration, the porosity continues to increase at a less expressive rate, reaching a maximum result of 33% with 15% concentration. These higher results, when compared to air incorporated, obtained in Figure 9, can be associated with the excessive water evaporation during the hydration process of the mixture.

3.5 Compressive strength

The mechanical strength of samples was verified through simple compression of samples with 28 days. Results of three polymers versus their concentrations are presented in Figure 10.

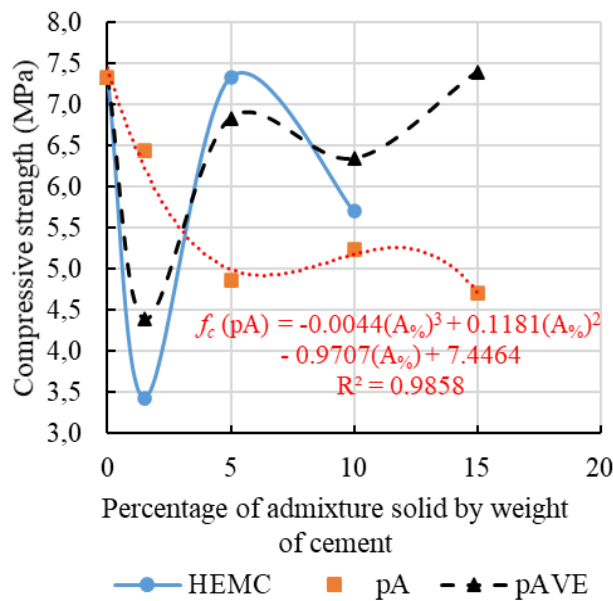


Figure 10. Compressive strength Results.

Analysing HEMC behaviour, it is possible to observe a sharply increase of porosity up to 1.5% of its concentration, which was responsible for a compression decrease (3.4 MPa) comparing with reference 0% (7.3 MPa), 210% smaller. However, the result start to increase in 5% concentration matching reference result, but after, it decreased one more time. Due to this behaviour, it is not possible to establish a prediction equation that fit the data. When theoretical porosity

(Figure 9) decreased in 15%, compressive strength also decreased, this could be associated to an inefficient moulding of samples, as they were dry, making densification difficult.

As seen for HEMC, it was not possible to establish a prediction equation for pAVE due to variability of results. Firstly, the results suffer a sharply decrease of compressive resistance (4.4 MPa), compared to the reference sample, with 1.5% concentration. After this concentration, the result increase expressively reaching 6,84 MPa in 5% polymer use. It is observed that even pAVE obtained a high porosity 26% in 5% of its concentration, this was the percentage that favoured mechanical resistance, in other words, when it obtained the highest result. For all exposed, HEMC and pAVE have their better concentration in 5% when compressive strength is analysed.

At last, Polymer pA obtained an inverse behaviour compared with theoretical porosity, being the porosity increase responsible for mechanical decrease, as its voids acted as points of tension accumulation in mortar [6], contrary to what happened in 5% of utilization of the two other polymers, as mentioned. The porosity decreased the growth rate between 5% and 10% concentrations, and because of this the compressive strength slightly increase, presented in Figure 10. As the results presented a pattern it was possible to establish a prediction equation with r^2 of 0.98.

It is important to notice that porosity up to 25% still corresponds to an adequate value, because it did not compromise the compressive strength. However, above this value, as seen with Polymer pA, the porosity compromised the mechanical resistance.

5 CONCLUSIONS

Due to all exposed, it is concluded:

- Consistency is reduced by HEMC, due to the association mechanism, where attraction forces between polymeric molecules may arise restricting the movement of water molecules, generating a gel and transforming the mortar on a dry material, making it impossible to conduct the experiment beyond 10% concentration. pAVE acted through the interlacing mechanism of the polymeric chains, which tends to increase viscosity, but in higher concentrations and the stresses of Flow table, fluidized the mixture. Due to this, pAVE also acted as a plasticizer in the mixture, increasing the spread diameter with the admixture increase content. Consistency almost did not change with pA admixture, despite being a superabsorbent polymer that usually increase viscosity of samples, but at Flow-Table experiment that was not observed.
- The water trapping mechanism can also be seen in water retention experiment in which HEMC obtained the maximum retention with 1.5% of its concentration. PA improved its water retention with concentration increase, reaching up to 94% (increase of 19%). It is important to highlight that HEMC high water retention result is associated with the dry mortar, due to the gel formation. Although pAVE fluidized the material, it presented increase in water retention, reaching maximum water retention with 15% of its concentration. PA presented the lowest water retention results compared with other samples, however it still presented higher results compared with reference, being appropriate its use as a retainer. Extremely high-water retention in mortars, presented by the other samples, must be carefully studied so it can not affect the mechanism of mechanical adherence to the substrate. It was found, that different from bibliography, it is not necessary to make several retention measures through time, using the standardized weight method, since the measure near the time of mixture preparation is suitable to measure this property.
- The difficult to mould dry mortars as the ones with HEMC, due to the gel formation because of the interlacing mechanism of the admixture generated voids in the matrix, resulting in a higher air entraining content and density decrease in the fresh state. PAVE action resulted in a more fluid mortar, allowing better accommodation of materials and densification of samples, maintaining density and entrained air content stable even with admixture increase. If consistency was maintained, water content could be reduced, increasing density and decreasing entrained air, corroborating that this admixture could also be used as a plasticizer. Samples with pA presented the highest increase rate of theoretical entrained air, due to these highest results the Flow-Table failed to measure the consistency variation, since the incorporated air is known to improve workability.
- It is noticed that until 5%, admixtures presented similar behaviour between hardened state density and fresh state density. Beyond this concentration, pA reduced density's result. Similar behaviour, but inverse, can be seen in the porosity, demonstrating that pA, commonly used in stabilized mortars tends to increase mortars' porosity if it is used at higher concentrations, justifying density decrease. HEMC and pAVE despite influence consistency differently, presented similar hardened density and porosity with approximately porosity of 25%. However, samples with pA presented exponential increase, which it is not good because higher porosities are harmful to mechanical properties.

- The mechanical behaviour was more influenced by the availability of water to hydrate and by the porosity, maintaining the results for HEMC and pAVE above 5% of its concentration, stabilizing the results in approximately 25%. Lower concentrations of these admixtures presented lower results compared to the reference, showing the inefficiency of its individual use.
- To obtain more satisfactory results, it is adequate to reduce water consumption with pAVE or to dose a plasticizer together with HEMC. PA showed to be inadequate in higher concentrations for use in the coating mortars analysed. Above 5% of pA concentrations, it had porosity greater than 25%, impairing the compressive strength of samples. Its use must be done carefully in adequate dosages, it is recommended to reduce the amount of water with the increase of PA's concentration, maintaining consistency, decreasing porosity and thus increasing mechanical strength.

These dosages adjustments tend to improve the mechanical behaviour and the other properties. The present research concluded that several admixtures that could be used as a water retainer can have several mechanisms of action that will influence mortars in different ways. Concentration and composition of admixtures must be studied according to the desired properties in the mortars.

ACKNOWLEDGEMENTS

The authors acknowledge the Brazilian agencies: National Council of Scientific and Technological Development (CNPq), Coordination of Improvement of Higher Education Personnel (CAPES) and Minas Gerais Research Support Foundation (FAPEMIG) for the support given to this study.

REFERENCES FORMATS

- [1] A. T. Souza, L. A. Riccio, G. C. Laquini, and W. J. Santos, "Behavior of mortar coatings subjected to extreme conditions: Lack of curing and no substrate moistening," *Int. J. Sci. Eng. Investig.*, vol. 7, no. 75, pp. 53–59, Apr 2018.
- [2] H. Paiva, L. Silva, J. Labrincha, and V. Ferreira, "Effects of a water-retaining agent on the rheological behavior of a single-coat render mortar," *Cement Concr. Res.*, vol. 36, pp. 1257–1262, 2006, <http://dx.doi.org/10.1016/j.cemconres.2006.02.018>.
- [3] R. W. Y. Zhao, C. Tuan, and A. Xu, "The influence of water/cement ratio and air entrainment on the electric resistivity of ionically conductive mortar," *Materials (Basel)*, vol. 12, no. 7, pp. 1125, 2019, <http://dx.doi.org/10.3390/ma12071125>.
- [4] A. G. Magalhães et al., "The Influence of the water/cement ratio in the open porosity and in the carbonation front advancing in cementitious matrix composites," *Appl. Mech. Mater.*, vol. 864, pp. 313–317, 2017, <http://dx.doi.org/10.4028/www.scientific.net/AMM.864.313>.
- [5] L. Patural, P. Marchal, A. Govin, P. Grosseau, B. Ruot, and O. Devès, "Cellulose ethers influence on water retention and consistency in cement-based mortars," *Cement Concr. Res.*, vol. 41, no. 1, pp. 46–55, 2011, <http://dx.doi.org/10.1016/j.cemconres.2010.09.004>.
- [6] H. Paiva, L. Esteves, P. Cachim, and V. Ferreira, "Rheology and hardened properties of single-coat render mortars with different types of water retaining agents," *Constr. Build. Mater.*, vol. 23, no. 2, pp. 1141–1146, 2009, <http://dx.doi.org/10.1016/j.conbuildmat.2008.06.001>.
- [7] S. W. do Ó and M. J. A. Salles, "Influência do aditivo retentor de água nas propriedades reológicas de argamassas de revestimentos," in *XI Enc. Nac. Tecnol. Ambient. Constr.*, Florianópolis, SC, Brasil, 2006.
- [8] M. Cappellari, A. Daubresse, and M. Chaouche, "Influence of organic thickening admixtures on the rheological properties of mortars: Relationship with water-retention," *Constr. Build. Mater.*, vol. 38, pp. 950–961, 2013, <http://dx.doi.org/10.1016/j.conbuildmat.2012.09.055>.
- [9] A. T. Souza, C. A. Carvalhais, and W. J. Santos, "Analysis of chemical admixtures combination on coating mortar using Simplex network method," *Constr. Build. Mater.*, vol. 239, 2020, <http://dx.doi.org/10.1016/j.conbuildmat.2019.117796>.
- [10] A. T. Souza, C. A. Carvalhais, and W. J. Santos, "Comparativo entre argamassas aditivadas e mista: análise dos aditivos incorporador de ar, retentor de água e plastificante," in *VI Congr. Eng. Civ.*, Juiz de Fora, Brasil, 2019.
- [11] M. Gołaszewska, J. Gołaszewski, G. Cygan, and J. Bochen, "Assessment of the impact of inaccuracy and variability of material and selected technological factors on physical and mechanical properties of fresh masonry mortars and plasters," *Materials (Basel)*, vol. 13, no. 6, pp. 1382, 2020, <http://dx.doi.org/10.3390/ma13061382>.
- [12] J. Pourchez, P. Grosseau, R. Guyonnet, B. Ruot, "HEC influence on cement hydration measured by conductometry," *Cem. Concr. Res.*, vol. 36, vol. 9, pp. 1777–1780, 2006, <https://doi.org/10.1016/j.cemconres.2006.06.002>.
- [13] J. Pourchez, B. Ruot, J. Debayle, E. Pourchez, and P. Grosseau, "Some aspects of cellulose ethers influence on water transport and porous structure of cement-based materials," *Cement Concr. Res.*, vol. 40, no. 2, pp. 242–252, 2010, <http://dx.doi.org/10.1016/j.cemconres.2009.09.028>.

- [14] A. T. Souza, R. B. Caldas, P. Ludvig, and W. J. Santos, "The effects of mixture's components on the mechanical properties and durability indicators of mixed mortar using simplex network method," *Constr. Build. Mater.*, vol. 249, 2020, <http://dx.doi.org/10.1016/j.conbuildmat.2020.118740>.
- [15] W. J. Santos et al., "Study of the effects of excessive cement or lime in mechanical properties and durability of the mortar coating," *Int. J. Develop. Res.*, vol. 9, no. 9, pp. 29923–29927, 2019.
- [16] A. L. Oliveira, B. P. Corrêa, I. F. R. Ribeiro, R. A. Souza, and L. M. L. Caçada, "Influence of water-retaining cellulose ethers on the properties of bedding mortar used in concrete structural masonry," *Ambiente Constr.*, vol. 15, no. 3, pp. 57–59, 2015. <https://doi.org/10.1590/s1678-86212015000300026>.
- [17] A. Izaguirre, J. Lanas, and J. Álvarez, "Characterization of aerial lime-based mortars modified by the addition of two different water-retaining agents," *Cement Concr. Compos.*, vol. 33, no. 2, pp. 309–318, 2011, <http://dx.doi.org/10.1016/j.cemconcomp.2010.09.008>.
- [18] O. Z. Hua, M. B. Guo, and J. S. Wei, "Influence of cellulose ethers molecular parameters on hydration kinetics of Portland cement at early ages," *Constr. Build. Mater.*, vol. 33, pp. 78–83, 2012, <http://dx.doi.org/10.1016/j.conbuildmat.2012.01.007>.
- [19] Dow, *WALOCEL™ MKX 60000 PF 01*. California: DOW, 2020.
- [20] Wacker, *VINNAPAS® 5010 N (GER)*. Munique: Wacker, 2011.
- [21] H. J. Kim, J. Y. Park, H. W. Suh, B. Y. Cho, W. J. Park, and S. C. Bae, "Mechanical Degradation and Thermal Decomposition of Ethylene-Vinyl Acetate (EVA) Polymer-Modified Cement Mortar (PCM) Exposed to High-Temperature," *Sustainability*, vol. 11, no. 2, pp. 500, 2019, <http://dx.doi.org/10.3390/su11020500>.
- [22] K. A. Khan, I. Ahmad, and M. Alam, "Effect of Ethylene Vinyl Acetate (EVA) on the Setting Time of Cement," *Arab. J. Sci. Eng.*, 2018.
- [23] Mc Bauchemie, *Centripor Kombi AC (antigo Powermix AC 1000)*. São Paulo: Mc Bauchemie, 2018.
- [24] W. J. Santos et al., "Proposal for a mix design method for coating mortar with artificial crushing sand," *Ambient. Constr.*, vol. 18, no. 1, pp. 225–243, 2018, <http://dx.doi.org/10.1590/s1678-86212018000100218>.
- [25] K. S. Yeon, K. K. Kim, J. Yeon, and H. J. Lee, "Compressive and flexural strengths of EVA-modified mortars for 3D additive construction," *Materials (Basel)*, vol. 12, no. 16, pp. 2600, 2019, <http://dx.doi.org/10.3390/ma12162600>.
- [26] Associação Brasileira de Normas Técnicas. *Mixing Water for Concrete Part 1: Requirements*, ABNT NBR 15900-1:2009, 2009.
- [27] Associação Brasileira de Normas Técnicas. *Mortars Applied on Walls and Ceilings - Determination of the Consistence Index*, ABNT NBR 13276:2016, 2016.
- [28] Associação Brasileira de Normas Técnicas. *Mortars Applied on Walls and Ceilings - Determination of the Water Retentivity*, ABNT NBR 13277:2005, 2005.
- [29] A. T. Souza, "Comparative analysis of mechanical properties and durability, between hydraulic lime mortar coating and additive mortar coating," M.S. thesis, Univ. Fed. Minas Ger., Belo Horizonte, Brasil, 2019.
- [30] Associação Brasileira de Normas Técnicas. *Mortars Applied on Walls and Ceilings - Determination of the Specific Gravity and the Air Entrained Content in the Fresh Stage*, ABNT NBR 13278:2005, 2005.
- [31] Associação Brasileira de Normas Técnicas. *Portland Cement - Determination of Compressive Strength of Cylindrical Test Specimens*, ABNT NBR 7215:2019, 2019.
- [32] M. P. Seabra, J. Labrincha, and V. M. Ferreira, "Rheological behavior of hidraulic lime-based mortars," *J. Eur. Ceram. Soc.*, vol. 27, no. 2-3, pp. 1735–1741, 2007, <http://dx.doi.org/10.1016/j.jeurceramsoc.2006.04.155>.
- [33] A. Pierre, A. Perrot, and Y. Guevel, "Cellulose ethers and cement paste permeability," *Cement Concr. Res.*, vol. 72, pp. 117–127, 2015, <http://dx.doi.org/10.1016/j.cemconres.2015.02.013>.
- [34] K. Khayat, "Viscosity-enhancing admixtures for cement-based materials – an overview," *Cement Concr. Compos.*, vol. 20, no. 2-3, pp. 171–188, 1998, [http://dx.doi.org/10.1016/S0958-9465\(98\)80006-1](http://dx.doi.org/10.1016/S0958-9465(98)80006-1).
- [35] E. Knapen and D. V. Gemert, "Cement hydration and microstructure formation in the presence of water-soluble polymers," *Cement Concr. Res.*, vol. 39, pp. 6–13, 2009., <http://dx.doi.org/10.1016/j.cemconres.2008.10.003>.
- [36] J. Pourchez, A. Peschard, P. Grosseau, R. Guyonnet, B. Guilhot, and F. Vallé, "HPMC and HEMC influence on cement hydration," *Cement Concr. Res.*, vol. 36, no. 2, pp. 288–294, 2006, <http://dx.doi.org/10.1016/j.cemconres.2005.08.003>.
- [37] N. J. D. Alves and S. W. do Ó, "Aditivos incorporadores de ar e retentores água," in *Revestimentos de Argamassa: Características e Peculiaridades*, E. Bauer, Ed., Brasília: LEM/Unb, 2005.
- [38] F. A. João, "The influence of superabsorbent polymer in conventional concrete properties," M.S. thesis, Univ. Estad. Sta. Catarina, Joinville, Brasil, 2015.
- [39] E. Bauer, G. G. J. Sousa, and E. A. Guimarães "Estudo da consistência de argamassas pelo método de penetração estática de cone," in *VI Simp. Bras. Tec. Argamassas/ I Int. Symp. Mortar Tech.*, Florianópolis, SC, Brasil, 2005.
- [40] I. Paes, E. Bauer, H. Carasek, and E. Pavón, "Influence of water transportation inside a mortar/block system on bonding resistance behavior," *Rev. Ing. Constr.*, vol. 29, no. 2, pp. 175–186, 2014.

- [41] A. C. A. Jantsch, "Permeability analysis of ready-to-use mortars with waterproofing treatment," M.S. thesis, Univ. Fed. Sta. Maria, Santa Maria, Brasil, 2015.
- [42] S. W. do Ó and E. Bauer, "Avaliação das metodologias empregadas para determinação da retenção de água em argamassas de revestimento aditivadas," in *I Conf. Latino-Amer. Constr. Sustent./ X Enc. Nac. Tec. Ambient. Constr.*, São Paulo, SP, Brasil, 2004.
- [43] E. Z. Forti, "Influence of hydrated lime on the characteristics of the coating mortar carried out on site," Graduation in Civil Engineering, Univ. Vale do Taquari - Univates, Lajeado, Brasil, 2017. [Online]. Available: <http://hdl.handle.net/10737/1645>
- [44] A. Hermann and J. P. A. Rocha, "Feasibility study of the use of modified stabilized mortar for coating without rough cast," Graduation in Civil Engineering, Univ. Tec. Fed. Paraná, Pato Branco, Brasil, 2013.
- [45] Association Française de Normalisation. *Norme Française: Travaux d'enduits de Mortiers - Partie 1-1: Cahier des Clauses Techniques*, NF DTU 26.1 P1-1, 2008.
- [46] W. J. Santos, "Development of methodology for determination of coating and settlement mortar," Doctoral dissertation. Univ. Fed. Viçosa. Viçosa, Brasil, 2014. [Online]. Available: <https://www.locus.ufv.br/handle/123456789/6865>
- [47] R. C. O. Romano, D. R. Torres, and R. G. Pileggi, "Impact of aggregate grading and air-entrainment on the properties of fresh and hardened mortars," *Constr. Build. Mater.*, vol. 82, pp. 219–226, 2015, <http://dx.doi.org/10.1016/j.conbuildmat.2015.02.067>.
- [48] V. Kontogiorgos, H. Vaikousi, A. Lazaridou, and C. G. Biliaderis, "A fractal analysis approach to viscoelasticity of physically cross-linked barley β -glucan gel networks," *Colloids Surf. B Biointerfaces*, vol. 49, no. 2, pp. 145–152, 2006, <http://dx.doi.org/10.1016/j.colsurfb.2006.03.011>.

Author contributions: ATS: conceptualization, methodology, writing-original draft preparation; CAC: methodology; WJS: conceptualization, methodology, supervision, writing- reviewing and editing.

Editors: Lia Pimentel Sousa, Guilherme Aris Parsekian.



ORIGINAL ARTICLE

A review on the evolution of Portland cement and chemical admixtures in Brazil

Uma revisão da evolução do cimento Portland e das misturas químicas no Brasil

Juliana Fadini Natalli^a Eduardo Christo Silveira Thomaz^b Júlia Castro Mendes^a Ricardo André Fiorotti Peixoto^a ^aUniversidade Federal de Ouro Preto – UFOP, Departamento de Engenharia Civil, Ouro Preto, MG, Brasil^bInstituto Militar de Engenharia – IME, Seção de Ensino de Engenharia de Fortificação e Construção, Rio de Janeiro, RJ, Brasil

Received 16 December 2020

Accepted 13 April 2021

Abstract: Over the years, Portland cement concretes have undergone increasing demands for constructability, cost, quality, and environmental impact. These demands were met, mainly, through changes in the cement composition and the introduction of chemical admixtures. In this sense, through a literature review, the authors sought to create a collection of information on the evolution of these materials and their standards from 1937 to 2020 in Brazil. This work is part of a research project that aims to elaborate a dating protocol for Brazilian concretes. From the review conducted, the authors observed that the absence of systematic records in the Brazilian civil construction sector hinders the attempt to create a chronology of the development of concrete in the country. In addition, we concluded that the knowledge of the evolution of Portland cement and chemical admixtures is relevant information that can assist in concrete dating processes. The reliable comparison data, posteriorly combined with microstructural characterisation techniques, may lay the basis for an effective dating methodology.

Keywords: Portland cement, chemical admixtures Brazil, cement industry, review, concrete dating.

Resumo: Ao longo dos anos, os concretos de cimento Portland têm sofrido demandas crescentes em termos de construtibilidade, custo, qualidade e impacto ambiental. Essas demandas foram atendidas, principalmente, por meio de mudanças na composição do cimento e introdução de aditivos químicos. Nesse sentido, por meio de uma revisão da literatura, os autores buscaram criar um conjunto de informações sobre a evolução desses materiais e seus padrões de 1937 a 2020 no Brasil. Este trabalho faz parte de um projeto de pesquisa que visa elaborar um protocolo de datação para concretos brasileiros. A partir da revisão realizada, os autores observaram que a ausência de registros sistemáticos no setor da construção civil brasileira dificulta a tentativa de se fazer uma cronologia do desenvolvimento do concreto no país. Além disso, concluiu-se que o conhecimento da evolução do cimento Portland e dos aditivos químicos é uma informação relevante que pode auxiliar em processos de datação de concretos. Os dados de comparação confiáveis, posteriormente combinados com técnicas de caracterização microestrutural, podem servir de base para uma metodologia de datação eficaz.

Palavras-chave: cimento Portland, aditivos químicos no Brasil, indústria cimentícia, revisão, datação de concretos.

How to cite: J. F. Natalli, E. C. S. Thomaz, J. C. Mendes, and R. A. F. Peixoto, “A review on the evolution of Portland cement and chemical admixtures in Brazil,” *Rev. IBRACON Estrut. Mater.*, vol. 14, no. 6, e14603, 2021, <https://doi.org/10.1590/S1983-41952021000600003>

1 INTRODUCTION

The Laboratory of Civil Construction Materials in the Federal University of Ouro Preto recently received the following demand: to date a building that was under legal dispute. The records and documents regarding the exact year

Corresponding author: Juliana Fadini Natalli. E-mail: juliananatali24@gmail.com

Financial support: FAPEMIG (Fundação de Amparo à Pesquisa do Estado de Minas Gerais).

Conflict of interest: Nothing to declare.



This is an Open Access article distributed under the terms of the Creative Commons Attribution License, which permits unrestricted use, distribution, and reproduction in any medium, provided the original work is properly cited.

of construction of this building were inconclusive and/or conflicting. Faced with this challenge, the authors decided to investigate if the dating would be possible through the building materials, more specifically, the concrete.

In addition to the case, knowledge about the age of a concrete structure allows for assessing material durability and determining repair procedures. It can also assist in restoration interventions and historic mapping of buildings. However, despite the relevance for both public and private sectors, no articles or systematic methods for this complex problem were found in the literature.

Carbonation depth has been studied to identify the approximate age of concrete cracks [1]. It is roughly precise as a comparative method (surface already carbonated along the years vs. recently exposed surface of the same concrete) [1]. However, in absolute terms, it has limitations, since the quality of the concrete mixing, pouring, and curing can strongly influence the carbonation depth [2], [3]. Additionally, this phenomenon can be influenced by the technology of chemical admixtures of its time.

The same can be said for chloride ion penetration. Different concrete structures with the same concrete mix proportion and age can have different penetration depths, depending on the curing and exposure conditions [4]. Thus, the age of construction of a concrete structure cannot be accurately associated with its durability parameters.

Regarding dating from the aggregates, most Brazilian aggregates originate from natural crushed rocks [5]. Normally, there are multiple quarries with different geological origins supplying the same city. Additionally, it is known that the mineral characteristics of a rock can vary slightly, even within the same deposit. Therefore, the aggregates' composition is also not a suitable approach for estimating the age of a concrete element.

On the other hand, given that the technological evolution of concrete reflects, above all, the development of Portland cement and the introduction of chemical admixtures to the matrices [6], knowledge on how these materials advance over the years can be useful in dating strategies. A database of the evolution of the use and composition of cement and admixtures in Brazil was not found in the literature and can assist researchers of various fields. In this sense, the present work seeks to create a collection of reliable data on the topic in Brazil. This study represents the initial step on the development of a methodology for dating Brazilian concretes.

1.1 Review Methodology

To gather the information on the evolution of these materials and their standards, a narrative literature review was conducted, focusing on the Brazilian construction industry. Since this work seeks to establish a critical historic overview, a systematic approach to the selection of sources was not adopted. The literature covers a wide variety of publication types (e.g., standards, books, reports, conference articles, news) and dates (1937-2020).

The review is divided into two parts. The first covers the development of Portland cement in Brazil, while the second covers the evolution of chemical admixtures in the country. On the Portland cement section, a concise historic background of the first Brazilian plants is presented, followed by the definition of the types currently sold in the market and their current consumption. Subsequently, the authors investigate how the Brazilian Portland cement standards have evolved along the past decades and trace parallels to the American and British ones. To conclude the study on the Portland cement, graphs show the changes in the proportion of clinker components along the last century. Afterwards, the advancements of the use of chemical admixtures and their standards in Brazil are discussed. Finally, the authors present their final remarks with the conclusions drawn from the investigations carried out.

2 A BRIEF HISTORY OF PORTLAND CEMENT

In 1824, Joseph Aspdin received a patent for a binder developed by burning limestone and clay. This fine powder received the name Portland cement due to its similarity, in colour and solidifying properties, to the limestone rocks of the British island of Portland. The product created by Aspdin back then had different mineralogy and properties from the Portland cement sold nowadays [7]-[9]. Some modifications performed by this English builder and his son, William Aspdin, in the second half of the 19th century, resulted in a product more similar to the modern material [6].

The well-known constituents of cement are tricalcium silicate ($3\text{CaOSiO}_2 - \text{C}_3\text{S}$), dicalcium silicate ($2\text{CaOSiO}_2 - \text{C}_2\text{S}$), tricalcium aluminate ($3\text{CaOAl}_2\text{O}_3 - \text{C}_3\text{A}$) and tetra-calcium aluminoferrite ($4\text{CaOAl}_2\text{O}_3\text{Fe}_2\text{O}_3 - \text{C}_4\text{AF}$). Additionally, other minerals can be formed in minor proportions, such as free lime (CaO), periclase (MgO) and various alkaline sulphates [10], [11]. According to studies carried out by Tennis and Bhatti [12], from 1950 to the present day, the chemical composition of the main constituents of this Portland cement remained essentially unchanged.

The first record of Portland cement production in Brazil dates from 1888, in a small industrial unit located in the state of São Paulo [13], [14]. This was the first attempt to manufacture hydraulic binders for civil construction purposes in the country [13]. Several isolated cement plants were developed in the following years [14]. However, only in 1933, with the consolidation of the Brazilian Portland Cement Company (Companhia Brasileira de Cimento Portland, in Portuguese), the country achieved a production capacity able to surpass the imports (226 thousand tons at the time), creating prospects for the opening of new plants [13]. In comparison, the first British cement association, the Associated Portland Cement Manufacturers Ltd, was founded in 1900 [15]. In the US, the Association of American Portland Cement Manufacturers (AAPCM) was created in 1902 (and renamed Portland Cement Association, PCA, in 1916) [16].

In 2019, according to the National Union of the Cement Industry (SNIC), the production of this binder reached 42 million tons [17]. In 2017, Brazil was the sixth largest cement producer in the world [18].

3 TYPES AND COMPOSITION OF BRAZILIAN PORTLAND CEMENT IN BRAZIL OVER THE DECADES

3.1 Standardisation in Brazil and comparison with American and British standards

The first batches of Brazilian-produced Portland cement had no mineral admixtures nor components other than clinker and plaster. This common type is now specified as CP I, where “CP” refers to “Cimento Portland” (Portland cement in Portuguese) and “I” marks the “ordinary” classification. The first Brazilian standard related to Portland cement was published in 1937 [19], approximately 33 years after the first American and British ones [20], [21]. Brazilian type CP I is equivalent to American ASTM type I and British BSI CEM I. The scientific and technological mastery of this product enabled the development of other types of cement in the following years.

One of the first new types was the high early strength Portland cement, specified nowadays in Brazil as CP V (equivalent to ASTM type III and BSI notations “-N” and “-R”). This type must reach a high mechanical resistance in the early ages, obtained from a higher C_3S content and by grinding the cement in finer particles, [6], [22]-[24]. In Brazil, its first standardisation dates from 1940.

Aiming to reduce the cost and energy consumption of the manufacturing process [25]-[27], the use of supplementary cementing materials (SCMs) to partially replace the clinker was gradually adopted worldwide. Granulated blast furnace slag was the initial solution, followed by pozzolanic materials [28]. The first cases of adoption of SCMs in the Brazilian cement industry date from 1952, while this practice was already regulated since 1946 in the USA (ASTM C250) and 1923 in the UK [20], [29].

The Portland Blast-Furnace slag cement (now CP III) was the first standardized cement with admixtures in Brazil (1966). It is equivalent to BSI type CEM III and ASTM binary blended cement type IS (“S” for slag), although the Brazilian type currently allows up to 10% limestone filler (which is not covered in BSI and ASTM binary blended cements).

The Portland-pozzolan cement (now CP IV) was the next blend to get its standard, in 1974. It is equivalent to BSI type CEM IV and ASTM binary blended cement type IP (“P” for pozzolan) but may also include up to 10% limestone filler. In 1991, the Brazilian Association of Technical Standards (ABNT) published the standard for Portland composite cements (CP II), whose composition is intermediate between ordinary Portland cement (CP I) and Portland cements with blast furnace slag and pozzolanic materials, CP III e CP IV.

The Portland-composite cement can be further divided in CP II – E (clinker + calcium sulphate partially replaced by blast furnace slag and limestone filler), CP II – Z (clinker + calcium sulphate partially replaced by pozzolanic materials and limestone filler) and CP II – F (clinker + calcium sulphate partially replaced by limestone filler). Brazilian types CP II – E and CP II – Z are equivalent to ASTM ternary blended cement (IT) but have no equivalent in the BSI standards, which do not include a cement type with high contents of slag + filler or pozzolan + filler. In turn, CP II – F is equivalent to ASTM limestone cement (IL) and, depending on the composition proportion and material quality, can be equivalent to BSI CEM II A-L, A-LL, B-L, or B-LL.

Until 2018, each type of cement had its specific ABNT standard. In that year, the standards were unified in NBR 16697, which, in line with its British and American counterparts, presents all the specifications and requirements for all types of cement. Table 1 summarises the latest Brazilian cement types and their equivalents in the US and UK. Due to its particularities, white cement is not included in the present study.

Table 1. Summary of current Brazilian cement types and their American and British equivalents [30]-[33].

Brazilian ABNT Type	Name	Composition (range of percentage by mass)				American ASTM equivalent	British BSI equivalent
		Clinker + calcium sulphate	Granulated blast furnace slag	pozzolanic materials	limestone filler		
CP I	Ordinary Portland cement	95-100		0-5		Type I	CEM I
CP I-S	Ordinary Portland cement with admixtures	90-94	0	0	6-10	Type I	CEM II A-L or A-LL ¹
CP II-E	Portland-composite cement with blast furnace slag	51-94	6-34	0	0-15	Type IT(L α)(S β) ²	-
CP II-Z	Portland-composite cement with pozzolanic materials	71-94	0	6-14	0-15	Type IT(L α) ₂ (P β)	-
CP II-F	Portland-composite cement with limestone filler	75-89	0	0	11-25	Type IL(α) ²	CEM II A-L, A-LL, B-L, or B-LL
CP III	Portland blast-furnace slag cement	25-65	35-75	0	0-10	Type IS(α) ^{2,3}	CEM III A or B ³
CP IV	Portland-pozzolan cement	45-85	0	15-50	0-10	Type IP(α) ^{2,3}	CEM IV A or B ³
CP V	High early strength Portland cement	90-100	0	0	0-10	Type III	Notation “-N” or “-R” to the other types

¹ Brazilian CP I-S may contain 6-10% limestone filler, while British CEM II/A may contain 6-20%. Therefore, they are only equivalent when the cement comprises up to 10% limestone filler. ² Where α and β are the replacement rate of the material. E.g. a) 20% slag (S) and 10% limestone filler (L) = Type IT(S20)(L10); b) 40% pozzolan (P) = IP(40). ³ Brazilian standards allow up to 10% limestone filler to binary blends CP III and CP IV since 2018, whereas their American and British counterparts do not. An American cement with both limestone filler and slag or pozzolan would be identified as a ternary blend. British BSI standard does allow up to 5% “minor additional constituents” but does not label them as limestone filler.

The American cement classifications are based on the intended use or resulting property (e.g., Type II - when moderate sulphate resistance is desired, or Type IV - when a low heat of hydration is desired). On the other hand, the Brazilian and British naming systems mostly consider the type and content of mineral admixtures. The current Brazilian standard, NBR 16697, allows the application of the suffixes “RS” for sulphate resistance and “BC” for low heat of hydration to any cement type, given that it fulfils the prescribed specifications.

Both American and British standards require some form of identification of how much mineral admixture is added to the cement. The American ASTM prescribes a straightforward approach: the percentage of each admixture must be clearly stated (e.g. IT(S20)(L10) or IP(40)). British standards have different ratings for different replacement percentages. For example, blast furnace cement (CEM III) can be classified as “A” if 36-65% of its clinker + calcium sulphate is replaced by blast furnace slag; “B”, for 66-80%; and “C” for 81-95%. Brazilian cement manufacturers are not required to display this information; they only use it to classify their cement in the broad ranges mentioned in Table 1.

Both ASTM and BSI allow blends with both slag and pozzolans, currently not allowed by Brazilian ABNT. Also, the British standard provides specifications on the type of pozzolanic addition, and the quality of the carbonaceous material used. The Brazilian standard does not require the manufacturer to specify whether only one or more than one type of pozzolan is used. There is also no mention of whether this is allowed.

While the British BSI standard allows any type of cement to have high initial strength, Brazilian ABNT and American ASTM standards restrict this characteristic to a specific type of cement. BSI also brings 2 classifications for high initial strength cement (according to performance limits), in addition to 1 classification for low initial strength cement, which does not happen for Brazilian and American cement types.

Finally, the American ASTM standards have the notation “-A” to indicate air-entrained cement. Since Brazil is a tropical country where temperatures rarely fall below 0°C, the concretes are not commonly required to ensure freezing and thawing durability.

Nowadays, all Brazilian types of cement (except for High Early Strength) must present one out of three strength classes: 25, 32 or 40 [30]. These values represent the minimum 28-days compressive strength (in MPa) required from a standard 1:3 mortar cast in $\phi 5 \times 10$ cm cylindrical specimens. High Early Strength Portland cement (CP V) must reach 14 MPa in 24 hours and 34 MPa in 7 days. Its strength class is called “ARI”, standing for “Alta Resistência Inicial” (High Early Strength).

3.2 Portland cement consumption in Brazil

Figure 1 presents the evolution of consumption of Brazilian Portland cement types according to data from the National Union of the Cement Industry (SNIC), presented at statistical yearbooks published by the Brazilian Institute of Geography and Statistics (IBGE) [34].

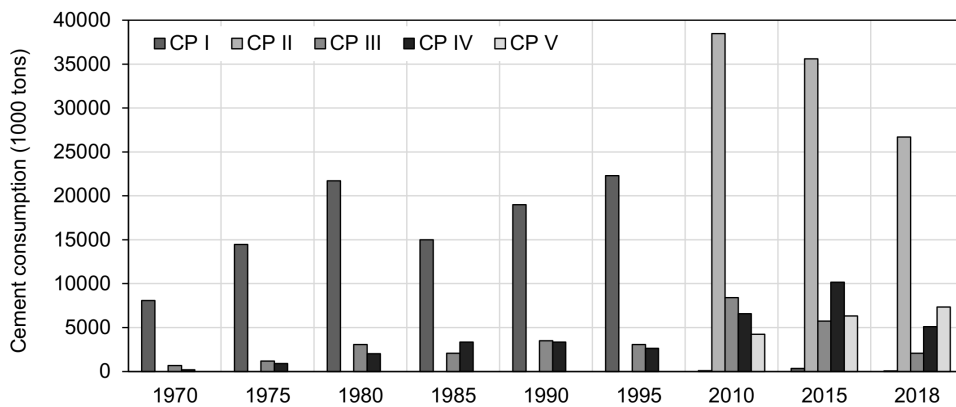


Figure 1. Brazilian consumption of Portland cement, by type. Note: the yearbooks of the 70s, 80s and 90s do not present values for CP V consumption, and there was no specification on the consumption of Portland cement in the years 2000 and 2005.

Ordinary Portland cement (CP I) was the most adopted in Brazilian constructions until 1995. From 1996 onwards, Portland-composite cement (CP II) takes its place as the favourite in the usual construction applications. The replacement of CP I by CP II is probably linked to the reduction of costs related to the use of SCMs, as will be later discussed. Nowadays, the commercial production of CP I is restricted to cement companies far from thermoelectric and steel industries, such as those in the Northern region of Brazil.

The graph also shows a significant increase in cement consumption (for all types) in the last decade, followed by a slight decrease in 2018 due to the economic recession in Brazil. CP III and CP IV have also been gaining space in the Brazilian market, attributed to the greater use of these types in concrete elements of large volume (such as dams and foundations), and in those that require greater durability. Finally, the increase in CP V consumption stands out in the past few years, probably related to the advance of precast concrete structures and the requirement for quicker formwork removal times, associated with the industrialisation of civil construction in the country.

3.3 Types of Portland cement in Brazil

3.3.1 Ordinary Portland cement (CP I and CP I-S)

The first cement type produced and sold in Brazil was the ordinary Portland cement (originally CP, now CP I), without any components other than clinker and calcium sulphate [28], [35]. Table 2 shows the evolution of the standardisation of CP I in Brazil. It is noteworthy that, from 1977 onwards, the addition of small amounts of SCMs to this type of cement was allowed, probably due to the cost, performance and environmental advantages achieved in CP III and CP IV, as will be seen in the next sections. In 1988, the CP I was broken down in three types (CPS, CPE, and CPZ), according to the mineral admixture added to it. In 1991 a new subtype for low levels of admixtures was established, the “ordinary Portland cement with admixture”, CP I-S, and CP I returned as the type without any.

Table 2. Evolution of standardisation of the ordinary Portland cement (CP I and CP I-S) in Brazil, in terms of maximum clinker + calcium sulphate replacement in mass.

Standard	Year	Allowed content of mineral admixtures for CP I	Allowed content of mineral admixtures for CP I-S	Strength classes
EB-1 (originally) NBR 5732	1937	0%	-	25
EB-1 (originally) NBR 5732	1973	0%	-	25 32 40
NBR 5732	1977	0 to 10% blast furnace slag	-	25 32
		0%		40
NBR 5732	1988	0 to 5% limestone filler (CPS)	-	25 32 40
		0% to 10% blast furnace slag (CPE)		
		0% to 10% pozzolanic materials (CPZ)		
NBR 5732	1991	0%	0% to 5% blast furnace slag or pozzolanic materials or limestone filler	25 32 40
NBR 16697	2018	0% to 5% blast furnace slag or pozzolanic materials or limestone filler	6 to 10% limestone filler	25 32 40

3.3.2 Portland Blast-Furnace slag cement (CP III)

Granulated blast furnace slag, a by-product of the conversion of iron ore into pig iron, is comprised mainly by CaO, SiO₂ and Al₂O₃ [36], and consists of a vitreous material with cementing properties [37], [38].

In Brazil, the addition of blast furnace slag to Portland cement began in 1952, with the Tupi company, in the city of Volta Redonda (state of Rio de Janeiro), using the residues from the National Steel Company (Companhia Siderúrgica Nacional – CSN) [39]. In 2017, Brazil was the ninth-largest steel producer in the world, manufacturing 34.4 million tons of the metal, and generating 8.8 million tons of blast furnace slag in the process [40]. Table 3 shows the evolution of the standardisation of CP III in Brazil.

Table 3. Evolution of standardisation of the Portland Blast-Furnace slag cement (CP III) in Brazil, in terms of maximum clinker + calcium sulphate replacement in mass.

Standard	Year	Allowed content of mineral admixtures for CP III	Strength classes
EB-208 (originally) NBR 5735	1966	25% to 65% blast furnace slag	25
NBR 5735	1974	25% to 65% blast furnace slag	25 32
NBR 5735	1987	35% to 70% blast furnace slag	25 32 40
		0% to 5% limestone filler	
NBR 5735	1991	35% to 70% blast furnace slag	25 32 40
		0% to 5% limestone filler	
NBR 16697	2018	35% to 75% blast furnace slag	25 32 40
		0% to 10% limestone filler	

In the 1960s, there was only one strength class for Portland blast furnace cement, 25. Classes 32 and 40 came in the 70s and 80s, respectively. Technological advances in the cement manufacturing process, such as the increase of grain fineness and changes in C₃S content, led to greater mechanical strength [22]-[24], [6].

The increasing trend in the replacement of clinker + calcium sulphate by blast furnace slag continued from the 1980s onwards. Several factors are favourable to this adoption. First, the increased use of SCMs promotes a reduction in CO₂ emissions, energy costs and consumption of natural resources. Secondly, the incorporation of slag into cement production also contributes to a more suitable destination for these residues. These scenarios also reduce the costs and environmental impacts of both steel and cement companies. Finally, there are major technological advantages in increasing the replacement of clinker by SCMs in cement-based composites, such as the reduction of the heat of hydration, lower permeability, and greater durability [41], [36], [38].

With all these advantages, coupled with the increase in cement consumption in recent years, in 2009 the steelmaker CSN inaugurated its own cement plant [42]. With the supply of blast furnace slag reduced, as the main supplier in the

Southeastern Region now consumes most of its production, some Brazilian cement companies started to import their slag from foreign steelmakers. Others began to invest in pozzolanic materials [14].

3.3.3 Portland-pozzolan cement (CP IV)

Pozzolans are SCMs that by themselves possess little or no cementing capacity, but finely divided and in presence of moisture chemically react with calcium hydroxide (Ca(OH)₂ or CH), forming calcium silicate hydrates (C-S-H) [11]. The reaction between the pozzolan and CH is called pozzolanic activity, and the resulting C-S-H increases the strength and decreases the permeability of the matrix.

In Brazil, the addition of pozzolanic materials to Portland cement began only in 1969 by Indústrias Reunidas Francisco Matarazzo, with the use of fly ash from the Charqueadas thermoelectric plant [39]. Table 4 shows the evolution of the standardisation of CP IV in Brazil. There has been an increase in the maximum allowed content of pozzolanic additions to cement over the years. This increase is also related to the environmental, economic, and technological factors previously mentioned for the blast furnace slag.

Table 4. Evolution of standardisation of Portland-pozzolan cement (CP IV) in Brazil, in terms of maximum clinker + calcium sulphate replacement in mass.

Standard	Year	Allowed content of mineral admixtures for CP IV	Strength classes
EB-758 (originally)	1974	10% to 40% pozzolanic materials	25
NBR 5735 (later)		10% to 30% pozzolanic materials	32
NBR 5736	1986	15% to 40% pozzolanic materials	25 32
NBR 5736	1991	15% to 50% pozzolanic materials 0% to 5% limestone filler	25 32
NBR 16697	2018	15% to 50% pozzolanic materials 0% to 10% limestone filler	25 32 40

The pozzolanic materials most used by the cement industries are silica fume, fly ash, volcanic ash, rice husk ash, and metakaolin [43]-[45]. In Brazil, given the size of the country, the type of pozzolana adopted varies with the availability of each region. In the Southern Region, for example, fly ash is widely used, obtained from the thermoelectric plants of the area. In the Northeastern region, calcined clays are the most common pozzolans adopted [28].

3.3.4 Portland-composite cement (CP II-E, CP-II Z and CP II-F)

Composite cement was the last one to be standardised. The three types of composite cement (CP II-E, CP II-Z and CP II-F) may have limestone fillers, with CP II-E and CP II-Z also presenting intermediate levels of blast furnace slag and pozzolanic materials, respectively. Table 5 shows the evolution of the standardisation of CP II in Brazil.

Table 5. Evolution of standardisation of Portland-composite cement (CP II) in Brazil, in terms of maximum clinker + calcium sulphate replacement in mass.

Standard	Year	Allowed content of mineral admixtures for CP II-E	Allowed content of mineral admixtures for CP II-Z	Allowed content of mineral admixtures for CP II-F	Strength classes
NBR 11578	1991	6% to 34% blast furnace slag filler0% to 10% limestone	6% to 14% pozzolanic materials limestone 0% to 10% filler	6% a 10% limestone filler	25 32 40
NBR 16697	2018	6% to 34% blast furnace slag 0% to 15% limestone filler	6% to 14% pozzolanic materials 0% to 15% limestone filler	11% a 25% limestone filler	25 32 40

Note that Brazilian standards only allow the use of “carbonate materials” as fillers, not referring to other types of inert minerals. The limestone filler is obtained from ground limestone rocks. Up to certain limits, this mineral admixture is known to increase concrete workability in the fresh state, as the fine particles act as a lubricant [46], [47]. In the hardened state, the fillers promote filling of voids and dispersion of grains [48], leading to enhanced mechanical strength

and lower porosity [46], [47]. Due to these technical advantages and its relatively low cost, the maximum allowed addition of limestone filler in Brazilian cement has been increased over the decades.

3.3.5 High Early Strength Portland Cement (CP V)

High Early Strength Portland cement (CP V) was first regulated in 1940, only 3 years after CP I. The mastery of Portland cement composition, grinding processes and hydration reactions enabled the development of CP I to a binder capable of producing matrices with high resistance already in early ages. Although its standardisation is relatively old, only in the past decade the CP V has gained space in the Brazilian market, due to the growth of the precast industries, the introduction of cast-in-place concrete wall systems, and the pressure for increasingly early removal of concrete formworks in conventional structures [28]. Table 6 shows the evolution of the standardisation of CP V in Brazil.

Table 6. Evolution of standardisation of the High Early Strength Portland cement (CP V) in Brazil, in terms of maximum clinker + calcium sulphate replacement in mass.

Standard	Year	Allowed content of mineral admixtures for CP V	Minimum strength (MPa)		
			1 day	3 days	7 days
EB-2 (originally)	1940	0% to 1% of any material	11	22	31
NBR 5733 (later)					
NBR 5733	1974	0%	11	22	31
NBR 5733	1991	0 to 5% limestone filler	14	24	34
NBR 16697	2018	0 to 10% limestone filler	14	24	34

As of the 1991 regulations, an increase in the mechanical strength is required at all ages. This demand is obtained through an enhanced grinding process and an increase in the clinker’s C₃S content, which accelerate the hydration reactions at early ages [2]-[5]. It is also noticeable that, related to the reduction in costs and environmental impacts, the 2018 version allows a greater amount of limestone filler addition to this type of cement.

3.4 Evolution of clinker components

Since the development of Portland cement, its most demanded properties are the speed and intensity of mechanical strength gain [6]. To this purpose, the proportion of cement constituents and the fineness of the grains have been changing over the years [2]-[5].

This development was made possible thanks to studies on cement chemistry and advances in micro and nanometric characterisation techniques [7]-[9]. These analyses allowed, above all, the better understanding of the hydration mechanisms of the Portland cement components [8], [10]-[12] and their interactions with other materials [13]-[15]. The improvement in the quality of the cement was also possible due to the evolution of kiln designs, which ensured a greater control of production and an increase in clinker uniformity [16], [17].

Figure 2 shows trends in the levels of constituents of Portland cements produced worldwide over time. Brazilian cement technology followed the same trends. The graphs were constructed from a series of data collected in books and scientific articles, shown in the Appendix.

The increase in the average C₃S content by about 100% and the reduction in the average C₂S content by approximately 66% are related to rapid strength gain of the concretes, a characteristic increasingly demanded by the construction industry [3], [4], [8]. Although the C-S-H produced by the hydration of C₃S and C₂S have similar structure, the hydration of C₃S occurs much earlier, contributing to almost half of the mechanical strength at 28 days [8].

These results agree with the literature. Gonnerman and Lerch [2] studied concrete samples collected between 1904 and 1950 and observed an increase in the specific surface of the grains and the C₃S content. More recently, Tennis and Bhatti [18] analysed cement samples from 1950 to 2004 and reached the same conclusions.

One of the consequences of the increase in the C₃S proportion and grain fineness is an increase in the heat released during hydration reactions. In this sense, the reduction of the average C₃A content by about 31% can be justified by the search for lower heat release, since C₃A is one of the components that most contribute to the exothermic nature of the hydration process [8], [19]. The only main constituent that remained roughly unaltered over the years was the C₄AF phase, possibly due to its low impact on the mechanical and rheological properties and in the hydration kinetics.

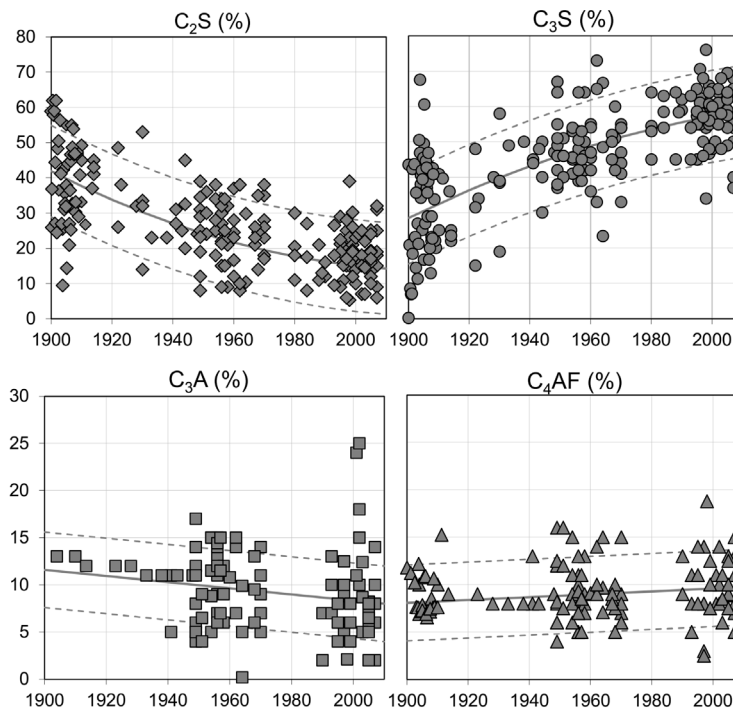


Figure 2. Variation in the proportion of the main components of Portland cements over the years in Brazil and worldwide.

4 TYPES OF CHEMICAL ADMIXTURES IN BRAZIL OVER THE DECADES

4.1 Use of admixtures in Brazilian concretes

The advances in concrete performance were promoted not only by modifications on the proportion of cement constituents and the increase in grain fineness, but also by the improvement of construction technologies and the emergence of chemical admixtures [5]. There are today over 20 commercial types of admixtures, which are capable of interfering with hydration kinetics, the amount of hydration products formed and the intermolecular attraction forces between cement grains [20].

Mehta and Monteiro [11] indicate that about 80 to 90% of the concrete produced in developed countries has at least one chemical admixture. In Brazil, there are no data on the use of admixtures, and there is no national syndicate or association of admixture manufacturers. It is believed that the percentage of concretes with admixtures is significantly lower, due to the predominance of self-built homes in the country [21], and the lack of technological control of concrete production in most construction sites [22]. However, in general lines, the concrete practices in the country have usually followed international trends.

Mehta and Burrows [24] point out that the industrial growth from 1950 onwards boosted the development of pumped concretes and the consolidation of immersion (or needle) vibrators. According to the authors, these factors triggered the need for more fluid concretes, which, before the advent of plasticizer admixtures in the 1960s, were only attained by increasing the water content.

The first plasticizer admixtures, developed in Japan in the 1960s [23], were introduced to the Brazilian market in the same decade [24]. Initially, they were mostly adopted by consumers with a high-level technical background, such as concrete plants.

In that same decade, the first superplasticizers based on sulfonated naphthalene-formaldehyde condensate were being formulated [24]. The dissemination of these admixtures reduced the water/cement ratio and improved the workability of fresh concrete. Due to these factors, these products have led to more resistant and less permeable concretes worldwide [25], [26]. In Brazil, these mixtures were introduced only in the mid-1970s [27].

This successful use of superplasticizers, coupled with labour shortages and construction time savings, encouraged the development of self-compacting concretes (SCC) in the 1980s in Japan [28]. According to Faria [49], SCC arrived in Brazil in the 1990s. The increase in productivity allowed this type of material to be used in the Brazilian precast

concrete industries [30]. There are no official data on the subject, but Costa and Cabral [31] state that the SCC in vertical constructions is still little used in Brazil, mainly due to the higher initial cost of the material.

The 1980s were also marked by the development of polycarboxylate-based superplasticizer admixtures by Japanese chemical industries [32], [33]. This new generation, which was popularized in Brazil and worldwide in the 1990s, promoted the development of high- and ultra-high-strength concretes [24].

There are no reports of when the set retarding admixtures started to be commercialised in the Brazilian market, however, it is assumed that their use has intensified since the consolidation of concrete plants in the country in the 1960s [34]. This type of admixture is especially important in hot climates, allowing a longer period for concrete mixing and pouring [24].

Ultimately, no records were found in the Brazilian literature regarding the beginning of the adoption of the other types of admixtures in the country. There was also no data on their production volume and when the first chemical industries were established. Records of when these admixtures were first introduced in the Brazilian concretes can lead to valuable clues as to the age of a concrete element. By identifying the chemical component of the admixture in the cement matrix, the age of the structure can be traced over a narrow range of years. The authors have ongoing initiatives seeking to recognize the type of admixture used in samples taken from hardened concrete.

4.2 Standardisation in Brazil and comparison with American and British standards

In Brazil, chemical admixtures for Portland cement concrete are currently specified by NBR 11768, whose first version was published in 1987 (originally EB-1763). In comparison, the first standards for admixtures in the US were published in 1977 (ASTM C 260) and 1979 (ASTM C 494); and, in the UK, 1974 (BS 5075-1, now BS EN 934-2).

NBR 11768 prescribes the required conditions related to homogeneity, colour, specific gravity, pH, solid residues content, and chlorides content; and determines the tests to be carried out on the concretes with admixtures. It also specifies that the mass of admixtures added during the concrete mixing should not exceed 5% in relation to the mass of Portland cement. The standard currently allows this amount to be exceeded in some specific applications, such as admixtures for shotcrete and shrinkage compensators.

In Brazil, there are no standards for admixtures for cement-based composites other than concrete (e.g., mortars and grouts). Table 7 shows the different types of standardised admixtures in the country and their equivalents in the US and UK.

Table 7. Types of chemical admixtures standardized in Brazil according to NBR 11768, and their American and British equivalents [35]-[38].

Brazilian ABNT Type	Chemical admixture	Characteristics	American ASTM Equivalent	British BSI Equivalent
PN	Water-reducing	First-generation plasticizer, based on lignosulfonates.	A ¹	Water reducing/plasticizing ¹
SP-I N	High-range water-reducing Type I	Second-generation superplasticizer, based on condensates of formaldehyde sulfonates.	F ¹	High range water reducing/superplasticizing ¹
SP-II N	High-range water-reducing Tipo II	Third generation superplasticizer, based on polycarboxylate.		
IA	Air-entraining	Incorporates uniformly distributed micropores of air during the mixing of the concrete, which remain in the hardened state.	Air-Entraining ²	Air entraining
AP	Set Accelerating	Decreases the transition time from the plastic to the rigid state of the concrete.	C	Set accelerating
AR	Strength accelerator	Increases the rate of development of the initial strength of the concrete, with or without affecting setting time.	- ³	Hardening accelerating
PP	Set Retarding	Increases the transition time from the plastic to the rigid state of the concrete.	B	Set retarding
PR	Water-reducing and Set Retarding	Combines the effects of a plasticizer (main function) and the effects of a retarder (secondary function)	D ¹	Set retarding/water reducing/plasticizing ¹
SP-I R or SP-II R	High-range water-reducing and Set Retarding	Combines the effects of type I or II superplasticizer (main function) and the effects of a retarder (secondary function).	G ¹	Set retarding/ high range water reducing/superplasticizing ¹

Table 7. Continued...

Brazilian ABNT Type	Chemical admixture	Characteristics	American ASTM Equivalent	British BSI Equivalent
PA	Water-reducing and Set Accelerating	Combines the effects of a plasticizer (main function) and the effects of an accelerator (secondary function)	E ¹	Set accelerating/water reducing/plasticizing ¹
SP-I A or SP-II A	High-range water-reducing and Set Accelerating	Combines the effects of type I or II superplasticizer (main function) and the effects of an accelerator (secondary function).	-	-
MV-RT	Water retainer viscosity modifier	Retains water inside the concrete reducing the bleeding effect	- ³	Water retaining
MV-AS	Anti-washout viscosity modifier	Reduces segregation of fluid or self-compacting concretes and allows the pouring of submerged concretes	- ³	Viscosity modifying ⁴

¹ Brazilian standard differentiates Water-reducing from High-range water-reducing admixtures according to the chemical composition. ASTM and BSI prescribe that the former should be able to reduce at least 5% of mixing water, and the latter at least 12%. ² ASTM C494 does not have a specific letter/classification for Air-entraining admixtures, which are separately regulated by ASTM C260. ³ While ASTM C494 covers admixture types A to G, it does present provisions for a Type S, adopted when specific performance characteristics are required. ⁴ Brazilian standard specifies the Anti-washout viscosity modifier for self-compacting and submerged concretes, while BSI only mentions that it is “incorporated in concrete to limit segregation by improving cohesion”.

Although the first Brazilian standards on chemical admixtures for concrete date from the late 1980s, there were reports of the use of plasticizers and set retarders decades before them, as seen in the previous section. The first standards launched in Brazil were EB-1763 (in 1987), with the specifications and requirements for various types, and EB-1842 (in 1987), specific for superplasticizers. In 1992, these standards were merged into NBR 11768.

The standards prior to 2011 did not establish maximum limits for the content of admixtures in concrete. Furthermore, they did not prescribe the specific requirements that the admixtures should meet, meaning that there was no standardised technological control of cement-based composites with admixtures at that time.

In 2019, the NBR 11768 was completely remodelled. It was split into three parts, where Part 1 refers to the classification and requirements, and Part 2 and 3 aggregate the specific tests for the various admixtures. While the 1992 standard classified the admixtures in 9 different types, and the 2011 version, 11 types, the 2019 standard brought 16 classifications (9 of them entirely new). Table 8 summarises the main differences observed throughout the years (note: the specified requirements are non-exclusive – only the most relevant ones were shown).

Table 8. Evolution of concrete admixture standards in Brazil and their main requirements

1992 (4 pages)		2011 (25 pages)		2019 (33 pages)	
Type	Description ¹	Type	Description ²	Type	Description ⁴
P	Plasticiser	PN	Water-reducing/Plasticiser	RA1	Water-reducing type 1
	· Minimum 6% water reduction ³ .		· Minimum 6% water reduction ³ .		· Minimum 8% water reduction ³ .
SP	· No references to chemical composition.	SP-I N	· First-generation plasticizer, based on lignosulfonates.	RA2	· No references to chemical composition.
	Superplasticiser		High-range water-reducing Type I		Water-reducing type 2
	· Minimum 12% water reduction ³ .	· Minimum 12% water reduction ³ .	· Minimum 15% water reduction ³ .		
	· No references to chemical composition.	· Second-generation superplasticizer, based on condensates of formaldehyde sulfonates.	· No references to chemical composition.		
A	Set Accelerating and Strength accelerator	SP-II N	High-range water-reducing Tipo II	AP	Set Accelerating
			· Minimum 20% water reduction ³ .		
A	· Minimum initial set time: -1:00h ³	AP	· Third generation superplasticizer, based on polycarboxylate.	APP	Set Accelerating for shotcrete
			· No requirements regarding minimum final set time.		

Table 8. Continued...

1992 (4 pages)		2011 (25 pages)		2019 (33 pages)	
Type	Description ¹	Type	Description ²	Type	Description ⁴
					· Initial setting of cement paste: ≤ 0:10h ³
					· Final setting of cement paste: ≤ 1:00h ³
			Strength accelerator		Strength accelerator
		AR	· Minimum strength increase in 24h: +120% ³	AR	· Minimum strength increase in 24h: 120% ³
			· No requirements regarding setting time (may or may not alter)		· Maximum initial set time: 120% ³
R	Set Retarding · Minimum initial set time: + 1:00h ³	RP	Set Retarding · Minimum initial set time: + 1:30h ³		-
PA	Plasticiser and Set Accelerating · Combined requirements	PA	Water-reducing and Set Accelerating · Combined requirements	RA1-A	Water-reducing type 1 and Set Accelerating · Minimum 8% water reduction ³ .
					· Minimum initial set time: - 0:30h ³
SPA	Superplasticiser and Set Accelerating · Combined requirements	SP-I A or SP-II A	High-range water-reducing and Set Accelerating · Combined requirements	RA2-A	Water-reducing type 2 and Set Accelerating · Minimum 15% water reduction ³ .
					· Minimum initial set time: - 0:30h ³
PR	Plasticiser and Set Retarding · Combined requirements	PR	Water-reducing and Set Retarding · Combined requirements	RA1-R	Water-reducing type 1 and Set Retarding · Minimum 8% water reduction ³ .
					· Minimum initial set time: +2:00h ³
SPR	Superplasticiser and Set Retarding · Combined requirements	SP-I R or SP-II R	High-range water-reducing and Set Retarding · Combined requirements	RA2-R	Water-reducing type 2 and Set Retarding · Minimum 15% water reduction ³ .
					· Minimum initial set time: +1:30h ³
IAR	Air-entraining · Maximum bleeding: 2% No references to air entrainment potential.	IA	Air-entraining · Minimum air-entrainment: +2.5% ³ Total air-entrainment content: 4 to 6%	IA	Air-entraining · Minimum air-entrainment: +2.5% ³ Total air-entrainment content: 4 to 6%
				IA-L	Air-entraining for lightweight concretes · No requirements specified ⁵
	-		-	CH	Hydration controller · Slump > 10mm ³ · No setting time or heat of hydration requirements specified.
	-		-	CR	Shrinkage compensating · Shrinkage at 28 days: ≤ 95% ³ · Final setting time: ≤ 1:30h ³ · Other physical and chemical requirements.
	-		-	RR	Shrinkage reducing · Shrinkage at 28 days: ≤ 95% ³ · Final setting time: ≤ 2:00h ³ · No other physical and chemical requirements specified.

Table 8. Continued...

1992 (4 pages)		2011 (25 pages)		2019 (33 pages)	
Type	Description ¹	Type	Description ²	Type	Description ⁴
-	-	-	-	RC	Corrosion-inhibiting · No requirements specified ⁵
-	-	-	-	MV-RT	Water retainer viscosity modifier · Bleeding < 15% · No workability requirements specified.
-	-	-	-	MV-AS	Anti-washout viscosity modifier · No requirements specified ⁵
-	-	-	-	RAC	Capillary absorption reducer · No requirements specified ⁵
-	-	-	-	RP	Permeability reducer · No requirements specified ⁵
-	-	-	-	CVP	Admixtures for vibro-pressed concrete · No requirements specified ⁵

¹ In the 1992 standard, excluding air-entraining admixtures (IAR), all others, when intended for concretes without entrained air, must not incorporate an air content greater than 3%. ² In the 2011 standard, excluding air-entraining admixtures (IA), all others, when intended for concretes without entrained air, must not incorporate an air content greater than 2%. ³ In relation to reference concrete. ⁴ In the 2019 standard, admixtures CH, AR, CR, and MV-RT were required to promote less than 2% air-entrainment in relation to reference concrete; AP, 4%; and RR, 1%. No air-entrainment requirements were specified for the other types. ⁵ These admixture types were defined, but no requirements were presented regarding any property other than the general requirements for all admixtures (homogeneity, colour, density, solid content, pH, and water-soluble chlorides).

5 FINAL REMARKS

The present bibliographic review made clear that there are no systematic records in the civil construction sector in Brazil, motivating the authors to develop a chronology of the standards related to cement and admixtures in the country. The National Union of the Cement Industry (SNIC) itself only published annual reports from 2001 to 2013. No national statistics were found on the sale or use of chemical admixtures. In this scenario, this work sought to contribute to the creation of a literary collection about Portland cement and chemical admixtures in Brazil.

It is undeniable that Brazil is mainly an importer of concrete-related technologies, even though its construction sector heavily relies on this material. The changes that occurred in the Brazilian types of cement over the decades, motivated mainly by industrial and urban growth, followed international trends with a certain delay. This delay, originally on the order of decades, has been gradually reducing in recent years. This reducing trend relates to the acceleration of the rate of technology transfer worldwide, a consequence of the globalisation of the economy, and was observed both concerning the adoption of new technologies and the evolution of the standards for the studied materials. Brazilian standards generally follow closely their American and British counterparts.

The literature review showed that knowledge about the evolution of Portland cement and chemical admixtures is relevant information that can assist in the dating process of Brazilian concretes. On one hand, although periodic changes in the maximum limits of the compositions do occur, manufacturers do not disclose the content of admixtures effectively employed in each cement type. Additionally, alterations in the standards and in the main components of the clinker are gradual and occur over decades. On the other hand, in specific time windows, significant changes can be identified, such as the introduction of a new type of cement or chemical admixture [39]. In this sense, the combination of the historical basis developed in the present work with microstructural characterisation techniques may lay the basis for an effective dating methodology of Brazilian concretes.

ACKNOWLEDGEMENTS

We gratefully acknowledge the agency FAPEMIG (Fundação de Amparo à Pesquisa do Estado de Minas Gerais) for providing financial support in the form of a scholarship. We are also grateful for the infrastructure and collaboration of the Research Group on Solid Wastes - RECICLOS - CNPq.

REFERENCES

- [1] K. J. Beasley, "Carbon dating concrete cracks," *J. Perform. Constr. Facil.*, vol. 29, no. 1, 02514002, 2015.

- [2] S. O. Ekololu, "A review on effects of curing, sheltering, and CO₂ concentration upon natural carbonation of concrete," *Constr. Build. Mater.*, vol. 127, pp. 306–320, 2016.
- [3] S. O. Ekololu, "Model for practical prediction of natural carbonation in reinforced concrete: Part 1-formulation," *Cement Concr. Compos.*, vol. 86, pp. 40–56, 2018.
- [4] S. Park, S. Kwon, and S. H. Jung, "Analysis technique for chloride penetration in cracked concrete using equivalent diffusion and permeation," *Constr. Build. Mater.*, vol. 29, pp. 183–192, 2012.
- [5] Associação Nacional das Entidades de Produtores de Agregados para Construção, *The Aggregate Market in Brazil*. São Paulo: ANEPAC, 2015.
- [6] J. J. Biernacki et al., "Cements in the 21st century: challenges, perspectives, and opportunities," *J. Am. Ceram. Soc.*, vol. 100, pp. 2746–2773, 2017.
- [7] R. G. Blezard, *Reflections on the History of the Chemistry of Cement* (SCI Lecture Papers Series). London: Soc. Chem. Ind., 1998, pp. 1–27.
- [8] R. G. Blezard, "The history of calcareous cements," in *Lea's Chemistry of Cement and Concrete*, P. C. Hewlett, Ed., Oxford: Elsevier Sci. Technol. Books, 2004.
- [9] F. Pintér and C. Gosselin, "The origin, composition and early age hydration mechanisms of Austrian," *Cement Concr. Res.*, vol. 110, pp. 1–12, 2018.
- [10] H. Taylor, *Cement Chemistry*, 2nd ed. London: Thomas Telford, 1997.
- [11] P. K. Mehta and P. J. M. Monteiro, *Concrete: Microstructure, Properties and Materials*, 4th ed. New York: McGraw-Hill Education, 2014.
- [12] P. Tennis and J. Bhatti, "Portland cement characteristics-2004," *Concr. Technol. Today*, vol. 26, pp. 1–3, 2005.
- [13] Cimento & Concreto, "Indústria do cimento nasce com a II Revolução Industrial," *Cimento Concr.*, no. 29, pp. 1–10, 1976.
- [14] A. F. Battagin and I. L. S. Battagin, "O cimento Portland no Brasil," in G. C. Isaia, Ed., *Materiais de Construção Civil e Princípios de Ciência e Engenharia de Materiais*, 2a ed. São Paulo: IBRACON, 2010.
- [15] Associated Portland Cement Manufacturers, *Grace's Guide to British Industrial History*. 2019. Accessed: June 18, 2020. [Online]. Available: https://www.gracesguide.co.uk/Associated_Portland_Cement_Manufacturers
- [16] PCA. "PCA (America's Cement Manufacturers)." cement.org (accessed June 18, 2019).
- [17] Sindicato Nacional da Indústria do Cimento. <http://snic.org.br/assets/pdf/numeros/1588788177.pdf> (accessed June 18, 2019).
- [18] Global Cement Magazine, *Global Cement Top 100 Report 2017-2018*. 2017. Accessed: June 18, 2020. [Online]. Available: <https://www.globalcement.com/magazine/articles/1054-global-cement-top-100-report-2017-2018>
- [19] Brazilian Portland Cement Association, *70 Years – a Success Story* (in portuguese). São Paulo: ABCP, 2006.
- [20] P. K. Mehta, *Cement Standards, Evolution and Trends: a Symposium Sponsored by ASTM Committee C-1 on Cement, American Society for Testing and Materials, St. Louis, Mo., 7 Dec. 1977*. Philadelphia: American Society for Testing and Materials, 1978.
- [21] J. M. Illston and P. Domone, *Construction Materials: Their Nature and Behaviour*, 3rd ed. CRC Press, 2001.
- [22] H. Gonnerman and W. Lerch, "Changes in characteristics of portland cement as exhibited by laboratory tests over the period 1904 to 1950," in *Changes in Characteristics of Portland Cement as Exhibited by Laboratory Tests Over the Period 1904 to 1950*, H. Gonnerman and W. Lerch, Eds., West Conshohocken: ASTM Internacional, 1952.
- [23] B. Raath and J. Horton, "Is faster and faster, better and better," in *Proc. Conf. Concr. 21st Century: Modern Concr. Prog. through Innov.: Concr. Soc. Southern Africa*, 2001, pp. 13–14.
- [24] P. K. Mehta and R. W. Burrows, "Building durable structures in the 21st century," *ACI Concr. Int.*, vol. 23, pp. 57–63, 2001.
- [25] E. Gartner, "Industrially interesting approaches to "low-CO₂" cements," *Cement Concr. Res.*, vol. 34, no. 9, pp. 1489–1498, 2004.
- [26] S. O. Ogbuide, "Developing an optimization model for CO₂ reduction in cement production process," *J. Eng. Sci. Technol.*, vol. 3, no. 1, pp. 85–88, 2010.
- [27] K. Yang, Y. Jung, M. Cho, and S. Tae, "Effect of supplementary cementitious materials on reduction of CO₂ emissions from concrete," *J. Clean. Prod.*, vol. 103, pp. 774–783, 2015.
- [28] A. F. Battagin "Cimento Portland," in *Concreto: Ciência e Tecnologia*, 1a ed., G. C. Isaia, Ed., São Paulo: IBRACON, 2011.
- [29] I. N. Grubeša, I. Barisic, A. Fucic, and S. S. Bansode, *Characteristics and Uses of Steel Slag in Building Construction*, 1st ed. Amsterdam: Woodhead Publishing, 2016.
- [30] Associação Brasileira de Normas Técnicas, *Portland Cement – Requirements*, NBR 16697, 2018.
- [31] ASTM International, *20 Standard Specification for Portland Cement*, ASTM C150/C150M, 2020.
- [32] ASTM International, *20 Standard Specification for Blended Hydraulic Cements*, ASTM C595/C595M, 2020.
- [33] BSI Group, *Cement - Composition, Specifications and Conformity Criteria for Common Cements*, BS EN 197-1:2011, 2011.

- [34] Instituto Brasileiro de Geografia e Estatística, *Anuário Estatístico do Brasil*, 2020. [Online]. Available: <https://biblioteca.ibge.gov.br/biblioteca-catalogo?id=720&view=detalhes>
- [35] Associação Brasileira de Cimento Portland, *Guia Básico de Utilização do Cimento Portland*, 7a ed. São Paulo: ABCP, 2002.
- [36] B. J. Ruijven, D. P. Vuuren, W. Boskaljon, M. Neelis, D. Saygin, and M. K. Patel, "Long-term model-based projections of energy use and CO₂ emissions from the global steel and cement industries," *Resour. Conserv. Recycling*, vol. 112, pp. 15–36, 2018.
- [37] Q. Wang, P. Yan, and G. Mi, "Effect of blended steel slag-GBFS mineral admixture on hydration and strength of cement," *Constr. Build. Mater.*, vol. 35, pp. 8–14, 2012.
- [38] S. Z. Carvalho, F. Vernilli, B. Almeida, M. Demarco, and S. N. Silva, "The recycling effect of BOF slag in the portland cement properties," *Resour. Conserv. Recycling*, vol. 127, pp. 216–220, 2017.
- [39] A. F. Battagin and S. L. Centurione, "Panorama do uso do gesso na indústria brasileira de cimento," in *An. 33º Cong. Bras. Cerâm.*, São Paulo, 1989.
- [40] Instituto Aço Brasil, *Relatório de Sustentabilidade 2016-2017*. Rio de Janeiro: IABR, 2018.
- [41] E. Belhadj, C. Diliberto, and A. Lecomte, "Characterization and activation of basic oxygen furnace slag," *Cement Concr. Compos.*, vol. 34, no. 1, pp. 34–40, 2012.
- [42] CSN. "Cimento." http://www.csn.com.br/conteudo_pti.asp?idioma=0&conta=45&tipo=59653. (accessed June 18, 2020).
- [43] M. Schneider, M. Romer, M. Tschudin, and H. Bolio, "Sustainable cement production--present and future," *Cement Concr. Res.*, vol. 41, no. 7, pp. 642–650, 2011.
- [44] L. Mlinárik and K. Kopeckó, "Impact of metakaolin - a new supplementary material - on the hydration mechanism of cements," *Acta Tech. Napocensis Civ. Eng. Archit.*, vol. 56, no. 2, pp. 100–110, 2013.
- [45] H. El-Diadamony, A. Amer, T. M. Sokkary, and S. El-Hoseny, "Hydration and characteristics of metakaolin pozzolanic cement pastes," *HBRC J.*, vol. 14, no. 2, pp. 150–158, 2018.
- [46] A. Ramezani-pour, E. Ghiasvand, I. Nickseresht, M. Mahdikhani, and F. Moodi, "Influence of various amounts of limestone powder on performance of Portland limestone cement concretes," *Cement Concr. Compos.*, vol. 31, pp. 715–720, 2009.
- [47] P. Thongsanitgarn, W. Wongkeo, A. Chaipanich, and C. S. Poon, "Heat of hydration of Portland high-calcium fly ash cement incorporating limestone powder: Effect of limestone particle size," *Constr. Build. Mater.*, vol. 66, no. 15, pp. 410–417, 2014.
- [48] V. Bonavetti, H. Donza, V. Rahhal, and E. Irassar, "Influence of initial curing on the properties of concrete containing limestone blended cement," *Cement Concr. Res.*, vol. 30, pp. 703–708, 2000.
- [49] R. Faria, "Solução fluida," *Rev. Técnica*, vol. 132, 2008.

Author contributions: JFN: data curation, formal analysis, methodology, writing; ECT: data curation, formal analysis; JCM: data curation, writing, methodology; RAFP: supervision, writing.

Editors: Fernando Pelisser, Guilherme Aris Parsekian.

APPENDIX

The sources for the chemical composition shown in Figure 2 are the following:

- Abrams, D. A., 1919. *Design of Concrete Mixtures – Bulletin 1*. Chicago: Structural Materials Research Laboratory, Lewis Institute.
- Abrams, D. A., 1919. *Effect of vibration, jiggling and pressure on fresh concrete - Bulletin 3*. Chicago: Structural Materials Research Laboratory, Lewis Institute.
- Abrams, D. A., 1922. *Flexural Strength of Plain Concrete - Bulletin*. Chicago: Structural Materials Research Laboratory.
- Abrams, D. A., 1925. *Quantities of materials for concrete - Bulletin*. 2 ed. Chicago: Structural Materials Research Laboratory.
- Adriolo, F. R., 1984. *Construções de Concreto – Manual de Práticas para controle e Execução*. s.l.:PINI.
- Aïtcin, P., 2008. *Binders for Durable and Sustainable Concrete – Modern Concrete Technology*. s.l.:Taylor & Francis.
- Aïtcin, P., Mindess, S. & Tagnit-Hamou, A., 2012. *Building Highly Sustainable Concrete (HSC) Structures - Symposium STOCKHOLM. Concrete Structures for Sustainable Community - KTH Royal Institute of Technology*.
- ASTM, 1904. *Report of Committee on Standard Specifications for Cements*. s.l.:American Society for Testing Materials.
- ASTM, 1994. *C150/C150M-20: Standard Specification for Portland Cement*, s.l.: American Society for Testing Materials.
- Bauer, L. A. F., 1995. *Materiais de Construção*. 5 ed. Rio de Janeiro: LTC.
- Benedix, R., 2005. *Bauchemie – Einführung in die Chemie für Bauingenieure*. 3 ed. s.l.:Teubner.
- Bensted, J. & Barnes, P., 2002. *Structure and Performance of Cements*. 2 ed. s.l.:Spon Press.
- Bentz, D. P., 1997. Three-Dimensional Computer Simulation of Portland Cement Hydration and Microstructure Development. *Journal of the American Ceramic Society*, 80(1), pp. 3-21.
- Bhatti, I. & Tennis, P. D., 2008. *U.S. and Canadian Cement Characteristics: 2004*. s.l.:Portland Cement Association, Research & Development Information.
- Blount, B., 1912. *Lectures on Cements*. s.l.:The Institute of Chemistry of Great Britain and Ireland .
- Boateng, A., 2008. *Rotary Kilns – Transport Phenomena and Transport Processes*. s.l.:Butterworth-Heinemann – Elsevier.
- Bogue, R. H., 1947. *The Chemistry of Portland Cement*. s.l.:Reinhold Book Corporation.
- Bogue, R. H. & Herman, R., 1955. *The chemistry of Portland Cement*. 2 ed. s.l.:Reinhold Publishing Corporation.
- Brown, W. L., 1899. *Elasticity of Portland Cement*. London.
- Butler, D. B., 1899. *Portland Cement, its Manufacture, testing and use*. London: E&F.N.Spon.
- Bye, G. C., 1999. *Portland Cement – Composition, Production and Properties*. 2 ed. s.l.:Thomas Telford.
- Carneiro, F. L. L. B., 1953. *Dosagem de Concretos*. 2 ed. Rio de Janeiro: INT.
- Chamecki, S., 1956. *Curso de Estática das Construções*. Rio de Janeiro: Editora Científica.
- Cummings, U., 1898. *American Cements*. Boston: Rogers & Manson.
- Da Silva, G. R., 1975. *Manual de Traços de Concreto*. 3 ed. São Paulo: Livraria Nobel S.A..
- Darwin, D., Young, J. F. & Mindess, S. F., 2003. *Concrete*. 2 ed. s.l.:Prentice Hall.
- Duda, W. H., 1984. *Cement Data Book, Volume 2: Automation, Storage, Transportation, Dispatch*. s.l.:French & European Pubns.
- Duda, W. H., 1985. *Cement Data Book, Volume One: International Process Engineering in the Cement Industry*. 3 ed. s.l.: French & European Pubns.
- Duda, W. H., 1988. *Cement Data Book, Volume 3: Raw Material for Cement Production*. s.l.:French & European Pubns.
- Duda, W. H., 2003. *Cemento, Manual Tecnológico*. s.l.:Editorial Reverté.
- Eisenmann, J., Leykauf, G. & Kupfer, H., 2003. *Beton-fahrbahnen*. s.l.:Ernst&Sohn.
- Falk, M. S., 1904. *Cements, Mortars and Concretes – Their Physical Properties*. New York: M.C. Clark.
- Federal Highway Administration – USA - Publication No. HIF -07-004, 2009. *Integrated Materials and Construction Practices for Concrete Pavement*. s.l.:A State of the Practice Manual.
- Fritz, K., 1971. *Zement - Herstellung und Eigenschaften*. s.l.:Springer-Verlag.
- Frohnsdorff, G. et al., 1997. *Guide to the Selection of Hydraulic Cements*, s.l.: ACI Committee 225.
- Furnas, E. d., 1997. *Concretos massa, estrutural, projetado e compactado com rolo: ensaios e propriedades*. São Paulo: PINI/Walton Pacelli de Andrade.

- Gatehouse, F. B., 1908. *A Handbook for Cement Works Chemists*. London: HardPress Publishing.
- Glasser, F. P., 2005. Thermodynamics of Cement Hydration. Em: F. Young & J. P. Skalny, eds. *Materials Science of Concrete VII*. s.l.:The American Ceramic.
- Graf, O., 1950. *Die Baustoffe, Ihre Eigenschaften und ihre Beurteilung*. Stuttgart: Konrad Wittwer.
- Helene, P., 2003. Por que trabalhar com concretos de resistências mais elevadas que as atuais?. Campinas: SindusCon/SP.
- Helene, P. & Terzian, P., 1992. *Manual de Dosagem e Controle do Concreto*. Brasília: PINI.
- Hewlett, P. C., 1998. *Lea's Chemistry of Cement and Concrete*. 14 ed. s.l.:John Wiley & Sons.
- Hooton, R. D., Boyd, A. J. & Bhadkamka, D. D., 2005. Effect of Cement Fineness and C3S Content on Properties of Concrete: A literature Review. *PCA R&D Series*, pp. 2-11.
- Johansen, V. C., Taylor, P. C. & Tennis, P. D., 2006. *Effect of Cement Characteristics on Concrete Properties*. s.l.:Portland Cement Association, Engineering Bulletin 226.
- Johansen, V. & Kouznetzova, T. V., 1992. Clinker formation and new processes. *9th International Congress on the Chemistry of Cement*, Volume 1, pp. 49-79.
- Kleinlogel, A., Hundeshagen, F. & Graff, O., 1930. *Einflüsse auf Beton*. s.l.:Wilhelm Ernst & Sohn.
- Kosmatka, S. H., Kerkhoff, B. & Panarese, W. C., 2005. *Design and Control of Concrete Mixtures*. 14 ed. s.l.:Portland Cement Association.
- Lea, F. M., 1935. *The chemistry of Cement and Concrete*. 1 ed. New York: Chemical Publishing Company.
- Lea, F. M., 1970. *The chemistry of Cement and Concrete*. 3 ed. New York: Chemical Publishing Company.
- Lin, L. et al., 2004. Development and Research of High Belite Cement Dam Concrete with low heat and high crack resistance. *International Workshop on Sustainable Development and Concrete Technology*.
- Locher, F. W., 2005. *Cement - Principles of Production and Use*. s.l.:Bau+Technik.
- Maekawa, K., Ishida, T. & Kishi, T., 2009. *Multi-Scale Modeling of Structural Concrete*. s.l.:Taylor & Francis.
- Meade, R. K., 1901. *Portland Cement – Chemical and Physical Examination*. Easton: The Chemical Publishing Company .
- Meade, R. K., 1909. *Portland Cement – Its Composition, Raw Materials Manufacture, Testing and Analysis*. Easton: The Chemical Publishing Company.
- Mehta, P. K., 1999. Concrete Technology for Sustainable Development. *ACI - Concrete International*, 21(11), pp. 47-53.
- Mehta, P. K. & Burrows, R. W., 2001. Building durable structures in the 21st century. *ACI Concrete Internacional*, Volume 23, pp. 57-63.
- Neville, A., 1994. *Cement and Concrete: Their Interrelation in Practice - Advances in Cement and Concrete*. s.l.:American Society of Civil Engineers.
- Neville, A., 2006. *Neville on Concrete – An Examination of issues in Concrete Practice*. 2 ed. s.l.:Booksurge LLC.
- Neville, A. M., 1985. *Properties of Concrete*. s.l.:Addison Wesley.
- Neville, A. M., 1994. *Cement and Concrete: Their Interrelation in Practice - Advances in Cement and Concrete*. s.l.:American Society of Civil Engineers.
- Newberry, S. B., 1899. *How to use Portland Cement*. Chicago: Forgotten Books.
- Odler, I., 2000. *Special Inorganic Cements - Modern Concrete Technology*. London: E&FN SPON.
- Peray, K. E., 1986. *Rotary Cement Kiln*. 2 ed. s.l.:CHS Press.
- Petrucci, E. G., 1968. *Concreto de Cimento Portland*. s.l.:Associação Brasileira de Cimento Portland.
- Pizarro, R. A., 1964. *Concreto: Cimentos, Agregados – Dosagem e Propriedades*. *Escola Nacional de Engenharia, Universidade do Brasil*.
- Poole, A. et al., 1998. *Concrete Petrography – A handbook of investigative techniques*. 5 ed. New York: Arnold - John Wiley.
- Ramachandran, V. S. & Beaudoin, J., 2001. *Handbook of Analytical Techniques in Concrete Science and Technology*. New Jersey: Noyes Publications.
- Redgrave, G. R., 1895. *Calcareous Cements: Their Nature And Uses With Some Observations Upon Cement Testing*. London: Forgotten Books.
- Reid, H., 1869. *A practical treatise on concrete and how to make it: with observations on the uses of cements, lime and mortars*. London: E.& F. SPON.
- Reid, H., 1877. *The Science and Art of the Manufacture of Portland Cement*. London: E.& F.N. SPON.
- Sabin, L. C., 1905. *Cement and Concrete*. New York: McGRAW Publishing Company.

- Skalny, J., Gebauer, J. & Odler, I., 2001. *Calcium Hydroxide in Concrete – Materials science of Concrete*. s.l.:American Ceramic Society /SA.
- Spalding, F. P., 1898. *Hydraulic Cement – Its Properties, Testing and Use*. New York: John Wiley & Sons.
- Srinivasan, D., 2008. *Guide for Good Concrete Construction*. s.l.:Indian Concrete Institute.
- Stark, J. & Wicht, B., 2000. *Zement und Kalk – Der Baustoff als Werkstoff*. s.l.:F. A. Finger.
- Stark, J. & Wicht, B., 2001. *Dauerhaftigkeit von Beton – Der Baustoff als Werkstoff*. s.l.:F. A. Finger.
- Sui, T. et al., 2004. Study on the Properties of High Strength Concrete using High Belite Cement. *Journal of Advanced Concrete Technology*, 2(2), pp. 201-208.
- Sui, T. et al., 2006. A Comparison of HBC & MHC Massive Concretes for Three Gorges Project in China. Em: M. S. Konsta-Gdoutos, ed. *Measuring, Monitoring and Modeling Concrete Properties: An International Symposium dedicated to Professor Surendra P. Shah*. 1 ed. s.l.:Springer.
- Taylor, H. F., 1997. *Cement Chemistry*. 2 ed. s.l.:Thomas Telford.
- Torres, A. F. & Rosman, C. E., 1956. *Método para dosagem racional do concreto*, São Paulo: ABCP.
- Young, F. & Skalny, J., 2005. *Materials Science of Concrete VII*. s.l.:American Ceramic Society.
- ZTV Beton-StB 07, 2007. *Zusätzliche Technische Vertragsbedingungen und Richtlinien für den Bau von Tragschichten mit hydraulischen Bindemitteln und Fahrbahndecken aus Beton*. s.l.:FGSV.



ORIGINAL ARTICLE

Numerical analyses of two-pile caps considering lateral friction between the piles and soil

Análise numérica de blocos sobre duas estacas considerando o atrito lateral entre as estacas e solo

Rodrigo Gustavo Delalibera^a

Gabriel Fernandes Sousa^a

^aUniversidade Federal de Uberlândia – UFU, Faculdade de Engenharia Civil, Uberlândia, MG, Brasil

Received 25 July 2019

Accepted 13 November 2020

Abstract: Pile caps are structural elements used to transfer loads from the superstructure to a group of piles. The design of caps is normally based on analytical formulations, considering the strut and tie method. Through the advance of computational technology, the use of an integrated soil and foundation model may suggest a behavioral trend to obtain a more realistic modeling for the structural element being studied. This work aimed at analyzing, in numerical fashion, the structural behavior of reinforced concrete two-pile caps considering the lateral friction between the piles and the ground through a continuous modeling, as well as to analyze the portion of the load that is transferred to the ground directly by the cap. The lateral friction was modeled considering node coupling and through contact elements. Simulations were performed considering three soil types (sandy, clayish, and soilless), three cap heights, and three pile lengths. Soil parameters were obtained through semi-empirical correlations. Through these analyses, the conclusion was reached that, on average, 4.50% of the force applied to the pillar is transferred directly to the ground by cap. In terms of the principal compression stresses, in the superior nodal region, the strut tends to form beyond the section of the column. Alternatively, increasing cap stiffness provided, on average, an increase in the load carrying capacity of the models.

Keywords: pile caps, reinforced concrete, soil, lateral friction, numerical analysis.

Resumo: Blocos sobre estacas são elementos estruturais usados para transferir ações da superestrutura para um conjunto de estacas. O dimensionamento de blocos é comumente realizado por meio de formulações analíticas, considerando-se o método de bielas e tirantes. Com o avanço da tecnologia computacional, a utilização de um modelo integrado, considerando a influência do solo e da rigidez das estacas, poderá surgir uma tendência de comportamento de modo a se obter uma modelagem mais próxima do comportamento real dos blocos. Este trabalho teve como objetivo analisar por meio de análises numéricas o comportamento estrutural de blocos de concreto armado sobre duas estacas, considerando o atrito lateral entre as estacas e o solo por meio de uma modelagem contínua, bem como analisar a parcela de força transferida ao solo diretamente através da base do bloco. O atrito lateral foi modelado considerando o acoplamento de nós e por meio de elementos de contato. Assim, foram realizadas simulações considerando três configurações: solo arenoso, solo argiloso e sem solo, três alturas de bloco e três comprimentos de estaca. Os parâmetros do solo, como módulo de elasticidade, ângulo de atrito e coeficiente de Poisson foram obtidos através de correlações semiempíricas, baseadas em ensaios de percussão simples. Constatou-se que, em média, 4,50% das forças aplicadas no pilar são transferidas diretamente ao solo por meio da base do bloco. Com relação às tensões principais de compressão, verificou-se que na região nodal superior, a biela tende a se formar além da seção do pilar. Já o aumento da rigidez do bloco proporcionou, em média, um aumento da capacidade portante dos modelos.

Palavras-chave: blocos sobre estacas, concreto armado, atrito lateral, análise numérica.

How to cite: R. G. Delalibera and G. F. Sousa, “Numerical analyses of two-pile caps considering lateral friction between the piles and soil,” *Rev. IBRACON Estrut. Mater.*, vol. 14, no. 6, e14604, 2021, <https://doi.org/10.1590/S1983-41952021000600004>

Corresponding author: Rodrigo Gustavo Delalibera. E-mail: delalibera@ufu.br

Financial support: FAPEMIG - Research Support Foundation of the State of Minas Gerais.

Conflict of interest: Nothing to declare.



This is an Open Access article distributed under the terms of the Creative Commons Attribution License, which permits unrestricted use, distribution, and reproduction in any medium, provided the original work is properly cited.

1 INTRODUCTION

The act of determining the type of foundation to be used in a construction is realized through technical studies, the main purpose behind these studies is to analyze the characteristics of the soil in terms of its load capacity and compressibility of the soil, along with the condition of the foundations of the neighboring buildings, as well as economic factors. Therefore, knowledge regarding soil parameters, the intensity of the forces that will be distributed through it, along with an understanding of the building limits, allows one can choose the type of foundation most suitable for a given construction.

There are situations in which the superficial layers of the soil do not have sufficient support capacity to absorb and distribute the forces arising from the superstructure. In such cases, it is necessary to use one of the deep foundation types.

It is understood that deep foundations are those that transmit the load to the soil through its base or through lateral friction, these being the piles and the caissons. The choice of foundation, however, requires the construction of structural elements - the pile cap.

According to NBR 6118 [1], pile caps are volume structures used to transmit foundation loads to the piles. Therefore, it can be said that all external dimensions have the same order of magnitude. These are treated as special structural elements, which do not respect the hypothesis that the flat sections remain flat after deformation, as these are not long enough for localized disturbances to dissipate.

1.1 Justification

The present research is justified through the importance that pile caps have in the structure of a building, as well as through the limited amount of research, in the literature, with numerical emphasis, which is directed toward the analysis of the integrated behavior associated with the pile cap-pile-soil set by the adoption of contact elements. The contact between the crown block and the soil promotes the transfer of a portion of the load directly to the soil, where there is not a total transfer of the force acting on the column onto the top of the piles. Taking the aforementioned into consideration, this study becomes of importance since the integrated analysis allows for the quantification of portions linked to the vertical force transferred directly to the soil through the block. In addition, the calculation methods used for the design of pile blocks do not cogitate the presence of soil, and as such do not deliberate on the variation in the stress field that occurs due to the direct contact between the structural elements and the soil.

1.2 Objective

This study aims at analyzing, through numerical modeling, the structural behavior of foundation blocks on two precast reinforced concrete piles, while allowing for the friction between the pile and the soil, by knot coupling (perfect stiffness) and by contact elements. Through a joint modeling (pile cap-pile-soil), an analysis of variance (ANOVA) was carried out, generating through such the study of the behavioral tendency associated with the bearing capacity of the models, and the portion of force transferred directly to the soil through the pile cap. Finally, an attempt was made at verifying whether there exists agreement between the pile repression in the numerical models studied with the repression obtained analytically.

2 DESIGN OF THE MODELS

Pile caps were analyzed on two piles, these were subjected to centered force loads, varying the following parameters: pile cap height (28 cm, 50 cm, and 70 cm), pile length (5 m, 7 m and 9 m), soil type (sand, clay and without soil), under conditions where bonding between the structure and the soil occurs (knot coupling and contact element). Figure 1 presents the geometries of the analyzed models and their conditions. In total 45 pile caps were modeled on two piles and numerical modeling was performed with the aid of a computational tool based on the finite element method - FEM.

As shown in Figure 2, the strength of 25 MPa and 50 MPa for the concrete in the pile caps, columns and piles was adopted, since the study dealt with the analysis of the bearing capacity of the pile caps. For steel bars, the NBR 6118 criterion [1] was used, admitting a perfect elastoplastic behavior for steel, with yield strength of 500 MPa.

The piles caps were checked and dimensioned using the strut and tie model, according to the criteria of Blévet and Frémy [2].

Noted herein was for the proposed block heights, the limit of the angle of inclination for the compression rod recommended by Blévet and Frémy [2], to guarantee rigidity of the pile cap ($45^\circ \leq \theta \leq 55^\circ$), was not met for the models with

height of 28 cm and 70 cm. However, the recommendations of NBR 6118 [1] were met, which suggests that the tangent of the compressed diagonal angle is between 0.57 (29.7°) and 2 (63.4°). This information can be found on Table 1.

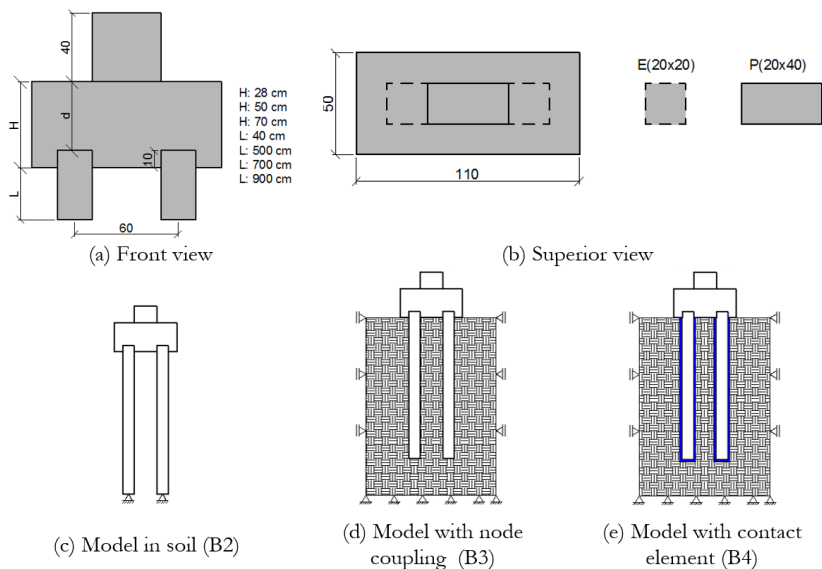


Figure 1. Characteristics of the models analyzed in the research (measured in centimeters).

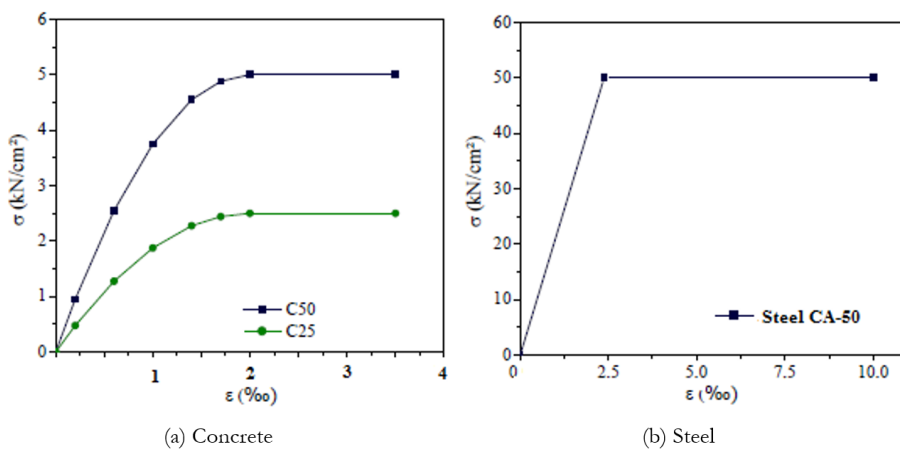


Figure 2. Material constitutive model: concrete and steel.

Regarding the dimensioning of column and pile reinforcement, the criteria of NBR 6118 [1] were considered. For the pile caps, only the existence of the main tensile reinforcement (tie) was considered. The quantity of steel bars for each structural element is provided on Table 2. Here A_{st} is the main reinforcement of the pile cap, A_{sp} the longitudinal reinforcement of the column and A_{sc} the longitudinal reinforcement of the piles.

Table 1 - Inclination of strut according to pile cap height.

Model height	Column	θ (degrees)	Useful height (cm)	Load
H28		30.96	18	Vertical e Centered
H50	20 x 40	53.13	40	
H70		63.4	60	

Table 2 - Quantitative reinforcement for structural elements

Model	A _{st}	A _{sp}	A _{se}
B2P40H28e0			
B3P40H28e0	3 ø 20 mm	6 ø 10 mm	4 ø 10 mm
B4P40H28e0			
B2P40H50e0			
B3P40H50e0	5 ø 16 mm	6 ø 12.5 mm	4 ø 10 mm
B4P40H50e0			
B2P40H70e0			
B3P40H70e0	4 ø 16 mm	8 ø 12.5 mm	4 ø 12.5 mm
B4P40H70e0			

3 NUMERIC MODELING

For modeling of the piles and columns, the ANSYS® computer program [3] was used. The concrete behavior was simulated using two constitutive models. For stress simulation, the CONCRETE model was used, which is based on the Willam-Warnke model [4], where it was possible to simulate cracked concrete when subjected to tensile stresses that exceed the pre-established limit. In the CONCRETE model, it is necessary to provide parameters such as the shear transfer coefficient through an open crack (β_a), shear transfer coefficient through a closed crack (β_f), ultimate tensile strength and ultimate compressive strength. However, as the compression behavior of the concrete will be modeled according to the Von Mises criterion (simulating the plasticization of the concrete), it is necessary to disable the compressive strength in the CONCRETE model, adopting the value of -1 for this parameter.

To quantify the ultimate tensile strength, the NBR 6118 criterion [1] was used, according to Equation 1.

$$f_{ct,m} = 0.3 \cdot f_{ck}^{2/3} \quad (1)$$

In Equation 1, f_{ck} is the characteristic compressive strength of concrete and $f_{ct,m}$ the average tensile strength of concrete, both expressed in MPa.

The behavior of concrete in compression was simulated according to the Multilinear model available in the Ansys® library [3], following the Von-Mises criterion. This criterion was used to improve the convergence of the models, since the CONCRETE model only presents numerical instability, which hinders convergence. The NBR 6118 stress-strain curve criteria were analyzed [1], along with the model proposed by Desay and Krishnan [5].

In Figure 2, the isotropic behavior of class C25 and C50 materials is established for block, column and pile respectively, in reference to the model proposed by NBR 6118 [1].

Regarding the shear transfer coefficients, Delalibera [6] used 1.0 for the β_a and β_f parameters, whereas Munhoz [7] suggests the use of 0.2 for β_a and 0.6 for β_f . In the present work, 0.2 was used for β_a and 0.8 for β_f , since a better convergence was noted with the use of such parameters.

For reinforcements, the Von-Mises plasticization criterion was considered, according to a perfect elasto-plastic model.

In the ANSYS® software [3], the simulation of the perfect elasto-plastic model is carried out using a bilinear isotropic model, where it is necessary to inform the steel elasticity module (E_s), the flow resistance (f_y) and the tangent elasticity module (ET). In the present work, CA-50 steel was used, with an elastic modulus of 210 GPa, yield strength of 500 MPa and the tangent modulus was null, as seen in Figure 2.

For the soil material, the Drucker-Prager model and the model representing elasto-plastic behavior were considered, where the flow is controlled by a combination of the hydrostatic stress and the deviation stress.

The concrete and soil elements were modeled with the finite element SOLID65. This element has eight nodes with three degrees of freedom per node - translations in the x, y and z directions. The element has plastic deformations, cracking and crushing in three orthogonal directions. In the SOLID65 element, cracking occurs when the main tensile stress in any direction reaches the breaking surface. After cracking, the modulus of elasticity of the concrete becomes equal to zero in the direction considered. Crushing occurs when the set of compressive stresses acting on the rupture planes exceeds the limit resistance established by a rupture surface, subsequently, the modulus of elasticity becomes equal to zero in all directions. The SOLID65 element is seen in Figure 3.

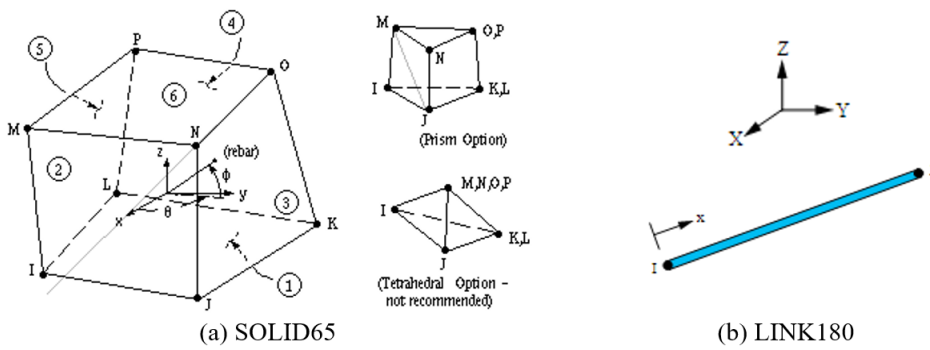


Figure 3. Finite elements used in modeling concrete, soil and steel bars.

In modeling the steel bars of the armature, the finite element LINK180 was used (Figure 3).

This element has two nodes, each node possessing three degrees of freedom - translations in the x, y, and z directions. Therefore, this element was chosen, as the reinforcement in the models was considered to be discrete.

The friction between the piles and the soil was simulated by coupling the nodes (perfect friction) and by using finite contact elements. The contact surfaces between the materials were represented by two finite elements, in which the association of these elements, called “contact pair”, is necessary to determine a contact surface and a target surface. For the contact surface (pile and block), the finite element CONTACT174 was used and for the target surface (soil), the finite element TARGET170 was used. These elements have three degrees of freedom on each node and the geometric properties are the same as the faces of the solid elements to which they are attached and may have triangular or quadrangular geometry. The finite elements CONTACT174 and TARGET170 are noted in Figure 4.

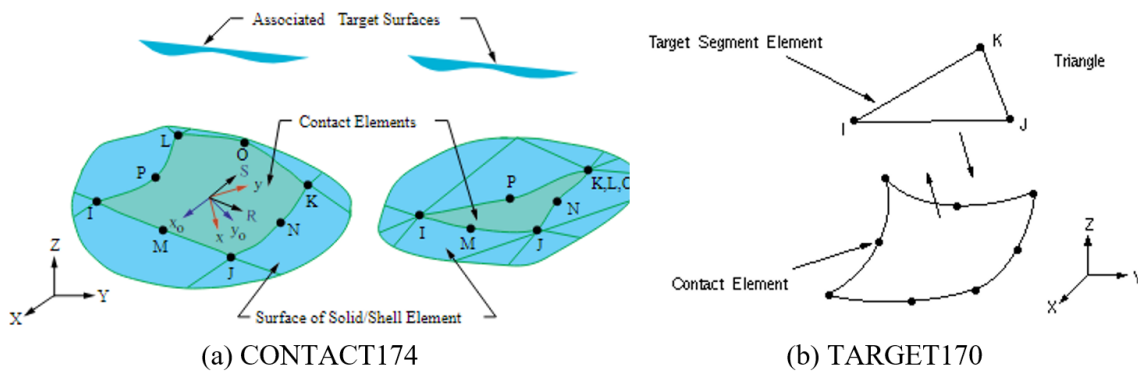


Figure 4. Finite elements used to model contact elements.

The models were named according to the type of connection (B2, B3 and B4), to the cross-sectional dimension of the column (P40), to the height of the block (H28, H50, H70), to the length of the pile (L5, L7 and L9), to the soil type (S0, S1 and S2) and finally to the loading eccentricity (e_0). As an example, the model B3P40H70L9S2e0 is a model in which we used node coupling as bonding, a 40 cm column in the transverse direction, a 70 cm high block, 900 centimeters piles, type 2 (clayish) soil and loading with zero eccentricity.

4 MEASURING OF THE MODELS

To verify which refinement is necessary for the finite element mesh, a mesh convergence test was carried out. Such a test is important so that the mesh used does not contain a very large quantity of elements, which would make the processing time impracticable. To perform this test, the B115P250R1 pile cap was used, tested experimentally by Munhoz [7]. Figure 5 shows the meshes used in the analysis. Emphasis is here placed on the different element division

sizes of 20 cm, 10 cm, 5 cm, 4 cm, 3 cm and 2.5 cm that were tested. Noteworthy here is that some elements presented non-standard values, since it was necessary to have divisions in the places where there are reinforcements.

As observed in Figure 6, verification is made into the incremental displacement history for each mesh. Through such, one notes that the mesh refinement reduced the linear phase of the material, as such producing the more recent cracks. However, with respect to the final displacement, convergence was identified at values close to 0.75 mm. Therefore, still in Figure 6, there is the convergence of the vertical displacement, according to the finite element mesh refinement. The meshes with 7920 elements, 9934 elements and 13570 elements showed very close displacements, confirming the tendency towards a convergence of behavior. As such, the conclusion was reached that a mesh with a division of approximately 3 cm led to an acceptable behavior trend, saving computational time for a mesh with more elements.

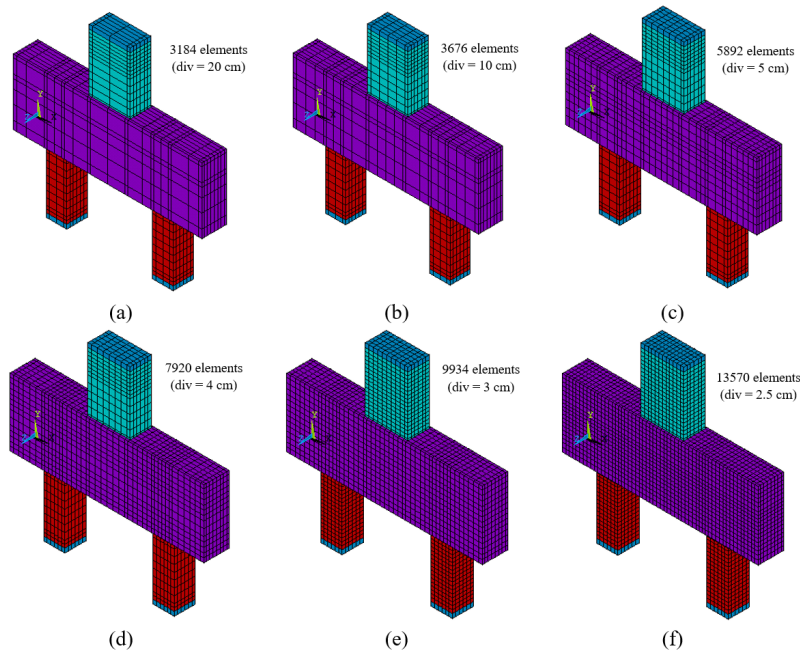


Figure 5. Finite element meshes tested.

To validate the modeling criteria, a numerical result behavior test was performed, comparing it with experimental data. Block B115P250R1 was used, experimentally tested by Munhoz [7].

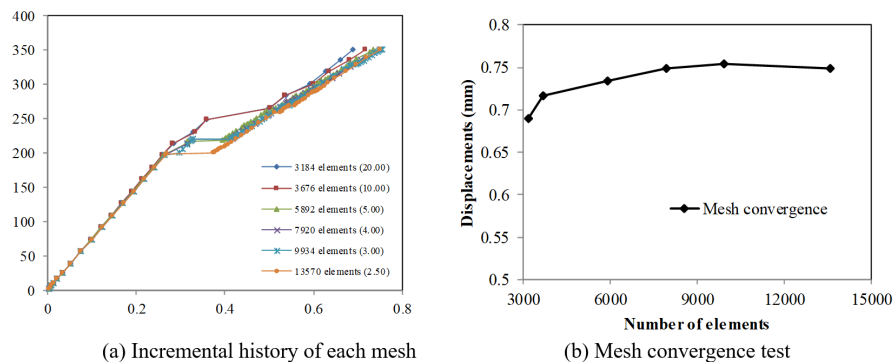


Figure 6. Convergence test of vertical displacement in the lower center of the pile cap according to mesh refinement.

In Figure 7, one notes the comparison between the Force-Displacement curves, which refers to the numerical and experimental models. The numerical models processed with the constitutive model CONCRETE (with experimental elasticity module) and Multilinear (according to the stress vs. concrete deformation curve calculated according to NBR 6118 [1]) were proven to be more rigid than the experimental model from Munhoz [7]. Therefore, a correction was made in the pile caps stiffness ($E_{cs} \cdot I$), modifying the pile caps elasticity module, with the intuition of making the model more flexible. The new modulus of elasticity was calculated based on Equation 2, taking into account the cracking of the block. The block was considered as a beam subjected to a concentrated force in the center of the span. Therefore, based on the displacement in which the first crack in the Munhoz block occurred [7], the corrected elastic modulus can be obtained.

$$E_{cor} = \frac{F \cdot L_{est}^3}{48 \cdot \delta \cdot I} \tag{2}$$

E_{cor} is the corrected elasticity module, L_{est} the distance between the pile axis, I the moment of inertia of the pile cap cross section, F the vertical force referring to the appearance of the first crack in the experimental model and δ the vertical displacement referring to the instant of the first fissure.

Elasticity modules with values of 3575.70 MPa, 4500 MPa and 6100 MPa were tested. The best approximation occurred with an E_{cor} of 6100 MPa. With the elasticity module corrected, the multilinear model proposed by Desay and Krishnan was tested [5]. As shown in Figure 7, this model led to an ultimate force of 770 kN, a force greater than that achieved only with the CONCRETE model.

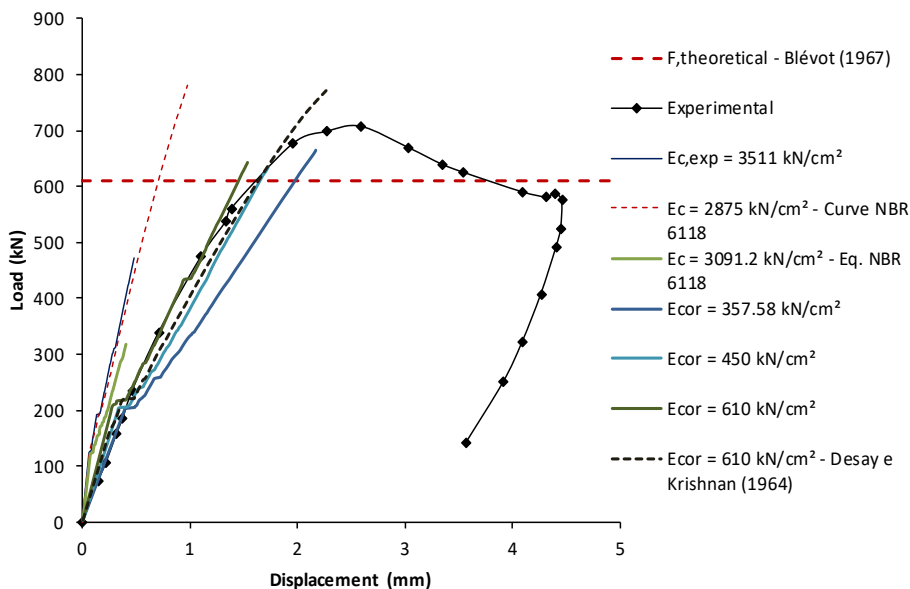


Figure 7. Calibration of the numerical model to Munhoz's experimental results [6].

The use of the Desay and Krishnan model [5] with $E_{cor} = 6100$ MPa led to a good approximation, producing in the model a higher carrying capacity than the model in which the CONCRETE criterion was used alone, for the same value of modulus of elasticity. The conclusion was reached, therefore, that the use of a Multilinear model associated with the CONCRETE model led to a better numerical representation of the Munhoz experimental model [7], being, therefore, the acceptable criteria for simulating the element. On Table 3, one can identify how the ultimate numerical strength ($F_{u,num}$) differs from the theoretical strength values (F_{Tco}), calculated according to the Blévoit and Frémy model [2], and the ultimate experimental ($F_{u,exp}$), obtained experimentally.

With the numerical modeling at hand, the authors herein noted the cracking panorama, connecting rods and stress flow obtained for the numerical model with E_{cor} of 6100 MPa approached the Munhoz experimental result [7], as seen in Figure 8.

By producing the ratio between the corrected elasticity modulus and the real elasticity modulus of the structure, one obtains the reduction coefficient for the modulus of elasticity for the models of the present study, according to Equation 3.

Table 3 - Quantitative reinforcement for structural elements.

Modeling	F_{Teo} (kN)	$F_{u,exp}$ (kN)	$F_{u,num}$ (kN)	$F_{u,exp}/F_{u,num}$	$F_{Teo}/F_{u,num}$
Curve – NBR 6118 [1]			781.25	0.91	0.78
$E_{c,exp} = 3511 \text{ kN/cm}^2$			437.29	1.63	1.39
$E_{cor} = 357.58 \text{ kN/cm}^2$			664.69	1.07	0.92
$E_{cor} = 450 \text{ kN/cm}^2$	609.40	712.67	634.53	1.12	0.96
$E_{cor} = 610 \text{ kN/cm}^2$			643.7	1.11	0.95
$E_{cor} = 610 \text{ kN/cm}^2$ - Desay and Krishnan [4]			770	0.93	0.79

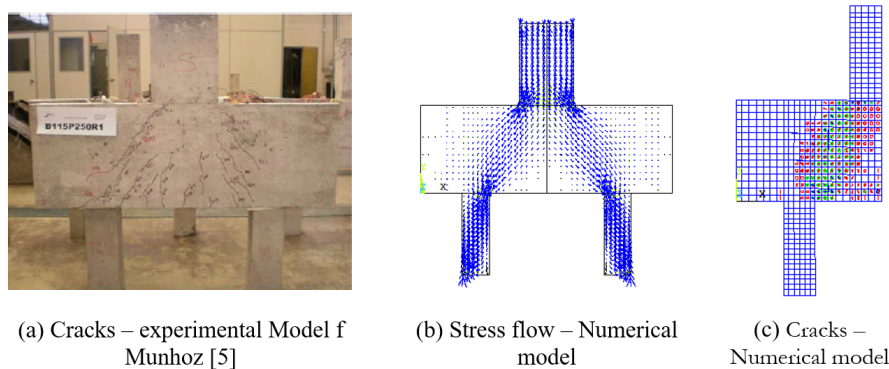


Figure 8. Conformity between the numerical model and the experimental model, through the stress flow and cracking pattern.

$$k_{red} = \frac{E_{cor}}{E_{c,exp}} = \frac{6100.00}{35110.00} = 0.174 \tag{3}$$

To assess the behavior of the contact elements, simulations were carried out, varying the normal contact stiffness (FKN) and analyzing how this would influence the maximum penetration, maximum pressure and number of iterations until convergence.

According to Silva [8], contact stiffness is inversely proportional to penetration. The author also states that, ideally, penetration should not occur between the bodies in contact with each other, as physically the bodies could not occupy the same position; however, numerical devices are commonly used in solutions of contact problems and allow for the existence of a small penetration, this penetration being defined according to a tolerance factor (FTLN).

The simulations were performed with a tolerance factor (FTLN) fixed at 10% in order to reduce the possibility of loss of stability of the finite element SOLID65. The hexahedral element of the soil in contact with the pile has a dimension of 50 cm while the hexagonal element of the pile has a maximum dimension of 5 cm. Therefore, when using a penetration tolerance factor $FTOLN = 0.10$, satisfactory results are those that lead to a maximum penetration equal to or less than 5 mm ($5 \text{ cm} \times 0.10 = 5 \text{ mm}$). Therefore, as noted in Figure 9, the maximum penetration values are acceptable and tend to stabilize as the FKN factor increases.

All simulations were carried out for three coefficients of friction between the concrete and the soil ($\mu = 0.20$; $\mu = 0.60$; $\mu = 1.00$), in order to analyze the behavior trend and verify how the analysis parameters behaved by stiffening the system. As noted from Figure 9, the reduction of the friction coefficient provided an increase in maximum penetration, by maintaining the penetration factor and by increasing the stiffness factor. However, although there is variation in penetration, the change in the friction coefficient was not seen as promoting significant variations in the

studied parameters and as the FKN value was added, the parameters analyzed (maximum penetration, maximum pressure, and total number of iterations) tended to match.

Noted by analyzing the contact pressure, seen in Figure 9, was that an initial variation, from 0.10 to 0.50, in the FKN factor promoted a significant drop (446%) in the average contact pressure, this being due to an increase in FKN, where a tendency towards stabilization was observed, as seen in Figure 9.

Finally, the number of iterations for the convergence of the results was analyzed, verifying that the increase in the stiffness factor FKN promoted an increase in the number of iterations, as shown in Figure 9, thus causing the problem to present greater convergence difficulties. After carrying out the analyses, the decision was reached to use in the simulations of the models the contact element, FKN = 15 and FTLN = 0.10. Regarding the friction coefficients, the requirements contained in NAVFAC [9] were followed, using for sandy soil, friction coefficient of 0.55 and for clay soil friction coefficient of 0.30. After the gauging tests and defining the characteristics of the numerical models, the parameters used to model the reinforced concrete structural elements are presented on Table 4.

Table 4 – Numerical parameters to modeling concrete and steel.

Material - Element	Linear properties	No-linear properties	
		Tension (CONCRETE)	
		βa = 0.2	
		βf = 0.8	
		f _{ct} = 2.56 MPa	
		Compression (multilinear isotropic)	
		Strain (‰)	Stress (MPa)
Pile Cap (SOLID65)	E _{cor} = 3915 MPa ν = 0.2	0	0
		0.0019157	7.50
		0.0032567	11.97
		0.0047893	16.44
		0.0058110	18.85
		0.0080000	22.49
		0.0100000	24.27
		0.0127714	25.00
		Tension and compression (CONCRETE)	
		βa = 0.2	
Piles e Column (SOLID65)	E _c = 39598 MPa ν = 0.2	βf = 0.8	
		f _{ct} = -1	
		f _c = -1	
Steel (LINK180)	E _s = 210000 MPa ν = 0.3	f _y = 500 MPa	
		Tangent module = 0	

In similar fashion to that presented for steel and concrete, Table 5 shows the soil analysis parameters used in the numerical models, showing the linear properties of each layer, as well as the Drucker-Prager model parameters.

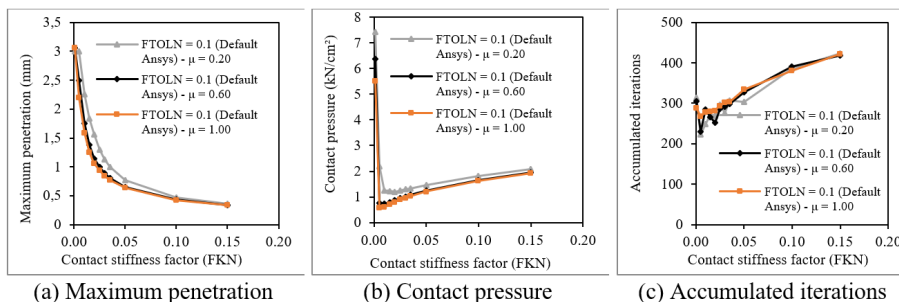


Figure 9. Calibration test of contact elements.

Table 5 – Numerical parameters for soil modeling - values obtained in the Technical Literature - Cintra and Aoki [10].

Layer	Element	Sandy soil Properties			Clay soil properties		
		E_{solo}	c	ϕ	E_{solo}	c	ϕ
-1	SOLID 65	$E_{solo}=5.4\text{MPa}$	Drucker-Prager		$E_{solo}=2.8\text{MPa}$	Drucker-Prager	
		$\nu = 0.30$	$c=3.5\text{kPa}$	$\phi = 21.2^\circ$	$\nu = 0.24$	$c=17.5\text{kPa}$	$\phi=17.5^\circ$
-2	SOLID 65	$E_{solo}=13.5\text{MPa}$	Drucker-Prager		$E_{solo}=7\text{MPa}$	Drucker-Prager	
		$\nu=0.29$	$c=3.5\text{kPa}$	$\phi = 25.00^\circ$	$\nu=0.23$	$c=17.5\text{kPa}$	$\phi=17.5^\circ$
-3	SOLID 65	$E_{solo}=27\text{MPa}$	Drucker-Prager		$E_{solo}=14\text{MPa}$	Drucker-Prager	
		$\nu = 0.28$	$c=7.5\text{kPa}$	$\phi = 29.14^\circ$	$\nu = 0.22$	$c=37.5\text{kPa}$	$\phi=20^\circ$
-4	SOLID 65	$E_{solo}=35.1\text{MPa}$	Drucker-Prager		$E_{solo}=18.2\text{MPa}$	Drucker-Prager	
		$\nu=0.28$	$c=15\text{kPa}$	$\phi = 31.12^\circ$	$\nu=0.21$	$c=75\text{kPa}$	$\phi = 25^\circ$
-5	SOLID 65	$E_{solo}=51.3\text{MPa}$	Drucker-Prager		$E_{solo}=26.6\text{MPa}$	Drucker-Prager	
		$\nu=0.27$	$c=15\text{kPa}$	$\phi = 34.49^\circ$	$\nu=0.21$	$c=75\text{kPa}$	$\phi = 25^\circ$
-6	SOLID 65	$E_{solo}=62.1\text{MPa}$	Drucker-Prager		$E_{solo}=32.2\text{MPa}$	Drucker-Prager	
		$\nu = 0.27$	$c=30\text{kPa}$	$\phi = 36.45^\circ$	$\nu = 0.21$	$c=150\text{kPa}$	$\phi = 30^\circ$
-7	SOLID 65	$E_{solo}=75.6\text{MPa}$	Drucker-Prager		$E_{solo}=39.2\text{MPa}$	Drucker-Prager	
		$\nu = 0.27$	$c=30\text{kPa}$	$\phi = 38.66^\circ$	$\nu=0.21$	$c=150\text{kPa}$	$\phi = 30^\circ$
-8	SOLID 65	$E_{solo}=94.5\text{MPa}$	Drucker-Prager		$E_{solo}=49\text{MPa}$	Drucker-Prager	
		$\nu = 0.27$	$c=30\text{kPa}$	$\phi = 41.46^\circ$	$\nu=0.21$	$c=150\text{kPa}$	$\phi = 30^\circ$
-9	SOLID 65	$E_{solo}=108\text{MPa}$	Drucker-Prager		$E_{solo}=56\text{MPa}$	Drucker-Prager	
		$\nu = 0.27$	$c=30\text{kPa}$	$\phi = 43.28^\circ$	$\nu=0.21$	$c=150\text{kPa}$	$\phi = 30^\circ$
-10	SOLID 65	$E_{solo}=113.4\text{MPa}$	Drucker-Prager		$E_{solo}=58.8\text{MPa}$	Drucker-Prager	
		$\nu = 0.26$	$c=30\text{kPa}$	$\phi = 43.98^\circ$	$\nu=0.21$	$c=150\text{kPa}$	$\phi = 30^\circ$

5 RESULTS AND DISCUSSION

5.1 Analysis of variance

To verify the relevance of the various parameters the analysis of variance (ANOVA) was used across those numerical models analyzed.

In the analysis of variance developed in this work, fixed factors were used, where four study variables were chosen, those being the height of the pile cap (28 cm, 50 cm and 70 cm), the type of soil (absence of soil, sand and clay), the length of the piles (5 m, 7 m and 9 m), and the type of pile-soil bond (coupling of nodes and contact elements). With respect to the dependent variable, the ultimate strength of the models was used in one analysis and the percentage of force transferred to the ground directly through the pile cap in another analysis. In models without the presence of soil, the non-occurrence of geometric non-linearity was admitted, and the tip of the piles was considered as possessing a simple support. Due to the absence of soil, all vertical force was transferred directly to the tip of the piles and the block was able to move freely in the vertical direction. Noteworthy here is that the length of the piles was defined in order to obtain a variation in the rigidity of the system without having a high computational cost, since the models were simulated as in the presence of soil.

As the analysis of variance is indicated for samples that have a Normal distribution, a Shapiro-Wilk test [11] was performed to analyze the normality of the data. In addition to the Shapiro-Wilk test [11], an analysis was made of the Quantile-Quantile graph.

In Figure 10, the normality test referring to the ultimate strength data of models B2 (model without soil) and B3 (model with node coupling between pile and soil), as well as the normality test referring to the ultimate strength data of models B2 (model without soil) and B4 (model with the use of contact elements).

Thus, for the two simulations the data adjusted notably well to the normal distribution, however, the simulation between models B2 and B4 showed that the samples obtained with the introduction of contact elements had greater adherence to the Normal distribution.

Through Table 6, one notes that the analysis of the variational parameters was reached. If the P-value is less than the 0.05 significance level, the variable is considered relevant.

If the value of F-value is higher than the values of F-critical, provided by Montgomery [12], the parameter can be considered relevant within the analysis. When comparing the models without soil presence with the models for which the connection of the soil with the piles occurs through the coupling of nodes, the conclusion reached is that the variable S (soil type) has relevant importance in relation to the bearing capacity of the blocks followed by variable H (block height). Based on the values of F-value and P-value, the length of the pile (L) was shown as not being a parameter of great relevance, when compared to the type of soil and height of the block, the same goes for interaction between variables S and H, S and L and between variables H and L.

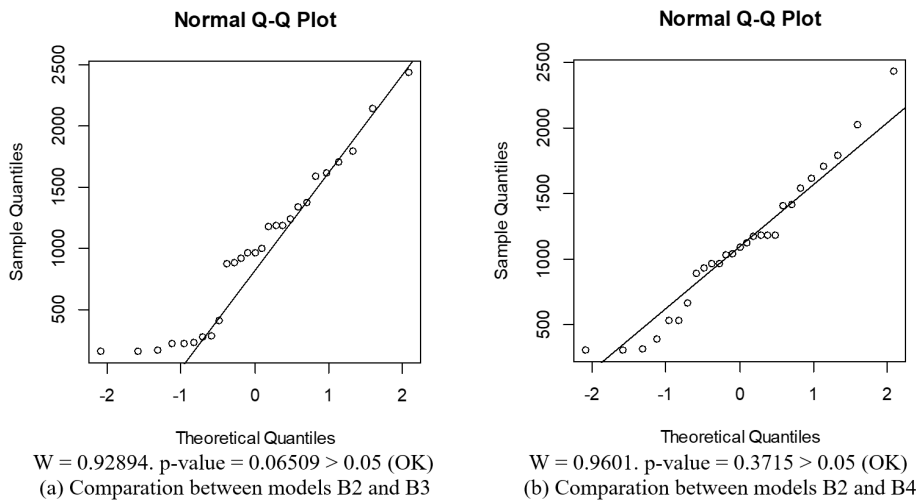


Figure 10. Normality test for ultimate strength.

Table 7 presents the results of analysis of variance between the models without the presence of soil and the models in which the bond between soil and pile was through the contact elements. Similar to ANOVA, in which the ultimate strength was analyzed for models with knot coupling, it was found that the variable S greatly influences the carrying capacity of the models; however, the interaction between the variables S and H has no relevance in the analysis of parameters. The same occurred for the interactions between variables S and L and between variables H and L.

Table 6 – Analysis of variance of the ultimate force between models B2 and B3.

Ultimate force (node coupling)						
Factors	Degrees of freedom	Sum of squares	Mean of squares	F-value	F-critical	P-value
S	2	7647491	3823745	65.15	3.40283	0.000
H	2	1488393	744197	12.68	3.40283	0.003
L	2	350747	175374	2.99	3.40283	0.107
S × H	4	642176	160544	2.74	2.92774	0.105
S × L	4	241892	60473	1.03	2.92774	0.448
H × L	4	81253	20313	0.35	2.92774	0.840
Error	8	469507	58688	-	-	-
Total	26	10921459	-	-	-	-

Table 7 – Analysis of variance of the ultimate force between models B2 and B4.

Força última (Elementos de Contato)						
Factors	Degrees of freedom	Sum of squares	Mean of squares	F-Value	F-critical	P-Value
S	2	3916510	1958255	24.22	3.40283	0.000
H	2	3916510	497607	6.15	3.40283	0.024
L	2	774459	387230	4.79	3.40283	0.043
S × H	4	531922	132981	1.64	2.92774	0.254
S × L	4	435281	108820	1.35	2.92774	0.333
H × L	4	216620	54155	0.67	2.92774	0.631
Error	8	646806	80851	-	-	-
Total	26	7516813	-	-	-	-

In Figure 11, one notes, based on the average of the results, how the ultimate strength of the pile caps is influenced by varying the type of soil, the rigidity of the pile cap and the length of the pile. For the soil parameters used in the

research, the higher level of stiffness in the sandy soil (S1) was noted in relation to the clayish soil (S2) and the superior strength of the models in which the soil is not considered. Noted also is that the increase in the height of the blocks directly influenced their bearing capacity, while generating greater impact when changing the parameter from 50 cm to 70 cm.

Regarding the length of the pile, there was noted for models with node coupling that on average the resistance of the models, for which the pile length is 7 meters (L7), was lower than for models with 5-meter piles, a fact that did not occur when simulating bonding by contact elements. For both analyzes the models with 9-meter piles had a much higher resistance.

To perform the analysis of variance for the percentage of force transferred directly to the soil through the pile cap, it was necessary to analyze whether the data have a normal distribution. Again, Shapiro-Wilk [11] and Quantile-Quantile plot methods were used. As seen from Figure 12, based on the P-value obtained, one is drawn to the conclusion that the data do not adhere to a Normal distribution. According to Gomes [13], if the data do not have a normal distribution, one can choose to treat and make them normal, where this is possible through the logarithmic transformations (log10) or through square root. The corroborators Santos et al. [14] obtained good adherence to the Normal distribution through a logarithmic transformation with base 10, obtaining a variation from $p < 0.05$ to $p > 0.10$ after the transformation. Therefore, in the present work, for the sample data of the percentage of force transferred to the soil through the block, the logarithmic transformation in base 10 was used as a data normalization tool. As identified in Figure 12, the transformation had an effect, ensuring the normality of the data.

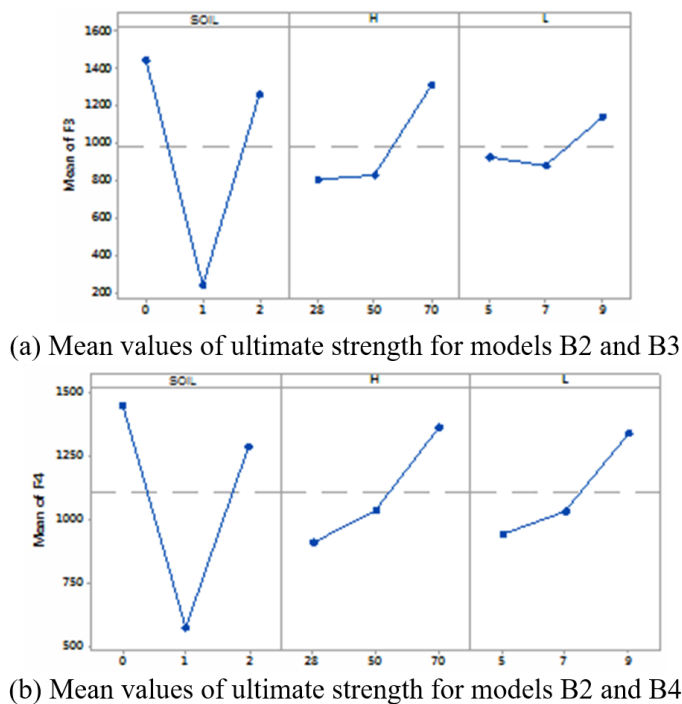


Figure 11. Parametric variation analysis, considering mean values of ultimate strength.

Table 8 shows the results of the analysis of variance for the portion of force transferred to the soil directly by the block, taking as variables the type of soil, the height of the block, the length of the piles and the type of piling-soil bonding.

Therefore, it is understood, through the analysis of the models, that the pile length (L) was the most relevant parameter, followed by the type of bond between the pile and the soil (coupling of nodes or contact elements) and the type soil (sand or clay). On the other hand, one recognizes that among the relevant parameters, the height of the block was the least relevant.

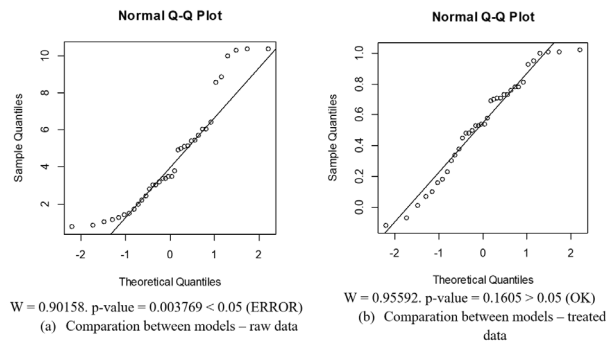


Figure 12. Normality test for data of percentage of force transferred to the ground through the pile-cap.

As shown in Figure 13, verification was made into how the interaction between the study variables influenced the percentage of force transferred from the block to the ground directly.

Table 8 – Analysis of variance about the percentage of force transferred to the soil through the pile cap.

Force transferred pile cap-Soil (%)						
Factors	Degrees of freedom	Sum of squares	Mean of squares	F-Value	F-critical	P-Value
SOIL	1	0.30582	0.30582	11.54	4.06705	0.004
H	2	0.19866	0.09933	3.75	3.21994	0.046
L	2	1.84826	0.92413	34.89	3.21994	0.000
LINK	1	0.47998	0.47998	18.12	4.06705	0.001
SOIL × H	2	0.06251	0.03126	1.18	3.23810	0.333
SOIL × L	2	0.11072	0.05536	2.09	3.23810	0.156
SOIL × LINK	1	0.07144	0.07144	2.70	4.07855	0.120
H × L	4	0.05107	0.01277	0.48	2.63353	0.749
H × LINK	2	0.03050	0.01525	0.58	3.23810	0.574
L × LINK	2	0.03958	0.01979	0.75	3.23810	0.490
Error	16	0.42385	0.02649	-	-	-
Total	35	3.62239	-	-	-	-

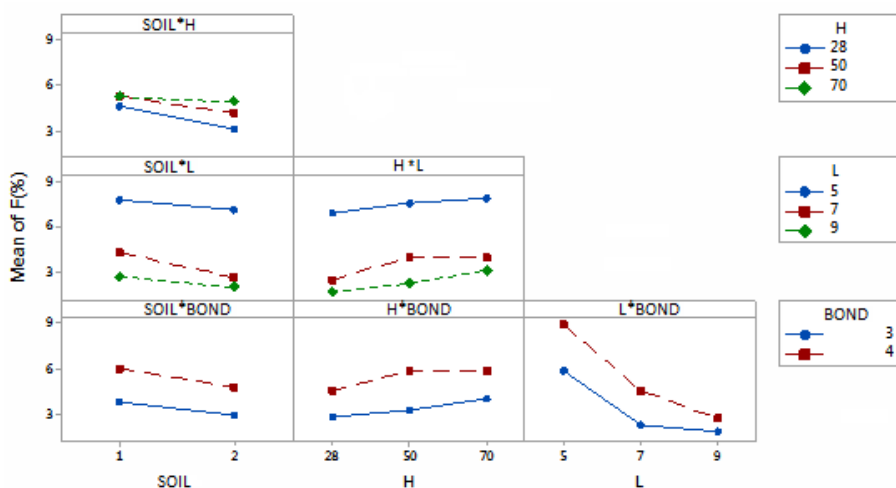


Figure 13. Interaction diagrams between control variables (Analysis between models B3 and B4) - Percentage of forces transferred to the ground through the pile-cap.

Regarding the interaction between the height of the block and the type of soil used in the study, it was found that for heights of 28 cm, 50 cm and 70 cm, the models with sandy soil transferred more force to the soil through the block, when compared to clayish soil, although, this discrepancy was less significant for blocks with a height of 70 cm. On the same graph it can be seen that the greater the block stiffness, the more significant the transfer of force from block to ground.

Another analysis performed corresponded to the interaction between the variables SOIL and L, as shown in Figure 13. It was found that for 9 m piles the load transfer to the soil through the block was lower than that of the models with a 7 m pile, which in turn was lower than that of the models with a 5 m pile. This is justified by the fact that the deeper layers of the soil have greater modulus of elasticity, therefore, being more rigid and having a greater tendency to absorb more activity than the more compressible layers, since the diameter of the piles and the material were fixed the same. It is important to note that this work, by itself theoretical, has chosen to adopt homogeneous behavior for the soil. Furthermore, in this work, the effect of the thickness of indescribable layers of soil and the effect of negative friction were not considered.

For the interaction between the types of bond with the type of soil, the same trend of less block-soil force transfer to the clay soil was noted. However, in the models in which a contact element was used, on average, a greater block-soil force transfer occurred. This fact is justified, as the coupling of nodes (bond 3) promotes a transfer of punctual forces through the piles (nodes coinciding between the pile and the soil), whereas in the models with contact elements (bond 4), this transfer occurs in a distributed way, according to relative displacements (displaceable model). As such, a greater rigidity of the soil pile set was noted in the models with knot coupling, creating in this way, greater force transference to the ground along the shaft.

The interaction between the height of the block and the length of the piles evidenced the reduction of force transferred to the soil through the block as the length of the pile increased. For the models with a 7 m pile, there was a tendency to stabilize the transferred force through increased rigidity of the block.

On the topic of the behavior of the models when analyzing the height of the block and the types of bond, little relevance was found in the analysis. An increase in the transferred force is perceived by increasing the stiffness for both types of bonding; however, this increase was not significant.

Finally, the interaction between the length of the piles and the type of piling-soil bonding was analyzed, the conclusion was thus reached that the variation of the transferred force, by increasing the length of the piles, was relevant and led to a tendency of stabilization by increasing the length of the pile. This fact was evident both for models with nodes coupling (bond 3), as well as for models in which contact elements were used (bond 4).

5.2 Force-displacement analysis

In this section, the force-displacement results for the analyzed models are presented. Through this analysis, the variation in the rigidity of the models can be identified, based on the support condition (bonding), block height, pile support level and soil type.

As seen from Figure 14, when taking into account the length of the pile, it was found that, in the models in which there is soil (S1 or S2), the support dimension of the pile influenced the overall stiffness of the model.

Verified also was the greater rigidity of the models without the presence of soil, since such models have as a boundary condition, the zero-vertical displacement. It is important to mention that, in models with no soil (S0), a reduction in stiffness was noted due to the increase in pile length. This is justified by the fact that the pile deformation is linked to its axial stiffness (constant for all piles) and its length (variable).

Through Figure 14, it is also possible to analyze the influence of the type of soil on the ultimate strength of the models. In (a), (b) and (c), force-displacement graphs are noted for models without soil (S0) and sandy soil (S1) and in (d), (e) and (f), the force-displacement graphs for models without soil (S0) and clay soil (S2). For the types of soil profiles adopted in the study, there was greater stiffness noted for the sandy soil, since it presented a lower settlement for the same applied force, in comparison to the clayish soil. This in turn, due to the set of parameters adopted (cohesion, modulus of elasticity, Poisson's ratio and friction angle), made the obtainment of a greater load capacity possible.

In terms of the type of bonding, those models simulated with sandy soil, along with the use of contact elements were found to show a higher bearing capacity and greater deformability, when compared with the models simulated with knot coupling. This discrepancy in results was not widely observed for clayish soils. It was found that, although the models with contact elements are more deformable and have a higher bearing capacity, the behavioral tendency of the models with coupling nodes (B3) and contact elements (B4) was similar.

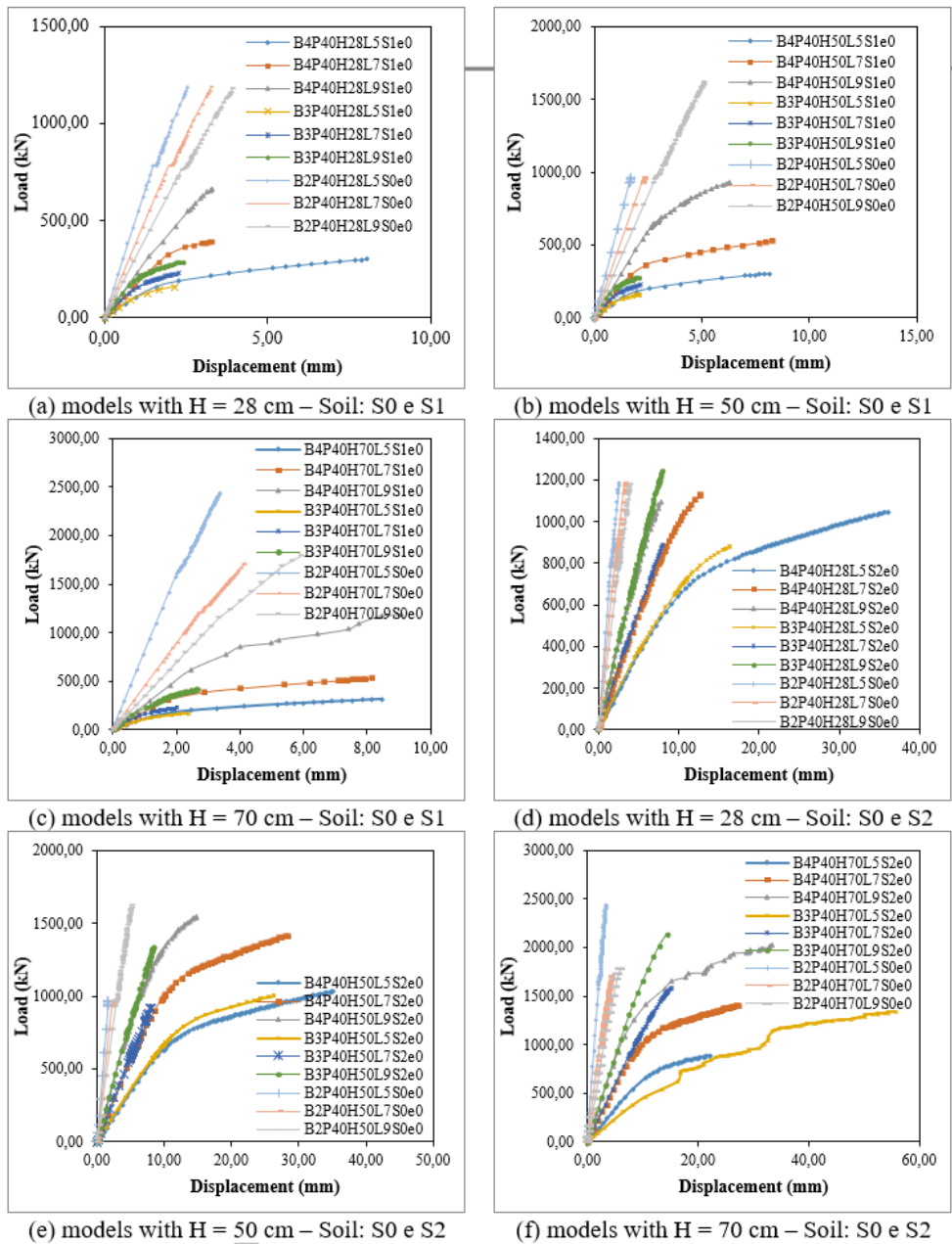


Figure 14. Graphics load-displacement of the analyzed models

5.3 Main compression stress

This session presents the results of the main compression stress on concrete blocks, obtained through numerical analysis. In Figure 15, the formation of the compressed diagonals is noted. Highlighted here was that in all models, the highest stress was noted as developing in the upper nodal region, a fact that was also observed by Munhoz [15] and Delalibera [6].

Regarding the field of stress, this was seen, through analysis, to have the tendency to form beyond the column section, contradicting the hypothesis proposed by Blévoit and Frémy [2]. In models B1P40H28 and B2P40H28, in the lower nodal region, an expansion of the stress field beyond the external region of the piles was observed, as noted from Figure 15. This fact was not observed in the models B3P40H28 and B4P40H28.

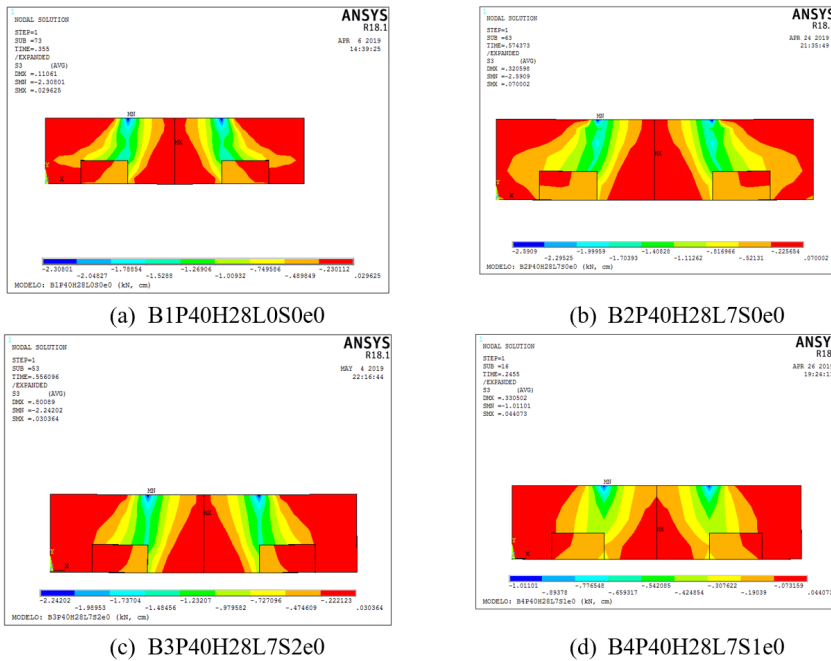


Figure 15. Main compression stresses in the pile-caps

In the models with H50 and H70, the expansion in the stress field in the lower nodal region occurred similarly to that in models B2, B3 and B4, where the expansion in the stress field in the regions outside the piles is observed, as shown in Figure 16. Emphasis is here placed on the fact that for all models with blocks of height 50 and 70 cm, the expansion of the stress field in the lower nodal region occurred in a similar way.

Another aspect for consideration refers to the fact that, in the sandy soil models (S1), the stresses acting on the blocks were below the fracture limits, this fact occurred due to the greater rigidity of the constitutive model of the studied sandy soil, causing the model to lose stability for lower forces more than expected.

Variations of the main compression stresses acting in the top of the piles were also verified.

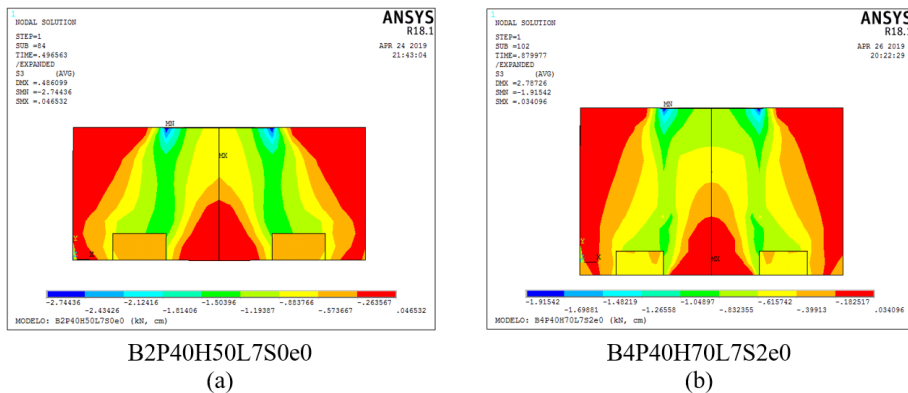


Figure 16. Main compression stresses in the pile-caps

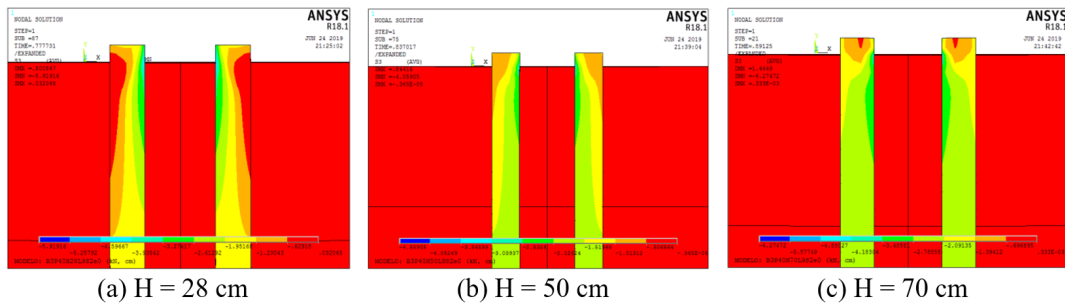


Figure 17. Main compression stresses in the piles

As seen in Figure 17, although the pillar is being exposed only by vertical compression force, the piles were exposed to flexion-compression. This effect proved to be more significant in blocks with a height of 28 cm, due to the lower rigidity of the model and greater tendency for flexion to occur. The reduced effect of flexion-compression in models with a height of 50 cm and 70 cm is noted in Figure 17, where there was less variation in the stress field, revealing the occurrence of a lesser effect from the bending moment on the top of the piles.

5.4 Settlement Analysis

The comparative analysis between settlements in piles obtained numerically with the ANSYS® software [3] and those obtained according to the method of Poulos and Davis [16] increased, due to the group effect, which is in agreement with the method proposed by Fleming et al. [17], and Equation 4 is found on Table 9.

$$\text{Increase factor of settlement} = n^k \tag{4}$$

In this context, n is the number of piles and k is a constant that varies between 0.40 and 0.60.

Table 9 – Comparison between settlements obtained numerically and analytically.

Model	Displ. numerical R _N (mm)	Displ. analytical R _A (mm)	R _A / R _N	Model	Displ. numerical R _N (mm)	Displ. analytical R _A (mm)	R _A / R _N
B3P40H28L5S1e0	2.14	2.09	0.98	B4P40H28L5S1e0	8.05	3.96	0.49
B3P40H28L7S1e0	2.28	1.13	0.50	B4P40H28L7S1e0	3.31	1.92	0.58
B3P40H28L9S1e0	2.41	0.87	0.36	B4P40H28L9S1e0	3.30	2.01	0.61
B3P40H50L5S1e0	2.12	2.11	1.00	B4P40H50L5S1e0	8.17	4.00	0.49
B3P40H50L7S1e0	2.13	1.12	0.53	B4P40H50L7S1e0	8.27	2.59	0.31
B3P40H50L9S1e0	2.07	0.42	0.20	B4P40H50L9S1e0	6.30	2.84	0.45
B3P40H70L5S1e0	2.37	2.20	0.93	B4P40H70L5S1e0	8.47	4.08	0.48
B3P40H70L7S1e0	1.99	1.09	0.55	B4P40H70L7S1e0	8.17	2.59	0.32
B3P40H70L9S1e0	2.66	1.25	0.47	B4P40H70L9S1e0	9.07	3.59	0.40
B3P40H28L5S2e0	16.33	20.02	1.23	B4P40H28L5S2e0	36.08	23.77	0.66
B3P40H28L7S2e0	8.01	7.45	0.93	B4P40H28L7S2e0	12.68	9.45	0.75
B3P40H28L9S2e0	7.94	6.05	0.76	B4P40H28L9S2e0	7.76	5.32	0.69
B3P40H50L5S2e0	26.29	22.83	0.87	B4P40H50L5S2e0	35.23	23.50	0.67
B3P40H50L7S2e0	7.97	7.70	0.97	B4P40H50L7S2e0	28.30	11.88	0.42
B3P40H50L9S2e0	8.44	6.51	0.77	B4P40H50L9S2e0	14.79	7.50	0.51
B3P40H70L5S2e0	75.19	31.19	0.41	B4P40H70L5S2e0	22.03	20.22	0.92
B3P40H70L7S2e0	15.25	13.35	0.88	B4P40H70L7S2e0	27.38	11.79	0.43
B3P40H70L9S2e0	14.44	10.40	0.72	B4P40H70L9S2e0	33.52	9.86	0.29

The numerical models were verified by use of the soil parameters, as such the displacements were shown to be superior to the displacements obtained analytically by the method of Poulos and Davis [16], even when considering the

increase in repression due to the group effect. In general, in the models in which bonding by contact elements was considered (B4), there was a discrepancy between the numerical and analytical models. In the models with sandy soil (S1) in which the bond was made by knot coupling (B3), it was found that the shorter the pile length, the greater the agreement between the numerical method and the analytical method. In general, the numerical models with node coupling bond presented a better agreement with the analytical method, representing with greater consistency the repression in the models.

6 CONCLUSIONS

By taking into consideration both the main compression stresses and the formation of compressed diagonals, in the upper nodal region the strut and tie model was understood to form beyond the column section, contrary to the hypothesis proposed by Blévoit and Frémy [2]. In the pile cap models with a height of 28 cm and with no soil, there was an expansion of the stress field in the lower nodal region beyond the external region of the piles, a fact also noted in the models of the same height, with soil presence. In models for which pile caps have a height of 50 cm and 70 cm, the expansion in the stress field in the lower nodal region occurred in similar fashion across models B2, B3 and B4. This was a fact highlighted more emphatically in the rigidity of the models in which the presence of sandy soil was considered (S1). In these models, due to the adopted soil parameters, the stresses acting on the pile caps were lower than the fracture limits, this occurred due to the fragility that was established in the sandy soil constitutive model, causing the system to lose numerical stability for forces lower than expected.

There was a tendency of flexion-compression occurring within the tops of the piles, therefore, verifying the piles and allowing that these be only subject to the normal compression force can lead to results not consistent with the real behavior of the structure, mainly for blocks with low stiffness. In the present research, the increase in the block stiffness was noted as leading to a reduction in the variation in the field of main compression stresses at the top of the piles, demonstrating that the increase in the pile cap stiffness has a favorable effect regarding the transfer of bending moments to the piles.

Considering the global stiffness of the models, in terms of the soil profiles adopted, the support level of the piles can be considered as a direct influence on this parameter, since, with an increase in the depth of the soil, the stiffness increases, and the deformability of the soil is reduced. Therefore, the result of increased rigidity by increasing the support quota is consistent. The models with no soil showed greater rigidity, however, still showing variation in displacement due to the variation in the length of the piles. This was justified by the fact that the axial rigidity of the pile is constant, and the deformation of the pile is directly proportional to its length. On average, the increase in the height of the models led to an increase in their ultimate strength.

Regarding the transfer of force to the soil through the block, it was found that for soil with sandy characteristics, the average transfer is approximately 5% of the total applied force, while for clay soils this value is close to 4%. It was also found that the increase in the rigidity of the pile cap provided, on average, an increase in the transfer of force from the pile cap to the ground. As for the length of the piles, once parameters such as diameter and material of the piles were fixed, the stiffness of the soil in the pile settlement level was noted as directly influencing the percentage of force transferred from the pile cap to the soil. Due to the aforementioned, the conclusion was reached that the more rigid soil-pile systems tended to transfer less force to the soil through the pile cap. This conclusion highlights the tendency for the force to be distributed primarily to regions of greater rigidity.

For the interaction between the types of bond with the type of soil, there was noted for the models in which contact element was used, on average, a greater block-soil transfer of force occurred. This fact is justified by the fact that the coupling of nodes promoted a transfer of punctual forces through the piles (nodes coinciding between the pile and the soil) whereas in the models with contact elements, this transfer occurs in a distributed manner, according to relative displacements (more displaceable model). A greater rigidity of the pile-soil set was thus noted in the models with node coupling, causing more force to be transferred to the soil along the shaft.

One can also conclude that to analyze the repression in the piles, the knot-coupling bond tends to represent more realistically the analytical model of Poulos and Davis. Added to this was a filter referring to the length of the piles, since it was evident, for sandy soils, that the shorter the length of the piles, the better the agreement between the settlements obtained numerically and those obtained analytically through the method of Poulos and Davis [16] and Fleming et al. [17].

7 ACKNOWLEDGMENTS

We are grateful for the support given by The Faculty of Civil Engineering linked to the Federal University of Uberlândia, FAPEMIG - Research Support Foundation of the State of Minas Gerais.

8 REFERENCES

- [1] Associação Brasileira de Normas Técnicas, *Design of Concrete Structures – Procedure*, NBR 6118, 2014.
- [2] J. Blévoit and R. Frémy, "Semelles sur pieux," *Annales Inst. Technique Batiment Trav. Publics Paris*, vol. 20, no. 230, pp. 223–295, 1967.
- [3] Ansys, Inc., *ANSYS 2020 R2: Theory Manual*. Canonsburg, PA: ANSYS, 2020.
- [4] K. J. Willam and E. P. Warnke, "Constitutive model for triaxial behavior of concrete," in *Proc. Int. Assoc. Bridge Struct. Eng. Conf.*, 1974, pp. 174–191.
- [5] P. Desay and S. Krishnan, "Equation for the stress-strain curve of concrete, ACI Journal," *Proc.*, vol. 61, no. 3, pp. 345–350, 1964.
- [6] R. G. Delalibera, "Numerical and experimental analysis of pile caps with two piles submitted to axial and eccentric forces," Ph.D. dissertation, Sch. Eng. São Carlos, São Paulo Univ., São Carlos, 2006 (in Portuguese).
- [7] F. S. Munhoz, "Experimental and numerical analysis of rigid blocks on two piles with pillars of square and rectangular sections and different reinforcement rates," Ph.D. dissertation, Sch. Eng. São Carlos, São Paulo Univ., São Carlos, 2014.
- [8] G. H. Silva, "Choice of parameters for contact analysis between elastic bodies using finite elements and neural networks," M.S. thesis, FEC, UNICAMP, Campinas, 2009.
- [9] NAVFAC, *Design Manual. 7.02, Foundations & Earth Structures*. Alexandria, VA: Dept. Navy, Nav. Facil. Eng. Command, 1986.
- [10] J. C. A. Cintra and N. Aoki, *Fundation for Piles: Geotechnical Project*. São Paulo: Oficina de Textos, 2010.
- [11] S. S. Shapiro and M. B. Wilk, "An analysis of variance test for normality (complete samples)," *Biometrika*, vol. 52, pp. 591–611, 1965.
- [12] D. C. Montgomery, *Design and Analysis of Experiments*, 4th ed. New York: John Wiley & Sons, 1996.
- [13] P. S. Gomes, "Asymmetric normal distribution for gene expression data," Ph.D. dissertation, Fed. Univ. São Carlos, São Carlos, 2009.
- [14] J. O. Santos, C. S. Munita, C. Vergne, and P. M. S. Oliveira, "Standardization and standardization through logarithmic transformation in archeometric studies of ceramics," in *52ª RBras*, 2007, pp. 1–5. Accessed: Apr. 29, 2019. [Online]. Available: <https://www.ipen.br/biblioteca/2007/eventos/13990.pdf>
- [15] F. S. Munhoz, "Analysis of the behavior of reinforced concrete blocks on piles subjected to the action of centered force," Ph.D. dissertation, Sch. Eng. São Carlos, São Paulo Univ., São Carlos, 2004.
- [16] H. G. Poulos and E. H. Davis, *Pile Foundation Analysis and Design*. New York: Wiley, 1980.
- [17] W. G. K. Fleming, A. Weltman, M. Randolph, and W. Elson, *Pile Engineering*. Glasgow, Scotland: Blackie & Son, 1985.

Author contributions: RGD: Orientation, writing, conceptualization essays, and analysis of results. GFS: writing, conceptualization and analysis of results.

Editors: Edgar Bacarji, José Luiz Antunes de Oliveira e Sousa, Guilherme Aris Parsekian.



ORIGINAL ARTICLE

Properties of recycled aggregates from different composition and its influence on concrete strength

Propriedades dos agregados reciclados de diferentes composições e sua influência na resistência do concreto

Fernanda de Andrade Salgado^a Flávio de Andrade Silva^a ^aPontifícia Universidade Católica do Rio de Janeiro – PUC-Rio, Department of Civil and Environmental Engineering, Rio de Janeiro, RJ, BrasilReceived 06 August 2020
Accepted 01 March 2021

Abstract: As a solution to the high depletion of natural resources and huge waste generated by the construction industry, the use of coarse recycled aggregate has become a trend in many countries. The construction and demolition waste is heterogeneous and mostly composed of concrete and masonry debris. The recycling process usually involves not only crushing and screening but also advanced techniques to separate these two fractions. These processes are costly and most frequently ineffective. Although most studies and international standards focused only on recycled concrete aggregate for structural use, it is possible to achieve similar characteristics with mixed recycled aggregates that have a ceramic fraction of up to 20%. This initiative can decrease recycling costs and make it more feasible. Therefore, this work presents an experimental investigation of a Brazilian recycled aggregate, which was separated into three fractions: mixed, concrete, and masonry aggregates. The analyses showed that the mixed recycled aggregate displayed geometric, physical, and mechanical properties similar to the recycled concrete aggregate. In addition, concrete made with 20% of mixed recycled aggregate presented a reduction of only 0.6% in maximum compressive strength and 36.8% in the modulus of elasticity compared with concrete made with the same amount of recycled concrete aggregate.

Keywords: sustainability, construction and demolition waste, recycled aggregate.

Resumo: Como solução para o esgotamento dos recursos naturais e o enorme desperdício gerado pela indústria da construção civil, o uso de agregado reciclado graúdo tornou-se uma tendência em muitos países. Os resíduos de construção e demolição são heterogêneos e compostos principalmente por detritos de concreto e cerâmicos. O processo de reciclagem geralmente envolve não apenas trituração e peneiramento, mas também técnicas avançadas para separar essas duas frações. Esses processos são caros e frequentemente ineficazes. Embora a maioria dos estudos e normas internacionais se concentrem apenas em agregados reciclado de concreto para uso estrutural, é possível obter características semelhantes utilizando-se agregados reciclados mistos com uma fração cerâmica de até 20%. Essa iniciativa pode diminuir os custos de reciclagem e torná-la mais viável. Portanto, este trabalho apresenta uma investigação experimental de um agregado reciclado brasileiro, que foi separado em três frações: agregado reciclado misto, de concreto e cerâmico. As análises mostraram que o agregado reciclado misto possui propriedades geométricas, físicas e mecânicas semelhantes ao agregado reciclado de concreto. Além disso, o concreto fabricado com 20% de agregado reciclado misto apresentou uma redução de apenas 0.6% na resistência máxima à compressão e 36.8% no módulo de elasticidade em comparação com o concreto fabricado com a mesma quantidade de agregado reciclado de concreto.

Palavras-chave: sustentabilidade, resíduos de construção e demolição, agregado reciclado.

How to cite: F. A. Salgado and F. A. Silva, “Properties of recycled aggregates from different composition and its influence on concrete strength,” *Rev. IBRACON Estrut. Mater.*, vol. 14, no. 6, e14605, 2021, <https://doi.org/10.1590/S1983-41952021000600005>

Corresponding author: Fernanda de Andrade Salgado. E-mail: fernanda.salgado@puc-rio.br

Financial support: None.

Conflict of interest: Nothing to declare.



This is an Open Access article distributed under the terms of the Creative Commons Attribution License, which permits unrestricted use, distribution, and reproduction in any medium, provided the original work is properly cited.

1 INTRODUCTION

The construction industry is responsible for approximately 23% of global emission and demands around 4×10^{13} kg per year of raw material since aggregate typically accounts for approximately 70% of concrete in volume [1], [2]. Besides that, construction of new buildings and demolition of existing structures generate an excessive amount of Construction and Demolition Waste (CDW).

On a global scale, CDW accounts for 36% by weight of the total waste produced on Earth [3]. The annual CDW production exceeds 1.5×10^{12} kg in China [4], 5.3×10^{11} kg in the USA [5], 8.5×10^{11} kg in European Union [6], and 1.06×10^{11} kg in Brazil [7]. Thus, improper CDW disposal is a huge problem faced by many countries. Irregular disposal in open dumps has great potential for environmental contamination, causes flooding and landscape damages, and is also harmful to human health as it enables disease proliferation.

Therefore, the use of recycled aggregate from CDW recycling as a replacement for natural coarse aggregate in concrete can promote not only a decrease in the number of irregular waste depositions but can also reduce the consumption of non-renewable natural resources. Thus, many countries, such as USA and European Union members, created waste management plans, looking for waste reduction, the prohibition of uncontrolled disposal, and an increase in the CDW recycling rate [8]. Meanwhile, in Brazil, the recycling plants work, on average, with only 35% of their capacity, and only 18% of CDW is recycled [7].

CDW is usually very heterogeneous, and its composition can be affected by several factors, such as the raw materials and the construction and demolition procedures. Frequently, CDW is composed not only of concrete rubble but also crushed clay bricks from partitioning walls and cladding. In Brazil, for example, 70% of the recycling plants claim to receive predominantly mixed material [7], since wall partitioning in most reinforced concrete buildings in Brazil have masonry and CDW collection is disorganized [9].

Because of this heterogeneity, recycled aggregates are usually classified as Recycled Concrete Aggregate (RCA) when it is composed mostly of cement-based fragments and natural rocks, and as Mixed Recycled Aggregate (MRA) when it is composed of a mixture of ceramic debris, bricks, cladding, concrete blocks, and mortar.

International standards usually limit the use of recycled aggregate in concrete depending on the desired concrete strength class and the characteristics of the recycled aggregate. For example, Spanish, British and Portuguese standards limit the use of RCA to 20% replacement ratio in structural concretes up to C40, while do not mention the use of MRA [10]–[12]. German and Italian standards only allow the use of MRA in non-structural concretes [13], [14]. Meanwhile, the Australian standard allows the use of 100% MRA in structural concrete C25 if its ceramic content is limited to 30% [15]. Brazilian standard NBR 15116:2004 [16], however, does not allow the use of either RCA or MRA in structural concrete of any strength class.

The use of RCA as a replacement for natural coarse aggregate has been extensively studied. Most research works have observed that an RCA replacement ratio smaller than 30% does not induce expressive variations in the mechanical properties and durability aspects of the resulting concrete [17]–[22]. The feasibility of using RCA in structural concrete had also been verified [23]–[26].

Nevertheless, regarding the use of MRA, because of its significantly variable composition, most research papers focused only on road construction and non-structural applications [27]–[32]. However, Yang et al. [33] analyzed the influence of using MRA from a British recycling plant containing different levels of ceramic debris and verified that it was still possible to produce quality concrete with MRA containing up to 20% of ceramic inclusion. Similar results were obtained with MRA from southwestern Spain and southeast Brazil [34], [35].

In Brazil, MRA are usually employed as road sub-base while RCA are used in non-structural concretes. In the present work, the geometric, physical, and mechanical properties of Brazilian recycled aggregates have been studied. Finally, uniaxial compression tests were assessed on concretes with 20% recycled aggregate in replacing natural aggregate. The impact of this substitution was evaluated through the analysis of the maximum compressive strength, the modulus of elasticity, and the behaviour of the stress-strain curve.

1.1 Research significance

Despite all environmental benefits and the growth potential of the CDW recycling sector, there are still some barriers that hamper the use of recycled aggregates on a larger scale. It is necessary, for example, to ensure that recycling plants will be able to guarantee a consistent supply of high-quality recycled aggregates [36].

Usually, the ordinary recycling process comprehends different stages of crushing, screening, and separation to remove contaminants like reinforcement bars, plastic, and glass, for example. Depending on the maximum size and on the desired composition of the final output, different recycled methods can be applied [37], [38].

The removal of contaminants can occur during construction/demolition, optimizing the crushing time in the recycling plant and increasing the quality of the recycled aggregate. However, pre-crushing separation demands more elaborate waste management plans and an organized CDW collection, being more expensive and time-consuming for the contractors. As a second option, CDW can be stockpiled according to major constituents in the recycling plant, and separation can be done only after crushing [39].

In the case of post-crushing separation, when it is necessary to separate the ceramic and the concrete-based fragments, further advanced sorting techniques are used, such as gravity concentration in the presence of water or air [40]. However, in addition to being very expensive, these advanced techniques do not guarantee a complete separation between the ceramic and the concrete-based fractions [41].

Therefore, a better comprehension of MRA properties and its impact on concrete would increase market demand for this material as this initiative can decrease recycling costs and make the recycling process more feasible. Thus, the CDW recycling rate would increase, generating not only numerous environmental benefits but also improving the recycling sector economically.

This paper presents the experimental assessment of a Brazilian recycled aggregate and analyses its influence on the concrete mechanical properties. This study adds to the field important parameters regarding locally available recycled aggregates, being an important step to legitimate its application by the construction sector.

1.2 Problem definition

For this work, mixed recycled aggregates (MRA) from a recycling plant located in Brazil was considered. Through manual separation, three samples were produced: (1) mixed recycled aggregates - MRA, (2) recycled concrete aggregates - RCA and (3) recycled masonry aggregates - RMA. The geometric, physical, and mechanical properties of these three samples were compared with a local natural coarse aggregate. Furthermore, to analyze the impact of using recycled aggregates in concrete, the compressive strength of cylindrical specimens containing 20% in volume of recycled aggregate was assessed at 28 days. This replacement ratio was adopted based on the minimum established by several international standards and codes [42]. The mechanical performance of these recycled concretes was compared with a reference concrete made with 100% of natural aggregate.

2 MATERIALS AND EXPERIMENTAL PROGRAM

2.1 Aggregates selection

The mixed recycled aggregates (MRA) were obtained from Reciclax Recycling Plant, Brazil. A certain amount of this MRA sample was cleaned with running water and then air-dried for five days. After that, it was manually separated, providing two other samples of recycled coarse aggregate: recycled concrete aggregate (RCA), composed only of cement-based fragments, and recycled masonry aggregate (RMA), composed only of ceramic debris, bricks and roof tiles. The non-mineral materials such as wood, plastic, bitumen, foam, glass, plaster and metal, were discarded.

Thus, in this study, four types of coarse aggregate were used: mixed recycled aggregate (MRA), recycled concrete aggregate (RCA), recycled masonry aggregate (RMA) and a natural granitic coarse aggregate (NA), as reference.

2.2 Recycled aggregate characterization

2.2.1 Mixed Recycled Aggregate (MRA) composition

To verify the MRA composition as received from the recycling plant, the percentage by weight of cementitious material, ceramic material, and contaminants/impurities were calculated using a 15 kg sample. Also, the fine content (< 4.75 mm) and the pulverulent content (< 0.75 μm) [43] were measured for 10 kg samples.

In this study, it is considered that the RCA sample is composed entirely of cement-based fragments and natural rocks, while the RMA sample is composed only by masonry elements such as ceramic debris, bricks and roof tiles.

2.2.2 Geometric properties

The grain size distribution curves were obtained according to the Brazilian standard NBR NM 248:2003 [44]. Each 8 kg sample was sieved for 10 minutes.

The shape index of each aggregate sample was also analyzed, according to the Brazilian standard NBR 7809:2019 [45]. It is used to indicate how rounded the particles are and it is calculated as a relationship between the average length and the average thickness of each material.

2.2.3 Physical properties

The specific gravity, the saturated surface-dry density, the oven-dry density, the water absorption and apparent porosity were measured according to the Brazilian standard NBR NM 53:2009 [46]. At first, the samples were oven-dried at 105 ± 5 °C for 24 ± 4 h. After being cooled in air-room for 1 to 3 h, the dry masses were obtained. Then, the samples were immersed in water at room temperature for another period of 24 ± 4 h. After being saturated, they were placed in a holed container and then submerged to determine their apparent masses in water using a hydrostatic scale. Then, samples were rolled in a large absorbent tissue until all visible water film was removed. Finally, saturated surface-dry mass was obtained. This procedure was repeated six times for each type of aggregate.

The bulk density and the void ratio of each sample were measured according to the Brazilian standard NBR NM 45:2006 [47]. This procedure was also repeated six times for each type of aggregate.

The water absorption curve of recycled aggregates was also determined. First, samples were oven-dried at 105 ± 5 °C for 24 ± 4 h. Then, they were placed in a holed container and submerged in water. Using a hydrostatic scale, the mass gain was measured as described below:

- up to the first 15 minutes, one reading every minute;
- from 15-30 minutes, one reading every 5 minutes;
- from 30-60 minutes, one reading every 10 minutes;
- from 1-2 h, one reading every 15 minutes;
- from 2-8 h, one reading every 1 h;
- one last reading after 24 h.

Finally, the packing density was measured to determine the degree of compaction of each type of aggregate. In the case of identical cubic particles and considering the packing of the grains one by one, the packing density would be the maximum possible ($\phi = 1$). Thus, to measure the packing density, a metal cylinder container was filled with oven-dried aggregates and closed with a metal plunger. A mean compression of 10 kPa was applied on the top. Then, it was submitted to a vibrating table for 2 minutes and, finally, the final height of the aggregate sample was measured. The packing density was calculated using the Equation 1 below [48]. The mean of two results was reported as the packing density of each type of aggregate.

$$\phi = \frac{m}{A_e h_t \delta} \quad (1)$$

where m = mass of the aggregate sample (kg); A_e = area of the cylinder container (m^2); h_t = final height of the aggregate sample inside the cylinder (m) and δ = aggregate specific gravity (kg/m^3).

2.2.4 Mechanical behaviour

The crushing value (ACV) is used to estimate the resistance of an aggregate to crushing under gradually applied compressive load. According to the British standard BS 812 Part 110 [49], the aggregate samples were oven-dried at 105 ± 5 °C for a period of not more than 4 h and then cooled to room temperature. Then, the samples were sifted on sieves 9.5 mm and 12.5 mm to remove the oversize and the undersize fractions. The samples were placed in a metal cylinder container in three layers of approximately the same height, being each layer subjected to 25 strokes. A metal plunger was placed carefully and horizontally over the surface of the aggregate. Also according to the British standard BS 812 Part 110 [49], the apparatus was placed on a testing machine and loaded at uniform rate so that the required force of 400 kN was reached in $10 \text{ min} \pm 30 \text{ s}$ (Figure 1). The aggregate crushing value (ACV) was calculated as a relationship between the mass of the material passing the sieve 2.36 mm after crushing and the total mass. Thus, as lower the crushing value, the higher is the resistance to crushing under a gradually applied compressive load.

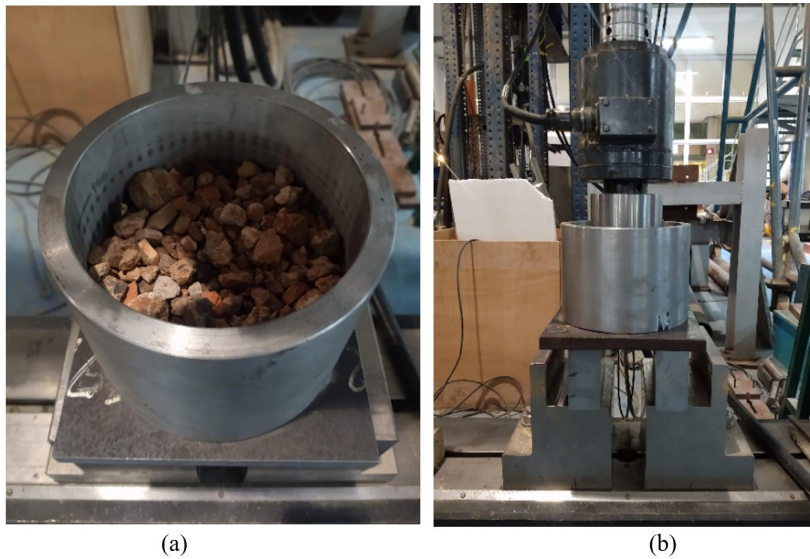


Figure 1. (a) Aggregate sample inside the metal container and (b) load application

The compressive strength of recycled aggregate concretes was measured at 28 days, using cylindrical specimens ($\phi = 100$ mm and $h = 200$ mm) [50]. The specimens were prepared with Portland cement CII F-32, which has a minimum compressive strength of 32 MPa at 28 days [51]. For workability control, a chemical admixture Master Glenium 51 with a solid concentration content of 30% and specific gravity of 1087 kg/m³ was used. The superplasticizer content was adjusted from a slump test [52]. Fine aggregate was a quartz natural sand with maximum size of 4.75 mm, specific gravity of 2656 kg/m³ and water absorption of 4.38%. A reference specimen was fabricated with only natural coarse aggregate (NA); meanwhile, for the recycled aggregate concrete specimens, 20% in volume of the natural coarse aggregate was replaced for recycled aggregate, as described in Table 1.

Table 1. Concrete samples specifications.

Sample Name	Percentage of Aggregates in Volume
NA-100	NA 100%
MRA-20	MRA 20%, NA 80%
RCA-20	RCA 20%, NA 80%
RMA-20	RMA 20%, NA 80%

The American Concrete Institute (ACI) mix design method was adopted, with 32 MPa as the desired resistance at 28 days. The w/c ratio was kept constant at 0.50. Table 2 shows the mix proportion.

Table 2. Mix proportion.

Material	Mix Proportion (kg/m ³)
Cement	360
Fine Aggregate	727
Coarse Aggregate	1091
Water	180
Superplasticizer	1.08

The mixing process was performed in a 30-liter planetary mixer. The addition of water was done in two parts: 70% of the total volume was added immediately after mixing the aggregates and the remainder volume (30%) was added along with the superplasticizer in the end of the mixture. After 24 h, the concrete specimens were demolded and taken

to a humid chamber for 28 days. The compressive strength tests were performed at a loading speed rate of 0.35 MPa/s on a Controls machine model MCC8, servo-controlled with a load capacity of 2000 kN.

3 RESULTS AND DISCUSSIONS

3.1 Composition, grain size distribution and shape index

MRA presented $9.26 \pm 0.65\%$ of fine content and $0.59 \pm 0.31\%$ of pulverulent material content. These values are under the limit established for the Brazilian standards NBR 15116:2004 [16] and NBR 7211:2009 [53], which limit the fine content to 10% and the pulverulent content to 1%, respectively.

Table 3 shows that the MRA is composed of less than 90% of cementitious materials, thus it is indeed classified as mixed recycled aggregates, according to the Brazilian standard NBR 15116:2004 [16]. Contaminants and impurities, such as foam, glass, plaster, plastic, cardboard, shells and even steel nails, represented 0.3%, therefore being within the limit ($< 3\%$) established by the Brazilian standard [16] for aggregates to be used in concrete. Similar results were obtained by Salles [35].

Table 3. Composition of mixed recycled aggregate (MRA).

Type of Material	%
Cementitious material	87.2%
Ceramic material	12.5%
Contaminants and impurities	0.3%

All recycled aggregates (MRA, RCA and RMA) presented a continuous (well-graded) grain size distribution curve, which were very similar to each other and also to the natural aggregate (NA) curve (Figure 2). Besides, the maximum size of the four types of aggregates was 19 mm. It can also be observed that the grain size distribution curves of the recycled aggregates were located between zones 4.75/12.5 and 9.5/25, as defined by NBR 7211:2009 [53]. Similar results were presented by Tenório [54].

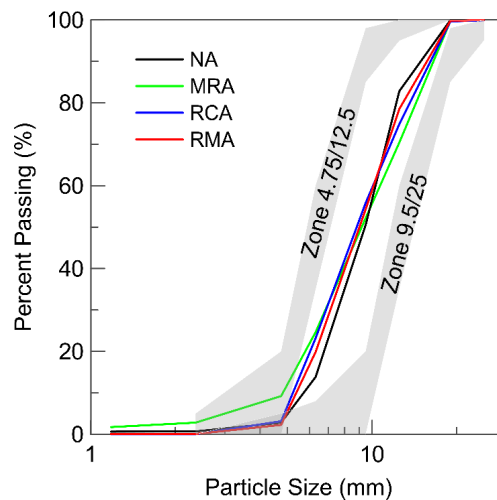


Figure 2. Grain size distribution curves of recycled and natural aggregates.

Moreover, the grain size distribution curve of the MRA used in this study and produced in São Paulo (Brazil) was very similar to those curves obtained for recycled aggregates from several other places in Brazil [35], [55], [56], and also from United Kingdom [33] and India [57] (Figure 3).

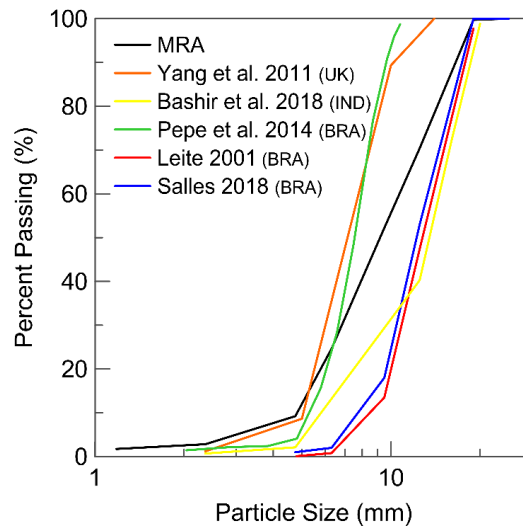


Figure 3. Grain size distribution curves of recycled aggregates from different locations [33], [35], [55]–[57].

Regarding the shape index, the difference between the values obtained for RCA and RMA (Table 4) was consistent with the visual observation of each sample (Figure 4). While RCA was composed of more rounded grains, such as mortar pieces, RMA presented some flatter and elongated grains, such as tiles. It is also possible to visually observe that RCA has a much rougher surface than RMA.

Table 4. Shape index of recycled and natural aggregates.

	NA	MRA	RCA	RMA
Average Length (mm)	19.43	20.90	19.67	20.54
Average Thickness (mm)	10.39	10.02	9.99	8.74
Shape Index	1.87	2.09	1.97	2.35



Figure 4. Picture showing the shapes for: (a) RCA sample and (b) RMA sample.

Meanwhile, Table 4 shows that the shape index of MRA was an intermediate value, which is coherent once MRA was a mixture of the concrete and the masonry fractions (RCA and RMA, respectively). Natural aggregate, however,

was the most rounded one. Nevertheless, all values were within the limit established by the Brazilian standard NBR 7211:2009 (< 3) [53].

3.2 Physical and mechanical behaviour

RCA was composed of a natural coarse aggregate with an adhered mortar which is characterized by micro cracks generated during recycling and pores accessible to water. Thus, when compared to the natural aggregate (NA), this adhered mortar was responsible for an increase of 364% in the apparent porosity and 433% in the water absorption (Table 5). Equally, RCA presented a reduction of 12% in oven-dry density in relation to the natural aggregate (NA). The influence of the presence of adherent mortar on the characteristics of RCA was analyzed by Pepe et al. [58]. The authors observed that, after autogenous cleaning, water absorption of RCA reduced almost 50% and the oven-dry density increased almost 16%. Limbachiya et al. [59] also investigated RCA with different amount of adhered mortar, observing an increase in water absorption and a reduction in both oven-dry density and SSD density for RCA when the amount of attached cement paste increased.

Meanwhile, as ceramic materials are naturally more porous than natural rocks, RMA presented an apparent porosity 616% higher, a water absorption 850% higher and an oven-dried density 25% lower than the natural aggregate (NA) (Table 5). Similar results were obtained for Cavalline and Weggel [60] when using brick masonry as recycled aggregate. In their study, water absorption increased from 0.34% for NA to 12.2% for RMA; while specific gravity reduced from 2840 kg/m³ for NA to 2190 kg/m³ for RMA.

Finally, as shown in Table 5, as RCA was responsible for almost 90% of the composition of the MRA, the results obtained for both were very similar. MRA also exhibited a higher apparent porosity, higher water absorption, and lower density than natural aggregate (NA).

Table 5. Physical properties of recycled and natural aggregates.

	NA	MRA	RCA	RMA
Specific Gravity (kg/m³)	2653 ± 3	2626 ± 12	2631 ± 9	2497 ± 8
SSD Density (kg/m³)	2601 ± 6	2350 ± 6	2396 ± 10	2164 ± 9
Oven-dry Density (kg/m³)	2570 ± 10	2181 ± 14	2253 ± 13	1942 ± 12
Bulk Density (kg/m³)	1424 ± 4	1262 ± 3	1315 ± 5	1120 ± 7
Apparent Porosity (%)	3.1 ± 0.5%	16.9 ± 0.9%	14.4 ± 0.3%	22.2 ± 0.3%
Water Absorption (%)	1.2 ± 0.2%	7.8 ± 0.5%	6.4 ± 0.2%	11.4 ± 0.2%

It was also possible to observe a relationship between the oven-dry density and the apparent porosity, as well as between the water absorption and the apparent porosity (Figure 5). The increase in apparent porosity means an increase in the number of pores, thus, the oven-dry density decreases, and the water absorption increases.

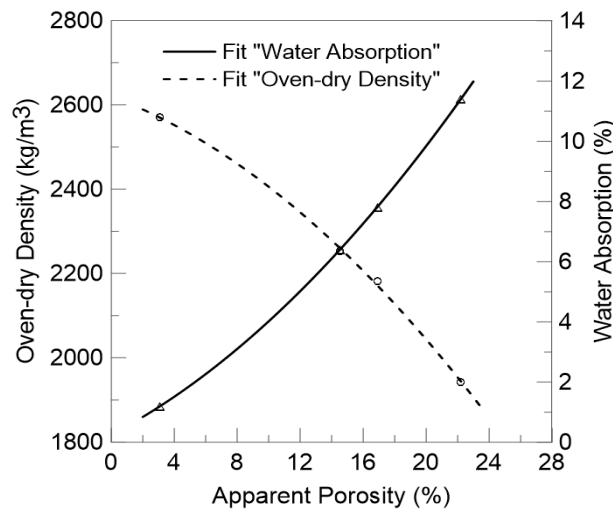


Figure 5. Oven-dry density and Water absorption versus Apparent porosity.

While the apparent porosity measures the total amount of void space accessible from the surface of the aggregate, the void ratio is the number of voids between the aggregates at a certain known volume. Table 6 shows the aggregates void ratio and packing density. It can be observed that the lower the void ratio, the greater was the packing density. However, regardless of the aggregate, the results obtained for void ratio and packing density were very similar to each other. This can be explained by the fact that all aggregates had the same maximum size ($d = 19 \text{ mm}$) and very similar values for shape indexes.

Table 6. Packing density of recycled and natural aggregates.

	NA	MRA	RCA	RMA
Void Ratio (%)	$46.2 \pm 0.2\%$	$51.8 \pm 0.1\%$	$50.4 \pm 0.2\%$	$55.0 \pm 0.3\%$
Packing Density, ϕ	0.66 ± 0.01	0.54 ± 0.0	0.57 ± 0.01	0.50 ± 0.01

Figure 6 shows the 24 h and the 15 minutes water absorption curves for each aggregate. It can be seen that while the natural aggregate presented a linear behaviour, the recycled aggregates initially showed a higher absorption rate and then reached a saturation plateau. In the first 10 minutes, the natural aggregate (NA) reached 66% of its total water absorption, while RCA, MRA, and RMA reached 81%, 82%, and 90%, respectively. This behaviour is related to the material's porosity: when the availability of pores is higher, the rate of water absorption in the initial period is also higher. In all cases, the maximum water absorption achieved for each aggregate was similar to the values in Table 5. Similar results were obtained by Salles [35]: more than 90% of the final water absorption occurred in the first five minutes of testing for the three types of recycled aggregate analysed (MRA, RCA and RMA).

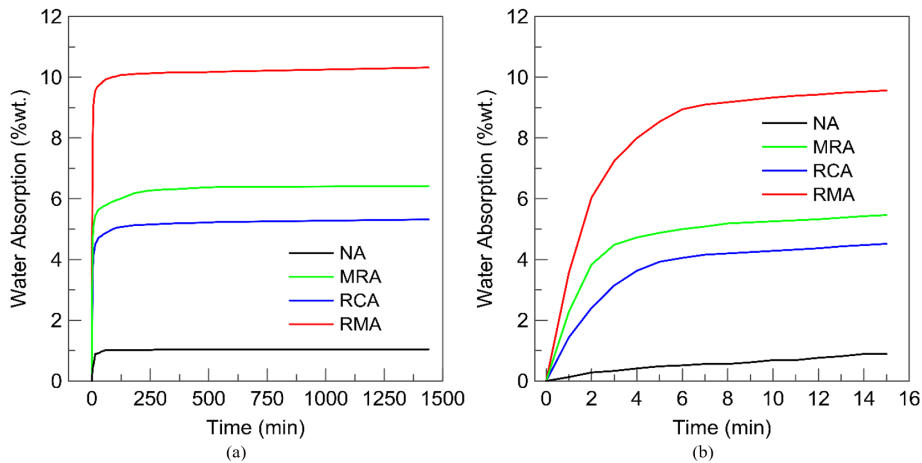


Figure 6. (a) 24 h and (b) 15 min water absorption curve of the recycled and the natural aggregates.

Regarding the strength of the aggregate (Table 7), RMA presented a lower resistance to gradually applied compressive load because of its porous and weak composition. Meanwhile, MRA and RCA presented a similar resistance to gradually applied compressive load, which was approximately 15% higher than RMA and 8% lower than the natural aggregate (NA). This reduction in strength of MRA and RCA when compared to NA could be explained by the presence of the adhered mortar in the CDW concrete-based fragments: when the adhered mortar increased, their strength decreased. Similar results were obtained by Duan and Poon [61]. The authors analyzed three RCA samples, with different ratios of rock/concrete, by mass, in their composition: 96%, 98%, and 99%. They observed that the RCA samples presented similar strength, with a variable reduction from 6% to 9% when compared to a natural aggregate sample.

Table 7. Aggregate Crushing Value (ACV) of recycled and natural aggregates.

	NA	MRA	RCA	RMA
ACV (%)	30.5 ± 0.2	33.4 ± 0.4	32.5 ± 0.5	38.9 ± 0.5

Table 8 shows the maximum compressive strength and the modulus of elasticity obtained for each concrete mixture in this study. When compared to the reference concrete (NA-100), concrete made with 20% of the recycled masonry aggregate (RMA-20) presented a reduction of almost 12% in the maximum compressive strength and 59% in the modulus of elasticity. This can be explained by the smoother surface of the RMA (Figure 4), which can lead to a lower adhesion between the aggregate and the matrix, and, consequently, to a lower concrete compressive strength.

Table 8. Maximum compressive strength and modulus of elasticity of concrete made with recycled and natural aggregates.

	NA-100	MRA-20	RCA-20	RMA-20
Maximum compressive strength (MPa)	31.6 ± 0.8	28.8 ± 0.7	29.0 ± 1.3	27.0 ± 1.8
Modulus of elasticity (GPa)	27.2 ± 1.8	24.4 ± 2.5	38.5 ± 11.1	24.2 ± 1.5

Meanwhile, when compared to the reference concrete (NA-100), concrete made with 20% of recycled concrete aggregate (RCA-20) presented maximum compressive strength 8% lower and modulus of elasticity 41.5 % higher (Table 8). In the meantime, concrete made with 20% of mixed recycled aggregate (MRA-20) showed an intermediate behaviour. While its maximum compressive strength was only 0.6% lower than RCA-20, its modulus of elasticity was 36.8% lower, being more similar to the modulus of elasticity of the RMA-20.

This reduction in the compressive strength and modulus of elasticity of the RCA-20 and the MRA-20, in comparison with the NA-100, can also be associated to the presence of the adhered mortar in the CDW concrete-based fragments. Some studies have shown that the adhered mortar has a higher tendency to crack, and, in general, the concrete failure happens through the recycled aggregate, within the adhered mortar [20], [62], [63].

Bravo et al. [18] related the maximum compressive strength and the modulus of elasticity with the replacement ratio of the recycled aggregate. While studying recycled aggregates from different locations in Portugal, the authors noted a reduction of approximately 5% and 26% in the concrete maximum compressive strength for a replacement ratio of 20% and 100%, respectively; meanwhile, the reduction for the modulus of elasticity was 7.5% and 37% for a replacement ratio of 20% and 100%, respectively.

It is also possible to verify in Table 8 that only the concrete made with 100% natural aggregate (NA-100) achieved the desired compressive strength (32 MPa). Thus, it can be inferred that the direct replacement of a certain volume of coarse aggregate with recycled aggregate was not effective because it did not take into account the intrinsic characteristics of the recycled aggregates. However, despite these differences in the maximum compressive strength and modulus of elasticity, the stress-strain curves of all concrete mixtures (NA-100, MRA-20, RCA-20, and RMA-20) presented a similar behaviour (Figure 7). It is also important to notice that all concrete samples made with 20% in volume of recycled aggregate achieved a compressive strength higher than 25 MPa. Thus, they could be considered for use in structural elements.

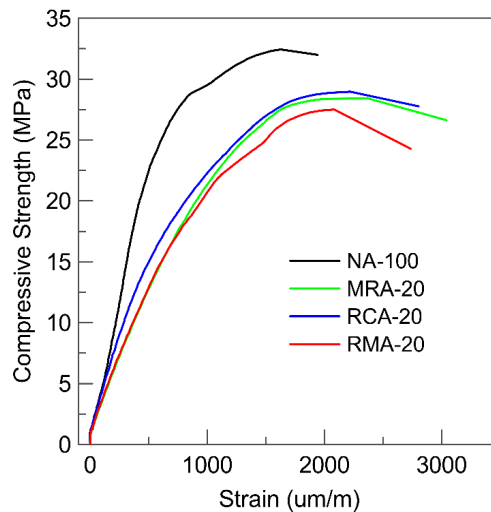


Figure 7. Compressive stress-strain curves.

Many authors investigated the relationship between the modulus of elasticity and the compressive strength of recycled aggregate concretes and different equations have been suggested. Some of these equations are presented in Table 9. It can be observed that there is an expressive variation between all equations not only because of the type of aggregate used in the concrete samples but also because of its physical and mechanical properties.

Table 9. Equations that correlate modulus of elasticity with compressive strength.

	Equation	Type of aggregate
Ravindrarajah et al. [64]	$E_c = 5.31 * f_c^{0.5} + 5.38$	Natural aggregate
	$E_c = 7.77 * f_c^{0.33}$	Coarse recycled aggregate
	$E_c = 3.48 * f_c^{0.5} - 13.1$	Coarse recycled aggregate
	$E_c = 3.02 * f_c^{0.5} - 10.7$	Coarse and fine recycled aggregate
Cabral et al. [65]	$E_c = 2.58 * f_c^{0.63}$	Coarse and fine recycled CDW waste
Leite [55]	$E_c = 4.63 * f_c^{0.5} - 3.48$	Coarse and fine recycled CDW waste
Lovato [66]	$E_c = 5.74 * f_c^{0.5} - 13.39$	Coarse and fine recycled CDW waste
Ravindrarajah and Tam [67]	$E_c = 4.63 * f_c^{0.5}$	Coarse recycled aggregate

Figure 8 shows the equations that correlate the modulus of elasticity with the compressive strength of all concrete mixtures analyzed in this study (NA-100, MRA-20, RCA-20, and RMA-20). It is possible to observe higher

deformability of concretes made mainly with MRA and RMA. This can be explained by the presence of ceramic materials in the composition of these two types of recycled aggregates.

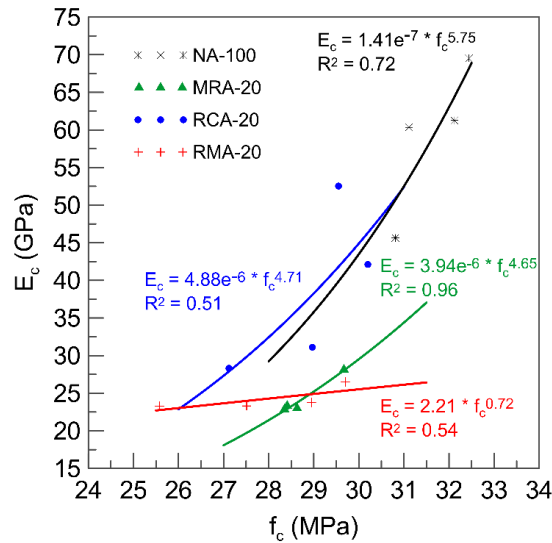


Figure 8. Correlation between modulus of elasticity and compressive strength.

It was also possible to observe a relationship between the apparent porosity and the maximum compressive strength, as well as between the aggregate crushing value and the maximum compressive strength (Figure 9). When the number of pores in the aggregate increases, the maximum compressive strength decrease. Furthermore, as higher is the aggregate crushing value, which means a lower strength of the aggregate, the lower is the concrete maximum compressive strength. Similar results were obtained in other studies. Gómez-Soberón [68] noted that an increase of approximately 4% in the aggregates total porosity caused a reduction of almost 21% in the concrete compressive strength. Meanwhile, Duan and Poon [61] observed that an increase of approximately 9% in the aggregate crushing value, caused a decrease of almost 20% in the concrete compressive strength.

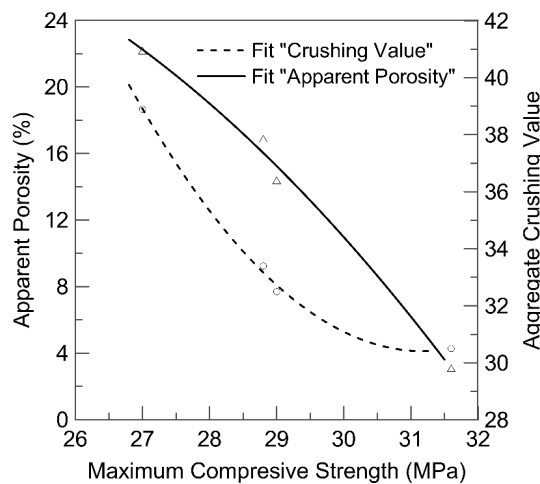


Figure 9. Apparent porosity and Aggregate crushing value versus Maximum compressive strength.

4 CONCLUSIONS

Based on the experimental results obtained in the present work, the following conclusions can be drawn:

- A reduction in the void ratio means a reduction in the number of voids between the aggregates at a certain known volume, thus generating an increase in the packing density. As all aggregates, including the natural one, presented comparable values for shape index and the same maximum size, they all had very similar values of void ratio and, consequently, for packing density;
- Because of its higher porosity, the recycled aggregates were less dense, less resistant and absorbed more water than the natural aggregate. All recycled aggregates absorbed almost 90% of the total water after approximately 12 minutes. This must be taken into account when mixing the concrete, since the water absorption by the aggregates can reduce the amount of water available for the cement hydration reaction;
- Only the concrete made with 100% natural aggregate achieved the desired maximum compressive strength, demonstrating that the strategy of applying a direct replacement ratio for the recycled aggregate must be rethought as a mix design method, since it does not take into account the inherent characteristics of these aggregates;
- Despite this reduction, it was possible to obtain a compressive strength greater than 25 MPa for all samples made with 20% in volume of recycled aggregates. This could be is a satisfactory result for the use of this material in structural elements. Furthermore, similarly to several international standards, this percentage of substitution could be seen as a starting point for a possible revision of the Brazilian standard NBR 15116:2004, which regulates the use of recycled aggregates in concrete;
- In general, the properties obtained for the mixed recycled aggregate (MRA) were very close to those obtained for the recycled aggregate composed only by the concrete fraction (RCA). There was also little variation in the mechanical strength of concretes manufactured with 20% in volume of MRA and RCA in substitution of the natural aggregate. This demonstrates that the MRA with a small ceramic fraction (< 15%) can be directly used by the construction industry, without the need to separate the masonry and concrete fractions. Thus, the recycling process becomes cheaper and more attractive for the use of the recycled aggregate on a large scale.

ACKNOWLEDGEMENTS

This study was financed in part by the Coordenação de Aperfeiçoamento de Pessoal de Nível Superior - Brasil (CAPES) - Finance Code 001. The authors would also like to acknowledge the support from CNPq, FINEP, FAPERJ and Reciclax Recycling Plant.

REFERENCES

- [1] S. Kosmatka, B. Kerkhoff, and W. Paranes, *Design and Control of Concrete Mixtures*, 14th ed. Portland Cement Association, 2008.
- [2] L. Huang, G. Krigsvoll, F. Johansen, Y. Liu, and X. Zhang, "Carbon emission of global construction sector," *Renew. Sustain. Energy Rev.*, vol. 81, pp. 1906–1916, 2018, <http://dx.doi.org/10.1016/j.rser.2017.06.001>.
- [3] International Solid Waste Association, *ISWA REPORT ISWA at a Glance*, Vienna, AUT, 2015.
- [4] B. Huang, X. Wang, H. Kua, Y. Geng, R. Bleischwitz, and J. Ren, "Construction and demolition waste management in China through the 3R principle," *Resour. Conserv. Recycling*, vol. 129, pp. 36–44, 2018., <http://dx.doi.org/10.1016/j.resconrec.2017.09.029>.
- [5] U.S. Environmental Protection Agency. *Advancing Sustainable Materials Management: 2014 Fact Sheet*. Washington: USEPA, 2016. Accessed: Apr. 4, 2018. [Online]. Available: https://www.epa.gov/sites/production/files/2016-11/documents/2014_smmfactsheet_508.pdf
- [6] European Environmental Agency. *ETC/SCP, EU as a Recycling Society - Present recycling levels of Municipal Waste and Construction & Demolition Waste in the EU*. Copenhagen: DNK, 2009, pp. 73.
- [7] Associação Brasileira para Reciclagem de Resíduos da Construção Civil e Demolição, *Relatório Pesquisa Setorial 2017/2018*. ABRECON, 2018, pp. 75.
- [8] U.S. Environmental Protection Agency. *Industrial and Construction and Demolition (C&D) Landfills*. Washington: USEPA, 2018. Accessed: Apr. 4, 2018. [Online]. Available: <https://www.epa.gov/landfills/industrial-and-construction-and-demolition-cd-landfills>
- [9] E. Vázquez, Ed. *Progress of Recycling in the Built Environment - Final Report of the RILEM Technical Committee 217-PRE*. Netherlands: Springer, 2013.
- [10] British Standards Institution, *Concrete – Complementary British Standard to BS EN 206 – Part 2: Specification for Constituent Materials and Concrete*, BS 8500-2, 2015, pp. 48.
- [11] EHE, *EHE-08 - Instrucción de Hormigón Estructural*. Ministerio de Fomento S.G.T. Centro de Publicaciones, ESP., 2008, pp. 258–266.
- [12] Lisboa. Ministério das Obras Públicas, Transportes e Comunicações. Laboratório Nacional de Engenharia Civil. *Guia para Utilização de Agregados Reciclados Grossos em Betões de Ligantes Hidráulicos*, E 471-2009. Lisboa: LNEC, 2009, pp. 8.

- [13] Deutsches Institut für Normung e.V., *Aggregates for Concrete*, DIN EN 12620, 2003, pp. 47.
- [14] Ministero delle Infrastrutture, *M_INF-TFE, NTC 2008 – Italian Building Code. D.M. 14/01/2008*. ITA, 2008, p. 448.
- [15] Commonwealth Scientific and Industrial Research Organisation, *Guide to the Use of Recycled Concrete and Masonry Materials*, CSIRO HB 155, 2002, pp. 80.
- [16] Associação Brasileira de Normas Técnicas, *Agregados Reciclados de Resíduos Sólidos da Construção Civil – Utilização em Pavimentação e Preparo de Concreto sem Função Estrutural – Requisitos*, NBR 15116, 2004.
- [17] G. Bai, C. Zhu, C. Liu, and B. Liu, "An evaluation of the recycled aggregate characteristics and the recycled aggregate concrete mechanical properties," *Constr. Build. Mater.*, vol. 240, pp. 117978, 2020, <http://dx.doi.org/10.1016/j.conbuildmat.2019.117978>.
- [18] M. Bravo, J. De Brito, J. Pontes, and L. Evangelista, "Mechanical performance of concrete made with aggregates from construction and demolition waste recycling plants," *J. Clean. Prod.*, vol. 99, pp. 59–74, 2015, <http://dx.doi.org/10.1016/j.jclepro.2015.03.012>.
- [19] V. Corinaldesi, "Mechanical and elastic behaviour of concretes made of recycled-concrete coarse aggregates," *Constr. Build. Mater.*, vol. 24, no. 9, pp. 1616–1620, 2010, <http://dx.doi.org/10.1016/j.conbuildmat.2010.02.031>.
- [20] M. Etxeberria, E. Vázquez, A. Marí, and M. Barra, "Influence of amount of recycled coarse aggregates and production process on properties of recycled aggregate concrete," *Cement Concr. Res.*, vol. 37, no. 5, pp. 735–742, 2007, <http://dx.doi.org/10.1016/j.cemconres.2007.02.002>.
- [21] V. W. Y. Tam, D. Kotrayothar, and J. Xiao, "Long-term deformation behaviour of recycled aggregate concrete," *Constr. Build. Mater.*, vol. 100, pp. 262–272, 2015, <http://dx.doi.org/10.1016/j.conbuildmat.2015.10.013>.
- [22] C. Thomas, J. Setién, J. A. Polanco, P. Alaejos, and M. Sánchez De Juan, "Durability of recycled aggregate concrete," *Constr. Build. Mater.*, vol. 40, pp. 1054–1065, 2013, <http://dx.doi.org/10.1016/j.conbuildmat.2012.11.106>.
- [23] M. Etxeberria, A. R. Marí, and E. Vázquez, "Recycled aggregate concrete as structural material," *Mater. Struct. Constr.*, vol. 40, no. 5, pp. 529–541, 2007, <http://dx.doi.org/10.1617/s11527-006-9161-5>.
- [24] X. Li, "Recycling and reuse of waste concrete in China. Part II. Structural behaviour of recycled aggregate concrete and engineering applications," *Resour. Conserv. Recycling*, vol. 53, no. 3, pp. 107–112, 2009, <http://dx.doi.org/10.1016/j.resconrec.2008.11.005>.
- [25] N. Mohamad, H. Khalifa, A. A. Abdul Samad, P. Mendis, and W. I. Goh, "Structural performance of recycled aggregate in CSP slab subjected to flexure load," *Constr. Build. Mater.*, vol. 115, pp. 669–680, 2016, <http://dx.doi.org/10.1016/j.conbuildmat.2016.04.086>.
- [26] H. Zhang and Y. Zhao, "Performance of recycled aggregate concrete in a real project," *Adv. Struct. Eng.*, vol. 17, no. 6, pp. 895–906, 2014, <http://dx.doi.org/10.1260/1369-4332.17.6.895>.
- [27] J. R. Jiménez, J. Ayuso, A. P. Galvín, M. López, and F. Agrela, "Use of mixed recycled aggregates with a low embodied energy from non-selected CDW in unpaved rural roads," *Constr. Build. Mater.*, vol. 34, pp. 34–43, 2012, <http://dx.doi.org/10.1016/j.conbuildmat.2012.02.042>.
- [28] F. D. C. Leite, R. D. S. Motta, K. L. Vasconcelos, and L. Bernucci, "Laboratory evaluation of recycled construction and demolition waste for pavements," *Constr. Build. Mater.*, vol. 25, no. 6, pp. 2972–2979, 2011, <http://dx.doi.org/10.1016/j.conbuildmat.2010.11.105>.
- [29] I. Martínez-Lage, F. Martínez-Abella, C. Vázquez-Herrero, and J. L. Pérez-Ordóñez, "Properties of plain concrete made with mixed recycled coarse aggregate," *Constr. Build. Mater.*, vol. 37, pp. 171–176, 2012, <http://dx.doi.org/10.1016/j.conbuildmat.2012.07.045>.
- [30] B. Mas et al., "Concrete with mixed recycled aggregates: Influence of the type of cement," *Constr. Build. Mater.*, vol. 34, pp. 430–441, 2012, <http://dx.doi.org/10.1016/j.conbuildmat.2012.02.092>.
- [31] J. Tavira, J. R. Jiménez, J. Ayuso, M. J. Sierra, and E. F. Ledesma, "Functional and structural parameters of a paved road section constructed with mixed recycled aggregates from non-selected construction and demolition waste with excavation soil," *Constr. Build. Mater.*, vol. 164, pp. 57–69, 2018, <http://dx.doi.org/10.1016/j.conbuildmat.2017.12.195>.
- [32] I. Vegas, J. A. Ibañez, A. Lisbona, A. Sáez De Cortazar, and M. Frías, "Pre-normative research on the use of mixed recycled aggregates in unbound road sections," *Constr. Build. Mater.*, vol. 25, no. 5, pp. 2674–2682, 2011, <http://dx.doi.org/10.1016/j.conbuildmat.2010.12.018>.
- [33] J. Yang, Q. Du, and Y. Bao, "Concrete with recycled concrete aggregate and crushed clay bricks," *Constr. Build. Mater.*, vol. 25, no. 4, pp. 1935–1945, 2011, <http://dx.doi.org/10.1016/j.conbuildmat.2010.11.063>.
- [34] B. Cantero, I. F. Sáez del Bosque, A. Matías, and C. Medina, "Statistically significant effects of mixed recycled aggregate on the physical-mechanical properties of structural concretes," *Constr. Build. Mater.*, vol. 185, pp. 93–101, 2018, <http://dx.doi.org/10.1016/j.conbuildmat.2018.07.060>.
- [35] P. V. Salles, "Avaliação mecânica e de durabilidade de concretos fabricados com resíduos de construção e demolição," M.S. thesis, Cent. Fed. Educ. Tecnol. Minas Gerais, Belo Horizonte, 2018.
- [36] Y. Kasai, K. D. Ravindra, A. H. Neil, and C. L. Mukesh, "Barriers to the reuse of construction by-products and the use of recycled aggregate in concrete in Japan," *Sustain. Constr. Use Recycl. Concr. Aggreg.*, 2015. Accessed: Apr. 4, 2018. [Online]. Available: <https://www.icevirtuallibrary.com/doi/abs/10.1680/scuorca.27268.0038>

- [37] C. Medina, W. Zhu, T. Howind, M. Frías, and M. I. Sánchez de Rojas, "Effect of the constituents (asphalt, clay materials, floating particles and fines) of construction and demolition waste on the properties of recycled concretes," *Constr. Build. Mater.*, vol. 79, pp. 22–33, 2015, <http://dx.doi.org/10.1016/j.conbuildmat.2014.12.070>.
- [38] M. Quattrone, S. C. Angulo, and V. M. John, "Energy and CO₂ from high performance recycled aggregate production," *Resour. Conserv. Recycling*, vol. 90, pp. 21–33, 2014, <http://dx.doi.org/10.1016/j.resconrec.2014.06.003>.
- [39] R. V. Silva, J. Brito, and R. K. Dhir, "Availability and processing of recycled aggregates within the construction and demolition supply chain: a review," *J. Clean. Prod.*, vol. 143, pp. 598–614, 2017, <http://dx.doi.org/10.1016/j.jclepro.2016.12.070>.
- [40] K. Hu, Y. Chen, F. Naz, C. Zeng, and S. Cao, "Separation studies of concrete and brick from construction and demolition waste," *Waste Manag.*, vol. 85, pp. 396–404, 2019, <http://dx.doi.org/10.1016/j.wasman.2019.01.007>.
- [41] I. Vegas, K. Broos, P. Nielsen, O. Lambertz, and A. Lisbona, "Upgrading the quality of mixed recycled aggregates from construction and demolition waste by using near-infrared sorting technology," *Constr. Build. Mater.*, vol. 75, pp. 121–128, 2015, <http://dx.doi.org/10.1016/j.conbuildmat.2014.09.109>.
- [42] V. W. Y. Tam, M. Soomro, and A. C. J. Evangelista, "A review of recycled aggregate in concrete applications (2000-2017)," *Constr. Build. Mater.*, vol. 172, pp. 272–292, 2018, <http://dx.doi.org/10.1016/j.conbuildmat.2018.03.240>.
- [43] Associação Brasileira de Normas Técnicas, *Agregados – Determinação do Material Fino que Passa Através da Peneira 75 um, por Lavagem*, NBR NM 46, 2003.
- [44] Associação Brasileira de Normas Técnicas, *Agregados – Determinação da Composição Granulométrica*, NBR NM 248, 2003.
- [45] Associação Brasileira de Normas Técnicas, *Agregado Graúdo – Determinação do Índice de Forma pelo Método do Paquímetro – Método de Ensaio*, NBR 7809, 2019.
- [46] Associação Brasileira de Normas Técnicas, *Agregado Graúdo – Determinação da Massa Específica, Massa Específica Aparente e Absorção de Água*, NBR NM 53, 2009.
- [47] Associação Brasileira de Normas Técnicas, *Agregados – Determinação da Massa Unitária e do Volume de Vazios*, NBR NM 45, 2006.
- [48] F. de Larrard, *Concrete Mixture Proportioning: a Scientific Approach*. London, UK: E&FN Spon, 1999.
- [49] British Standards Institution, *Part 110 – Aggregate Crushing Value*, BS 812, 1990.
- [50] Associação Brasileira de Normas Técnicas, *Concreto – Ensaio de Compressão de Corpos de Prova Cilíndricos*, NBR 5739, 2018.
- [51] Associação Brasileira de Normas Técnicas, *Cimento Portland – Requisitos*, NBR 16697, 2018.
- [52] Associação Brasileira de Normas Técnicas, *Concreto – Determinação da Consistência pelo Abatimento do Tronco de Cone*, NBR NM 67, 1998.
- [53] Associação Brasileira de Normas Técnicas, *Agregado para Concreto – Especificação*, NBR 7211, 2009.
- [54] J. J. L. Tenório, "Avaliação de propriedades do concreto produzido com agregados reciclados de resíduos de construção e demolição visando aplicações estruturais," M.S. thesis, Univ. Fed. Alagoas, 2007.
- [55] M. B. Leite, "Avaliação de propriedades mecânicas de concretos produzidos com agregados reciclados de resíduos de construção e demolição," Ph.D. dissertation, Univ. Fed. Rio Grande do Sul, 2001.
- [56] M. Pepe, R. D. Toledo Fo., E. A. B. Koenders, and E. Martinelli, "Alternative processing procedures for recycled aggregates in structural concrete," *Constr. Build. Mater.*, vol. 69, pp. 124–132, 2014, <http://dx.doi.org/10.1016/j.conbuildmat.2014.06.084>.
- [57] A. Bashir, G. Chhavi, A. M. Abubakar, and S. I. Abba, "Comparison of properties of coarse aggregate obtained from recycled concrete with that of conventional coarse aggregates," *Eur. J. Adv. Eng. Technol.*, vol. 5, no. 8, pp. 628–637, 2018., <http://dx.doi.org/10.13140/RG.2.2.35863.83361>.
- [58] M. Pepe, R. D. Toledo Fo., E. A. B. Koenders, and E. Martinelli, "A novel mix design methodology for Recycled Aggregate Concrete," *Constr. Build. Mater.*, vol. 122, pp. 362–372, 2016, <http://dx.doi.org/10.1016/j.conbuildmat.2016.06.061>.
- [59] M. C. Limbachiya, T. Leelawat, and R. K. Dhir, "Use of recycled concrete aggregate in high-strength concrete," *Mater. Struct.*, vol. 33, no. 9, pp. 574–580, 2000, <http://dx.doi.org/10.1007/BF02480538>.
- [60] T. L. Cavalline and D. C. Weggel, "Recycled brick masonry aggregate concrete: Use of brick masonry from construction and demolition waste as recycled aggregate in concrete," *Struct. Surv.*, vol. 31, no. 3, pp. 160–180, 2013, <http://dx.doi.org/10.1108/SS-09-2012-0029>.
- [61] Z. H. Duan and C. S. Poon, "Properties of recycled aggregate concrete made with recycled aggregates with different amounts of old adhered mortars," *Mater. Des.*, vol. 58, pp. 19–29, 2014, <http://dx.doi.org/10.1016/j.matdes.2014.01.044>.
- [62] G. C. Lee and H. B. Choi, "Study on interfacial transition zone properties of recycled aggregate by micro-hardness test," *Constr. Build. Mater.*, vol. 40, pp. 455–460, 2013, <http://dx.doi.org/10.1016/j.conbuildmat.2012.09.114>.
- [63] Q. Liu, J. Xiao, and Z. Sun, "Experimental study on the failure mechanism of recycled concrete," *Cement Concr. Res.*, vol. 41, no. 10, pp. 1050–1057, 2011, <http://dx.doi.org/10.1016/j.cemconres.2011.06.007>.

- [64] R. S. Ravindrarajah, M. Stewart, and D. Greco, "Variability of recycled concrete aggregate and its effects on the properties of concrete," in *Proc. 2nd Int. Conf. Eng. Mater.*, California, USA, 2001.
- [65] A. E. B. Cabral, V. Schalch, D. C. C. D. Molin, and J. L. D. Ribeiro, "Mechanical properties modeling of recycled aggregate concrete," *Constr. Build. Mater.*, vol. 24, no. 4, pp. 421–430, 2010, <http://dx.doi.org/10.1016/j.conbuildmat.2009.10.011>.
- [66] P. S. Lovato, "Verificação dos parâmetros de controle de agregados reciclados de resíduos de construção e demolição para utilização em concreto," M.S. thesis, Univ. Fed. Rio Grande do Sul, 2007.
- [67] R. S. Ravindrarajah and C. Tam, "Properties of concrete made with crushed concrete as coarse aggregate," *Mag. Concr. Res.*, vol. 37, no. 130, pp. 29–38, 1985, <http://dx.doi.org/10.1680/mac.1985.37.130.29>.
- [68] J. M. V. Gómez-Soberón, "Porosity of recycled concrete with substitution of recycled concrete aggregate: an experimental study," *Cement Concr. Res.*, vol. 32, no. 8, pp. 1301–1311, 2002, [http://dx.doi.org/10.1016/S0008-8846\(02\)00795-0](http://dx.doi.org/10.1016/S0008-8846(02)00795-0).

Author contributions: SALGADO, FA: conceptualization, formal analysis, methodology, writing; SILVA, FA: funding acquisition, supervision.

Editors: Yury Andrés Villagrán Zaccardi, Guilherme Aris Parsekian.



ORIGINAL ARTICLE

Influence of internal sulfate attack on cement paste properties: contamination by pyrite

Influência do ataque interno de sulfatos em pastas cimentícias: contaminação por pirita

Ana Paula Brandão Capraro^a Juarez Hoppe Filho^b Marcelo Henrique Medeiros^a ^aUniversidade Federal do Paraná – UFPR, Programa de Pós-graduação em Engenharia Civil – PPGCEC, Curitiba, PR, Brasil^bUniversidade Federal do Oeste da Bahia – UFOB, Barreiras, BA, Brasil

Received 30 August 2020

Accepted 08 March 2021

Abstract: The objective of this work was to evaluate the influence of the presence of sulfate in the microstructure and compressive strength of cement pastes. The lack of availability of more suitable aggregates, for reasons of distance or costs, sometimes leads to the use of materials that contain sulfate in their composition, which is harmful to cement mixtures. Currently, there are normative recommendations that limit the content of contaminants in the aggregates. However, there are still divergences as to the content that does not damage the concrete. In order to discuss the levels presented in the standards and the values above those allowed by them, tests were carried out on cementitious compounds contaminated by pyrite in different levels of sulfates (0.0%, 0.5%, 1.0% and 5.0% of SO₃). SEM, XRD, compressive strength, ultrasonic pulse velocity and porosity analyses were performed in samples at different ages until 720 days of age. During early ages until the first year, the most contaminated samples presented an increase in their strength (1.0% and 5.0% of SO₃). This behavior was explained by SEM, XRD and porosity analyses by filling the pores with products of sulfate attack, such as ettringite. At the end of the tests (720 days) the series that presented the lowest compressive strength, the presence of cracks and large amounts of ettringite was the one that had 5.0% SO₃ contamination, proving the importance of a normative limit content.

Keywords: sulfate, normative limit content, porosity, ettringite, internal sulfate attack.

Resumo: O objetivo deste trabalho foi avaliar a influência da presença de sulfato na microestrutura e resistência à compressão de pastas de cimento. Por vezes, a falta de disponibilidade de agregados mais adequados, por razões de distância ou custos, leva à utilização de materiais que contenham em sua composição a presença de sulfato, prejudicial às misturas de cimento. Atualmente existem recomendações normativas que limitam os teores de contaminação dos agregados, entretanto, ainda existem divergências quanto ao teor que não agride o concreto. A fim de discutir os teores apresentados nas normas e também os valores acima dos permitidos por elas, foram realizados ensaios em compostos cimentícios contaminados por diferentes teores de sulfatos (0,0%, 0,5%, 1,0% e 5,0% de SO₃). As análises de MEV, DRX, resistência à compressão, velocidade de ultrassom e porosidade foram realizadas em diferentes idades, até 720 dias de idade, nas amostras. Durante as primeiras idades, até o primeiro ano, as amostras mais contaminadas apresentaram aumento em sua resistência (1,0% e 5,0% de SO₃). Este comportamento foi explicado pelas análises de MEV, DRX e porosidade pelo preenchimento dos poros por produtos do ataque de sulfato, como a etringita. Ao final dos ensaios (720 dias) a série que apresentou menor resistência à compressão, presença de fissuras e grande quantidade de etringita foi a que apresentou 5,0% de contaminação de SO₃, comprovando a importância de um teor limite normativo.

Palavras-chave: sulfato, teor limite normativo, porosidade, etringita, resistência à compressão e ataque interno de sulfatos.

How to cite: A. P. B. Capraro, J. Hoppe Filho, and M. H. Medeiros, “Influence of internal sulfate attack on cement paste properties: contamination by pyrite,” *Rev. IBRACON Estrut. Mater.*, vol. 14, no. 6, e14606, 2021, <https://doi.org/10.1590/S1983-41952021000600006>

Corresponding author: Ana Paula Brandão Capraro. E-mail: anapcapraro@gmail.com

Financial support: None.

Conflict of interest: Nothing to declare.



This is an Open Access article distributed under the terms of the Creative Commons Attribution License, which permits unrestricted use, distribution, and reproduction in any medium, provided the original work is properly cited.

1 INTRODUCTION

Internal sulfate attack (ISA) has been considered a serious degradation in concrete structures [1]. The degradation of concrete due to the presence of iron sulfides (such as pyrite and pyrrhotite) in aggregates has been widely studied in recent years [2]. Iron sulfides are common minor constituents in many rock types in various regions in the world. They have been implicated in causing damage in concrete, such as expansion [3].

The condition of the environment may favor the oxidation of the sulfide, and, consequently, the occurrence of the attack. Casanova et al. [4] presented some factors that favor the kinetics of the reaction, which are: oxygen and humidity availability, strongly acidic conditions (pH typically lower than 4), surface area, and iron content.

The internal sulfate attack is caused by the reaction of sulfate ions, present in the aggregates of concrete, with the cement products. The attack mechanism involves several chemical reactions that may generate products such as ettringite, gypsum and thaumasite [5], [6].

The study of the products formed by the attack and the form of their occurrence is of extreme importance, since these cause modifications in the matrix of the cementitious compounds [6]. Schmidt et al. [7] comparatively studied the expansions caused by the deleterious products originated from the presence of pyrite and pyrrhotite in the cement compounds. It was verified that the contaminated aggregates caused expansions in the cement pastes, and the results were close to pyrite and pyrrhotite.

Aggregates contaminated by sulfides are considered unsuitable for use in concrete structures [8]; however, specific situations of distance and lack of more adequate inputs make its use necessary. Considering the consequences of the use of contaminated aggregates, their utilization is restricted by most international standards [4]. However, the limited content of the standards differs from one another. The ACI [9], for example, allows the use of contaminated aggregate if the contamination is less than 0.5% SO₃ of the total aggregate mass. The French standard [10] allows the contamination value to be less than 1.0% SO₃. The Brazilian standard [11] limits the aggregate content to 0.1% SO₄, and if the content is greater than this, the sum of all the constituents of the concrete cannot exceed 0.2% SO₄.

In Brazil, there is a real example of the need to adopt a maximum contamination content for the construction of the Irapé Hydroelectric Plant in Minas Gerais. The analysis of the rock masses indicated the presence of pyrite between 4 to 10% of the total volume. The use of the aggregates was conditioned to the limit of 0.5% sulfur in relation to the total mass of the aggregates [12].

The degradation of the concrete produced with aggregate contaminated by sulfide minerals is the result of the interaction of the contaminant with the Portland cement paste. Therefore, this research aimed to illustrate the effects of the internal sulphatic reaction by evaluating the behavior of cementitious composites with the addition of pyrite (FeS₂). In this context, the aim of this work was to evaluate the influence of the presence of sulfates, in different contents, in the microstructure and compressive strength of cement pastes. For this purpose, the two limits suggested by the standards cited (0.5% and 1.0% SO₃), one above that mentioned by them (5.0% SO₃) and one reference (0.0% SO₃) were considered.

2 LITERATURE REVIEW

In nature there are geological formations of endogenous and metamorphic species that contain the presence of sulfides, most often as pyrite and pyrrhotite. Figure 1 shows the image of an aggregate particle with evident and proven pyrite contamination. The use of these materials as aggregates for concrete causes deleterious reactions, as these minerals are unstable in the presence of water [13].

The deleterious reactions begin with the oxidation of the sulfide mineral in the presence of water and oxygen, causing the formation of iron hydroxide and sulfuric acid [14]. As an example, Equation 1 presents the oxidation of pyrite, a material used as a contaminant in this study.



The oxidation of sulfides triggers a series of chemical reactions in the compound, forming products with greater volumes than the initial volume of the materials [15]. The formation of ettringite, for example, generates dimensional variation, internal stresses and cracks in the concrete, compromising the durability of the structures [13].

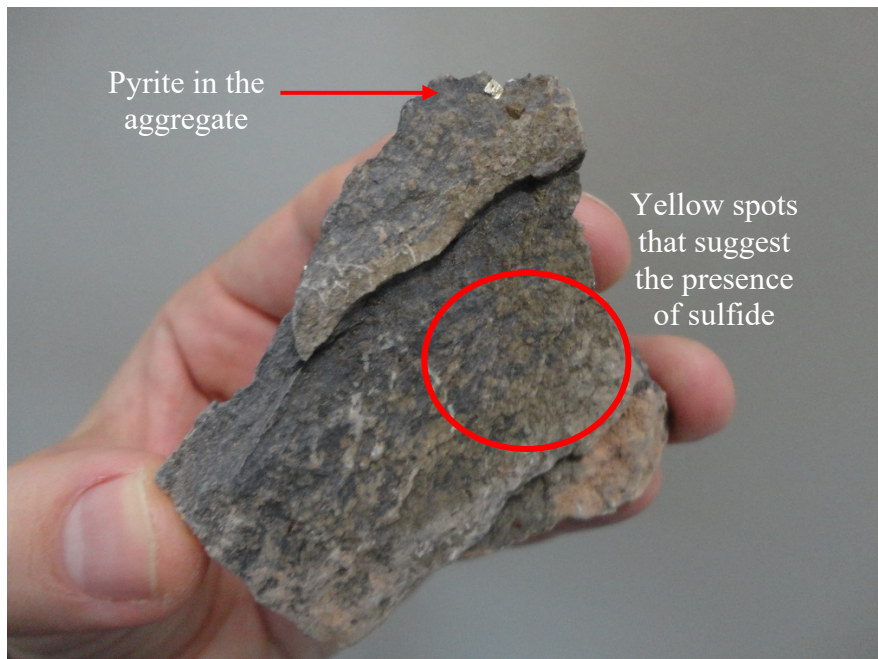


Figure 1. Example of Brazilian civil construction aggregate with verified pyrite contamination and generation of internal sulphatic reaction.

In recent years, studies have been carried out to assess the impacts caused using sulfate-contaminated aggregates.

Goto et al. [16] studied the influence of particle size, pH of the medium and pyrite concentration on the oxidation of diabase aggregates with sulfide minerals. The results indicated that the reduced grain size and alkaline medium accelerate the oxidation reactions.

Recent studies [17]–[19] related to the attack of sulfates investigate the impact that the presence of contaminants in recycled aggregates, such as gypsum, can cause on the properties of cementitious compounds such as: mechanics, microstructure, and porosity. Analyses analogous to those proposed in these studies were performed in the present study.

Other research has used artificial simulation for an environmental exposure more favorable to attack. The results indicate degradation in the microstructure of cementitious compounds due to the presence of sulfate, caused by the formation of expansive products and the consumption of hydrated products. Degradation in the mechanical properties was also noted by the reduction of the dynamic elastic modulus [20]. Similarly, this research also proposes an accelerated analysis of the internal attack of sulfates and aims to identify the expansive products and the consumption of the hydrated phases through the XRD and SEM tests.

Capraro et al. [21] studied the impact of internal sulfate attack on reinforcement corrosion. The results indicated a greater susceptibility to corrosion in the series with the highest contamination in the study (5.0% SO_3), due to the consumption of portlandite and the chemical instability in the series.

The study of the use of aggregates with the presence of sulfides in cementitious compounds is of great importance, since the presence of contaminants has an influence on the properties of the materials. It is also worth noting that, due to the need to use these aggregates, a limit of contamination that does not damage the properties of concrete structures must be established.

3 EXPERIMENTAL PROCEDURES

Molding cement pastes contaminated by different sulfate contents was a method used in the experimental campaign. After the curing period (28 days), the pastes were submitted to a favorable exposure condition for the occurrence of the attack: wetting and drying cycles. The materials were evaluated until 720 days of age in the tests of compressive strength, ultrasonic pulse velocity, porosity, SEM, and XRD.

3.1. Materials and mixture characteristics

The binder used in this experiment is a mixture composed of 65% Portland cement of high initial strength (CP V ARI – NBR 5733 [22] equivalent to Type III – ASTM C150 [23]) and 35% fly ash (equivalent to ASTM C618 [24] class F). Table 1 shows the properties of the Portland cement and the fly ash using the X-Ray fluorescence technique.

Table 1. Chemical characterization (%) of cement and mineral addition.

	Cement (CP V ARI)	Fly ash
CaO	60	1.60
SiO ₂	19.58	57.80
Al ₂ O ₃	4.88	26.60
Fe ₂ O ₃	2.85	6.70
MgO	4.37	0.80
SO ₃	2.82	0.30
K ₂ O	-	3.80
Na ₂ O	-	0.80
TiO ₂	-	1.60
Free CaO	0.87	-
Ignition loss	2.97	-
Insoluble waste	0.88	-
Alkaline equivalent	0.78	-

The final composite cement is close to the CP IV cement of the Brazilian standard [25] and the Type IV cement of the American standard [23]. The specific mass of the cement and the fly ash, obtained in conformity with ASTM C188 [26], are 3.14 g/cm³ and 1.95 g/cm³, respectively.

The contaminant used for the cement paste mixture was pyrite (FeS₂), a remainder of mineral coal processing. In this study, only one degree of particle size of the contaminated material was analyzed. The influence of the fineness of pyrite on the kinetics of the attack by internal sulfates was not evaluated. A hammer mill carried out the crushing of the contaminated material, and the passage of all the material through the 2.4 mm sieve was the condition to stop the activity.

The pyrite used has a specific mass of 4.95 g/cm³, obtained in conformity with ASTM C128 [27], and the diffractogram of the material is shown in Figure 2.

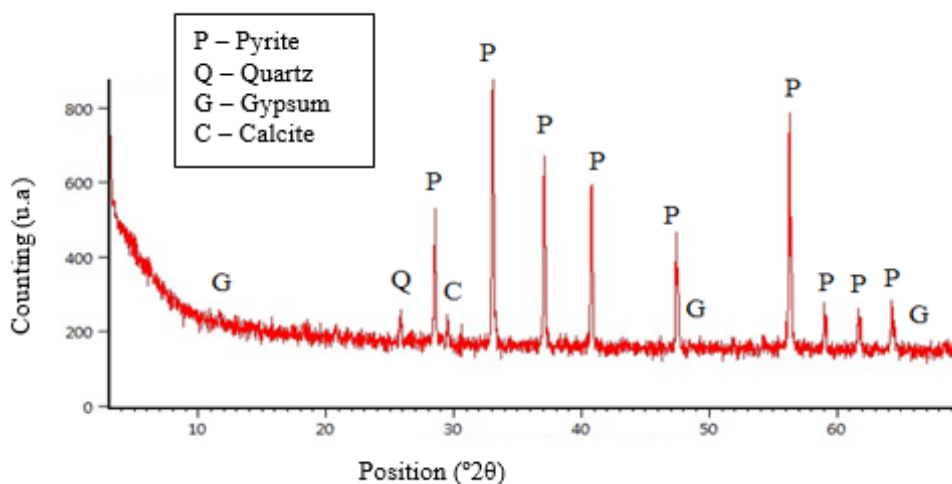


Figure 2. X-Ray Diffractogram of pyrite.

The limits of internationally disseminated regulations determined the levels of contamination chosen for the cement pastes. Considering that four levels were chosen: 0.0% SO₃ (reference series, without contamination), 0.5% SO₃ (established by the ACI [9]), 1.0% SO₃ (established by the French Standard [10]) and 5.0% SO₃ (higher than allowed by both). The intention of this choice was to evaluate two different levels recommended by current standards and one above those allowed by them.

As the contaminant was pyrite, a calculation of the proportion of mass to determine the equivalent amounts of sulfur quantity between FeS₂ and SO₃ was necessary. Considering that when oxidized, the pyrite becomes entirely SO₃ and performs stoichiometric calculations, it follows that: $FeS_2 = 0.75 SO_3$.

The previously mentioned standards limit the amount of materials containing sulfides regarding the total mass of aggregates. Since the cement pastes have no aggregate to apply the amounts, a mix proportion of base concrete was used to then determine the amounts regarding the mass of cement.

The concrete mix proportion adopted was: 1.0 kg of cement, 2.7 kg of fine aggregate, 2.7 kg of coarse aggregate and 0.6 kg of water. The choice of this mix proportion comes from the application of this dosage in the execution of conventional concrete in a hydroelectric plant in Brazil. Contamination percentages were applied over the total mass of aggregates (2.7 kg of fine aggregate + 2.7 kg of coarse aggregate) and determined the proportional contamination regarding the cement mass, according to results presented in Table 2.

Table 2. Proportional contamination levels.

Studied groups	Contamination content in SO ₃ *	Contamination content in Pyrite*	Content of pyrite in relation to the mass of binder
Ref. (0.0%)	0.00%	0.00%	0.00%
SO ₃ (0.5%)	0.50%	0.38%	2.05%
SO ₃ (1.0%)	1.00%	0.75%	4.05%
SO ₃ (5.0%)	5.00%	3.75%	20.25%

* in relation to the total mass of aggregates

The applied contaminant was used as an addition to the cement pastes. However, an inert material (limestone filler) was used to compensate the volumes of the mixtures in order for the four series to have the same cement consumption, allowing the evaluation of the mechanical properties between them.

The limestone filler has a specific mass of 2.84 g/cm³ and bulk density of 0.85 g/cm³.

The mix proportion of four cement pastes was presented in Table 3. The cement consumption is the same for all groups, being equal to 973.8 kg/m³.

Table 3. Mix proportion for the four studied groups.

Studied groups	Binder*(g)	Pyrite (g)	Limestone filler (g)	water/binder*
Ref. (0.0%)	1000	0 g	115	0.6
SO ₃ (0.5%)	1000	20 g	104	0.6
SO ₃ (1.0%)	1000	40 g	92	0.6
SO ₃ (5.0%)	1000	200 g	0	0.6

*binder = (65%) cement CPV ARI + (35%) fly ash.

3.2. Experimental procedure

3.2.1 Specimen preparation and exposure conditions

For the compressive strength and ultrasonic pulse velocity tests, 4 x 4 x 16 cm³ prismatic samples were molded, in conformity with NBR 13276 [28]. To statistically analyze the results, 5 specimens were molded for each group at each age analyzed using the Tukey test (95% confidence). For the porosity, SEM and XRD tests, little cylindrical samples were molded, each with a diameter of 1.5 cm and a height of 0.5 cm.

The cement pastes were mixed following the methodology: the water was added to the bowl mixer and the previously homogenized solid materials (binder + filler limestone + pyrite) were released. The materials were mixed for 6 minutes with the equipment operated at the lowest speed. When the mixing was finished, the molds were filled.

The cement paste was poured in the molds ($4 \times 4 \times 16 \text{ cm}^3$) gradually, in three steps. After each step, the material was manually compacted. The cement paste cylinders used for porosity, SEM and XRD tests were molded in 20 ml plastic bottles. The specimens were demolded 24 hours later, after which they were cured, being submerged in lime saturated water for 28 days. The objective was for the cement pastes to reach an advanced hydrated condition.

After the submerged cure, all the specimens were submitted to wetting and drying cycle conditions. The cycle consisted of the weekly exchange of specimens between a tank that was constantly aerated by pump-water, and a dry chamber with controlled temperature ($23 \pm 2^\circ\text{C}$) and humidity ($\leq 50\%$).

The alternating wetting and drying cycle were carried out in other studies with the objective of accelerating the deleterious reactions, due to the greater availability of water and oxygen [29]–[31].

3.2.2 Performed tests

For 720 days the cement pastes were evaluated in laboratory tests. The prismatic specimens were used for the test of compressive strength and ultrasonic pulse velocity. In both tests the specimens were tested in a saturated dry surface condition. The analysis ages of the compressive strength test were: 28, 84, 168, 360 and 720 days. For the ultrasonic pulse velocity, because it is non-destructive, analyses were performed at all ages already mentioned and also at 1, 7, 56, 112, 140, 210 days.

The first test to be performed was the ultrasound pulse velocity test, because it was non-destructive. For the test, Proceq Ultrasonic Pulse Velocity – Pundit Lab was used. The 250 kHz transducer was used, according to the fabricator's recommendations for the size of the specimen faces ($4 \times 4 \text{ cm}^2$). The test was performed in accordance with ASTM C597 [32].

After the ultrasound readings, the compression strength test was performed in accordance with NBR 13279 [33].

Samples used for the porosity, SEM and XRD tests underwent a hydration stoppage process at the test ages (28, 84, 168, 360 and 720 days for the porosity test, 360 and 720 days for the SEM test and 28 and 720 days for XDR test). The process consisted of the immersion of the samples in pure ethyl alcohol for 24 hours, and later, placing them in an oven at 40°C for another 24 hours. The procedure followed that described by Pan et al. [34] and Hoppe et al. [35].

The porosity test consisted of obtaining the total porosity of the sample [36]. The difference between the saturated sample mass (immersed in water for 24 hours) and the dry sample mass (oven dried at 40°C for 24 hours) is divided by the difference between the saturated sample mass (immersed in water for 24 hours) and the submerged sample mass, determined in hydrostatic condition. After the process, the samples were stored in a gel silica desiccator.

Microscopy images were obtained with a Tescan SEM FEG microscope, Mira 3 and Oxford X-Max 50 X-ray analytical microprobe (EDS). First, the samples were glued to the stub with graphite enamel for the identification of the elements by EDS. Afterwards, they were removed from the equipment, metalized with gold, and the images were obtained. The gold metallization was not carried out from the beginning to avoid overlapping elements during the obtaining of the EDS spectra.

X-ray diffraction analysis was performed with the powdered samples, which were sprayed with pistil until being passed through the $200\mu\text{m}$ mesh. The equipment used in the test had 40 kV/30 mA of power and the start and end position of the test were: Start Position [$^\circ 2\text{Th.}$] 5.0084 and End Position [$^\circ 2\text{Th.}$] 74.9634.

4 RESULTS AND DISCUSSION

4.1. Ultrasonic pulse velocity test

Figure 3 shows the ultrasonic pulse velocity results. The studied parameter presented great evolution for all the analyzed series, close to 2250 m/s at one day of age and 3500 m/s at 720 days.

The increase in ultrasonic pulse velocity over the analyzed ages indicates the densification of the matrices. There is a great evolution for all the series until 84 days of age, and after that, small fluctuations and stabilization of the values are noticed. The initial growth was expected, since the occurrence of hydration reactions causes a trend of water consumption and product formation, buffering the pores and decreasing the matrix voids. The same behavior was observed and justified by Godinho et al. [37].

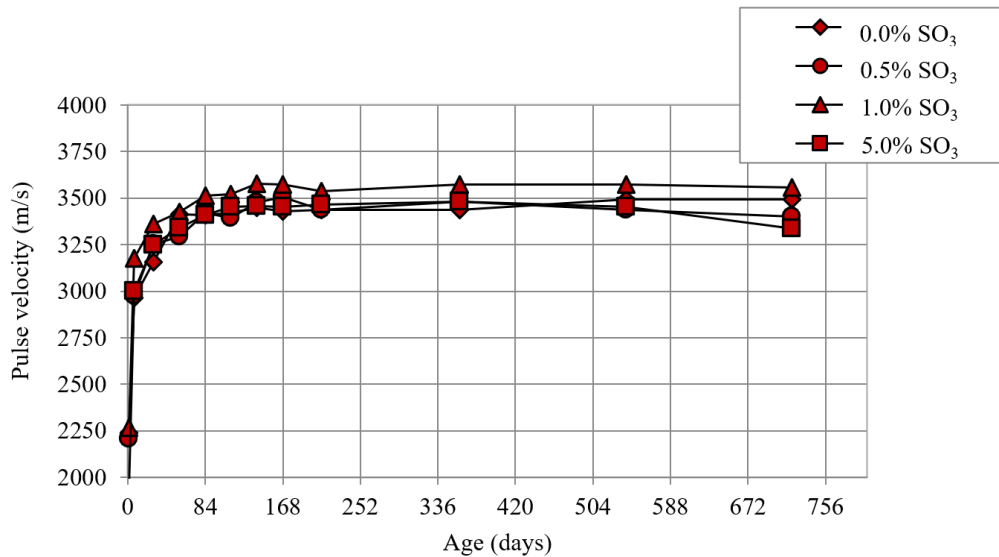


Figure 3. Pulse velocity monitoring for the series (0.0%, 0.5%, 1.0% and 5.0% SO₃).

Based on the Tukey test, the series could be considered statistically equivalent in practically the whole study. At 720 days of age, the 0.5% SO₃ and 5.0% SO₃ series showed a small decrease, which made them statistically smaller when compared to the 0.0% SO₃ and 1.0% SO₃.

The fact that the 1.0% SO₃ series presents some of the highest values for the ultrasonic pulse velocity can indicate the densification of the matrix, generated by the filling of the pores and fissures by the products of the deleterious reactions, a clue already observed and reported by Biczók [38] and Ouyang et al. [39].

However, the 0.5% SO₃ series showed a reduction in propagation of ultrasonic pulse velocity. Therefore, in this case the ultrasound test was not a suitable technique to identify the degradation by internal sulfate in the studied period of time.

The pulse velocity test can be used to evaluate the dynamic elastic modulus of cementitious compounds. Chen et al. [20] indicated in their study that, at an early age, the formation of expansive products and consumption of hydrated products caused an increase in the dynamic elastic modulus. However, at advanced ages, the same study reported a reduction in modulus, similar to what occurred in this study for the 5.0% SO₃ series.

4.2. Compressive strength

At the first analyzed age, 28 days, the series of higher contaminations (1.0% and 5.0% SO₃) were responsible for the higher compressive strength. At that age, the series Ref. (0.0%) and 0.5% SO₃ were considered statistically equivalent by the Tukey test, as well as the 1.0% SO₃ and 5.0% SO₃ series. The higher values of compressive strength for the series of higher contamination, at an initial age, can be justified by the initial filling of the pores by products from the sulfate attack. This agrees with Araujo [40], since the formation of the products from the internal sulfate attack in the voids filled the spaces, promoting the increase of compressive strength in an initial stage. Figure 4 shows the compressive strength results for all studied ages.

At 84 days of age, all series presented increased compressive strength when compared to the results at 28 days. The result was expected, since the cement used in the cement pastes had a high percentage of pozzolanic addition (35%). At that age, the 1.0% SO₃ series remained that with the highest compressive strength, followed by the others, which were equivalent to each other.

From 168 days up to 720 days, the Ref. (0.0%), 0.5% SO₃ and 1.0% SO₃ series showed neither increase nor reduction of compressive strength, remaining constant. The three series were considered statistically similar at all three ages.

The 5.0% SO₃ can be considered similar to the others at the age of 168 and 360 days. However, at the age of 720 days, it was considered similar only to 0.5% SO₃ and 1.0% SO₃, with lower compressive strength when compared to the reference series (approximately 12% lower). This indicates that, for this degree of contamination, the reaction products may have filled the pores and caused enough stresses to microcrack the cementitious matrix.

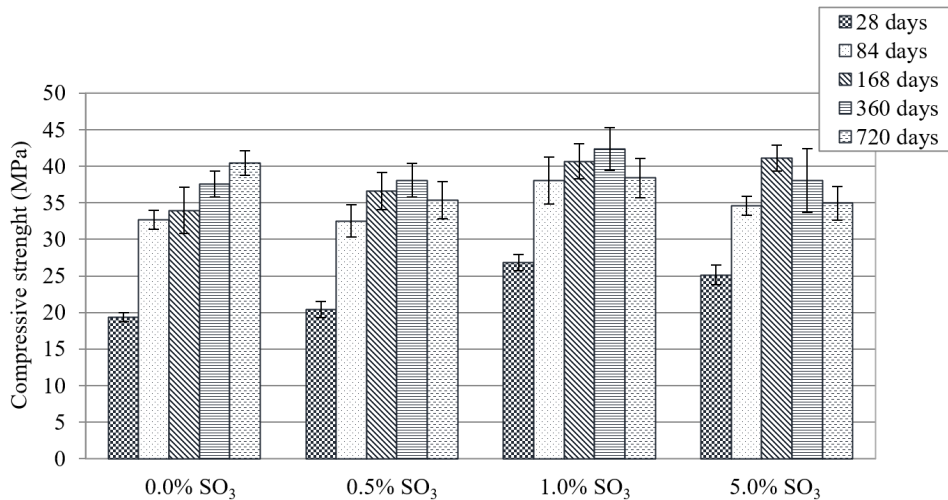


Figure 4. Compressive strength monitoring for the series (0.0%, 0.5%, 1.0% and 5.0% SO₃).

In the last studied age, a tendency of strength decreases for the three contaminated series (0.5, 1.0 and 5.0% SO₃) is noticed, which did not happen for the reference series.

Similarly, Xiao et al. [41] demonstrated that the higher the content of substitution of natural aggregate for recycled aggregate with the presence of sulfur, the lower the compressive strength of mortars.

4.3. Total porosity

Similar to that observed in the previously presented tests, the results of porosity indicated a higher densification of the matrix at initial ages in the series of greater contamination (1.0% and 5.0% SO₃). The porosity of samples exposed to sulfates is also discussed by Zou et al. [42]. The authors justify the reduction in the property at an early age by the refinement of the pores, caused by the products created in the chemical reactions with the sulfate.

Figure 5 shows the results for the total porosity. Throughout all ages, the series 0.0% and 0.5% SO₃ were considered statistically equivalent, as were the series 1.0% and 5.0% SO₃.

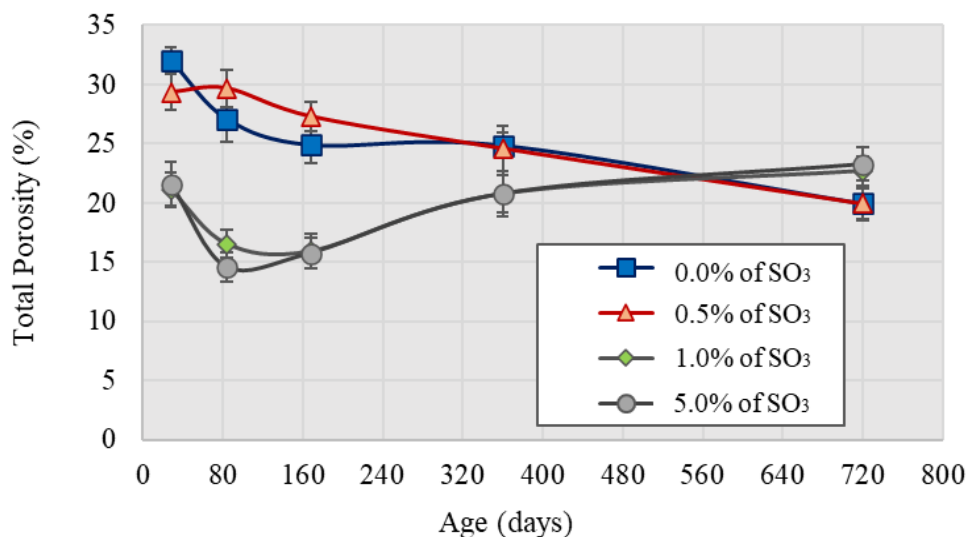


Figure 5. Total porosity monitoring for the series studied (0.0%, 0.5%, 1.0% and 5.0% SO₃).

For the 0.5% content, there was no interference in the apparent porosity of the cement paste. For the contents of 1.0% and 5.0%, there was a significant reduction in porosity up to the age of 168 days due to the formation of ettringite/gypsite. Although there are still empty spaces available at this age, the microstructure became subjected to internal stresses, which caused the cracking of the matrix and thereby progressively increased the porosity of cement pastes. For the 1.0% content, despite the progressive increase of the porosity since the age of 168 days, the compressive strength was not affected, and its decrease was observed only after 360 days. For the 5.0% content, the increase in porosity after 168 days caused a decrease in the compressive strength at the same age.

Thus, in the last analyzed age (720 days) there was inversion of the behavior of the parameter evaluated, since the series with 1.0% and 5.0% presented higher porosity. The series of higher contaminations (1.0% and 5.0% SO_3) had the highest porosities, indicating a possible fragility of the matrix. Yan et al. [43] observed a similar behavior in samples exposed to Na_2SO_4 solution (external sulfate attack). At initial ages (up to 180 days) samples exposed to 5% Na_2SO_4 solution presented smaller porosities than those exposed to the reference solution (confirmed by the crystallization of deteriorating products in the pores). At advanced ages (540 days), with the advance of the attack, the samples had larger porosities than the references.

Sun et al. [44] also demonstrated in their study that at an initial period, there is a decrease in the porosity of concretes exposed to sulfate solubilities. However, since the age of 20 days of exposure, they noticed an increase in porosity. The authors associate porosity reduction with the formation of ettringite and gypsum in concrete pores. In this work, the SEM and XRD tests were done to prove the products related to the initial increase in porosity.

Thus, according to the studies of Yan et al. [43], in the series of higher contamination (5%), porosity reduction up to 300 days should occur due to the formation of ettringite and gypsite crystals in the concrete pores. On the other hand, the porosity increase after this period must have occurred due to the appearance of microcracks caused by the complete filling of the pores and the generation of internal stresses. The SEM test with EDS was used in this work to prove this theory.

4.4. SEM and EDS

Comparable to what was observed in other studies, the SEM images indicated the presence of acicular crystals, similar to those of ettringite, for the contaminated cementitious pastes.

In their study, Ayora et al. [5] indicate the deposition of products such as gypsum or ettringite in the pores of concretes with advanced stage of alteration by the presence of sulfides. Campos et al. [45] used the SEM technique to verify the occurrence of the internal attack of sulfates in a dam in Spain. Once again, the presence of ettringite and gypsum is a indicative factor of the occurrence of the advanced stage attack.

In this work, an analysis of the evolution of pore filling was carried out, considering the different contamination levels. For this analysis, it was necessary to work with the same magnification for all series, 4kx, since the pores should have similar dimensions for comparative effect.

Figure 6A shows that at 360 days of age, the Ref. (0.0% SO_3) series still had free pores inside. The pore, approximately 40 μm in diameter, had no product deposited inside.

On the other hand, the 0.5% SO_3 group (Figure 6B) showed some acicular crystals with a shape like that of ettringite (indicated by the arrow) within the observed pore. However, there is a small amount of these, which would not justify a filling for the elevation of compressive strength at the early stages of the attack.

For the 1.0% SO_3 group, the pore found was approximately 20 μm , as observed in Figure 6C. However, it appeared with a much higher filling due to deposited acicular crystals (indicated by the arrow), evidence of the occurrence of generating reactions of the ettringite in the porous structure of this test series. The filling of the pore of the mentioned series corroborates with the results of addition of compressive strength and reduction of porosity at early ages, already discussed beforehand.

The pore analyzed for the 5.0% SO_3 series, Figure 6D, was the one that presented greater filling by more defined crystals of ettringite.

The EDS analysis of the point highlighted in Figure 6D (5.0% SO_3 series), presented in Table 4, confirms the presence of ettringite in the analyzed area. This can be confirmed because the elements found in the EDS have exceeded the theoretical percentages of the elements of the ettringite (remaining contents).

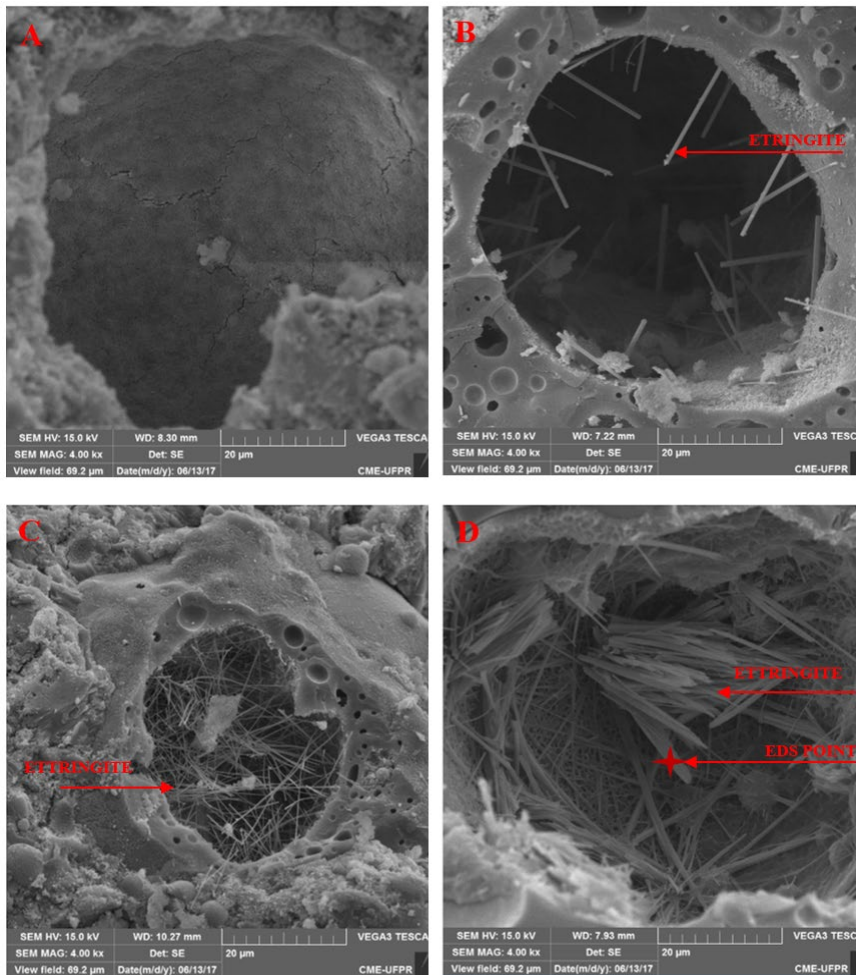


Figure 6. Comparative analysis of pore evolution for the series studied (A - 0.0%, B - 0.5%, C - 1.0% and D - 5.0% SO₃) at 360 days of age.

Table 4. Proportion of elements for EDS analysis of ettringite.

Elements	Theoretical percentage of ettringite elements	Percentages obtained in EDS	Adoption of the critical content (Al)	Remaining contents*
Ca	19.13%	23.30%	12.50%	10.80%
Al	4.30%	2.80%	2.80%	0.00%
S	7.67%	5.70%	5.00%	0.70%
O	63.74%	50.10%	41.50%	8.60%
H	5.14%	-	-	-

*Difference between the percentages obtained in the EDS and the adoption of the critical content

The comparative analysis between the four images shows that the higher the content of the contaminant used in the mixtures, the greater the matrices are compromised.

At 720 days of age, the presence of cracks (indicated by the arrow) near the pores was observed in the series of higher contamination (5.0% SO₃ – Figure 6B), indicating a possible fragility of the matrix due to the high contaminant content. In their study, Kazmi et al. [18] also showed the presence of cracks in samples contaminated by sulfate, justified by the stress caused by the generation of expansive products.

The continued presence of acicular crystals in the most contaminated series (Figure 7B) is indicative of the attack. Under normal conditions, as previously noted for the reference series, healthy cementitious compositions tend not to

present crystals of ettringite. This is because without a new source of sulfate, the primary ettringite becomes monosulfoaluminate (AFm) [46], having a different morphology and volume.

The images of Figure 6 shows that in initial stages up to one year of age, there is deposition of products in the pores of concretes contaminated by sulfides. These results confirm the one mentioned in the other tests: increase of compressive strength and drop in the porosity of the series with higher contamination (1.0% and 5.0% SO₃). However, at 720 days, in the case of this study, images with the appearance of cracks could already be observed for the series of greater contamination. The observed cracks are the consequence of tensions generated by the deleterious products, also confirmed by the decrease of resistance, and increase of the porosity in the 1.0% and 5.0% SO₃ series. In the reference series at that same age, the cracks noted in the 5.0% SO₃ series were not identified (Figure 7A).

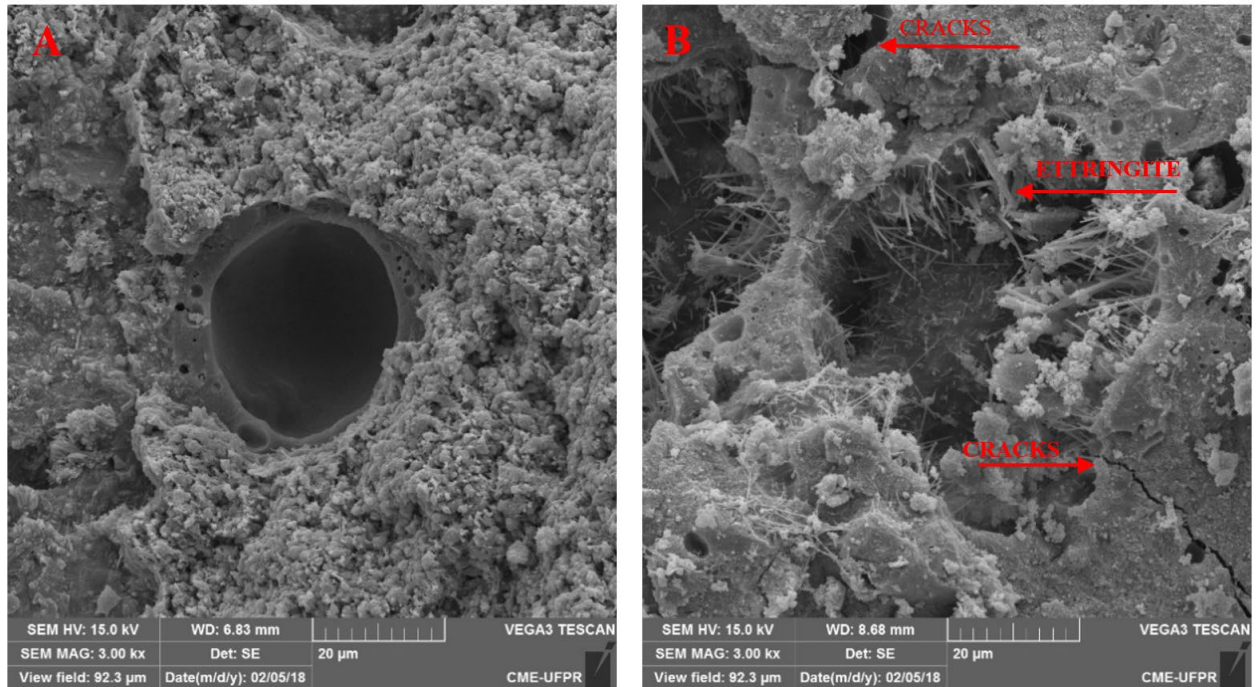


Figure 7. Images obtained at 720 days from reference and 5.0% SO₃ series. A – Reference series with pore free of products and without cracks. B – 5.0% SO₃ series with ettringite and cracks.

4.5. XRD

The XRD confirmed the higher presence of ettringite in the series of higher contamination (5.0% SO₃). The behavior of the reference series, the 0.5% and the 1.0% SO₃ were similar in terms of identified products and peak intensity. Figure 8 presents a comparative analysis between the reference sample (Ref. 0.0% SO₃) and the sample of higher contamination (5.0% SO₃) at 28 and 720 days of age. Figure 8A and B, both of Ref. (0.0% SO₃) shows that there was no difference in the intensity of the main ettringite peak (9.01°) when compared to both ages, with the intensities close to 1100 counts. The same did not occur with the 5.0% SO₃ series (Figure 8C and D), which since 28-days of age (Figure 8A versus Figure 8C) presented the greatest intensity when compared to the reference (1100 versus 1300), and showed an increase between the ages of 28 and 720 days (1300 versus 1400), indicating the formation of ettringite over time in that series.

The high concentration of ettringite in materials attacked by sulfates has also been confirmed in other studies, justifying the expansion tensions caused by the attack [17], [18], [42], [47].

According to Souza et al. [48], ettringite peaks with greater intensity were found in mortars exposed to sulfate-contaminated solutions (Na₂SO₄ and MgSO₄).

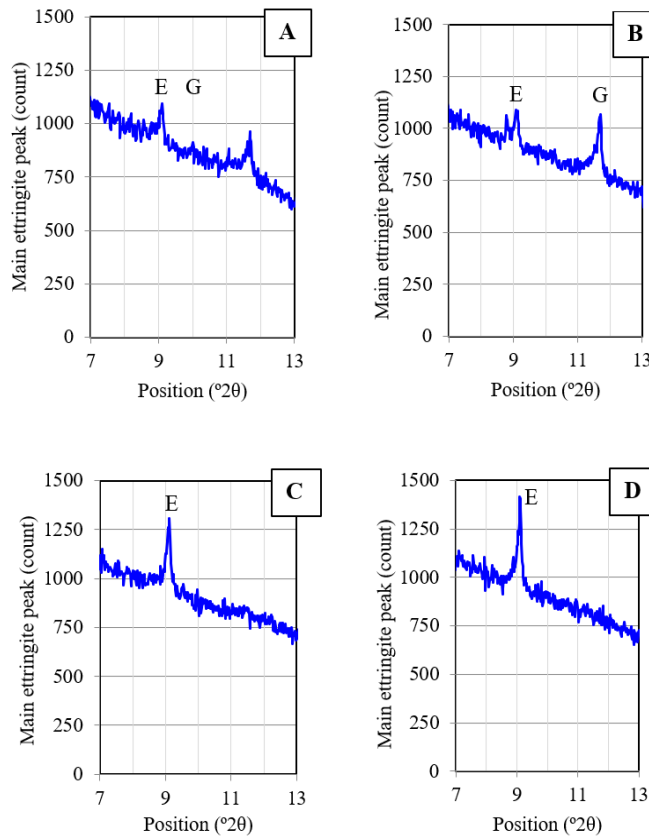


Figure 8. Comparative analysis of the main ettringite (E) peak in the diffractograms. A – Ref. (0.0% SO₃) at 28 days; B - Ref. (0.0% SO₃) at 720 days; C - (5.0% SO₃) at 28 days; D - (5.0% SO₃) at 720 days. (E – ettringite; G – Gypsum)

5 CONCLUSIONS

The different levels of contamination evaluated in this study allowed the comparative analysis of the properties of the cementitious pastes, indicating greater damages to the pastes with higher levels of contamination.

The development of the research described in this work has led to the following conclusions:

- At the initial ages of the compounds, up to 168 days, the contamination levels of 1.0% and 5.0% SO₃ were responsible for the increase of mechanical resistance and decrease of the porosity of the materials. This behavior is justified by the chemical reactions resulting from the presence of sulfates.
- At 720 days of age, the series with 5.0% SO₃ was the one with the lowest compressive strength, being approximately 13% lower than the reference series at the same age and 10% lower than its own strength at the previous age.
- All the contaminated series showed strength drop from 360 to 720 days, ranging from 5.4% for 0.5% SO₃, 9.5% for 1.0% SO₃ and 10.2% for 5.0% SO₃. The reduction in mechanical properties proves the importance in defining a maximum contamination content to be accepted.
- The porosity test showed a change in its tendency at 168 days of age. Before, the series of higher contamination (1.0% and 5.0% SO₃) had the smallest porosities, whereas after that age they had the largest porosities. The higher porosity for these series at the end of the study indicates the fragility in the matrix due to the presence of sulfate, alerting to the levels used in concrete structures.
- The SEM images indicated a larger filling of the pores for the higher contamination contents, confirming the occurrence of the attack and consequent formation of ettringite. In the images, the degree of damage of the sample of 1.0% and 5.0% SO₃ is evident. The appearance of cracks, evidenced in the SEM, indicates the fragility of the materials and contributes to the results of increased porosity and compressive strength drop;
- The XRD analysis showed a higher presence of ettringite in the series of higher contamination (5.0% SO₃) at 28 days of age. Comparing the age of 28 days to the age of 720 days, an increase in the main peak of ettringite was noticed;

- The results obtained in this study show the need for standardization of the levels of maximum sulfide contamination allowed for aggregates to be used in concrete structures. The contamination of 5.0% SO₃ showed the worst results in terms of strength, porosity and matrix damage. However, behavioral changes were also noticed for the series of 0.5% and 1.0% SO₃, levels currently allowed by standards. The use of aggregates with 1.0% of contamination can be complicated, since the presented results were similar to those of the 5.0% SO₃ series.

ACKNOWLEDGEMENTS

The authors thank the Araucária Foundation for the support and scholarships. Thanks are also given for the availability of the infrastructure and human resources made available by the Federal University of Paraná (PPGECC/UFPR-Brazil). Our gratitude also goes to the Center of Electron Microscopy of UFPR (CME/UFPR) for the support during the SEM tests.

REFERENCES

- [1] J. Duchesne and B. Fournier, "Deterioration of concrete by the oxidation of sulphide minerals in the aggregate," *J. Civ. Eng. Archit.*, vol. 7, no. 8, pp. 922–931, 2013.
- [2] A. Campos, C. M. López, and A. Aguado, "Diffusion-reaction model for the internal sulfate attack in concrete," *Constr. Build. Mater.*, vol. 102, pp. 531–540, 2016.
- [3] M. D. A. Thomas, R. J. Kettle, and J. A. Morton, "Expansion of Cement-Stabilized Minestone due to the Oxidation of Pyrite," *Geotech. Eng. Transp. Res. Rec.*, vol. 1219, pp. 113–120, 1989.
- [4] I. Casanova, L. Agulló, and A. Aguado, "Aggregate expansivity due to sulfide oxidation – I. reaction system and rate model," *Cement Concr. Res.*, vol. 26, pp. 993–998, 1996.
- [5] C. Ayora, S. Chinchón, A. Aguado, and F. Guirado, "Weathering of iron sulfides and concrete alteration: thermodynamic model and observation in dams from Central Pyrenees, Spain," *Cement Concr. Res.*, vol. 28, pp. 1223–1235, 1998.
- [6] T. Ikumi, I. Segura, and S. H. P. Cavalaro, "Influence of early sulfate exposure on the pore network development of mortars," *Constr. Build. Mater.*, vol. 143, pp. 33–47, 2017.
- [7] T. Schmidt, A. Leemann, E. Galluci, and K. Scrivener, "Physical and microstructural aspects of iron sulfide degradation in concrete," *Cement Concr. Res.*, vol. 41, pp. 263–269, 2011.
- [8] N. P. Hasparyk, F. C. Muniz, M. A. S. Andrade, M. J. Gomides, R. M. Bittencourt, and H. Carasek, "A deterioração de estruturas de concreto contendo agregados com sulfetos," in *Sim. EPUSP Estrut. Concr.*, 2003.
- [9] American Concrete Institute, *Guide to Durable Concrete*, ACI 201, 1991.
- [10] Association Française De Normalisation, *Granulats – Définitions, Conformité, Spécifications*, XP P18-540, 1997.
- [11] Associação Brasileira de Normas Técnicas, *Aggregates for Concrete – Specification*, NBR 7211, 2009.
- [12] A. L. C. Lima, "Influência da presença de sulfetos na implantação da UHE Irapé – Vale do Jequetinhonha – Minas Gerais," M.S. thesis, Univ. Fed. Ouro Preto, 2009.
- [13] I. Oliveira, S. H. P. Cavalaro, and A. Aguado, "New kinetic model to quantify the internal sulfate attack in concrete," *Cement Concr. Res.*, vol. 43, pp. 95–104, 2013.
- [14] M. A. Czerewko and J. C. Cripps, *Sources of Sulfur Species. Identification and Quantification. Thauasite and Other Forms of Concrete Deterioration and Protection*. Halifax Hall: University of Sheffield, 1999.
- [15] A. Tagnit-Hamou, M. Saric-Coric, and P. Rivard, "Internal deterioration of concrete by the oxidation of pyrrhotite aggregates," *Cement Concr. Res.*, vol. 35, pp. 99–107, 2005.
- [16] H. Goto et al., "Physicochemical evaluation of oxidation of diabase aggregates with sulfide minerals: influence of particle size, pH of the medium and pyrite concentration," *J. Build. Pathol. Rehabil.*, vol. 1, pp. 1–10, 2016.
- [17] C. Colman, D. Bulteel, V. Thiery, S. Rémond, F. Michel, and L. Courard, "Internal sulfate attack in mortars containing contaminated fine recycled concrete aggregates," *Constr. Build. Mater.*, vol. 272, pp. 121851, 2021.
- [18] S. M. Kazmi, M. J. Munir, Y. F. Wu, I. Patnaikuni, Y. Zhou, and F. Xing, "Effect of diferente aggregate tratment techniques on the freeze-thaw and sulfate resistance of recycled aggregate concrete," *Cold Reg. Sci. Technol.*, vol. 178, pp. 103126, 2020.
- [19] F. Xie, J. Li, G. Zhao, P. Zhou, and H. Zheng, "Experimental study on performance of cast-in-situ recycled aggregate concrete under different sulfate attack exposures," *Constr. Build. Mater.*, vol. 253, pp. 119144, 2020.
- [20] Y. Chen, P. Liu, and Z. Yu, "Study on degradation of macro performances and micro structure of concrete attacked by sulfate under artificial simulated environment," *Constr. Build. Mater.*, vol. 260, pp. 119951, 2020.
- [21] A. P. B. Capraro, G. Macioski, and M. H. F. Medeiros, "Effect of aggregate contamination with pyrite on reinforcement corrosion in concrete," *Eng. Fail. Anal.*, vol. 23, pp. 105116, 2020.

- [22] Associação Brasileira de Normas Técnicas, *High Early Strength Portland Cement – Specification*, NBR 5733, 1991.
- [23] American Society for Testing and Materials, *Standard Specification for Portland Cement*, ASTM C150, 2018.
- [24] American Society for Testing and Materials, *Standard Specification for Coal Fly Ash and Raw or Calcined Natural Pozzolan For use in Concrete*, ASTM C618, 2017.
- [25] Associação Brasileira de Normas Técnicas, *Pozzolanic Portland Cement – Specification*, NBR 5736, 1999.
- [26] American Society for Testing and Materials, *Standard Test Method for Density of Hydraulic Cement*, ASTM C188, 2017.
- [27] American Society for Testing and Materials, *Standard Test Method for Relative Density and Absorption of Fine Aggregate*, ASTM C128, 2015.
- [28] Associação Brasileira de Normas Técnicas, *Mortars Applied on Walls and Ceilings – Determination of the Consistence Index*, NBR 13276, 2016.
- [29] J. Gao, Z. Yu, L. Song, T. Wang, and S. Wei, "Durability of concrete exposed to sulfate attack under flexural loading and drying-wetting cycles," *Constr. Build. Mater.*, vol. 39, pp. 33–38, 2013.
- [30] J. Gong, J. Cao, and Y. Wang, "Effects of sulfate attack and dry-wet circulation on creep of fly-ash slag concrete," *Constr. Build. Mater.*, vol. 125, pp. 12–20, 2016.
- [31] L. Jinag and D. Niu, "Study of deterioration of concrete exposed to different types of sulfate solutions under drying-wetting cycles," *Constr. Build. Mater.*, vol. 117, pp. 88–98, 2016.
- [32] American Society for Testing and Materials, *Standard Test Method for Pulse Velocity Through Concrete*, ASTM C597, 2016.
- [33] Associação Brasileira de Normas Técnicas, *Mortars Applied on Walls and Ceilings – Determination of the Flexural and the Compressive Strength in the Hardened Stage*, NBR 13279, 2005.
- [34] Z. Pan, L. Cheng, Y. Lu, and N. Yang, "Hydration products of alkali-activated slag-red mud cementitious material," *Cement Concr. Res.*, vol. 32, pp. 357–362, 2002.
- [35] J. Hoppe Fo., C. S. Rodrigues, L. S. O. P. Ribeiro, and M. H. F. Medeiros, "Evaluation of sample drying methods to determine the apparent porosity and estimation of degree of hydration of portland cement pastes," *J. Bulding Pathol. Rehabil.*, vol. 6, pp. 1–11, 2021.
- [36] F. Montes, S. Valavala, and L. M. Haselbach, "A new test method for porosity measurements of Portland Cement Pervious Concrete," *J. ASTM Int.*, vol. 2, pp. 1–13, 2005.
- [37] J. P. Godinho, T. F. Souza Jr., M. H. F. Medeiros, and M. S. A. Silva, "Factors influencing ultrasonic pulse velocity in concrete," *Rev. IBRACON Estrut. Mater.*, vol. 13, pp. 235–247, 2020.
- [38] I. Biczók, *Concrete Corrosion and Concrete Protection*. New York: Chemical Publishing Company, 1972.
- [39] W. Ouyang, J. Chen, and M. Jiang, "Evolution of surface hardness of concrete under sulfate attack," *Constr. Build. Mater.*, vol. 53, pp. 419–424, 2014.
- [40] A. Araujo, *Corrosion Study in Concrete Structures*. Rio de Janeiro: Inst. Technol. Res., 2013.
- [41] Q. H. Xiao, Z. Y. Cao, X. Guan, Q. Li, and X. L. Liu, "Damage to recycled concrete with diferente aggregate substitution rates from the coupled action of freeze-thaw cycles and sulfate attack," *Constr. Build. Mater.*, vol. 221, pp. 74–83, 2019.
- [42] D. Zou, S. Qin, T. Liu, and A. Jivkov, "Experimental and numerical study of the effects of solution concentration and temperature on concrete under external sulfate attack," *Cement Concr. Res.*, vol. 139, 106284, 2021.
- [43] X. Yan, L. Jiang, M. Guo, Y. Chen, Z. Song, and R. Bian, "Evaluation of sulfate resistance of slag contained concrete steam curing," *Constr. Build. Mater.*, vol. 195, pp. 231–237, 2019.
- [44] S. Sun, K. Wu, H. Shi, L. Zhang, and L. Zhang, "Effect of interfacial transition zone on the transport of sulfate ions in concrete," *Constr. Build. Mater.*, vol. 192, pp. 28–37, 2018.
- [45] A. Campos, C. M. López, A. Blanco, and A. Aguado, "Effects of an internal sulfate attack and an alkali-aggregate reaction in a concrete dam," *Constr. Build. Mater.*, vol. 166, pp. 668–683, 2018.
- [46] X. Wang, Z. Pan, X. Shen, and W. Liu, "Stability and decomposition mechanism of ettringite in presence of ammonium sulfate solution," *Constr. Build. Mater.*, vol. 124, pp. 786–793, 2016.
- [47] Y. Tian et al., "Internal transport and corrosion behaviors of sulfate corrosion media carried by recycled aggregate in concrete," *Constr. Build. Mater.*, vol. 260, 120480, 2020.
- [48] D. J. Souza, A. H. F. Medeiros, and J. Hoppe Fo., "Evaluation of external sulfate attack (Na₂SO₄ and MgSO₄): Portland cement mortars containing siliceous supplementary cementitious materials," *Rev. IBRACON Estrut. Mater.*, vol. 13, no. 4, e13403, 2020.

Author contributions: CAPB: conducting tests, formal analyzing, methodology, writing the article; HFJ: formal analyzing, review of article writing; MMHF: formal analyzing, methodology, review of article writing.

Editors: Mark Alexander, Guilherme Aris Parsekian.



ORIGINAL ARTICLE

Analysis of structural masonry buildings taking into account the construction sequence loads and soil-structure interaction

Análise de edifícios de alvenaria estrutural considerando a sequência construtiva e a interação solo-estrutura

Anna Christinna Secundo Lopes^a

Joel Araújo do Nascimento Neto^a

Rodrigo Barros^a

^aUniversidade Federal do Rio Grande do Norte – UFRN, Programa de Pós-graduação em Engenharia Civil, Natal, RN, Brasil

Received 26 October 2020

Accepted 03 March 2021

Abstract: The present study assesses conventionally used design standards, analyzing the effects caused by the construction loads, that is, a gradual increase in load and stiffness during construction, and soil-structure interaction (SSI), with soil represented by linear springs, in a structural masonry building over a support structure of reinforced concrete. The equivalent frame model, developed by Nascimento Neto, was used to simulate the support structure and the first masonry floor, and a specific three-dimensional frame model to simulate the other floors. Four analysis models were applied to assess stress distribution at the base of the walls, and the stresses and displacements of the support structure. The results show that introducing SSI and the construction loads causes relief or the possible need to reinforce elements designed in Ultimate Limit State (ULS) and Serviceability Limit State (SLS), as well as uniform settlement.

Keywords: structural masonry, reinforced concrete support structure, soil-structure interaction, construction sequence loads.

Resumo: O presente estudo realiza uma avaliação crítica de critérios de projeto convencionalmente utilizados, consistindo em uma análise dos efeitos causados pela sequência construtiva, ou seja, incremento gradativo de carregamento e rigidez dos elementos com a evolução da construção, e pela interação solo-estrutura (ISE), representando o solo por molas lineares, em um edifício de alvenaria estrutural sobre estrutura de transição em concreto armado. Foi utilizado o modelo de barras equivalentes, desenvolvido por Nascimento Neto, para discretização da estrutura de transição e do primeiro pavimento em alvenaria, e o modelo de pórtico tridimensional específico para discretização dos demais pavimentos. Mediante quatro modelos de análises, foram avaliadas as distribuições das tensões na base das paredes, e os esforços e deslocamentos da estrutura de transição. Os resultados evidenciam que a introdução da ISE e do efeito construtivo provocam alívio ou possível necessidade de reforço em elementos dimensionados no Estado Limite Último (ELU) e no Estado Limite de Serviço (ELS), assim como uniformização de recalques.

Palavras-chave: alvenaria estrutural, estrutura de transição em concreto armado, interação solo-estrutura, efeito construtivo.

How to cite: A. C. S. Lopes, J. A. Nascimento Neto, and R. Barros, “Analysis of structural masonry buildings taking into account the construction sequence loads and soil-structure interaction,” *Rev. IBRACON Estrut. Mater.*, vol. 14, no. 6, e14607, 2021, <https://doi.org/10.1590/S1983-41952021000600007>

1 INTRODUCTION

The use of structural masonry buildings has been increasing due to the proven optimization of materials and labor, thereby reducing costs. For this reason, tall buildings have been constructed with structural masonry in some regions

Corresponding author: Anna Christinna Secundo Lopes. E-mail: annasecundolopes@gmail.com

Financial support: The author gratefully acknowledges the support of the Civil Engineering Graduate Program of the Federal University of Rio Grande do Norte. This paper was financed in part by the Coordenação de Aperfeiçoamento de Pessoal de Nível superior (CAPES) - Financing Code 001.

Conflict of interest: Nothing to declare.



This is an Open Access article distributed under the terms of the Creative Commons Attribution License, which permits unrestricted use, distribution, and reproduction in any medium, provided the original work is properly cited.

of Brazil. However, simultaneously to this development, there is a need to improve research and technologies and increase the use of structural masonry to the levels of reinforced concrete.

The most widely used methods, which are conservative and out-of-date, do not fully exploit the potential of masonry. From the standpoint of analytical research, the interaction between structural masonry walls and reinforced concrete support structures – whether in first floors or foundations – deserves mention, since the arch effect may lead to incorrect design when incorrectly interpreted or overly large cross sections properties of concrete structural elements when ignored.

Item 11.5 of Brazilian Standard Code NBR 16055 [1] makes it mandatory to analyze soil-structure interaction (SSI) in buildings constructed with concrete walls and more than five floors high. In the case of Brazilian standard NBR 16868-1 [2], concerning structural masonry buildings, there is no mention of the need to incorporate soil-structure interaction in analyses, but recent studies, such as those by Testoni [3] and Santos [4], report that soil interaction provokes significantly changes in the stress flow in walls, thereby producing more realistic results.

In addition to the effects of SSI, it is important to underscore that the structure may be submitted to considerably different stress levels from those of conventional analysis, which considers the instantaneous action of total loading in the structure. Structural analysis considering the construction effects, and, as such, closer to reality, is relevant in the study of stress distribution in walls, and to evaluate the shear forces and bending moments in support structures and SSI effects.

Thus, the present study arises from the need for further research on structural masonry, to assess the consequences of soil-structure interaction, considering the progressive effects of construction.

Given the aspects described, the primary aim was to investigate the effects caused by the deformability of support structures and analyze the progressive sequence and increased stiffness associated with the construction stages of buildings. This research, therefore, hopes to contribute with a critical assessment of the conventional analysis method, which considers the hypothesis of total load acting instantaneously and fully-fixed foundation supports.

2 THEORETICAL FRAMEWORK

2.1 Interaction of wall-beam systems

According to Barbosa [5], a structural masonry wall can be supported by continuous strip footings, or by discontinuous arrangement conditions associated to the columns position in a frame structure or to pile foundation. In the first case, vertical loads are distributed nearly uniformly at the base of the wall, while in the second, the loads tend to be directed towards the supports, since they are the stiffest regions, raising the stress concentration in these areas. This phenomenon is designated wall-beam system or the so-called arch effect, as illustrated in Figure 1, which changes stress distribution at the base of the wall and shear forces and bending moments on the support beam.

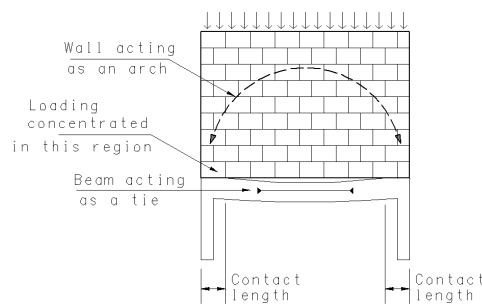


Figure 1. Continuous action of the wall-beam system. Adapted from Barbosa [5].

Normal vertical tensile stress may occur at the wall-beam interface, which can cause the two elements to separate when maximum joint tensile strength is reached. The possible loss of contact intensifies the load transfer to the supports, as reported by Barbosa [5]. Transferring loads to the supports concentrates vertical compression and horizontal shear stress at the base of the wall.

2.2 Computational modeling

Computational modeling based on the finite element method (FEM) is currently used in studies on support structures. A new computational model able to consistently simulate wall-beam interaction was developed by Nascimento et al. [6], corresponding to a set of vertical and horizontal bars denominated equivalent frame model (EqFM). The authors established the efficiency of the model by comparing their results with those obtained by shell finite element modeling.

Medeiros [7] confirmed the new equivalent frame model by studying different generic walls, comparing the results with the Rosenhaupt experimental model, and the three-dimensional frame modeling of a number of walls of a real building design. The results showed the efficiency of the modeling proposed, which consisted of wall discretization by a set of vertical and horizontal bars spaced 15 cm and 20 cm apart, respectively (Figure 2). This disposition of the bars was selected after a consistent mesh study comparing the results with those obtained by similar discretization in shell finite elements. Due to the orthotropic nature of structural masonry, especially when using hollow concrete blocks, it is recommended that longitudinal and transverse elasticity modulus be adopted for horizontal bars with half the value used for vertical bars, as reported by Parsekian et al. [8]. An exception for this assumption is the section of horizontal bars with grouting, usually related to lintel blocks. In relation to the connection between the EqFM and support beams, it is necessary to adopt bars with pinned end in the connection to the beam.

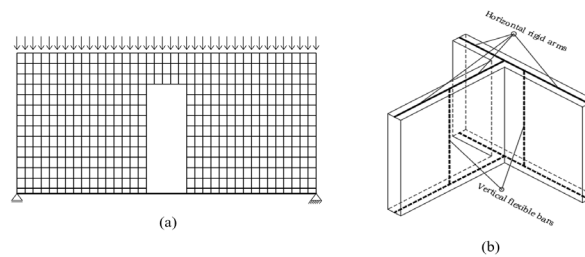


Figure 2. Numerical modeling: (a) Equivalent frame model (EqFM); (b) Three-dimensional frame model (TFM).

Lopes [9] made adjustments in the model ratified by Medeiros [7], including fitting the areas and stiffnesses established for the bars. The author assessed different models that considered the properties of the bars in terms of gross and net sections, concluding that adopting gross sections with elastic properties produces satisfactory results. Thus, it is reasonable to adopt the elastic properties of masonry grouted to the section of the masonry that contains vertical grouting, and the elastic properties of ungrouted masonry to the section without grouting, both with respect to the gross area of the bar section.

Nascimento [10] used the three-dimensional frame model (Figure 2b) to study the effects of shear strain and global torsion of building on shear walls of structural masonry buildings subjected to wind loads. The model consisted of shear walls discretized by three-dimensional frame elements, which had six degrees of freedom at each end. These frames exhibited the same geometric properties as the respective walls that they represented, and was positioned at the center of gravity of the rectangular section of the wall. The walls that intercept one another were connected by rigid horizontal bars (rigid arms), the ends being common to the two adjacent walls. The ends of the flexible vertical bars were continuously connected to the rigid horizontal counterparts, which, in turn, were arranged at the level of the floors. Their purpose was to simulate the effect of the length of the walls and the interaction between them. The length and number of rigid arms in the modeling depends on the intersections between these walls and the inclusion or not of lintels. Slab modeling was designed as a rigid diaphragm in its plane, in order to simulate displacement at the floor level. These displacements were associated with the two independent translation movements in the plane of the floor and rotation around the normal axis to this plane.

The two aforementioned models were used simultaneously in the analyses conducted, whose details are described in the following items.

2.3 Soil-structure interaction

In general, building design consider the simplified hypothesis in which foundations are joined to the built structure through fixed supports. Modeling best fit the physical reality, considering soil deformability, which is denominated soil-structure interaction (SSI). Several studies have demonstrated that adopting elastic supports (deformable soil

hypothesis) using SSI leads to stresses different from those calculated considering a foundation over fixed supports (rigid soil hypothesis), according to Gusmão and Gusmão [11], Prado [12] and Testoni [3].

Dutta and Roy [13] provided an extensive review of literature to gather the possible alternative models available for SSI, with emphasis to the physical modeling of the soil media. According to authors, studies seeking model to represent soil behavior result in two classical models: Winkler's model and continuous model. Winkler's model is the oldest and the simplest one and can be defined as a set of linear, discrete, independent, closely spaced springs, in which the deformation of foundation due to applied load is confined to loaded regions only. As the formulation of this model depends only the linear spring stiffness, it is classified as one parameter discrete model. Over the years some researchers developed studies to improve the Winkler's model, such as Filonenko-Borodich [14], Hetenyi [15], Pasternak [16], Kerr [17], Horvath [18] and Kurian and Manojkumar [19]. All these studies were developed with the main objective to consider continuity among springs, extending the deformation of foundation beyond the regions of applied loads.

For deep foundations, the use of discrete models indicates that the response of the soil at a certain point does not depend on pile displacement at different points. Thus, soil response consists of independent discrete mechanisms, which does not perfectly characterize the continuous method. When simulating soil with a discrete spring model, the corresponding stiffness is represented by the coefficient of vertical reaction k_v , defined by Terzaghi [20] as the ratio between pressure acting on the contact surface and vertical displacement due to the applied load. This coefficient can be obtained by plate tests, typical values in correlation to SPT tests, and correlations to settlement and foundation geometry. When deep foundations are subjected to horizontal actions, the Winkler model approach is non-linear elastic. Hence the use of p-y curves is an excellent alternative to represent this behaviour. The geotechnical parameter that feeds the model is the coefficient of horizontal reaction k_h , which can be obtained by a load test on the pile in a natural scale, plate tests developed by Terzaghi [20] in 1955, or through empirical correlations with other soil properties. According to Araújo [21], concerning piles subjected to horizontal forces numerous studies have been made, such as: Matlock and Reese [22], Broms [23], Alizadeh and Davisson [24], Poulos [25], Cintra [26], Miguel [27], Del Pino [28], Fan and Long [29]; and Zammataro [30].

The coefficient of horizontal reaction of the soil (k_h) is also interpreted as a pile-soil horizontal contact stiffness. According to Terzaghi [20] this coefficient is calculated by dividing the stress (p_r) by the corresponding horizontal displacement (y), Equation 1. A more comprehensive explanation for the coefficient of horizontal reaction of the soil is based on distributed load (p) over the pile length instead of horizontal normal stress (p_r). This consideration establishes the definition of the modulus of horizontal reaction of the soil (K). The K value is calculated by dividing the soil reaction, or distributed load over the pile length, by the horizontal displacement (y), Equation 2. Considering that p is calculated multiplying p_r by the pile diameter (B), the Equation 3 is obtained, which expresses the correlation between the coefficient of horizontal reaction and the modulus of horizontal reaction of the soil.

$$k_h = \frac{p_r}{y} \quad (1)$$

$$K = \frac{p}{y} \quad (2)$$

$$K = k_h \cdot B \quad (3)$$

The determination of K value is too complex due to its variation with depth, and due to the difficulty to obtain an experimental value. For most of the researchers, the K value is constant for pre-consolidated clay and obeys a linear function for sand, according to Cintra [26]. Hence, Equation 4 expresses the K values for sand, in which n_h denotes the constant of horizontal reaction of the soil, and Z denotes the depth.

$$K = n_h \cdot Z \quad (4)$$

The n_h values obtained using Araújo's [21] load test results were used in this research. Lopes [31] describes in detail and indicates all the parameters used in this research to calculate the coefficients k_h and n_h .

2.4 Construction sequence loads

Analysis of structures conventionally considers the final effect of loads and concrete with reference age for the specified f_{ck} (concrete characteristic compressive strength). However, analyses considering the construction stages, that is, the evolution of shoring and corresponding age of the concrete, tend to produce different results. In addition, the removal of shoring and consequent load applied to early-age elements demonstrates the importance of verifying not only the Ultimate Limit State (ULS), but also the Serviceability Limit States (SLS), which can be considerably influenced by early-age cracking and deformation of elements.

Santos [4] used DIANA® software to confirm Prado’s results [12]. The author found that the vertical reactions in columns tend to be smaller in sequential analysis, while in relation to the normal stresses on masonry, analysis of the construction effect showed a significant influence only on the first floor.

According to Gusmão and Gusmão [11], during the construction process, the increase in structure stiffness as the floors are being built produces a trend to settlement uniformization.

The variation in the mechanical properties of concrete with age is prescribed in NBR 6118 [32], according to the evolution of compression strength, up to 28 days. With respect to masonry, unlike concrete structures, the variation in mechanical properties with age can be disregarded, depending on the analysis. Parsekian and Franco [33] conducted three-block prism tests for various ages with concrete and ceramic blocks, and found that for ages up to three days, prisms exhibit nearly characteristic compressive strength. It is important to underscore that this trend is associated with the use of fabricated structural blocks more than 28 days old. Thus, resistance values as a function of the variation in age are influenced only by mortar, which, in turn, if adequately specified, may not significantly influence prism behavior.

3 MODELS ADOPTED IN ANALYSES

All the computational models were developed with the SAP2000 structural analysis program, version 14.0.0. The first masonry floor and the support structure in reinforced concrete were discretized using the previously described equivalent frame model (EqFM). The other floors of the building were discretized with the three-dimensional-frame model. This procedure was adopted to reduce the computational effort and model processing time, given that the EqFM, exhibited far more unknowns than the three-dimensional frame model.

For the EqFM adopted for the first floor, the optimal mesh proposed by Medeiros [7] was used, as previously described. Discretization consisted of arranging the vertical and horizontal bars spaced 15 and 20 cm apart, with cross-sections measuring $(14 \times 15) \text{ cm}^2$ and $(14 \times 20) \text{ cm}^2$, respectively. All the masonry walls had 14 courses (2.80m) consisting of M15 modulation blocks $(14 \times 29 \times 19) \text{ cm}^3$ containing bonding beams at the upper course, lintels and sills. For support structure beams, 15 cm-long bar elements were used for each stretch, as well as the cross-section depth indicated in the original structural design. The first floor is 3.2 m high, which was therefore the height of the support structure columns. The first and second floors were connected using the same rigid bar of the three-dimensional frame model. This rigid bar was connected to the last course of the EqFM by additional vertical bars pinned at the base, as illustrated in Figure 3.

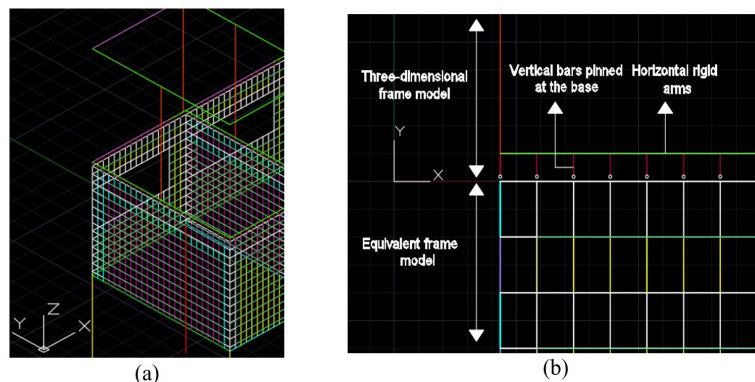


Figure 3. Connection between the equivalent frame and three-dimensional frame model: (a) General overview of first, second and third floors; (b) Connection details.

For concrete support structure and first floor of the structural masonry, the longitudinal and transverse elasticity modulus of concrete and masonry were determined based on Brazilian Standard Codes NBR 6118 [32]

and NBR 16868-1 [2], for a concrete with $f_{ck} = 25$ MPa and concrete blocks with $f_{bk} = 22$ MPa. Moreover, a relationship between characteristic compressive strength of the prism and block (f_{pk}/f_{bk}) of 65% and a relationship between the resistance of the grouted and hollow prisms of 1.85 were adopted. The Brazilian Standard Code for masonry structures NBR 16868-1 [2] establishes the calculation of the longitudinal elasticity modulus, via the following equations:

$$E_{masonry} = 800 \cdot f_{pk} \text{ (for } f_{bk} \leq 16 \text{ MPa)} \tag{5}$$

$$E_{masonry} = 650 \cdot f_{pk} \text{ (for } f_{bk} > 16 \text{ MPa)} \tag{6}$$

When following the NBR 6118 [32], item 15.7.3, for non-linear analysis of global second order effects, the approximate physical non-linearity caused by cracking must be considered, to reduce structural element stiffness according to Equation 3 for beams and Equation 4 for columns and shear-walls:

$$(E \cdot I)_{sec} = 0,4 \cdot E_{ci} \cdot I_c \text{ (for } A'_s \neq A_s) \tag{7}$$

$$(E \cdot I)_{sec} = 0,8 \cdot E_{ci} \cdot I_c \text{ (for } A'_s = A_s) \tag{8}$$

Where: E_{ci} denotes the tangent/initial elasticity longitudinal modulus of concrete; I_c denotes the cross-section moment of inertia; A'_s denotes the cross-section reinforcement acting in compression; and A_s denotes the cross-section reinforcement acting in tension.

Table 1 summarizes the material properties for the reinforced concrete support structure and the first masonry floor.

Table 1. Properties of the materials: equivalent frame model.

Material	Specific weight (kN/m ³)	Elasticity Modulus (MPa)	
		Longitudinal	Transverse
Concrete (beams)	25	9660	4025
Concrete (columns)	25	19320	8050
Non-grouted masonry	14	9295	4648
Grouted masonry	22	17196	8598

For the other masonry floors, discretized with the three-dimensional frame model described by Nascimento [10], the longitudinal elasticity modulus followed the evolution of f_{pk} values for each floor in establishing the flexible bars properties, as presented in Table 2. In the case of lintels, the same properties as grouted masonry from the 1st floor were attributed.

Table 2. Longitudinal modulus of elasticity of flexible bars per floor.

Floor	f_{pk} (MPa)	Modulus of elasticity E_m (MPa)	Floor	f_{pk} (MPa)	Modulus of elasticity E_m (MPa)
1	14.3	7436	11	9.1	5824
2	14.3	7436	12	9.1	5824
3	14.3	7436	13	7.5	4800
4	13.0	6760	14	7.5	4800
5	13.0	6760	15	8.0	5120
6	13.0	6760	16	8.0	5120
7	11.7	6084	17	6.4	4096
8	11.7	6084	18	6.4	4096
9	10.4	6656	19	4.8	3072
10	10.4	6656	20	4.8	3072

A value of $n_h = 37.2 \text{ MN/m}^3$ was applied for the averaged continuous helix pile ($\text{CHP}_{\text{Averaged}}$) related to displacement of 9 mm, since it was the average value of the respective soil. Moreover, the fit proposed by Araújo [21] for Décourt's [37] equation was used, obtaining a new constant for the local soil. Araújo [21] explains in detail the initial value of n_h and the Equation 10.

$$(n_h)_{\text{Décourt}[37]} = 1,6 \cdot N_{\text{SPT}} \tag{9}$$

$$(n_h)_{\text{Araújo}[21]} = 2,65 \cdot N_{\text{SPT}} \tag{10}$$

In preliminary studies with planar models, Lopes [31] obtained low values for the settlements. The author also identified that the usual iterative procedure to update the coefficients of vertical reaction, and stiffnesses of the springs, didn't produce a large variation in these values. Structural masonry buildings usually exhibit greater stiffness than concrete buildings, which can justify this tendency for ISS. Hence, the tridimensional modeling for SSI uses the initial stiffnesses of the springs only.

Table 4 shows the coefficients of horizontal reaction, calculated for piles (10 m long and 60 cm in diameter) designed to support a axial force in columns between 1500 kN and 2100 kN. The value of the modulus of horizontal reaction (K) was obtained by multiplying the value of n_h by depth z ; then dividing by the pile diameter was obtained the coefficient of horizontal reaction (k_h); and finally, multiplying by the contact area was obtained the spring stiffness (k_{spring}). The contact area was obtained by multiplying the diameter of the foundation by the 1 m length of influence.

Table 4. Coefficients of horizontal reaction of the soil.

Load range (kN)	Layer	NSPT	Depth z (m)	n_h (kN/m ³)	K (kN/m ²)	Diameter (m)	k_h (kN/m ³)	Contact area (m ²)	k_{spring} (kN/m)
1500 - 2100	Top	-	-	37200	37200	0.6	62000	0.6	37200
	1	4	1	10600	10600		17666.67		10600
	2	9	2	23850	47700		79500		47700
	3	5	3	13250	39750		66250		39750
	4	9	4	23850	95400		159000		95400
	5	12	5	31800	159000		265000		159000
	6	24	6	63600	381600		636000		381600
	7	19	7	50350	352450		587416.67		352450
	8	14	8	37100	296800		494666.67		296800
	9	12	9	31800	286200		477000		286200
10	15	10	39750	397500	662500	397500			

The design of the continuous helix-type foundation piles was based on the support reactions obtained by the classical reference model (rigid supports and instantaneous loads). To that end, the normal forces on the columns, and consequent foundation loads, were placed within a range of values to reduce the variation in pile design. Therefore, the geometry of piles, and the corresponding coefficients of vertical and horizontal reactions, were obtained. From these coefficients, the stiffnesses of the corresponding springs were calculated. The ranges for the values of normal forces on columns were specified as follows: 1500kN up to 2100kN; 2500kN up to 3100kN; 4500kN up to 5800kN; and 17900kN as the total axial force for a specific pile cap with seven columns, as shown in Figure 6b. Table 3 and Table 4 show the results for the first range only.

After the stiffness values were calculated, the linear springs were introduced into their respective nodes via the corresponding coefficients in the kN/m unit. Using 1 m soil layers, the horizontal springs were considered from the top of the pile, with vertical springs arranged in the middle of each layer, as shown in Figure 4.

The Aoki-Velloso [36] method was considered to calculate load-bearing capacity, the Cintra and Aoki [35] method to calculate settlements, and the Blévoit and Frémy [38] method to determine pile cap geometry. It is important to underscore that the scope of the study is restricted to structural analysis and, as such, the design of these elements was not investigated in depth.

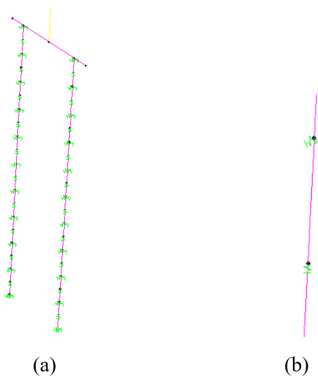


Figure 4. Soil-structure interaction: (a) 3D view of a block on two piles; (b) Horizontal and vertical springs applied at the nodes.

Figure 5 to Figure 7 show the layout of the reinforced concrete support structure, the masonry first course (highlighting the walls used in analysis), the foundation details, and the building discretization.

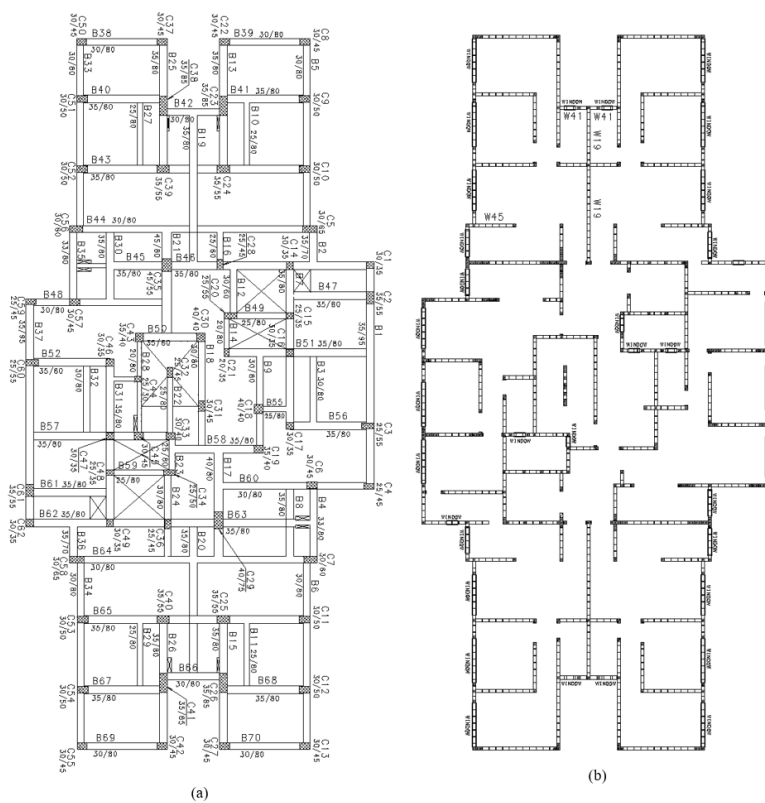


Figure 5. Building structure: (a) Reinforced concrete support structure; (b) Structural masonry first course.

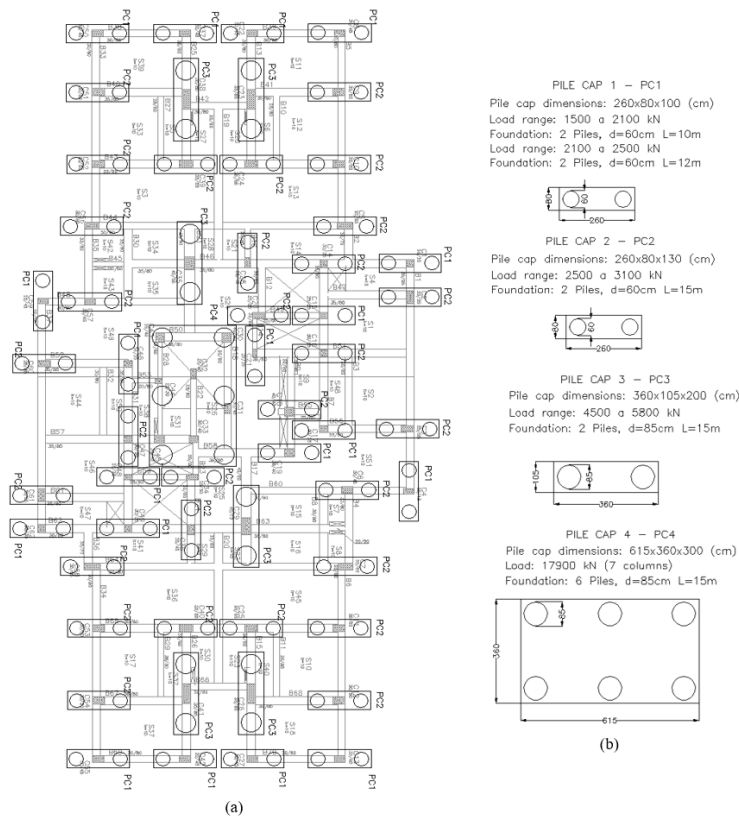


Figure 6. Foundations: (a) Floor plan; (b) Pile caps grouping by load ranges.

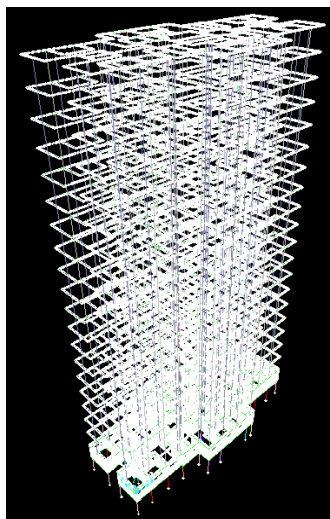


Figure 7. Building discretized in SAP2000 (fully-fixed base – model 1).

For purposes of assessing the results, the same subjective interpretation adopted by Testoni [3] and Santos [4] was used, based on NBR 8681 [39]. According to Santos [4], with coefficient γ_f for normal combinations of 1.4 and adopting $\gamma_{f1} = \gamma_{f3}$, it results that γ_{f3} is the square root of γ_f , assessed at 1.18. Based on these findings, it is assumed that variations up to 18% are covered by the safety factors (SF) of the design standards, corresponding to the deficiencies of the calculation method applied. For purposes of qualitative analysis, the same variation ranges for the differences used by Santos [4] were applied, as depicted in Table 5.

Table 5. Ranges of the differences for the classical reference model.

Range	Quality of the difference
$-5\% \leq DIF \leq 5\%$	Good/excellent
$5\% < DIF \leq 18\%$ or $-18\% \leq DIF < -5\%$	Fair
$DIF < -18\%$ or $DIF > 18\%$	Poor/very poor

4 RESULTS AND DISCUSSION

Two walls from the building were selected for analyses: walls 41 and 45, illustrated in Figure 8. As a criterion, in addition to the vertical loads in the walls, the type of support and the existence of different openings were also considered. Thus, wall 41 contains two window openings and wall 45 has one end coincident with a column of the support beam and the other in an intermediate section of this beam, which, in turn, exhibits a relatively large span for this type of structure.

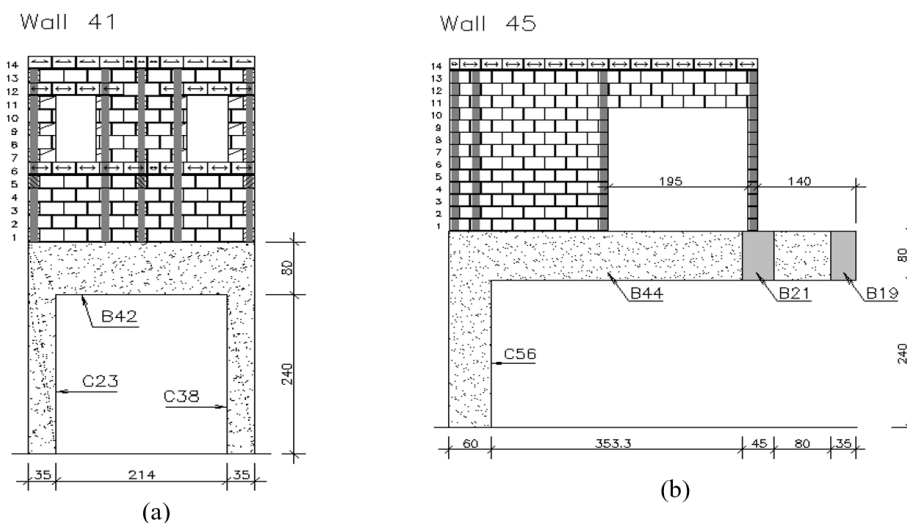


Figure 8. Wall's elevations: (a) Wall 41; (b) Wall 45.

4.1 Results of wall 41

Figure 9 illustrates the distribution of stresses at the base of wall 41, and Table 6 indicate their values in the regions of the end of support beam. The stress distribution indicated greater variations between the analysis models. The curves in Figure 9(a) and values presented in Table 6 demonstrate that for this wall, the normal stresses of model 2 in relation to model 1 were higher in the two peak regions and central region. Introducing the construction effect into the analyses caused a redistribution of stresses, thereby reducing normal stresses in the central region, despite continuing to display higher values at the ends. It is important to underscore that SSI in combination with the construction effect in model 4 intensified peak stress even more at the ends. With respect to these results, it is worth mentioning the results of wall 19, which exhibited low normal stress intensity at the intersection with wall 41. Lopes [31] shows all results of the research. Since this intersection is a support point for the support beam, higher-intensity peaks were expected, which did not occur. Thus, the likely peaks at the end of wall 19 were redistributed to the two ends of wall 41 and intensified when the construction effect and SSI were considered. The vertical interfaces at the connection can withstand the shear stresses; otherwise, the redistribution cannot occur, completely changing the stresses on the walls and the forces on the support beams.

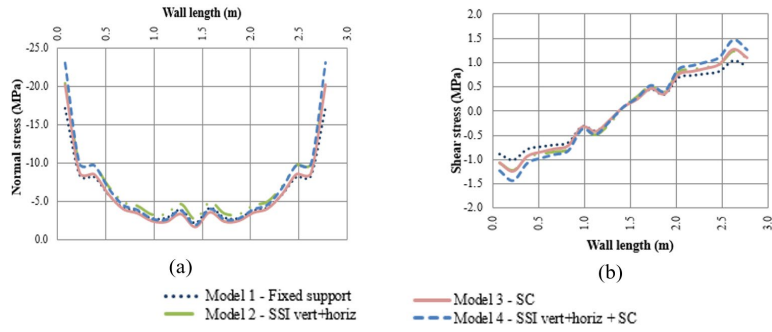


Figure 9. Distribution of stresses at the base of wall 41: (a) Normal stresses; (b) Shear stresses.

Table 6. Maximum values of normal and shear stresses of wall 41.

Model	Normal stress (MPa)				Shear stress (MPa)			
	Region P38	Δ fixed support	Region P23	Δ fixed support	Region P38	Δ fixed support	Region P23	Δ fixed support
Model 1	-17.07	-	-17.18	-	-1.01	-	1.04	-
Model 2	-20.42	20%	-20.49	19%	-1.22	21%	1.24	20%
Model 3	-20.15	18%	-20.23	18%	-1.25	23%	1.27	22%
Model 4	-23.08	35%	-23.13	35%	-1.44	42%	1.46	40%

Regarding shear stresses, at the two ends, models 2, 3 and 4 exhibit greater intensities than in model 1. The differences are high, the highest being those associated with model 4, as shown in Table 6.

Figure 10 illustrates the forces on the support beam of wall 41, and Table 7 contains the maximum intensities obtained. The axial force on the beam exhibited high differences between the models, where models 2, 3 and 4 resulted in tensile forces alone and at higher intensity than in model 1 – which has a short portion submitted to compression forces, albeit at low intensity, on the right-hand support. When compared to model 1, all the values varied beyond the SF.

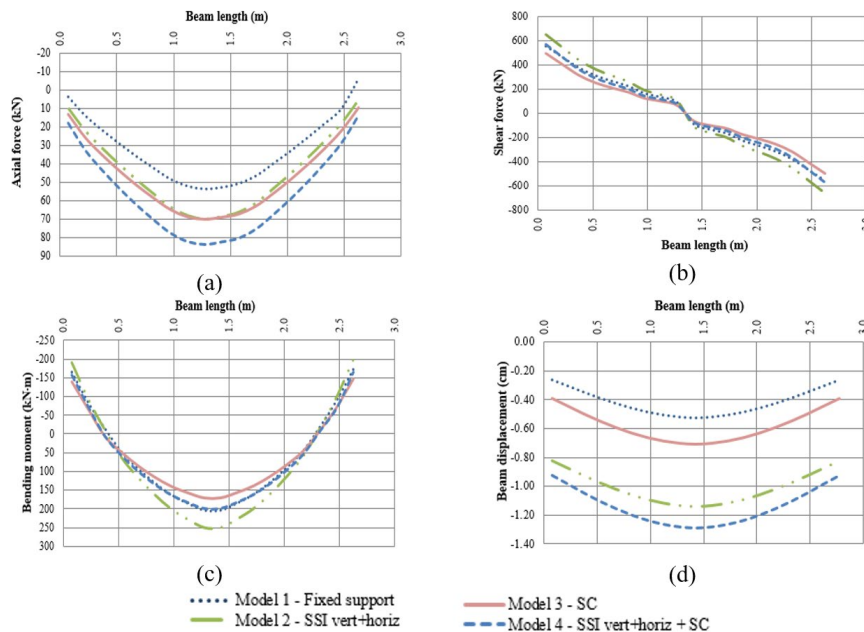


Figure 10. Forces on the support beam of wall 41: (a) Axial force; (b) Shear force; (c) Bending moment; (d) Displacements.

Table 7. Maximum forces on the support beam of wall 41.

Model	Axial Force (kN)		Shear force (kN)		Bending moment (kN·m)		Displacements (cm)	
	Maximum	Δ fixed support	Maximum	Δ fixed support	Maximum	Δ fixed support	Maximum	Δ fixed support
Model 1	53.48	-	556.19	-	204.82	-	0.52	-
Model 2	70.01	31%	659.17	19%	249.37	22%	1.14	118%
Model 3	69.82	31%	500.00	-10%	169.78	-17%	0.71	36%
Model 4	83.65	56%	572.41	3%	199.57	-3%	1.29	147%

In cases of shear force, the model 2 displays higher shear force and bending moment, which are mitigated when the construction stages in models 3 and 4 are considered. Moreover, displacements show high percentage differences, primarily when one considers interaction with the soil, reaching the normative limit of SLS (1.0 cm), when strain associated with the corresponding supports is disregarded.

4.2 Results of wall 45

The distribution of normal and shear stresses at the base of wall 45 are illustrated in Figure 11. In this case, the four models behaved similarly, with peaks occurring only at the left end, where column P56 is located, and slight variations along the entire length of the wall. It is important to underscore that the stress-free portion corresponds to that of the beam with no vertical load from structural masonry, and that the diagrams are represented until slightly to the right of the support provided by beam V44 on beam V19. With respect to the intensity of normal and shear stress peaks, considering the construction stages and the SSI resulted in considerable increases, even exceeding the limits of the SF, like what occurred in wall 41, according to Table 8. This wall shows the same typology as wall 25, with one of the ends on the support of beam V22 and the other on the span of this beam. The difference refers to the higher support beam stiffness of wall 25 which, in addition to exhibiting a shorter span, has established supports in columns at both ends. This produced normal and shear stresses low peaks at the base of wall 25 in the span of beam V22, which did not occur in wall 45.

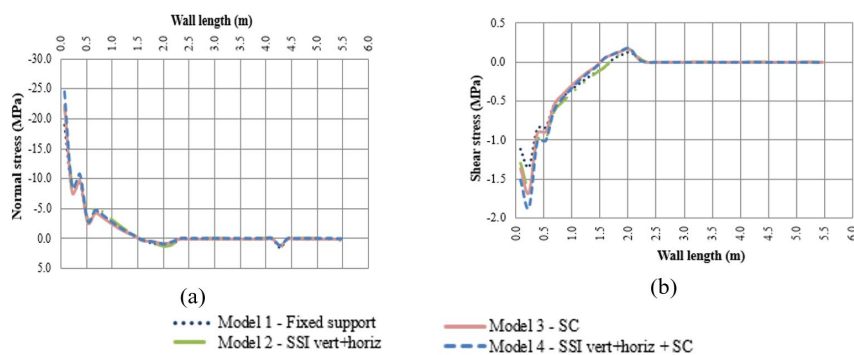


Figure 11. Distribution of stresses at the base of wall 45: (a) Normal stresses; (b) Shear stresses.

Table 8. Maximum values of normal and shear stresses of wall 45.

Model	Normal stress (MPa)		Shear stress (MPa)	
	Region P56	Δ fixed support	Region P56	Δ fixed support
Model 1	-18.91	-	-1.35	-
Model 2	-22.31	18%	-1.59	18%
Model 3	-21.94	16%	-1.67	24%
Model 4	-24.55	30%	-1.86	38%

In terms of the forces on the support beam illustrated in Figure 12 and Table 9, axial force showed a decline in compression and rise in tension when considering the SSI and the construction stages in models 2, 3 and 4, with the latter considering the simultaneous effects, resulting in a greater difference than in model 1. With respect to shear forces, bending moments and displacements, the same aspects described in previous walls are repeated as follows: considering only the SSI is the most unfavorable situation, with an increase in maximum intensities, while introducing the construction effect reduced these values, with models 2 and 4 being the least favorable in terms of displacements.

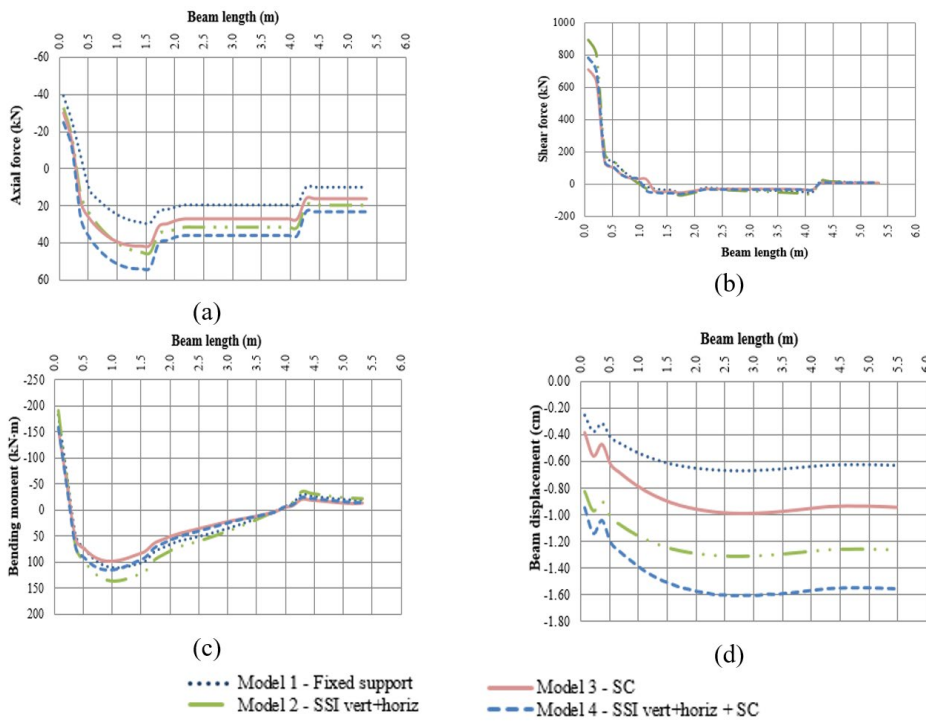


Figure 12. Forces on the support beam of wall 45: (a) Axial force; (b) Shear force; (c) Bending moment; (d) Displacements.

Table 9. Maximum forces on the support beam of wall 45.

Model	Axial Force (kN)		Shear force (kN)		Bending moment (kN.m)		Displacements (cm)	
	Maximum	Δ fixed support	Maximum	Δ fixed support	Maximum	Δ fixed support	Maximum	Δ fixed support
Model 1	39.32	-	783.13	-	183.13	-	0.67	-
Model 2	45.27	15%	894.65	14%	191.87	5%	1.31	96%
Model 3	41.50	6%	708.27	-10%	155.01	-15%	0.99	48%
Model 4	53.72	37%	780.93	-0,3%	158.76	-13%	1.61	141%

4.3 Columns and foundations

As shown in Figure 13a, the distribution of axial forces between the columns of the building when considering interaction with the soil, and the gradual rise in loading in the structure demonstrate that the smallest differences in relation to model 1 occur in model 3, with a fully-fixed base and only the construction effect. Considering soil deformation in models 2 and 4 causes more pronounced variations, in line with the results illustrated in Figure 13a. Model 4 mitigates the variations of model 2 in relation to 1, that is, promotes a trend to redistribution.

The effects of the SSI in models 2 and 4 demonstrate that corner columns had the largest declines in axial forces in relation to model 1. Columns such as P1, P4, P8, P13, P22, P27, P37, P42, P50, P55, P59 and P62 (Figure 5), exhibited considerable reductions, resulting in an increase in axial forces in the closest columns.

Figure 13b illustrates the foundation settlements. Geotechnical settlements refer to those in models with a fully-fixed base, calculated using the Cintra and Aoki method. The axial forces in the columns underwent considerable variations after introducing interaction with the soil (models 2 and 4). As such, the settlements also exhibited variations, displaying the expected behavior: reduced settlements in the columns that underwent a decline in axial forces, and an increase in settlements in columns that experienced a rise in these forces. SSI reduced the differential settlements between the elements. It is important to underscore that the settlement values associated with model 1 did not consider the effect of structure stiffness, since they were calculated individually from the support reactions in the columns. In the case of models 3 and 4, given that soil deformation was simulated by the springs, the corresponding settlements are affected by the stiffness of the structure.

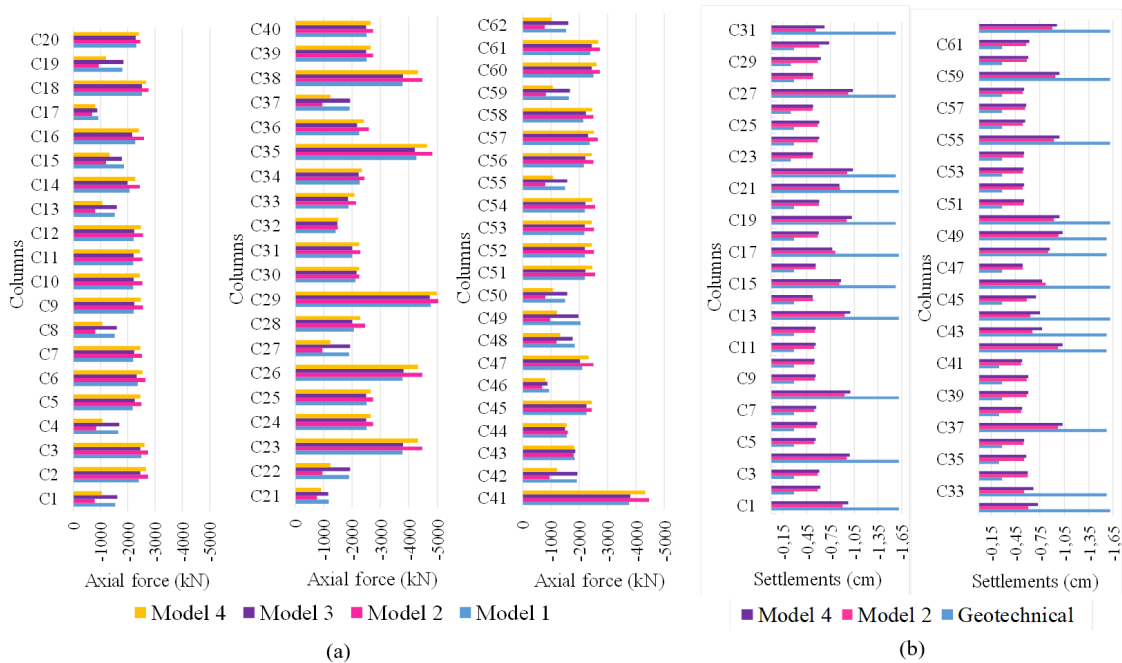


Figure 13. Columns and foundations results: (a) Maximum axial forces of the columns; (b) Foundation settlements.

5 CONCLUSIONS

The results analyzed and discussed here showed important behavior intrinsic to the interaction between masonry structures, as wall-beam systems, and the soil, and loading in the construction stages, as follows:

- In terms of normal and shear stresses at the base of the walls, the behavior observed showed no significant changes. The highest variations occurred in the peak regions, where the model that considers soil-structure interaction and gradual load application was the least favorable, except in the case of one of the walls analyzed, in which the most unfavorable was the model that considers only the SSI. As such, a model that considers interaction with the soil is essential for stress redistribution in the structure. The model that simultaneously considers soil-structure interaction and the effects of construction loads does not correspond to a simple overlap of these effects considered separately. Furthermore, it is important to emphasize that two of the three walls assessed showed variations in stress that do not comply with the safety factor (SF) stipulated by the Brazilian Standard Code, demonstrating the need to include the effects in the structural analysis of buildings similar to that assessed here;
- The forces on the reinforced concrete support beams show more significant differences between the results of the models. Axial force exhibited the greatest differences, demonstrating no behavioral trend. In the case of wall 19, for example, tensile axial force declined when SSI and the construction effect were incorporated, while in wall 41 it increased. A completely different trend occurred in wall 45, where compressive force declined, and tensile force rose. Akin to the case of stress at the base of the walls, two of the three support beams showed variations in axial force that are not covered by the SF of the Brazilian Standard Code, once again emphasizing the need to include

soil-structure interaction and the construction effects in the structural analysis of buildings similar to that assessed here;

- By contrast, for all the beams analyzed, shear force and the bending moment increased when only the SSI was considered, and incorporating the construction effect reduced these forces, with the results of the model that considers both effects closely resembling those of the model with fully-fixed column bases.
- As a rule, absolute displacement of the beams in the models that considered interaction with the soil were more than twice as large as those obtained in the model without interaction. In some of the beams analyzed, these absolute displacements exceeded the serviceability limit state established by the Brazilian Standard Code. However, when strain associated with beam supports is disregarded, these limits were fully complied;
- In terms of the axial forces on support structure columns, the models that considered SSI resulted in greater variations in intensities. As expected, the most significant reductions were compensated by increases in this force in nearby columns. These forces variations in the columns caused considerable changes in settlements. Nevertheless, SSI reduced the differential settlements between the elements.

Incorporating SSI and construction effect provoked stress redistribution in the structure, leading to relief in some of the elements and the need for reinforcement increase in others. In conclusion, there is a need to incorporate the construction effects and, especially, soil-structure interaction in the analyses of structural masonry buildings, since these aspects may generate stresses on the walls and forces on the support beams that are not covered by the SF in terms of variations in results as a function of simplifying the model. However, models that use soil discretization in finite elements and other geometric typologies of buildings should be developed to corroborate this critical analysis of the conventionally used design method.

4 REFERENCES

- [1] Associação Brasileira de Normas Técnicas, *Concrete Wall Castes in Place for Building Construction – Requirements and Procedure*, NBR 16055, 2012.
- [2] Associação Brasileira de Normas Técnicas, *Structural Masonry. Part 1: Design*, NBR 16868-1, 2020.
- [3] E. Testoni, "Análise estrutural de edifícios de paredes de concreto por meio de pórtico tridimensional sobre apoios elásticos," M.S. thesis, Esc. Eng. São Carlos, Univ. São Paulo, São Carlos, SP, 2013.
- [4] P. V. S. Santos, "Ações evolutivas em edifícios de paredes de concreto e de alvenaria, considerando a interação com o solo," M.S. thesis, Esc. Eng. São Carlos, Univ. São Paulo, São Carlos, SP, 2016.
- [5] P. C. Barbosa, "Estudo da interação de paredes de alvenaria estrutural com vigas de concreto armado," M.S. thesis, Esc. Eng. de São Carlos, Univ. São Paulo, São Carlos, SP, 2000.
- [6] J. A. Nascimento No., K. A. S. Medeiros, and F. Quim, "Nova modelagem para análise da interação entre painéis de alvenaria e estrutura de suporte," *Rev. Prisma*, no. 52, pp. 39–48, 2014.
- [7] K. A. S. Medeiros, "Modelagem computacional para avaliação da interação entre painéis de alvenaria e estrutura de suporte em concreto armado," M.S. thesis, Prog. Pós-grad. Eng. Civil, Univ. Fed. Rio Grande do Norte, Natal, RN, 2015.
- [8] G. A. Parsekian, A. A. Hamid, and R. G. Drysdale, *Behavior and Design of Structural Masonry*, 2a ed. São Carlos: EDUFSCar, 2013.
- [9] A. C. S. Lopes, "Aperfeiçoamento de modelagem computacional para análise da interação entre painéis de alvenaria e estrutura de suporte em concreto armado," B.S. thesis, Dept. Eng. Civil, Univ. Fed. Rio Grande do Norte, Natal, RN, 2016.
- [10] J. A. Nascimento No., "Investigação das solicitações de cisalhamento em edifícios de alvenaria estrutural submetidos a ações horizontais," M.S. thesis, Esc. Eng. São Carlos, Univ. São Paulo, São Carlos, SP, 1999.
- [11] A. D. Gusmão and J. A. Gusmão Fo., "Avaliação da influência da interação solo-estrutura em edificações," in *X COBRAMSEF*, Foz do Iguaçu, PR, 1994, pp. 67–74.
- [12] J. F. M. A. Prado, "Estruturas de edifícios em concreto armado submetidas a ações de construção," D.S. dissertation, Esc. Eng. São Carlos, Univ. São Paulo, São Carlos, SP, 1999.
- [13] S. C. Dutta and R. Roy, "A critical review on idealization and modeling for interaction among soil–foundation–structure system," *Comput. Struc.*, vol. 80, no. 20–21, pp. 1579–1594, 2002.
- [14] M. M. Filonenko-Borodich, "Some approximate theories of elastic foundation," [in Russian] *Uch. Zap. Mosk. Gos. Univ. Mekh.*, vol. 46, pp. 3–18, 1940.
- [15] M. Hetenyi, *Beams on Elastic Foundations*. Ann Arbor: Univ. Michigan Press; 1946.
- [16] P. L. Pasternak, *On a New Method of Analysis of an Elastic Foundation by Means of Two Foundation Constants* [in Russian]. Moscow, USSR: Gosud. Izd. Lit. po Stroi. Arkh., 1954.
- [17] A. D. Kerr, "Viscoelastic Winkler foundation with shear interactions," *J. Eng. Mech. Div.*, vol. 87, no. EM3, pp. 13–30, 1961.

- [18] J. S. Horvath, "Beam-column-analogy model for soil-structure interaction analysis," *J. Geotech. Eng.*, vol. 119, no. 2, pp. 358–364, 1993.
- [19] N. P. Kurian and N. G. Manojkumar, "A new continuous model for soil-structure interaction," *J. Struct. Eng.*, vol. 27, no. 4, pp. 269–276, 2001.
- [20] K. Terzaghi, "Evaluation of coefficients of subgrade reaction," *Geotechnique*, vol. 5, no. 4, pp. 297–326, 1955.
- [21] A. G. D. Araújo, "Provas de carga estática com carregamento lateral em estacas escavadas hélice contínua e cravadas metálicas em areia," M.S. thesis, Prog. Pós-grad. Eng. Civil, Univ. Fed. Rio Grande do Norte, Natal, RN, 2013.
- [22] H. Matlock and L. C. Reese, "Foundation analysis of offshore pile supported structures," in *Proc. V Int. Conf. Soil Mech. Found. Eng. ICSMFE*, vol. 2, Paris, France, 1961, pp. 91–97.
- [23] B. B. Broms, "Lateral resistance of piles in cohesive soils," *J. Soil Mech. Found. Div.*, vol. 90, no. 2, pp. 27–63, 1964.
- [24] M. Alizadeh and M. T. Davissou, "Lateral load tests on piles," *J. Soil Mech. Found. Div.*, vol. 96, no. 5, pp. 1583–1604, 1970.
- [25] H. G. Poulos, "Behavior of laterally loaded piles: I – single piles," *J. Soil Mech. Found. Eng. Div. ASCE*, vol. 97, no. 5, pp. 711–731, 1971.
- [26] J. C. A. Cintra, "Uma análise de provas de carga lateral em estacas e comparação com os métodos da teoria de reação horizontal do solo," M.S. thesis, Esc. Eng. São Carlos, Univ. São Paulo, São Carlos, SP, 1981.
- [27] M. G. Miguel, "Execução e análise de provas de carga horizontal em estacas em solo colapsível," M.S. thesis, Esc. Eng. São Carlos, Univ. São Paulo, São Carlos, SP, 1996.
- [28] A. Del Pino Jr., "Análise do comportamento de estacas do tipo broca escavada com trado mecânico solicitadas por esforços transversais," M.S. thesis, Fac. Eng. Ilha Solteira, Univ. Est. Paulista, Ilha Solteira, SP, 2003.
- [29] C. C. Fan and J. H. Long, "Assessment of existing methods for predicting soil response of the laterally loaded piles in sand," *Comput. Geotech.*, vol. 32, no. 4, pp. 274–289, 2005.
- [30] B. B. Zammataro, "Comportamento de estacas tipo escavada e hélice contínua submetidas a esforços horizontais," M.S. thesis, Fac. Eng. Civ. Arq. Urb., UNICAMP, Campinas, SP, 2007.
- [31] A. C. S. Lopes, "Avaliação do comportamento de edifícios de alvenaria estrutural sobre estrutura de transição considerando a interação solo-estrutura e o efeito construtivo," M.S. thesis, Prog. Pós-grad. Eng. Civil, Univ. Fed. Rio Grande do Norte, Natal, RN, 2019.
- [32] Associação Brasileira de Normas Técnicas, *Concrete Structures Design – Procedure*, NBR 6118, 2014.
- [33] G. A. Parsekian and L. S. Franco, "Time-dependent strength and creep in masonry," *TMS J.*, vol. 24, no. 1, pp. 83–94, 2006.
- [34] Associação Brasileira de Normas Técnicas, *Building Construction – Bases for design of structures – Wind Loads – Procedure*, NBR 6123, 1988.
- [35] J. C. A. Cintra and N. Aoki, *Fundações por Estacas: Projeto Geotécnico*, 1a ed. São Paulo: Oficina de Textos, 2010.
- [36] N. Aoki and D. A. Velloso, "An approximate method to estimate the bearing capacity of piles," in *Vth Pan Am. Conf. Soil Mech. Found. Eng.*, vol. 1, Buenos Aires, 1975, pp. 367–376.
- [37] L. Décourt, "Load-deflection prediction for laterally loaded piles based on N-SPT values," in *Proc. 4 Int. Conf. Piling and Deep Found.*, vol. 1, 1991, pp. 549–555.
- [38] J. Blévoit and R. Frémy, "Semelles sur pieux," *Annales L'Institut Tech. Batiment Trav. Publics Paris*, vol. 20, no. 230, pp. 223–295, 1967.
- [39] Associação Brasileira de Normas Técnicas, *Actions and Safety of Structures – Procedure*, NBR 8681, 2004.

Author contributions: ACSL: development of the primary research and writing the manuscript; JANN: supervision of the primary research, results discussions and manuscript review; RB: contributions to the primary research, results discussions and manuscript review.

Editors: Fernando Soares Fonseca, Guilherme Aris Parsekian.



ORIGINAL ARTICLE

Study of red ceramic residues as pigments in matrices based on white Portland cement

Estudo de resíduos de cerâmica vermelha como pigmentos em matrizes de cimento Portland branco

Letícia Andreolli Dias^a Fernanda Boll Birck^a Lucas Kaefer^a Daiana Cristina Metz Arnold^a Alexandre Silva de Vargas^b ^aUniversidade Feevale, Engenharia Civil, Novo Hamburgo, RS, Brasil^bUniversidade Federal de Santa Maria – UFSM, Engenharia Civil, Santa Maria, RS, Brasil

Received 06 June 2020

Accepted 11 March 2021

Abstract: The present study evaluated the use of red ceramic residues (RCR) as pigments in matrices based on White Portland cement. Five mortars were prepared for the present study: control mortar (M0), at 1:2,3 ratio (cement: sand) and water/cement ratio of 0.60, other four mortars were prepared containing RCR in 10% (M10), 20% (M20), 50% (M50), 100% (M100) of volume in replace to the sand. Colorimetric tests indicated a significant increase in the coloring, due to the increase of the RCR used. Tests of resistance to compression strength indicated a significant increase in the results as there was an increase in the substitution content of the sand by RCR. In the flexural tensile strength was no significant influence for contents of up to 50%. Therefore, the RCR showed potential as a pigmentation product and can contribute to the increase in compressive strength in Portland cement-based matrices.

Keywords: sand, pigments for mortar, red ceramic residues.

Resumo: O presente estudo avaliou a utilização de resíduos de cerâmica vermelha (RCR) como pigmentos em matrizes à base de cimento Portland Branco. Para o presente estudo foram preparadas cinco argamassas: argamassa de controle (M0), com traço, em massa, de 1: 2,3 (cimento: areia) e relação água/cimento de 0,60; outras quatro argamassas foram preparadas contendo RCR, em substituição ao volume da areia, em teores de 10% (M10), 20% (M20), 50% (M50) e 100% (M100). Os testes colorimétricos indicaram um aumento significativo na coloração, devido ao aumento do RCR utilizado. Ensaios de resistência à compressão indicaram aumento significativo nos resultados, com o aumento da substituição da areia pelo RCV. Na resistência à tração na flexão não houve influência significativa para teores de até 50% do RCR. Portanto, o RCR apresentou potencial como produto de pigmentação e pode contribuir para o aumento da resistência à compressão em matrizes à base de cimento Portland.

Palavras-chave: areia natural, pigmento para argamassa, resíduo de cerâmica vermelha.

How to cite: L. A. Dias, F. B. Birck, L. Kaefer, D. C. M. Arnold, and A. S. Vargas, “Study of red ceramic residues as pigments in matrices based on white Portland cement,” *Rev. IBRACON Estrut. Mater.*, vol. 14, no. 6, e14608, 2021, <https://doi.org/10.1590/S1983-41952021000600008>

1 INTRODUCTION

Sustainability is a major subject in construction industry nowadays, since a large fraction of solid residues is generated in constructions, resulting in high levels of environmental, social and economic impacts. The red ceramic

Corresponding author: Letícia Andreolli Dias. E-mail: leticia.dias.nh@hotmail.com

Financial support: None.

Conflict of interest: Nothing to declare.



This is an Open Access article distributed under the terms of the Creative Commons Attribution License, which permits unrestricted use, distribution, and reproduction in any medium, provided the original work is properly cited.

industry generates a representative amount of residues (RCR) because, due to requirements of quality, many products are discarded for presenting defects of production or for inadequate transportation [1].

By incorporating RCR in mortars and concretes, it is possible to partially replace the constituents of the mixtures, thus reducing the consumption of natural aggregates or binders. In the case of aggregates (sand), its excessive extraction can lead to disastrous environmental consequences, reason why, the incorporation of residues for its replacement can offer advantages in environmental, economic, and technical aspects.

Considering the above, the potential of the red ceramic residues (RCR) generated, due to their colorimetric characteristics and due to the inert materials they are made of, make them an attractive alternative for the incorporation in mortars and concretes for pigmentation purposes, reducing the inadequate deposition of the waste generated [2].

Buildings with colored mortars are an attractive alternative compared to traditional mortars that exhibit poor aesthetic properties, from the architectural point of view [3]. Pigmented constructions become popular among engineers and architects, in the application of facades, coatings and other decorative monuments. A very important aspect is to obtain permanent colors without producing adverse effects on mortars and the environment [4].

In this sense, the pigmentation of mortars is widely used in developed countries to replace the painting, considering that low price is an important characteristic to the advantage of decorative mortar, the use of residues can help in the process of diversifying the production, reducing final costs and allowing new possibilities for the reuse of this waste in order to minimize the environmental impacts of the ceramic industry [5].

Diamanti et al. [6] and Lemaire et al. [7] affirm that from the moment in which mortars and concrete are used as decorative material, the coloring becomes essential for the building, and not only its structural function. However, it is becoming increasingly important that mortars and concretes become more economical, durable and sustainable [1].

The organic and inorganic pigments used in mortars and concretes show very fine grains, as well as the RCR, causing greater absorption of water in the mixture and consequent decrease in the workability, when carrying out the tests of consistency [3]. López et al. [8] complements that since the pigment has particles of similar or smaller sizes of the cement particles, it is necessary to evaluate the increase in the water demand, emphasizing that a study of the mixture can improve the performance of it, considering the effects of the pigments on material cohesion and the adoption of plasticizing additives.

Concrete and mortar structures must have good resistance, since they must maintain their integrity for a long time, by analyzing the tensile resistance in the bending, Lee et al. [9] expose the importance of water absorption, because according to their study, the greater the water absorption was, the lower the tensile resistance was in the samples. According to Sales and Alferes [10], the characteristics of the materials incorporated to the mixture also have great influence in the resistance of the concrete, being verified that by the incorporation of the ceramic powder into concretes, the chemical and microstructural compositions of that residue reduced the tensile resistance in the bending.

Corinaldesi et al. [11] verified the decrease in compressive resistance of concretes and mortars that commercial pigments were added, when compared to the resistance of the materials without the pigment. On the other hand, Matias et al. [2] found that, unlike the commercial pigments, the RCR presented pozzolanic properties and filler effect, which contributes to increasing the mechanical strength by incorporating the residues in matrices based by Portland cement, due to the increased voids filled by having smaller grains (fillers) and pozzolanic reactions with the cement hydration products (Portlandite - $\text{Ca}(\text{OH})_2$). Thus, it is possible to observe that the RCR has potential to pigment cement matrices without damaging the mechanical properties of the composite.

Colorimetry is a good tool to rapidly evaluate the pigment anchoring on the hardened mortar a few weeks after demolding [12]. Li et al. [5] show that the chemical constituents of the residues used as pigments in mortars and concretes define their coloration, such as, for example, wastes with higher Fe^{3+} and Pb^{3+} ions, have a red coloring.

Considering the above, this article aims to analyze the influence of the replacement of natural quartz sand by RCR in the production of pigments for mortars, considering the physical properties of the residue, the mechanical performance of each mortar in the hardened state and the colorimetry test of the samples.

2 MATERIALS AND EXPERIMENTAL PROGRAM

2.1 Materials

The cement used for the preparation of the mortars was Structural White Portland cement (WPC - 40). The physical characteristics and chemical composition of cement are presented in Tables 1 and 2.

Table 1. Physical characteristics of White Portland Cement.

	White Portland Cement	Sand
Specific mass	2,97 g/cm ³	-
Finess- residue on the sieve of 75µm	0,3%	-
Finess- residue on the sieve of 45µm	1%	-
Unit mass	-	1,615 g/cm ³
Finesse module	-	2,19
Maximum grain size (mm)	-	2,4mm

Table 2 shows the chemical composition of the cement used in the study, according to the tests performed by the manufacturer.

Table 2. Chemical characteristics of White Portland Cement.

Assay	% of mass
SiO ₂	20,86
Al ₂ O ₃	4,16
Fe ₂ O ₃	0,24
CaO	63,3
MgO	1,17
SO ₃	2,89
Na ₂ O	0,10
K ₂ O	0,43
TiO ₂	0,21
SrO	0,04
P ₄ O ₁₀	0,04
MnO ₂	0,02
CaO	1,79
Insoluble residue	0,57
CO ₂	3,99
Equivalent Alkaline in Na ₂ O	0,38

As fine aggregate, it was used river quartz sand. Data on sand characterization are presented in Table 1.

It was used red ceramic residue derived from broken or defective bricks from an industry located in the Valley of the Sinos - Brazil. The firing temperature of the bricks is controlled at 900 ° C. For the correct use of the residue, it underwent a beneficiation process, in which it was ground in a TS 2X20 / 600 Crusher, and milled in CT-241 Ball Mill for 12 minutes. The value of the specific mass and unit mass of the residue used was 2,57 g/cm³ and 0,84 g/cm³, respectively. Figure 1 shows the granulometric curve of the RCR, determined by laser granulometry. The mean RCR diameter was 8 µm.

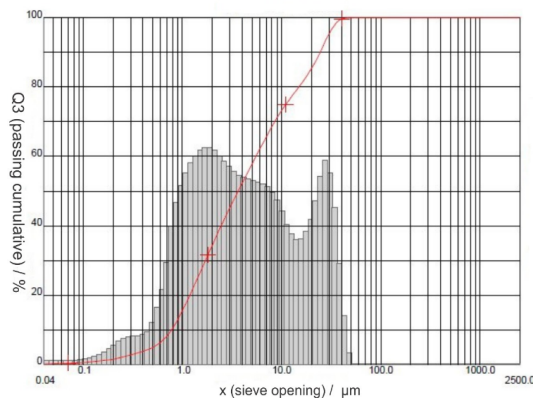


Figure 1. Laser granulometry ceramic process.

Figures 2 and 3 show micrographs of the RCR obtained with the help of the scanning electron microscope (SEM). It is observed that the majority of the RCR particles are irregularly shaped and have a rough surface, which increases the exposed area of the grain.

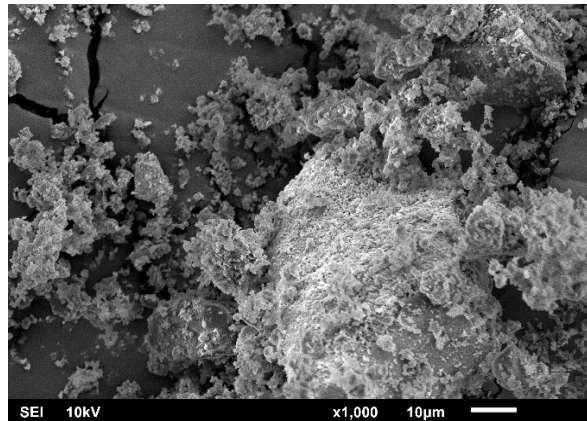


Figure 2. SEM Red ceramic – increase of 1.000x.

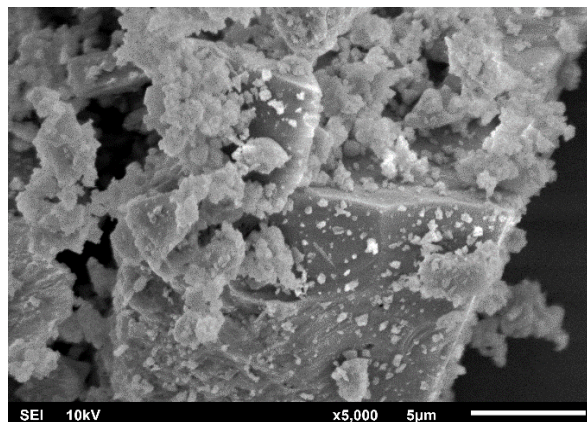


Figure 3. SEM Red ceramic – increase of 5.000x.

2.2 Method

Five mortars were prepared for the present study: control mortar (M0), at 1:2,3 ratio (cement: sand) and water/cement ratio of 0.60; other four mortars were prepared containing RCR in 10% (M10), 20% (M20), 50% (M50), 100% (M100) of volume in replace to the natural sand, as shown in Table 3.

Table 3. Studied proportions.

Matrix	Cement (kg)	Sand (kg)	Residue of RCR (kg)	Water (kg)	Additive content (%)	Flow table (mm)
M0	0,850	1,955	0	0,51	0	292
M10	0,850	1,7595	0,1017	0,51	0	281
M20	0,850	1,564	0,2034	0,51	0	297
M50	0,850	0,9775	0,7206	0,51	0	289
M100	0,850	0	1,0168	0,51	3,85	260

Since the specific masses of the sand and the RCR are different, the following equation was adopted to determine the masses of RCR and sand to be used for volume replacement of the contents presented previously.

$$Ma = \frac{Mb}{Yb} \times Ya \quad (1)$$

Where is mass of material (Ma), mass of material to be replaced (Mb), unit mass of material (Ya) and unit mass of material to be replaced (Yb).

The preparation of the mortars was performed in a vertical axis mixer, for 90 seconds, at slow speed, according to the terms of the norm NBR 13276 [13]. Table 3 shows the traits and Consistency Index for each sample studied. In this work, it was adopted the consistency index of the mortars, measured at the flow table, of $280 \text{ mm} \pm 20 \text{ mm}$. According to Table 3, only for the sample M100 it was necessary to use a plasticizer additive in order to achieve that consistency index.

For the colorimetric assays, four prismatic samples ($4 \times 4 \times 8 \text{ cm}$) were prepared for each mixture studied. In the compression strength and tensile strength tests, three prismatic samples ($4 \times 4 \times 16 \text{ cm}$) were prepared for each mixture studied. After 48 hours the samples were removed from the prismatic molds, remaining at a controlled temperature of $23 \pm 2 \text{ }^\circ\text{C}$.

2.3 Colorimetric Analysis

For the colorimetric analysis of the samples M0, M10, M20, M50 and M100, were used metal molds with the dimensions of $4 \times 4 \times 8 \text{ cm}$. These samples were submitted to two different environments, during 28 days, described as follows:

- Environment exposed to atmospheric conditions: In this environment, two samples of each residue level remained outside the laboratory, exposed to the weather, in order to evaluate the effect of this environment on the coloration. In the 28-day period, temperatures ranged between 11.4°C and 38.1°C , the relative air humidity varied between 20% and 95%, with rainfall occurring in 11 of the 28 days evaluated [14];
- Controlled environment: the two samples of each residue content remained in a environment of laboratory with a temperature of $23 \pm 2 \text{ }^\circ\text{C}$.

At the ages of 14 and 28 days, chromatic measurements were performed with the help of the Konica Minolta spectrophotometer, model CM-2600D.

The analyses were made using the CIElab method, in which it is used a mathematical treatment for the relative intensities of red, yellow, green, and blue radiation, seeking the uniformity of color spacing in the colorimetric space. Given its three-dimensional character, the color can be represented graphically by a system of perpendicular coordinates: L^* , a^* , b^* ; the L^* being associated with the luminosity of the sample that varies from black to white. The coordinate a^* when positive, means red tones and when negative, green tones, and b^* that oscillates between yellow and blue tones when positive and negative, respectively [15].

Horgnies et al. [12] report that this method is effective for the fast evaluation of pigmentation in different areas of a sample, due to its three-dimensionality, and also presents precision when used with comparison effect of pigmentation, as will be carried out in the research.

Thus, the analyses were performed using the parameters L^* , a^* , b^* . The transfer of the data collected for the On Color software enabled the configuration of the readings and the automatic calculation of the parameters L^* , a^* , b^* . However, since the color change is not originated only by the parameter L^* or shades, the color variation (ΔE) and the variation in the L^* axis were used as a criterion of comparison, since these are the parameters most noticeable to the observer.

2.4 Tensile Strength

For Tensile Strength analysis, 3 prismatic specimens with dimensions of $4 \times 4 \times 16 \text{ cm}$ were molded for each RCR level, according to the requirements of NBR 13279 [16]. The specimens were demolded after 48 hours of molding, in a way that the rupture occurred at 28 days of cure.

2.5 Compressive Strength

The compressive strength test used the ruptured half of the test specimens of the testing of Tensile Strength at 28 days of cure, according to NBR 13279 [16].

3 RESULTS AND DISCUSSIONS

Figures 4 and 5 show the samples in a laboratory environment and those exposed to the atmospheric conditions, at age of 28 days, in which it is possible to visualize the increase of the coloration with the addition of the replacement of the sand by the RCR.

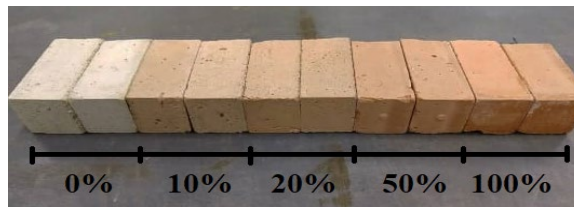


Figure 4. Samples of mortars in laboratory environment, aged 28 days.



Figure 5. Samples of mortars exposed to atmospheric conditions, aged 28 days.

3.1 Colorimetric Analysis

The determination of the color change is specified for a total variation, not being possible to know if the differences are due to luminosity (L^*) or hue. Therefore, the color variation ΔE and the variation in the L^* axis were used as a comparison criterion, since these are the parameters with the most visually perceptible differences.

3.1.1 Parameter L^*

Figures 6, 7 and 8 show the values of the parameter L^* compared to the effect of red ceramic residue content and curing environment. In order to understand the analysis of the parameter L^* , it can be said in a more simplified way that the smaller the value of this parameter “the darker the color”.

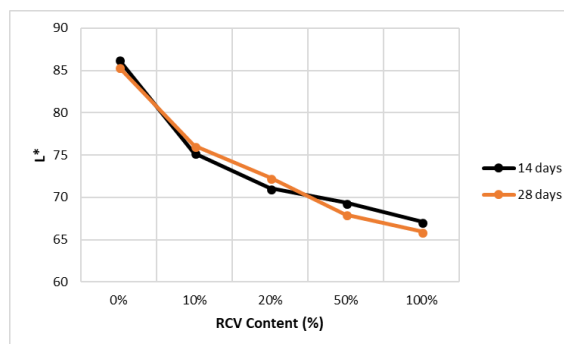


Figure 6. Effects of the content of RCR and of age of luminosity of L^* of samples with cure in laboratory ($23 \pm 2 \text{ }^\circ\text{C}$).

It is realizable that the variable of time of cure does not importantly interfere at the luminosity of samples cured in controlled temperature ($23 \pm 2 \text{ }^\circ\text{C}$), identical situation as samples exposed to inclement weather according to Figure 7.

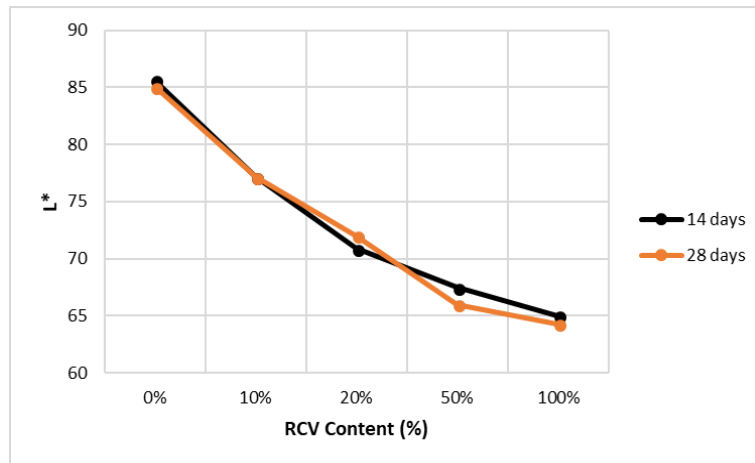


Figure 7. Effects of the content of RCR and of age of luminosity of L* of samples with cure in an environment exposed to atmospheric conditions.

However, when the content of incorporated residue in reason to luminosity is analyzed, a decrease in the results of this property due to the increase of residue used is realized (Figure 8).

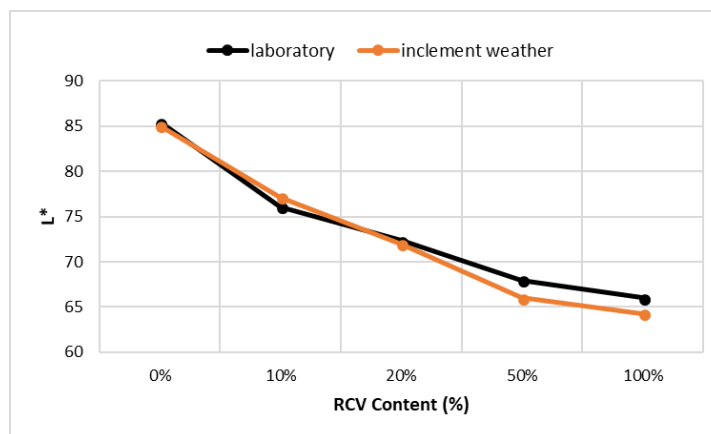


Figure 8. Effects of the content of waste and cured environments in luminosity L* of samples.

Starting from analysis of Figures 6, 7 and 8, it is noticeable that as there was an increase in the substitution of natural sand to RCR, the darker the surface of grout samples gets, independent of condition and time of cure. The residue, for showing bigger power of coloring, probably justified by the low dimension of its particles, resulted in darker toned samples.

Matias et al. [2], confirmed this result in their study, which verified that the RCR presented filler effect on cement mixtures, due to its fine particles. With the use of 100% of residue for example, the samples presented a tone in order of 22% and 2% darker, respectively, to controllable cure ($23 \pm 2 \text{ }^\circ\text{C}$) and not controllable cure at age of 28 days, when compared to reference sample (M0). In the comparison of samples in different environments of cure, it is noticeable the same tendency presented in the figures, where the luminosity suffers significant effects only in variation of content of waste.

The variance analysis (ANOVA) for the parameter L* is presented on Tables 4 and 5, as well as the significance of variables of study and its interactions.

Table 4. ANOVA of the independent factors and of the interaction between them in relation to the evolution of luminosity L* with red ceramic residue in environment exposed to atmosphere conditions.

Variation source	SS	DF	AS	Testing F	value – p	Critical F	Significant Effect
Environment of cure (EC)	0,876	1	0,876	0,654	0,464	7,709	No
EC*Residue percentage	500,29	4	125,07	93,374	0,000	6,388	Yes

SS- Sum of the squares, DF- Degree of freedom, AS- Average square, Testing F- Statistics F, Value P- Proof Value, Critical F - acceptance zone

Table 5. ANOVA of the independent factors and interactions between them in relation to the luminosity L* evolution with red ceramic residue in laboratory environment.

Variation source	SS	DF	AS	Testing F	Value – p	Critical F	Significant Effect
Environment of cure (EC)	1,176	1	1,176	1,584	0,277	7,709	No
EC*Residue percentage	522,05	4	130,51	175,765	0,000	6,388	Yes

SS- Sum of the squares, DF- Degree of freedom, AS- Average square, Testing F- Statistics F, Value P- Proof Value, Critical F - acceptance zone

As expected, the increase in the content of residue influences significantly on final colorimetric features, presenting a big decrease on luminosity as the increase of RCR happens, demonstrating the waste’s potential as pigment, justified fact by the iron oxide contained in ceramic materials [17]. In relation to the influence of the cure environment, this did not present significant effect on luminosity, as much on the comparison to exposition to atmospheric conditions as in laboratory environment.

3.1.2 Parameter ΔE

The global chromatic modification ΔE represents the color variation of a material in relation to a reference pattern. In this work, the reference pattern consisted of two parameters L* and b* obtained in the testing at 14 days and its end at 28 days, in different conditions of exposure and used content, during different cycles which they were submitted to. This comparison allows establishing the increments or decreases on parameters and its chromatic implications. All results are mandatorily positive once they result from the hypotenuse formed by coordinates ΔL*, Δa*, Δb*.

The graphics presented on sequence (Figures 9 and 10) show the values of parameter ΔE in relation to the red ceramic residue content effect and cure time.

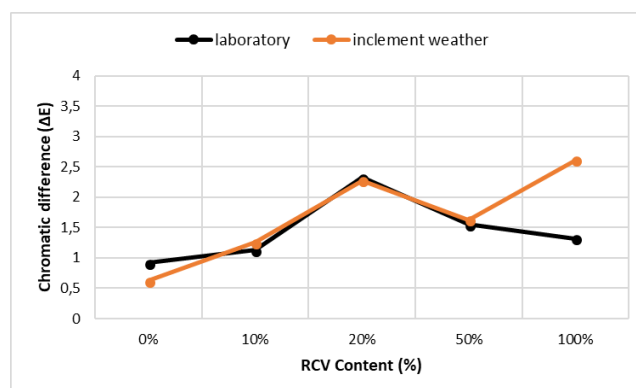


Figure 9. Effect of the content of residue and colorimetric difference ΔE in different environment and same ages.

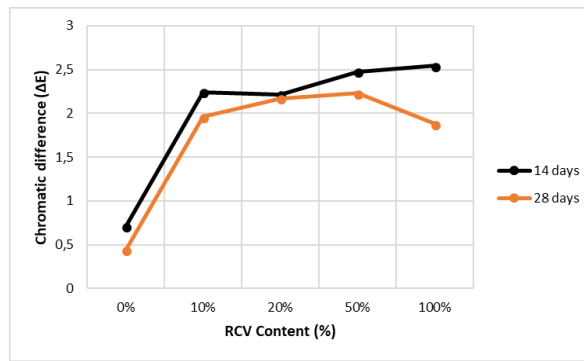


Figure 10. Effect of the content of waste and hydration ages to colorimetric difference ΔE between 14 and 28 days.

Once the red ceramic residue was incorporated in the cement matrix, an increase in the colorimetric difference is noticed, besides that the comparison in different ages proves what was showed on Table 6, which exposed to environment with inclement weather, the samples present a bigger colorimetric difference (Figure 10).

Table 6. ANOVA of the independent factors and interactions between them in relation to colorimetric variation ΔE to atmospheric conditions exposed environment.

Variation source	SS	DF	AS	Testing F	Value – p	Critical F	Significant Effect
Hydration time (HT)	0,229	1	0,229	9,185	0,039	7,708	Yes
HT*Residue percentage	4,370	4	1,092	43,722	0,001	6,388	Yes

SS- Sum of the squares, DF- Degree of freedom, AS- Average square, Testing F- Statistics F, Value P- Proof Value, Critical F - acceptance zone

In relation to the coloring differences to samples with different hydration time, but same exposure environment, it is noticeable that the results were very close to both environments, however Horgnies et al. [12] reports that the hydration rates must also influence in the final grout aesthetics, besides other factors as relation water/cement, additions and mixture composition, that in case of this present research, the last one caused bigger impact.

The analysis of variance (ANOVA) to the parameter ΔE is presented on Tables 6 and 7.

Table 7. ANOVA of the independent factors and interactions between them in relation to colorimetric ΔE variation to laboratory environment.

Variation source	SS	DF	AS	Testing F	Value – p	Critical F	Significant Effect
Hydration time (HT)	0,133	1	0,133	0,701	0,449	7,708	No
HT*Residue percentage	2,947	4	0,737	3,887	0,108	6,388	No

SS- Sum of the squares, DF- Degree of freedom, AS- Average square, Testing F- Statistics F, Value P- Proof Value, Critical F - acceptance zone

After the analysis of the variance performed, it was verified that some of the control factors and some interactions of first and second order presented significant effect. Besides that, the analysis shows that in the comparison of samples exposed to laboratory environment, the hydration time factor did not have significant influence in the coloring change. Opposite situation is observed on samples exposed to natural environment, showing that the exposure to inclement weather can damage the samples colorimetric intensity.

3.2 Tensile Strength

Figure 11 presents the average results of tensile in Tensile Strength performed at 28 days.

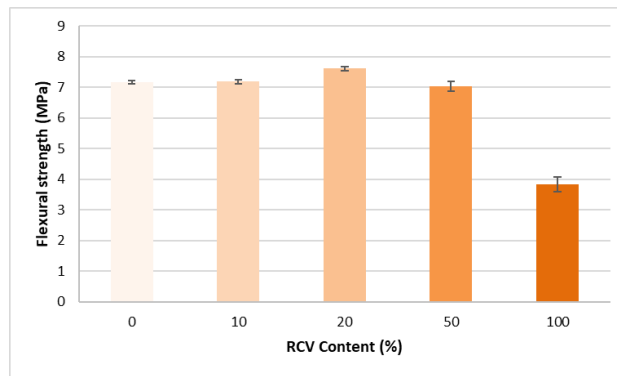


Figure 11. Average results of Resistance to Tensile Strength.

By analyzing Figure 11, it is noticeable that tendency to decrease in the Tensile Strength occurred, while the RCR was incorporated, emphasizing that the trace that showed bigger performance was the 20% one, validating the testing of compressive strength, similar result to Sales and Alferes [10], that by incorporating ceramic powder in concretes verified that the chemical and microstructural properties of residue decreased the Tensile Strength of the cement matrix. However, to evaluate if there was significant decrease among the analyzed traces, a variance analysis (ANOVA) was performed (Table 8).

Table 8. ANOVA of the influence of the content of residues in the Tensile Strength.

Variation source	SS	DF	AS	Testing F	Value – p	Critical F	Significant Effect
Up to 50% RCR content	0,564	3	0,188	0,419	0,744	4,066	No
All RCR levels	28,580	4	7,145	16,272	0,000	3,478	Yes

SS- Sum of the squares, DF- Degree of freedom, AS- Average square, Testing F- Statistics F, Value P- Proof Value, Critical F - acceptance zone

After the analysis ANOVA, it is noticeable that the testing of Tensile Strength demonstrated a significant decrease only to the content of 100% of incorporation, to the other content the samples presented stable resistance when compared the reference sample. Li et al. [5], at using Galvanized Sludge as pigment in grouts, the same stability of traction strength was found, justifying the fact by the fill of the empties in the process of hydration of the paste, as the waste presents smaller granulometry and it has filler effect. However, the authors cited did not replace the small aggregate as in the present research, that in the content with 100% did not use small aggregate in the mixture, only RCR, which generated difficulty of particle bearing, so, many may have been in the perpendicular sense of force applied in the testing of resistance to Tensile Strength, whereas the ceramic waste presents more lamellar grains than the sand ones and generated fragile areas of rupture, justifying the decrease of resistance in this trace.

At evaluating the performance of the mixtures with the ABNT NBR 13281 [18], according to Table 9, it is possible to verify that all grouts were classified as R6, being superior to 3,5 MPa, fact the makes the use of RCR to the increase of mechanical resistance attractive, besides the pigment in grouts.

Table 9. Classification NBR 13281 [18] Tensile Strength.

Class	Tensile Strength MPa	Method of testing
R1	≤ 1,5	ABNT NBR 13279
R2	1,0 to 2,0	
R3	1,5 to 2,7	
R4	2,0 to 3,5	
R5	2,7 to 4,5	
R6	>3,5	

3.3 Compressive Strength

The results obtained in the testing of resistance to compressive strength were performed at 28 days and are presented in the Figure 12 below.

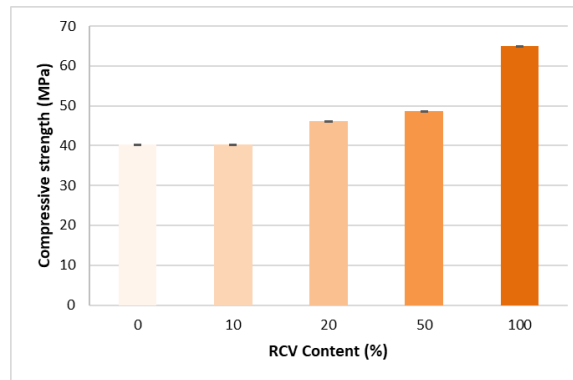


Figure 12. Average results of compressive strength.

It was verified that the content of replacement of sand by the RCR influenced in a significant way in the compression strength, as the variance (ANOVA) analysis shows (Table 10). This is related to the filler effect, with the fill of empties in the cement matrix, and probably to the pozzolan effect of the RCR, which was already verified by Amorim et al. [19], Jacoby and Pelisser [1] and Jang et al. [3], by using pozzolan materials, it occurs addition of compression strength of grouts. Jacoby and Pelisser [1] and Matias et al. [2], affirm that the pozzolan effect along with the fine particles, that is, the filler, reduce the porosity and guarantee bigger compactness of the cement matrix, consequently justifying the increase of compressive strength of the same.

Table 10. ANOVA of the influence of content of residue in compressive strength.

Variation source	SS	DF	AS	Testing F	Value – p	Critical F	Significant Effect
Residue percentage	2.459,947	4	614,987	70,294	0,00	2,759	Yes

SS- Sum of the squares, DF- Degree of freedom, AS- Average square, Testing F- Statistics F, Value P- Proof Value, Critical F - acceptance zone

The increment of compressive strength of cement matrices at incorporating itself pozzolan waste as pigments, besides the adequate destination to a reject like the RCR, are attractive features in civil construction, since as according to Corinaldesi et al. [11] the commercial pigments reduce the compressive strength of concretes and grouts besides not being a sustainable alternative. By comparing the compression strength with the classifications of ABNT NBR 13281 [18], it is noticeable on Table 11 that all grouts are classified as P6, which is >8 MPa, thus reaffirming the viability in the use of RCR, since it contributes on mechanical properties of composite.

Table 11. Classification of grouts in relation to compressive strength.

Class	Compressive strength MPa	Method of testing
P1	≤ 2,0	ABNT NBR 13279
P2	1,5 to 3,0	
P3	2,5 to 4,5	
P4	4,0 to 6,5	
P5	5,5 to 9,0	
P6	> 8,0	

3.4 Relation Between the Compressive and to Tensile Strength

By analyzing Table 12 and the results cited above, it is noticeable that the residue of RCR influences more significantly in the compressive strength, whereas in the Tensile Strength, it is noticed a tendency of constancy of the results with different content of incorporation of residue. Authors as Amorim et al. [19], Jacoby and Pelisser [1] and Jang et al. [3] report that because the ceramic residue has pozzolan effect and microparticles, it tends to react in the mixture so by their chemical properties and generate better packing of the grains with the filler effect, thus generating an addition in the resistance of the grout. Yet Li et al. [5], found the same stability of Tensile Strength in their studies by incorporating galvanized sludge in the grouts. The common sense of the performed researches in materials similar to RCR is that the residue generates better fill of the empties in the mixture and it provides a pozzolan reaction, avoiding the significant decrease of the resistances of the grouts, even if the small aggregate is removed from the compositions of it. Thus, seen that the traces frame themselves inside the limits of the Brazilian standards, the RCR presents potential of application in grouts [19].

Table 12. Compression and to Tensile Strength.

Content (%)	Compression strength (MPa)	Average detour Rc	Tensile Strength (MPa)	Average detour (Rt)
0	40,31	1,32	7,17	0,22
10	40,23	1,05	7,19	0,35
20	46,19	0,92	7,62	0,33
50	48,57	4,29	7,03	0,79
100	64,94	2,05	3,84	0,64

4 CONCLUSIONS

Based on the results obtained with this study, it was possible to verify the following findings:

- By analyzing the L parameter, which is, the luminosity, it is noticeable that the increase of the content of replacement of sand by RCR influenced in a significant way on the colorimetric properties of the grouts, presenting lower luminosity, in other words, a bigger coloring, while the RCR was incorporated, having the distinct cure environment not influenced significantly on this property. The content of 100% was the one that presented lower luminosity and consequently better coloring.
- The different environments used in the cure process, caused colorimetric variations in the grouts by analyzing the parameter ΔE , whereas the samples exposed to inclement weather presented bigger differences of pigment in the time gaps analyzed.
- Concomitantly to the increase of the content of RCR in the grouts there has been an addition of compression strength.
- The trace with the content of 20% presented the best performance of Tensile Strength, whereas in the others, a decrease occurred in this property when adding RCR.
- Relating the compressive strength and the tensile strength to the color of the samples, it was found that the trace that guaranteed the appropriate mechanical properties and satisfactory coloring in relation to the reference was the 50% incorporation of red ceramic, since the trace with 100% of incorporation obtained the most pigmented color, but presented a brittle surface. However, even with the drop in tensile strength in the line with 100% RCR incorporation, all mortars obtained classification according to NBR 13281 of P6 and R6 for compressive strength and tensile strength, respectively, being thus indicated for use and reaffirming the feasibility of incorporating RCR into the mixtures.
- Therefore, the viability of RCR use to replace the small aggregate in grouts being demonstrated, studies, in order to analyze the real influence of this residue in a long-term within the composite, are required.

REFERENCES

- [1] P. C. Jacoby and F. Pelisser, "Pozzolanic effect of porcelain polishing residue in Portland cement," *J. Clean. Prod.*, vol. 100, pp. 84–88, Aug 2015.
- [2] G. Matias, P. Faria, and I. Torres, "Lime mortars with ceramic wastes: characterization of components and their influence on the mechanical behaviour," *Constr. Build. Mater.*, vol. 73, pp. 523–534, Dec 2014.

- [3] H. Jang, H. Kang, and S. So, "Color expression characteristics and physical properties of colored mortar using ground granulated blast furnace slag and white Portland cement," *KSCCE J. Civ. Eng.*, vol. 18, no. 4, pp. 1125–1132, Apr 2014.
- [4] M. C. Zurita Ares, E. Villa González, A. I. Torres Gómez, and J. M. Fernández, "An easy method to estimate the concentration of mineral pigments in colored mortars," *Dyes Pigments*, vol. 101, pp. 329–337, Feb 2014.
- [5] H. Li, X. Yang, Z. Suo, Y. Xia, and D. He, "Red cement-based decorative mortar prepared with dry electroplating sludge containing Pb as red pigment," *Journal of Wuhan University of Technology-Mater. Sci. Ed.*, vol. 29, pp. 291–297, Apr 2014.
- [6] M. V. Diamanti, B. Del Curto, M. Ormellese, and M. P. Pedferri, "Photocatalytic and self-cleaning activity of colored mortars containing TiO₂," *Constr. Build. Mater.*, vol. 46, pp. 167–174, Sep 2013.
- [7] G. Lemaire, G. Escadeillas, and E. Ringot, "Evaluating concrete surfaces using an image analysis process," *Constr. Build. Mater.*, vol. 19, no. 8, pp. 604–611, Oct 2005.
- [8] A. López, J. M. Tobes, G. Giaccio, and R. Zerbino, "Advantages of mortar-based design for coloured self-compacting concrete," *Cement Concr. Compos.*, vol. 31, no. 10, pp. 754–761, Nov 2009.
- [9] H. Lee, J. Lee, and M. Yu, "Influence of iron oxide pigments on the properties of concrete interlocking blocks," *Cement Concr. Res.*, vol. 33, no. 11, pp. 1889–1896, Nov 2003, [http://dx.doi.org/10.1016/S0008-8846\(03\)00209-6](http://dx.doi.org/10.1016/S0008-8846(03)00209-6).
- [10] A. T. C. Sales and R. S. Alferes Fo., "Efeito do pó de resíduo cerâmico como adição ativa para concreto," *Ambient. Constr.*, vol. 14, no. 1, pp. 113–125, Jan/Mar 2014.
- [11] V. Corinaldesi, S. Monosi, and M. L. Ruello, "Influence of inorganic pigments' addition on the performance of coloured SCC," *Constr. Build. Mater.*, vol. 30, pp. 289–293, 2012.
- [12] M. Horgnies, E. Darque-Ceretti, E. Gueit, and M. Aucouturier, "Characterisation of the variations of tint and the adhesion of pigments onto the surface of mortar," *Constr. Build. Mater.*, vol. 94, pp. 380–386, Sep 2015.
- [13] Associação Brasileira de Normas Técnicas, *Argamassa para Assentamento e Revestimento de Paredes e Tetos – Preparo da Mistura e Determinação do Índice de Consistência*, NBR 13276: 2016, 2005.
- [14] Instituto Nacional de Meteorologia. "Estações e dados." INMET. <http://www.inmet.gov.br> (accessed May 22, 2018).
- [15] D. Vázquez-Nion, P. Sanmartin, B. Silva, and B. Prieto, "Reliability of color measurements for monitoring pigment content in a biofilm-forming cyanobacterium," *Int. Biodeterior. Biodegradation*, vol. 84, pp. 220–226, Oct 2013.
- [16] Associação Brasileira de Normas Técnicas, *Argamassa para Assentamento e Revestimento de Paredes e Tetos – Determinação da Resistência à Tração na Flexão e à Compressão*, NBR 13279: 2005, 2005.
- [17] S. R. Prim, M. V. Folgueras, M. A. de Lima, and D. Hotza, "Synthesis and characterization of hematite pigment obtained from a steel waste industry," *J. Hazard. Mater.*, vol. 192, no. 3, pp. 1307–1313, Sep 2011.
- [18] Associação Brasileira de Normas Técnicas, *Argamassa para Assentamento e Revestimento de Paredes e Tetos – Requisitos*, NBR 13281: 2005, 2005.
- [19] L. V. Amorim, H. L. Lira, and H. C. Ferreira, "Use of residential construction waste and residues from red ceramic industry in alternative mortars," *J. Environ. Eng.*, vol. 129, no. 10, pp. 916–920, Oct 2003.

Author contributions: LAD: funding acquisition, methodology, conceptualization, writing, analysis; FBB and LK: methodology, conceptualization, analysis; DCMA and ASV: conceptualization, writing, supervision.

Editors: Bernardo Tutikian, Guilherme Aris Parsekian.



ORIGINAL ARTICLE

Probabilistic analysis of slab-column connections subjected to punching shear according to the ABNT NBR 6118 (2014) recommendations considering the model error measure

Análise probabilística de ligações laje-pilar submetidas à punção segundo as recomendações da ABNT NBR 6118 (2014) considerando a medida do erro de modelo

Náyra Louise Alonso Marque^a 
 Caio Gorla Nogueira^a 

^aUniversidade Estadual Paulista – UNESP, Departamento de Engenharia Civil e Ambiental, Bauru, SP, Brasil

Received 12 November 2020
 Accepted 15 March 2021

Abstract: Reinforced concrete flat slabs are structural systems in which slabs are directly supported by columns, without the use of beams. A structural phenomenon that deserves attention in these systems is the punching shear, characterized by the occurrence of shear stresses close to the slab-column interface, which can produce fragile rupture in those regions. This study presents some results of reliability index β obtained for slab-column connections based on FORM, according to the Brazilian standard's model, considering the model error. The critical contours C and C' without shear reinforcement are analyzed. The results showed that failure in the C contour is very unlikely, while the probabilities of rupture in the C' contour when considering the influence of the model error are greater than the target values recommended in the literature for the ULS.

Keywords: slab-column connection, punching shear, reliability, reinforced concrete.

Resumo: Lajes lisas de concreto armado são sistemas estruturais compostos por lajes diretamente apoiadas em pilares, sem o uso de vigas. Um fenômeno estrutural que merece atenção nesses sistemas é a punção, caracterizada pela ocorrência de tensões de cisalhamento nas proximidades da interface laje-pilar, que podem produzir ruptura frágil nessas regiões. Este estudo apresenta resultados do índice de confiabilidade β obtidos para ligações laje-pilar a partir de análises de confiabilidade utilizando o FORM, segundo o modelo da norma brasileira, considerando o erro de modelo. Os contornos críticos C e C' sem armadura de punção são analisados. Os resultados mostraram que a falha no contorno C é muito improvável, enquanto que as probabilidades de ruptura no contorno C' quando se considera a influência do erro de modelo são maiores que valores alvo recomendados na literatura para o ELU.

Palavras-chave: ligação laje-pilar, punção, confiabilidade, concreto armado.

How to cite: N. L. A. Marque and C. G. Nogueira, "Probabilistic analysis of slab-column connections subjected to punching shear according to the ABNT NBR 6118 (2014) recommendations considering the model error measure," *Rev. IBRACON Estrut. Mater.*, vol. 14, no. 6, e14609, 2021, <https://doi.org/10.1590/S1983-41952021000600009>

1 INTRODUCTION

Flat slab systems have been used frequently in multi-storey buildings replacing conventional systems defined by slabs, beams and columns. The main characteristic of flat slabs is the absence of beams and the load direct transference from slabs to columns. Regarding the conventional mentioned system, the flat slabs have some advantages: agility to execute the framework of the slab panels, reduction in the interference between the structural elements and the hydro-sanitary installations; better standardization of the shoring; reduction in the total height of the building; less concrete

Corresponding author: Caio Gorla Nogueira. E-mail: caio.nogueira@unesp.br

Financial support: The authors would like to thank FAPESP (process number 2018/06562-4) for the financial support to this research work.

Conflict of interest: Nothing to declare.



This is an Open Access article distributed under the terms of the Creative Commons Attribution License, which permits unrestricted use, distribution, and reproduction in any medium, provided the original work is properly cited.

waste [1]. However, there are some aspects on the structural behavior of these systems that must be carefully analyzed, which are: global stability of the building and the punching shear phenomenon in the slab-column connection. The absence of rigid frames (no beams in the structural system) may lead to excessive transversal displacements overcoming the allowable values recommended by the normative codes. In such cases, different bracing systems must be combined to the columns to provide the global stability of the building.

Punching shear is an Ultimate Limit State – ULS [2] caused by the stress concentration in specific regions of the slab around the column. The column tends to penetrate the slab leading to a brittle failure mode as depicted in Figure 1b. When the rupture is imminent, a punching cone can be seen around the column due to the principal tensile stresses produced by the acting shear stresses in the slab-column connection. In a building floor, the position of the column (central, border or edge) acts directly on the punching shear phenomenon because the boundary conditions affect the stress distribution in the slabs (Figure 1a).

The stress distribution in the slab at the proximities of the column has a complex behavior, especially because, besides the shear stresses, there are also the presence of normal stresses come from the negative bending moments acting at the top of the slab. In this way, there are several mechanisms of energy dissipation produced by the stress transference process at the slab-column connections, which makes difficult to develop accurate and simple analytical models to predict the punching shear resistance of those connections. In general, the normative codes present analytical models to estimate the punching shear resistance of the slab-column connection. These models can also be used to design shear reinforcement disposed around the slab-column interface, in order to prevent the formation of the punching cone. The theoretical bases of these normative predicting models are the Surface Control Method, which compares the acting and resistant shear stresses in particular regions near the slab-column interface [4]. Each standard code differs from each other by the definition of these particular regions, in which the safety requirements are evaluated.

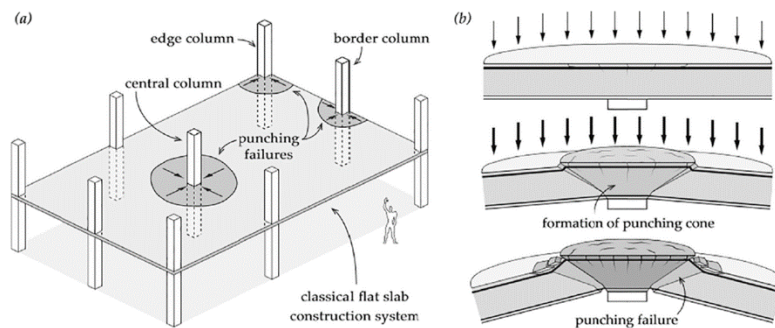


Figure 1. (a) Slab regions submitted to punching shear for the three different column positions; (b) first cracks formation; punching cone at the imminence of rupture for central columns; punching shear failure at the slab-column connection [3].

Several national [5]–[18] and international [19]–[28] researches have been performed to better understand the punching shear phenomenon, since the first cracks initiation until failure, with or without shear reinforcement. The combination of these two areas, which are the experimental study of the phenomenon and the application of the normative/theoretical analytical models to predict bearing capacity is a relevant effort in order to estimate the precision and uncertainties associated to those models [6], [29]–[32]. Regarding the uncertainties field, the design parameters of the slab-column connections, which are concrete and steel strength, slab thickness and column cross section dimensions can be also considered as random quantities because of the inherent variability, lack of knowledge and data about them and even human errors that can occur in the execution phase. Therefore, a well-known fact must be remembered here: if there are uncertainties on the input data to predict punching shear behavior, there will be uncertainty on the final response of such process, which is the punching bearing capacity of a slab-column connection.

In this scenario, the Reliability Theory has been adopted to estimate probabilities of failure for ULS in different types of slab-columns connections, considering parameters uncertainties. Reliability analysis estimates on the adequacy of normative design procedures, including the accuracy of the prediction models and the recommended set of partial design factors [33], [34]. In such regard, model errors are also defined as a good indicator of general quality and accuracy of the analytical prediction models. These errors are constructed by comparison between experimental and predicted analytical values of ultimate load, for example. This is a procedure to incorporate the model uncertainty in the reliability analysis and will be better illustrated later.

In this context, this article presents a set of reliability analyzes for slab-column connections applied to central, border and edge columns without shear reinforcement, considering the ABNT NBR 6118 [35] theoretical prediction model. The model uncertainty was obtained for each type of column and taken into account in the reliability analyzes carried out by FORM (First Order Reliability Method).

2 ABNT NBR 6118 PREDICTION MODEL FOR PUNCHING SHEAR

According to the Brazilian code ABNT NBR 6118 [35], some special regions around de slab-column connection must be verified in order to guarantee the safety of the system. These regions are called critical perimeters and are defined for each type of column (central, border and edge). In cases without shear reinforcement, there are two regions to verify: interface of the slab and column (critical perimeter C); a region around the column defined by $2d$ distance from the interface slab-column (critical perimeter C'). Figure 2 illustrates the critical perimeters C and C' for each type of analyzed column, in which d is the slab serviceable thickness.

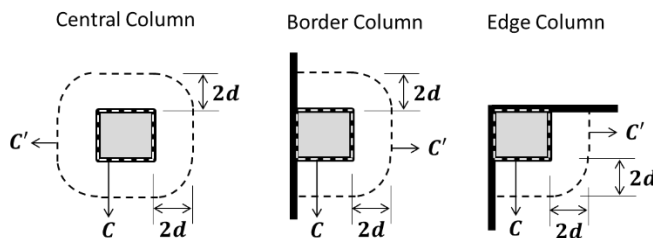


Figure 2. Critical perimeters C and C' defined for central, border and edge columns according ABNT NBR 6118 [35].

For the critical perimeters C and C' , the verifications refer to the safety of the concrete diagonal compression τ_{Rd2} along the slab thickness and the concrete diagonal tensile τ_{Rd1} , respectively. The analytical models to assess the slab-column connection resistance for the two cited critical perimeters are given by:

$$\tau_{Rd2} = 0,27 \left(1 - \frac{f_{ck}}{250} \right) f_{cd} \tag{1}$$

$$\tau_{Rd1} = 0,13 \left(1 + \sqrt{\frac{20}{d}} \right) (100 \rho f_{ck})^{\frac{1}{3}} \tag{2}$$

In which: f_{ck} is the characteristic concrete compressive strength; f_{cd} is the design concrete compressive strength given by $f_{ck} / 1,4$; d is the slab serviceable thickness; ρ corresponds to the bending reinforcement geometric ratio of the slab given by $\sqrt{\rho_x \rho_y}$; ρ_x and ρ_y are the bending reinforcement geometric ratio of the slab at the orthogonal directions x and y .

The acting shear stress for central and border columns are given by Equation 3, in which the concentrated load (F) applied by the columns at the slab, as well as the presence of the two bending moments (M_1 e M_2) are considered. Regarding the edge columns and the existence of two free borders, the acting shear stress must be addressed for each border separately, considering the bending moment which is perpendicular to the adopted free border [35]. The ABNT NBR 6118 [35] make some recommendations about when to consider or not the presence of bending moment in central, border and even edge columns. However, such recommendations will be not discussed in this article, but they can be found at the cited code and [4]–[6].

$$\tau_{sd} = \frac{F}{u d} + \frac{K_1 M_1}{W_{p1} d} + \frac{K_2 M_2}{W_{p2} d} \tag{3}$$

In which: τ_{sd} is acting shear stress; u is the critical perimeter depending on the type of the column and the respective analyzed region; K_1 and K_2 are the coefficients that represent the bending moment portion transferred to the column by shear. The resultant values for K_1 and K_2 can be found in Lima [4]. W_{p1} e W_{p2} are the plastic resistance modulus of the critical perimeter, whose equations for rectangular central column can be found in ABNT NBR 6118 [35] and in Melges [6] for rectangular border and edge columns. The Brazilian code adopts, for central columns, a surface $2d$ from the interface slab-column (Figure 2) as the critical contour C' with perimeter $u = 2(C_1+C_2) + 4\pi d$. For instance, C_1 and C_2 are, respectively, the column cross section dimensions parallel and orthogonal to the considered eccentricity. On the other hand, for border and edge columns, the critical perimeter of C' surface can be evaluated with a reduction, as depicted in Figure 3.

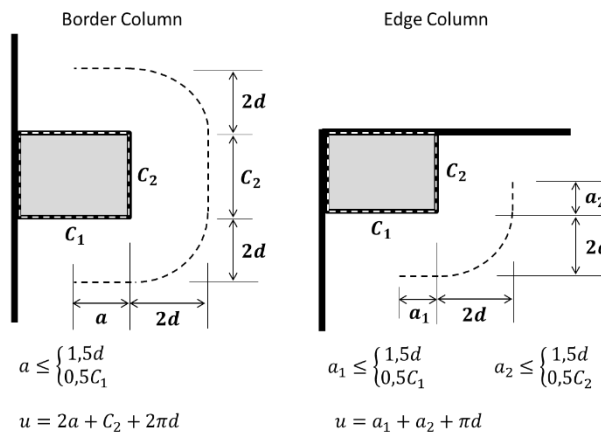


Figure 3. Reduced critical perimeters of C' contour for border and edge columns.

The acting shear stress (Equation 3) is still valid for cases with just one bending moment or even only the normal force. In such cases, the referred portions must be zero for the assessing of τ_{sd} .

3 MODEL ERROR UNCERTAINTY QUANTIFICATION

A model error variable was defined to consider the uncertainty of the ABNT NBR 6118 [35] punching shear resistance prediction model. The model error (E_m), for each type of column, is given by the ratio between experimental rupture load (F_{exp}) and normative theoretical prediction (F_{teo}) as:

$$E_m = \frac{F_{exp}}{F_{teo}} \tag{4}$$

The normative theoretical prediction force was obtained by Equation (3) for critical perimeter C' . In all the analyzed experimental results in literature [1], [5], [7], [9]–[18], [19]–[28], [36]–[42], no punching shear failure in critical contour C was observed, but only near at the critical perimeter C' . Therefore, the model error refers only to the C' . Another aspect worth to mention is about the implicit safety factor (1,4) in the Equation 2 at the coefficient 0,13. According to Carvalho et al. [1], the Brazilian code adopts the same model as the Eurocode 2 [43], in which the value of 0,13 is reached by 0,18/1,4. Thus, in the reliability analyzes, the new coefficient that will be used is 0,18 instead 0,13 in order to eliminate such safety factor. Regarding the concrete compressive strength, the used value to assess the theoretical prediction force was always the same value that was considered at the experimental results, which is f_c instead f_{ck} .

The model error was calculated for each type of column from comparisons between experimental and theoretical rupture forces (Equation 4) considering: 126, 74 and 13 experimental results for central, border and edge column, respectively [1], [5], [7], [9]–[18], [19]–[28], [36]–[42]. Only experimental slab-column connections failed by punching shear were considered in the model error calibration. Flexural failures were all rejected. The experimental data were not separated in different sub-sets with specific ranges of slab thickness or longitudinal reinforcement rates; they are

treated as a single set of data. In order to choose the best probability distribution for each model error, the Kolmogorov-Smirnov test was performed for normal and lognormal distributions with significance level of 5%. The model error uncertainty quantification results are shown in Table 1. The significant differences among the mean value and the respective coefficients of variation for the three slab-column connections could be associated to the different stress distribution around the columns and to the differences from the longitudinal reinforcement rates. All the consulted data used to perform the error model quantification are presented in Tables A1, A2 and A3 in the Appendix. It is also shown in the Appendix the identified tendencies of the error model according to some design parameters of the slab-column connections.

In order to make some comparisons, the model error statistics was evaluated considering more than 120 experimental results for slab-central column connections and the ABNT NBR 6118 [35] punching shear resistance prediction model without shear reinforcement [29]. The related results shown 0,96 mean value and coefficient of variation equal to 14,1%.

Table 1. Model error random variable for critical perimeter C' .

	Mean Value	Standard Deviation	Coefficient of Variation	Probability Distribution
Central Column	0,962	0,197	20,5%	Normal
Border Column	1,151	0,246	21,4%	Lognormal
Edge Column	1,363	0,404	29,7%	Lognormal

4 STRUCTURAL RELIABILITY APPLIED TO PUNCHING SHEAR ANALYSIS

The scientific and technical demand for uncertainty quantification has grown significantly in the last decade. The following basic premises support such demand: i) the growing perception that everything is surrounded by uncertainties; ii) if there are uncertainties in the input, there will be uncertainties in the output [44]. Hence, there will always be a probability that designed engineering system does not achieve the defined specifications of operation, generating undesirable engineering scenarios.

The concept of probability of failure must be understood as a propensity measure (subjective or Bayesian definition) that a component and/or system is unable to meet the design requirements along a specific lifetime, even when the recommendations and operation conditions are respected [45]. The Reliability Theory can be an interesting approach to estimate those probabilities of limit state violation for isolated components and/or structural systems.

In this article, the analyzed failure modes are due to the ruin (ULS) of the slab-column connection by punching shear in pre-defined regions according to ABNT NBR 6118 [35]. The Limit State Functions (LSF) of the failure modes are defined in terms of safety margin as $G = R - S$, in which R and S stands for the resistance and solicitation of the slab-column connection and are represented by shear stresses at specific regions.

The failure punching shear event occurs when $G = R - S < 0$ condition is achieved; otherwise the safety/survival event of the slab-column connection is represented by $G > 0$. When $G = 0$, the event $R = S$ is defined meaning the imminence of the failure. Therefore, the reliability analyzes aim to estimate de probability of failure, which represents the event $G \leq 0$.

The reliability problem is solved in the Standard Gaussian space Y . In this space, the random variables are dimensionless with mean value zero and standard deviation equal to 1. The condition $G = 0$ in the Y space refers to the boundary of failure and safety domain. The shortest distance between the origin of the Y space and the limit state equation $G = 0$ represents the reliability index β [46]. The point located at the surface $G = 0$ is called design point Y^* and provides the probability of failure P_f for that failure mode. Therefore, the reliability index can also be interpreted as a safety measure because the higher β , the lower probability of failure. For instance: for $\beta = 0 \rightarrow P_f = 0,50$; $\beta = 1,645 \rightarrow P_f = 0,05$; $\beta = 3,8 \rightarrow P_f = 5 \times 10^{-5}$; $\beta = 5,0 \rightarrow P_f = 2,9 \times 10^{-7}$. The probability of failure is given by $P[G \leq 0] = \Phi(-\beta)$, in which $\Phi(\cdot)$ represents the cumulative density function of probabilities at the Standard Gaussian space Y .

It is important, after the reliability index and probability of failure assessment, to compare the obtained values to target references. The punching shear failure is an occurrence of ULS, with moderate to high failure consequences [47], according to total and building construction costs ratio. Table 2 shows minimum values for β and P_f in ULS recommended by the European code EN 1990:2002 [48], for three risk classes, defined by the consequences of failure with 50 years return period [49].

For effect of comparison, in this article, it was adopted $\beta_{min} = 3,8$ for ULS with moderate consequences of failure.

Table 2. Minimum reliability index recommended by EN 1990:2002 for a 50-year return period [48].

Failure Consequences		
Low	Moderate	High
$\beta_{min} = 3,3 \quad P_f \approx 5 \times 10^{-4}$	$\beta_{min} = 3,8 \quad P_f \approx 5 \times 10^{-5}$	$\beta_{min} = 4,3 \quad P_f \approx 10^{-5}$

The reliability problem is formulated from the following information: limit state functions definition for each critical perimeter of the all three columns; table with the all the random variables including the model error. The Figure 4 shows two flowcharts illustrating the performed reliability analyzes. They are explained below.

There are two sets of analyzes in which the legend C, B, E means central, border and edge column, respectively.

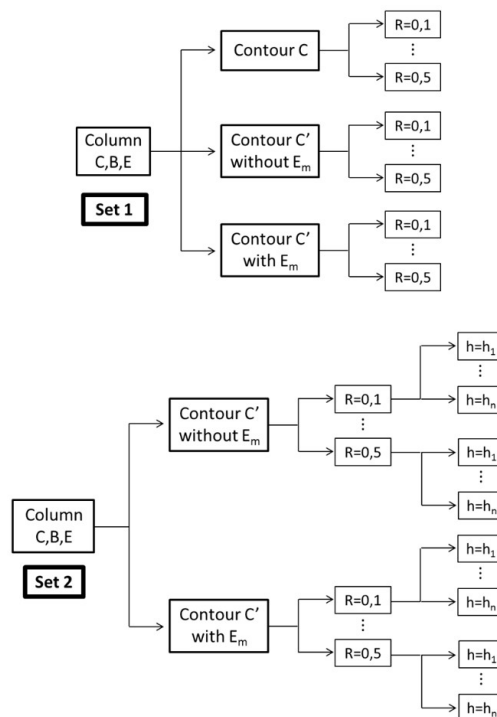


Figure 4. Flowchart of the performed reliability analyzes.

Regarding the set 1, three sub-sets for each type of column were performed: at sub-set 1, the failure mode is given by the critical perimeter C without the model error; at sub-sets 2 and 3, the failure mode is given by the critical perimeter C' without and with the model error, respectively. For all these performed analyzes, the mean value of the slab thickness is kept constant, but the loading ratio R varies between 0,1 and 0,5 with increment of 0,1. The loading ratio R is defined by the ratio between the live load q and the total load $g + q$ (dead load plus living load), given by $R = \frac{q}{(g + q)}$.

The second set of analyzes considers the same three types of columns, but only for the sub-sets 2 and 3, which are failure mode given by the critical perimeter C' without and with the model error, respectively. The main difference between the sub-sets 1 and 2 is that the mean slab thickness, at sub-set 2, varies with an increase of 1 cm in a pre-fixed range, but keeping the coefficient of variation constant. For each value of the loading ratio R (0,1 to 0,5), this slab thickness variation is performed.

The analyzed slab-column connections (central, border and edge column) in this paper belong to a flat slab building studied and presented by Lima [4]. The rectangular flat slab was designed with thickness = 18 cm; concrete cover = 2 cm; reinforcement bars at the two orthogonal directions according with the parallel borders of the slab = 12,5 mm diameter; $f_{ck} = 30$ MPa. The distance between two parallel longitudinal bars varies with the type of column and will be mentioned later for each analyzed case.

The limit state functions for each described failure mode were defined by the safety margin written as: $G(\mathbf{X}) = R(\mathbf{X}) - S(\mathbf{X})$, in which \mathbf{X} is the random variable vector. For each critical perimeter, the limit state functions of the central and border columns are listed below. In case of the edge column, it is only necessary to eliminate the last term of the acting shear stress in all the limit state functions.

- Critical Perimeter C:

$$R(\mathbf{X}) = 0,27 \left(1 - \frac{f_c}{250} \right) f_c \tag{5}$$

- Critical Perimeter C' without Model Error:

$$R(\mathbf{X}) = 0,18 \left(1 + \sqrt{\frac{20}{d}} \right) (100 \rho f_c)^{\frac{1}{3}} \tag{6}$$

- Critical Perimeter C' with Model Error:

$$R(\mathbf{X}) = E_m \times \left[0,18 \left(1 + \sqrt{\frac{20}{d}} \right) (100 \rho f_c)^{\frac{1}{3}} \right] \tag{7}$$

The $S(\mathbf{X})$ in all cases is given by:

$$S(\mathbf{X}) = \left(\frac{F_g + F_q}{u d} + \frac{K_1 (M_{g,1} + M_{q,1})}{W_{p1} d} + \frac{K_2 (M_{g,2} + M_{q,2})}{W_{p2} d} \right) 10 \tag{8}$$

In which: F_g and F_q in kN are, respectively, the dead and live load; $M_{g,1}$, $M_{q,1}$, $M_{g,2}$ and $M_{q,2}$ in kNcm are, respectively, the dead and live bending moment at directions 1 and 2. In the reliability analyzes, no safety factor was used. The constant number 10 multiplying $S(\mathbf{X})$ was adopted to guarantee the MPa unity as the same for $R(\mathbf{X})$. The acting bending moments were calculated from the product between the corresponding portion of the load (dead or live) and the respective eccentricity. The values of eccentricities were adopted, for each direction and each column, according with Lima [4].

Table 3. Adopted random variables: general presentation.

Random Variable	Symbol	Coefficient of Variation	Probability Distribution
Concrete compressive strength [50]	f_c (MPa)	14%	Lognormal
Slab thickness [51]	h (cm)	4%	Normal
Distance between the geometrical center of the upper negative reinforcement and the compressed concrete bottom face [52]	d' (cm)	12,5%	Normal
Column dimension parallel to the load eccentricity [52]	C_1 (cm)	4%	Normal
Column dimension orthogonal to the load eccentricity [52]	C_2 (cm)	4%	Normal
Total load eccentricities [52]	e_x, e_y (cm)	10%	Normal
Dead load [53]	F_g (kN)	10%	Normal
Live load [53]	F_q (kN)	25%	Gumbel max type I

Table 3 presents all the random variables of the reliability problem. The serviceable thickness of the slab d is given by $h - d'$. The coefficient of variation and probability density function for all the random variables were defined from the literature information, except the statistics of the model error. No correlation between pair of random variables was adopted.

Table 4 gathers the random variables values for the three slab-column connections. The used legend in the table stands for: R.V. is the symbol of the random variable according to the definition in Table 3; μ and σ correspond, respectively, to the mean value and the standard deviation for each random variable.

Table 4. Values of the Random Variables for the three types of columns: set 1.

R.V.	Central Column		Border Column		Edge Column	
	μ	σ	μ	σ	μ	σ
f_c (MPa)	38,98	5,46	38,98	5,46	38,98	5,46
h (cm)	18,00	0,72	18,00	0,72	18,00	0,72
d' (cm)	3,25	0,41	3,25	0,41	3,25	0,41
C_1 (cm)	30,00	1,20	40,00	1,60	30,00	1,20
C_2 (cm)	40,00	1,60	30,00	1,20	30,00	1,20
e_x (cm)	3,98	0,40	48,00	4,80	56,31	5,63
e_y (cm)	9,12	0,91	11,52	1,15	-	-
F_g (kN)	R = 0,1 \rightarrow 311,18	31,12	R = 0,1 \rightarrow 168,08	16,81	R = 0,1 \rightarrow 72,90	7,29
	R = 0,2 \rightarrow 276,60	27,66	R = 0,2 \rightarrow 149,40	14,94	R = 0,2 \rightarrow 64,80	6,48
	R = 0,3 \rightarrow 242,03	24,20	R = 0,3 \rightarrow 130,73	13,07	R = 0,3 \rightarrow 56,70	5,67
	R = 0,4 \rightarrow 207,45	20,75	R = 0,4 \rightarrow 112,05	11,21	R = 0,4 \rightarrow 48,60	4,86
	R = 0,5 \rightarrow 172,88	17,29	R = 0,5 \rightarrow 93,38	9,34	R = 0,5 \rightarrow 40,50	4,05
F_q (kN)	R = 0,1 \rightarrow 32,93	8,23	R = 0,1 \rightarrow 17,79	4,45	R = 0,1 \rightarrow 7,71	1,93
	R = 0,2 \rightarrow 65,86	16,46	R = 0,2 \rightarrow 35,57	8,89	R = 0,2 \rightarrow 15,43	3,86
	R = 0,3 \rightarrow 98,79	24,70	R = 0,3 \rightarrow 53,36	13,34	R = 0,3 \rightarrow 23,14	5,79
	R = 0,4 \rightarrow 131,71	32,93	R = 0,4 \rightarrow 71,14	17,79	R = 0,4 \rightarrow 30,86	7,71
	R = 0,5 \rightarrow 164,64	41,16	R = 0,5 \rightarrow 88,93	22,23	R = 0,5 \rightarrow 38,57	9,64

According to Lima [4], the bending reinforcement geometric ratio ρ of the slab for central, border and edge columns are, respectively: 0,856%; 0,663% and 0,482%. These values were directly adopted from the cases analyzed by Lima [4] for all the reliability analysis of set 1. For the set 2, as the slab thickness varied, new bending reinforcement geometric ratios were calculated, remaining the same concrete strength.

5 RESULTS AND DISCUSSION

5.1 Central Column

Figure 5 shows the evolution of the reliability index for each loading ratio considering the two critical contours C and C' . Two cases of solicitation were analyzed: only the axial force F and axial force plus the two bending moments M_x and M_y . The model error E_m was considered only in the contour C' with all the solicitations simultaneously.

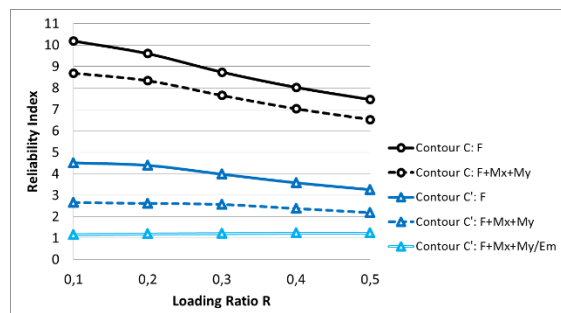


Figure 5. Reliability index × loading ratio: set 1 central column.

The sensitivity factors of the random variables are depicted in Figure 6. These sensitivity factors represent the relative importance of each R.V. in the reliability indices for the analyzed failure modes. The higher the sensitivity factor, the higher is the influence of that R.V. on the safety measure of the slab-column connection. As we can see, for the critical perimeter C , the reliability indices were very high (above 6,0), indicating high safety levels for this failure mode. The results represent the consulted experimental test and are in agreement with the evidences, in which, there was no observed punching shear failure at the interface slab-central column. For the critical perimeter C , the sensitivity factors showed the most influential random variables on the probability of failure: concrete compressive strength f_c and the live load F_q for $R \geq 0,2$ (Figure 6a). These results are coherent, since the concrete compressive strength is the only random variable in the $R(X)$ for the limit state function of the contour C . On the other hand, the live load has the higher coefficient of variation (25%), which means the higher variability among the solicitation random variables.

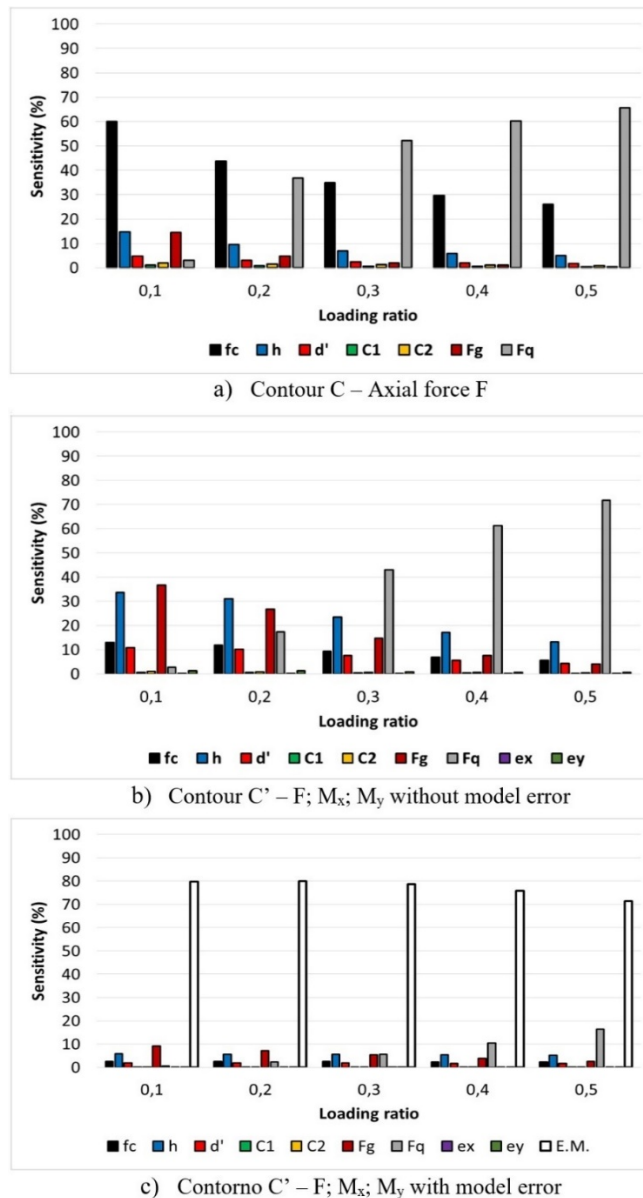


Figure 6. Sensitivity factors × loading ratio: set 1 central column.

In general, for cases without model error, the reliability index decreased as the loading ratio increased because the influence of the live load portion at the total solicitation increased too. However, as shown in Figure 6b, the most

significant random variables for the contour C' was the slab thickness and the live load. The slab thickness plays a doubly important role on the slab-column connections punching shear resistance, since they increase the resistant portion $R(X)$ and decrease the solicitation portion $S(X)$. In comparison to the target (minimum) reliability index of 3,8, the observed safety levels were below the referenced target value. Thus, depending on the sensitivity of the random variables, for the analyzed case, it is possible to recommend increasing the slab thickness to improve the safety of the connection against punching shear.

When the model error E_m was considered, the reliability index remained practically constant regardless of the increase in R . The sensitivity factors (Figure 6c) showed that the influence of the model error was always preponderant, even with the increase of the live load. For central columns, the model error has mean value less than 1,0 and almost 20% coefficient of variation, which means a reduction on the $R(X)$ with high variability. Therefore, a large decrease in β was observed when compared to the same case of failure in the contour C' without model error. This evidence is coherent and may be an indication of the need to improve the quality of the punching shear theoretical prediction model and/or the partial design factor for punching failure should be revised. For all the analyzed cases, the random variables of geometry, which are, cross section column dimensions and eccentricities did not show significant influence on P_f .

Figure 7 shows the set 2 of analyzes. The results shown refer only to the β for the contour C' with axial force and both bending moments, without and with model error. The analytical analysis based on the punching shear prediction model presented in the Brazilian code indicated that the acting shear stress is less than the contour C' resistance only when the slab thickness reaches 23 cm. Regardless of the loading ratio, for $h = 23 \text{ cm}$, the reliability indices were greater than 4,0, indicating a sufficient safety level for the slab-column connection. However, for $h = 22 \text{ cm}$, considering the probabilistic analysis via structural reliability theory, the target condition of $\beta \geq 3,8$ is satisfied. When the model error (Figure 7b) is considered, it was observed that the lack of uniformity of β for different values of R (Figure 7a) was eliminated. On the other hand, a great reduction in β values was observed, even for high slab thickness. Again, this occurred due to a mean value of the model error less than 1 and high uncertainty associated with the prediction model of the Brazilian code.

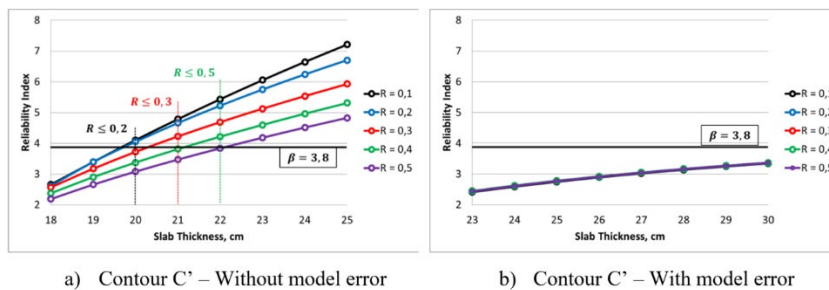


Figure 7. Reliability index \times slab thickness: set 2 central columns.

5.2 Border Column

Figure 8 shows the results in terms of β for the critical contours C, C' with and without E_m for all the loading ratios in two situations: the axial force F plus the bending moment M_x and axial force F plus the two bending moments M_x and M_y . The model error was considered only for contour C' with the presence of axial force and the two bending moments acting simultaneously.

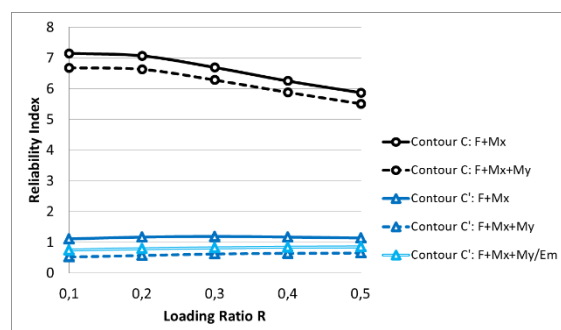


Figure 8. Reliability index \times loading ratio: set 1 border column.

As observed for the central pillar, the reliability indices obtained for the contour C were very high (above 5,0), indicating high safety levels.

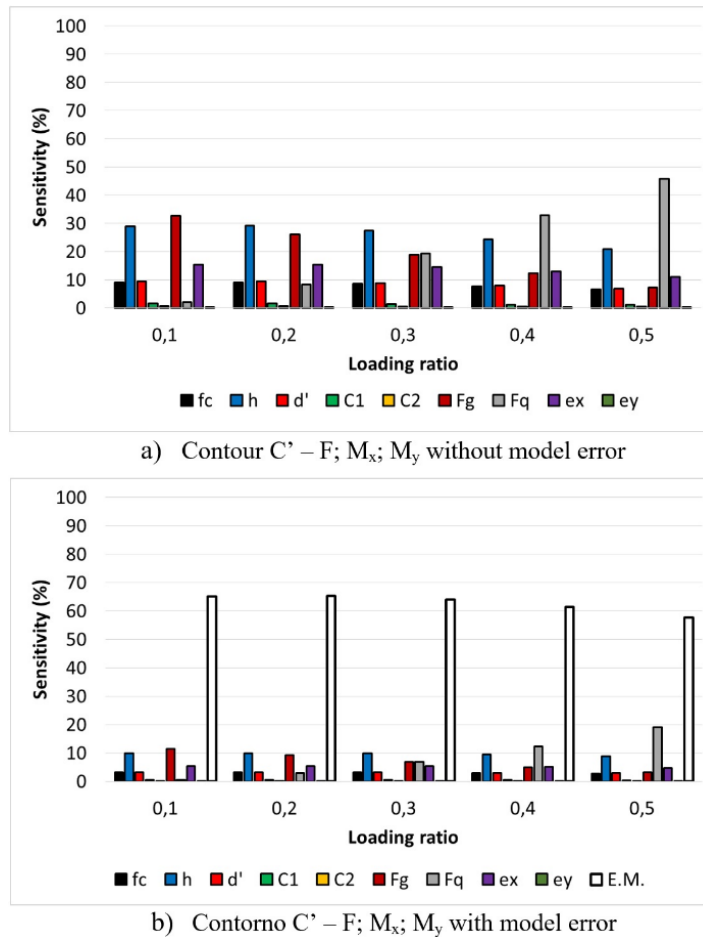


Figure 9. Sensitivity factors \times loading ratio: set 1 border column.

Figure 9 presents the sensitivity factors for some of the contour C' analyzes. Regarding the contour C , the same observed behavior in the central column was maintained. For the contour C' , the reliability indices showed little variation for all the loading ratios, differently from the central column. The most important random variables were the eccentricity $e_x = 48$ cm, in addition with slab thickness and the live load. The inclusion of the model error, in this case, increased the reliability indices regarding the same condition in contour C' without model error. The model error was also the most influent variable, with sensitivity factor varying between 55% and 65%.

When the model error was considered, the reliability indices have increased because of the elevated mean value, even with coefficient of variation equal to 21,4% (Table 1). As we can see, slab thickness of 18 cm is insufficient ($\beta < 1.0$) for the contour C' , when the probabilistic approach is adopted.

The results shown in Figure 10 refer to the analyzes of set 2 only to the β for the contour C' , with axial force and both bending moments, without and with model error, for different loading ratios. The theoretical analysis based on the prediction model of the Brazilian code indicated that the minimum slab thickness for the contour C' is 25 cm (Figure 10a). Regardless of the loading ratio, for $h = 25$ cm without model error, β is greater than or equal to 4,0, indicating a sufficient safety level when compared to the $\beta_{target} = 3,8$. Therefore, both analyzes (normative and probabilistic) resulted in the same slab thickness, regardless of the adopted loading ratio. When the model error was considered, the reliability indices resulted lower than those without E_m (Figure 10b). This result is coherent, since the coefficient of variation of the model error is high, which introduces more uncertainty in the predicted mechanical response by the normative theoretical model.

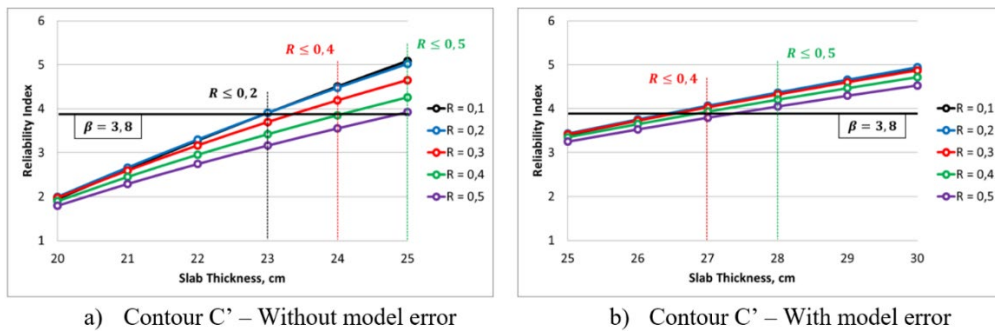


Figure 10. Reliability index \times slab thickness: set 2 border column.

5.3 Edge Column

Figure 11 shows the results in terms of β for the critical contours C , C' with and without E_m for all the loading ratios in just one situation: the axial force F plus the most important bending moment, M_x . Regarding the contour C , the same observed behavior for the central and border columns has occurred with very high reliability index values (above 6,0). The reliability indices remained almost constant for all the loading ratio values. When the model error was considered, the reliability indices increased compared to those values for the contour C' without E_m . It is important to mention that, even with a high coefficient of variation (29,7%), the mean value of 1,363 (Table 1) increased significantly the contour C' reliability indices. However, the statistical characterization of the edge column model error was not really adequate as done for the central and border column, since the experimental sample size was reduced. The obtained results for the contour C' clearly showed that the adopted slab thickness of 18 cm is insufficient to resist punching shear without transversal reinforcement.

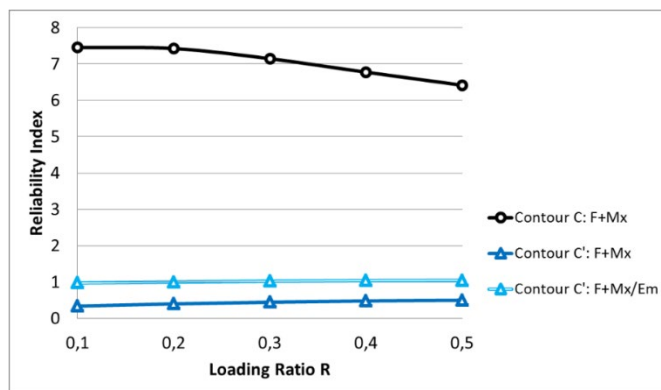


Figure 11. Reliability index \times loading ratio: set 1 edge column.

Figure 12 presents the sensitivity factors of the random variables for some analyzed cases. Regarding the contour C' without model error, the most important random variables were the slab thickness, live load and the eccentricity e_x . The model error remained dominant when compared to the other random variables, achieving almost 80% of sensitivity for all loading ratios.

Figure 13 presents the reliability indices evolution for the set 2. As observed for the border column, the minimum slab thickness to achieve the normative requirements was 25 cm. In the reliability analysis, for $h = 25$ cm, the $\beta_{target} = 3,8$ was also achieved for all the loading ratios, in the case without model error. When the model error was considered, the minimum value for the slab thickness to achieve the β_{target} increased to 29 cm, due to the high value of the coefficient of variation of the E_m .

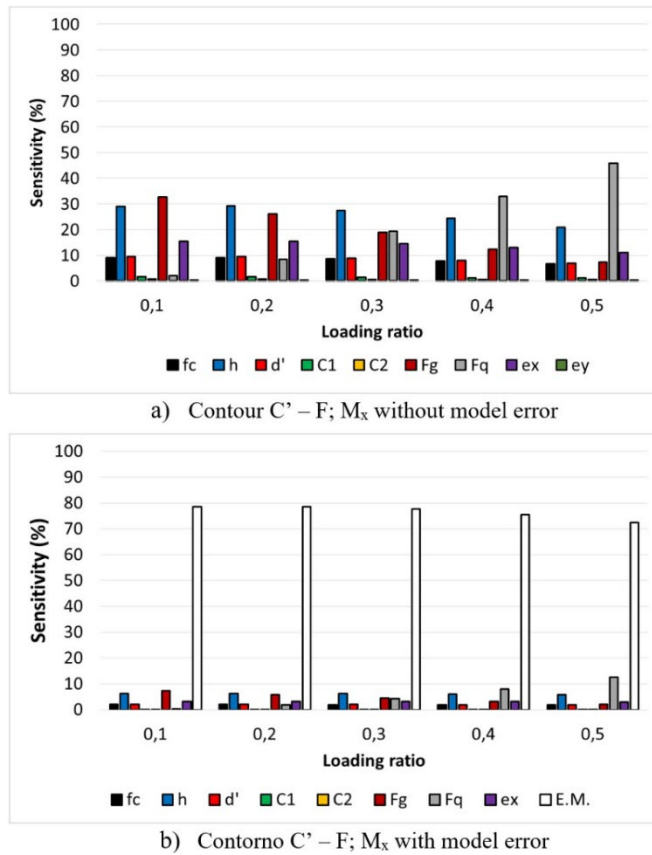


Figure 12. Sensitivity factors × loading ratio: set 1 edge column.

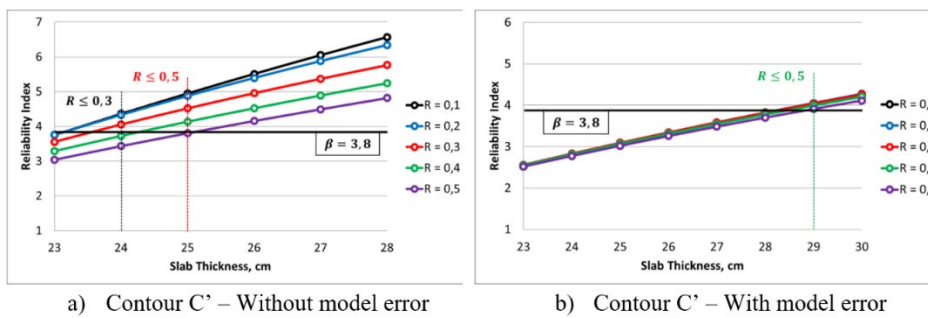


Figure 13. Reliability index × slab thickness: set 2 edge columns.

6 CONCLUSIONS

This paper presented a study about the safety of the slab-column connections subjected to punching shear for central, border and edge columns in a flat slab reinforced concrete building proposed by Lima [4]. From a probabilistic approach via Structural Reliability Theory, combined with the ABNT NBR 6118 [35] analytical punching shear prediction model and the model error random variable, the performance of these connections in terms of the reliability index was evaluated. The model error was characterized from several experimental results consulted in the literature for the three analyzed columns.

The conclusions of this study are summarized below:

- The high β values associated with the contour C proved to be consistent with the type of failure observed in the experimental tests, in which these always occurred in the vicinity of the contour C'. Therefore, it can be concluded that the punching shear rupture will hardly occur at the slab-column interface, since the normative recommendations in the project be respected;

- When the model error was considered as a random variable in the performed analyzes, especially for the central and border column, it was observed a strong uniformity of the results in terms of β , in comparison to the results without the model error. The constructed statistics of the model error showed, in general, that the Brazilian code punching shear prediction model presented good quality in average terms, but with loss of precision because of its high values of coefficient variation. This is due to the complexity of the punching shear phenomenon and the difficulty of translating it into a simple and direct analytical model, as well as the lack of standardization of the experimental tests until mechanical failure. The improvement of the theoretical prediction models is a complex task and should not be seen, in the light of what has been presented here, simply by multiplying the resistant portion $R(X)$ by the obtained model error calibrated value;
- In terms of the slab-column connection failure to punching shear, the most important parameters, without model error, were the total slab thickness and the concrete compressive strength. There was no significant influence of the column cross section dimensions on the probability of failure of the analyzed cases. However, the axial force eccentricities that generate the bending moments have shown some importance when their values were higher. This further emphasizes the stage of structural analysis of the flat slab systems, in order to accurately obtain the bending moments acting on the slab-column connections; Thus, in the flat slab design subjected to punching shear, the most important parameters of the slab-column connections can be controlled by the engineer, which can be an important measure to structural safety guarantee. On the other hand, when the model error was considered, it was the most important variable with more than 60% of influence on the probability of failure, followed by the slab thickness and concrete compressive strength, regardless the variations on the loading ratio;
- As observed in this study, the appropriate slab thickness, for all the considered loading ratio, was achieved based on a target reliability-based criterion. The obtained values for h without E_m were very close to those obtained according to the semi-probabilistic procedure adopted by the Brazilian normative, when considering the partial safety factors and all the code recommendations. However, when the model error was considered, the safety levels significantly decreased, suggesting the importance of improving the quality of the Brazilian normative prediction model for punching shear.

ACKNOWLEDGMENTS

The authors would like to thank FAPESP (process nº 2018/06562-4) for the scholarship granted to the student and the UNESP – Bauru Campus for all the support.

REFERENCES

- [1] M. L. Carvalho, C. R. Silva, and F. R. Stucchi, "Estudo da confiabilidade da punção em lajes lisas sem armadura de cisalhamento de acordo com a NBR 6118," *Rev. IBRACON Estrut. Mater.*, vol. 10, no. 2, pp. 276–297, Apr 2017.
- [2] J. Einpaul, C. E. Ospina, M. F. Ruiz, and A. Muttoni, "Punching shear capacity of continuous slabs," *ACI Struct. J.*, vol. 113, pp. 861–872, 2016.
- [3] E. A. P. Liberati, M. G. Marques, E. D. Leonel, L. C. Almeida, and L. C. Trautwein, "Failure analysis of punching in reinforced concrete flat slabs with openings adjacent to the column," *Eng. Struct.*, no. 182, pp. 331–343, 2019.
- [4] J. S. Lima, "Verificações da punção e da estabilidade global em edifícios de concreto: desenvolvimento e aplicações normativas," M.S. thesis, Esc. Eng. São Carlos, Univ. São Paulo, São Carlos, 2001.
- [5] N. G. B. Albuquerque, "Comportamento das ligações de lajes lisas de concreto armado com pilares de borda sujeitas a excentricidades interna e externas," Ph.D. dissertation, Fac. Tecnol., Univ. Brasília, Brasília, 2014.
- [6] J. L. P. Melges, "Punção em lajes: exemplos de cálculo e análise teórico-experimental," M.S. thesis, Esc. Eng. São Carlos, Univ. São Paulo, São Carlos, 1995.
- [7] J. L. P. Melges, "Análise experimental da punção em lajes de concreto armado e protendido," Ph.D. dissertation, Esc. Eng. São Carlos, Univ. São Paulo. São Carlos, 2001.
- [8] D. R. C. Oliveira, "Análise experimental de lajes cogumelo de concreto de alta resistência com armadura inclinada de punção," M.S. thesis, Univ. Brasília, Brasília, 1998.
- [9] W. L. A. Oliveira, "Análise teórico-experimental de pilares mistos preenchidos de seção circular," Ph.D. dissertation, Univ. São Paulo, São Carlos, 2008.
- [10] O. S. Paiva, "Análise do efeito da retangularidade dos pilares nos critérios normativos de dimensionamento à punção em lajes lisas de concreto armado," M.S. thesis, Univ. Fed. Pará, Belém, 2013.

- [11] J. B. L. Libório, “Estudo experimental da ruína de ligações laje-pilar em bordas com pilares de seção retangular,” M.S. thesis, Esc. Eng. São Carlos, Univ. São Paulo, São Carlos, 1985.
- [12] L. S. R. Damasceno, “Análise experimental de lajes lisas unidirecionais de concreto armado com pilares retangulares ao puncionamento,” M.S. thesis, Univ. Fed. Pará, Inst. Tecnol., Dep. Eng. Civ., Belém, 2007.
- [13] M. P. Ferreira, “Análise experimental de lajes lisas unidirecionais de concreto armado ao puncionamento simétrico ou assimétrico,” M.S. thesis, Univ. Fed. Pará, Cent. Tecnol., Belém, 2006.
- [14] D. A. O. Martinelli, “A ruína das ligações laje-pilar nos cantos de lajes-cogumelo,” Ph.D. dissertation, Esc. Eng. São Carlos, Univ. São Paulo, São Carlos, 1974.
- [15] F. M. H. Feliciano, “Punção em lajes lisas de concreto armado com pilares de borda e excentricidade externa,” M.S. thesis, Fac. Tecnol., Univ. Brasília, Brasília, 2011.
- [16] R. M. Gonçalves, “Estudo experimental da ruína de ligações laje-pilar em bordas de lajes cogumelo com reforço transversal constituído de perfis metálicos,” M.S. thesis, Univ. São Paulo, São Carlos, 1986.
- [17] V. C. Mouro, “Punção em lajes cogumelo: estudo da retangularidade dos pilares,” M.S. thesis, Univ. Fed. Goiás, Goiânia, 2006.
- [18] T. Takeya, “Estudo experimental da ruína de ligações laje-pilar em bordas de lajes-cogumelo,” M.S. thesis, Esc. Eng. São Carlos, Univ. São Paulo, São Carlos, 1981.
- [19] N. J. Gardner, "Relationship of the punching shear capacity of reinforced concrete slabs with concrete strength," *ACI Struct. J.*, vol. 87, no. 1, pp. 66–71, 1990.
- [20] R. B. Gomes and P. E. Regan, "Punching resistance of RC flat slabs with shear reinforcement," *J. Struct. Eng.*, vol. 125, no. 6, pp. 684–692, Jun 1999.
- [21] N. M. Hawkins, H. B. Falssen, and R. C. Hinojosa, *Influence of Column Rectangularity on the Behaviour of Flat Plate Structures* (Publication SP-30). Detroit: Am. Concr. Inst., 1971, pp. 127–146.
- [22] H. Marzouk and A. Hussien, "Experimental investigation on the behavior of high-strength concrete slabs," *ACI Struct. J.*, vol. 88, no. 6, pp. 701–713, 1992.
- [23] J. D. Mortin and A. Ghali, "Connection of flat plates to edge columns," *ACI Struct. J.*, vol. 88, no. 2, pp. 191–198, 1991.
- [24] P. E. Regan and H. Rezai-Jorabi, "Shear resistance of one-way slabs under concentrated loads," *ACI Struct. J.*, vol. 85, no. 2, pp. 150–158, Mar-Apr 1988.
- [25] P. E. Regan, *Tests of Connections between Flat Slabs and Edge Columns*. London: Sch. Archit. Eng., Univ. Westminster, 1993
- [26] A. Sherif, M. B. Emara, A. Hassanein, and S. A. Magd, “Effect of the column dimensions on the punching shear strength of edge column-slab connections,” in *Punching Shear in Reinforced Concrete Slabs* (ACI Special Publication 232), 2005, pp. 175–192.
- [27] A. G. Sherif and W. H. Dilger, “Punching failure of full-scale high strength concrete flat slabs,” in *Int. Workshop on Punching Shear Capacity of RC Slabs* (TRITA-BKN Bulletin 57), Stockholm, Sweden, 2000, pp. 235–243.
- [28] E. R. F. Zaghlool, “Strength and behavior of corner and edge column-slab connections in reinforced concrete flat plates,” Ph.D. dissertation, Dept. Civ. Eng., Univ. Calgary, 1971.
- [29] M. J. M. Pereira Fo., M. V. P. Freitas, D. F. A. Santos, A. J. C. Nascimento, and M. P. Ferreira, "Slabs strengthened for punching shear with post-installed steel and CFRP connectors," *Ibracon Struct. Mater. J.*, vol. 12, no. 3, pp. 445–478, 2019.
- [30] A. M. D. Souza and M. K. El Debs, "Shear strength analysis of slabs without transverse reinforcement under concentrated loads according to ABNT NBR 6118:2014," *Ibracon Struct. Mater. J.*, vol. 12, no. 3, pp. 658–693, Jun 2019.
- [31] C. B. Carvalho, “Análise crítica dos critérios normativos de dimensionamento à punção em lajes lisas,” M.S. thesis, Esc. Eng., Univ. Fed. Minas Gerais, Belo Horizonte, 2008.
- [32] V. P. Barros, A. T. Beck, and T. N. Bittencourt, "Shear failure in reinforced concrete members without transverse reinforcement: analysis of model error of NBR 6118:2014," *Ibracon Struct. Mater. J.*, vol. 14, no. 1, 2020.
- [33] G. R. Silva, A. Campos Fo., and M. V. Real, "Reliability of internal column-slab connection under punching according to NBR 6118:2014," *Ibracon Struct. Mater. J.*, vol. 11, no. 5, pp. 931–948, Oct 2018.
- [34] E. A. P. Liberati, “Análise de confiabilidade de lajes lisas de concreto armado submetidas à punção,” Ph.D. dissertation, Fac. Eng. Civil, Arquit. Urban., Univ. Est. Campinas, Campinas, 2019.
- [35] Associação Brasileira de Normas Técnicas, *Projeto de Estruturas de Concreto – Procedimento*, NBR 6118, 2014.
- [36] L. L. J. Borges, G. S. Melo, R. B. Gomes, and R. M. Bittencourt, “Influência da geometria do pilar na resistência ao puncionamento de lajes cogumelo de concreto armado,” in *An. V Simp. EPUSP Estrut. Concr.*, São Paulo, 2003.
- [37] J. A. Silva and R. B. Gomes, “Resistência à punção de lajes cogumelo de concreto armado com armadura de cisalhamento, furos e colunas retangulares,” in *An. V Simpósio EPUSP sobre Estrut. Concr.*, São Paulo, 2003.
- [38] B. N. Moraes No., “Análise experimental de lajes lisas bidirecionais de concreto armado com estribos inclinados e pilares retangulares sujeitas a puncionamento simétrico,” M.S. thesis, Univ. Fed. Pará, Belém, 2007.

- [39] N. Narasimhan, "Shear reinforcement in reinforced concrete column heads," Ph.D. dissertation, Fac. Eng. Univ. London, London, 1971.
- [40] E. F. El-Salakawy, M. A. Polak, and M. H. Soliman, "Slab-column edge connections subjected to high moments," *Can. J. Civ. Eng.*, vol. 25, no. 3, pp. 526–538, 1998.
- [41] K. Sudarsana, "Punching shear in edge and corner column slab connections of flat plate structures," Ph.D. dissertation, Univ. Ottawa, Ottawa, 2001.
- [42] D. A. O. Martinelli, "A ruína das ligações laje-pilar nos cantos de lajes-cogumelo," Ph.D. dissertation, Esc. Eng. São Carlos, Univ. São Paulo, São Carlos, 1974.
- [43] Comitê Europeu de Normalização, *Design of Concrete Structures – Part 1-1: General Rules and Rules for Buildings*, Eurocode 2, 2010.
- [44] A. H.-S. Ang and W. H. Tang, *Probability Concepts in Engineering Planning and Design – vol. II: Decision, Risk and Reliability*. New York: John Wiley & Sons, 1984.
- [45] A. T. Beck, *Confiabilidade e Segurança das Estruturas*, 1ª ed. Rio de Janeiro: Elsevier, 2019.
- [46] A. M. Hasofer and N. C. Lind, "Exact and invariant second moment code format," *J. Eng. Mech. Div.*, vol. 100, no. EM1, pp. 111–121, Feb 1974.
- [47] Joint Committee on Structural Safety, *Probabilistic Model Code: Part 1 - Basis of Design*. Denmark: JCSS, 2000, 64 p.
- [48] Comitê Europeu de Normalização, *Eurocode – Basis of Structural Design*, EN 1990, 2002.
- [49] G. P. Pellizzer, "Sobre a modelagem numérica da difusão de cloretos no concreto: uma abordagem pelo método dos elementos de contorno com aplicação de modelos de confiabilidade e otimização," Ph.D. dissertation, Univ. São Paulo, 2019.
- [50] C. G. Nogueira, W. S. Venturini, and A. T. Beck, "Avaliação da confiabilidade de ligações laje-pilar à punção a partir do Modelo da NBR 6118:2003," in *An. XXVIII Cong. Ibero Latino-Am. Métodos Comput. Eng., Congresso de Mét. Num. Eng. CMNE 2007*, Portugal, 2007.
- [51] G. R. Silva, "Análise da confiabilidade da ligação laje-pilar interno sob punção de acordo com a NBR-6118:2014," M.S. thesis, Univ. Fed. Rio Grande do Sul, Porto Alegre, 2017.
- [52] M. L. Carvalho, C. R. Silva, and F. R. Stucchi, "Study on reliability of punching shear of flat slabs without shear reinforcement according to NBR6118," *Rev. IBRACON Estrut. Mater.*, vol. 10, no. 2, pp. 276–297, Apr 2017.
- [53] B. Ellingwood and T. V. Galambos, "Probability-based criteria for structural design," *Struct. Saf.*, vol. 1, pp. 15–26, 1982.
- [54] R. Rachwitz and B. Fiessler, "Structural reliability under combined random load sequences," *Comput. Struct.*, vol. 9, pp. 489–494, 1978.
- [55] A. S. Nowak and K. R. Collins, *Reliability of Structures*. Michigan: McGraw Hill, 2000.
- [56] C. G. Nogueira, "Desenvolvimento de modelos mecânicos, de confiabilidade e de otimização para aplicação em estruturas de concreto armado," Ph.D. dissertation, Esc. Eng. São Carlos, Univ. São Paulo, 2010.
- [57] E. S. Santos, "Avaliação estatística do erro de modelos de resistência para elementos lineares de concreto armado da ABNT NBR6118:2007," M.S. thesis, Univ. São Paulo, São Carlos, 2012.
- [58] E. A. Bolandim, "Análise de confiabilidade em ligações parafusadas em chapas finas e perfis de aço formados a frio," M.S. thesis, Univ. São Paulo, São Carlos, 2011.
- [59] W. L. A. Oliveira, "Análise teórico-experimental de pilares mistos preenchidos de seção circular," Ph.D. dissertation, Univ. São Paulo, São Carlos, 2008.
- [60] E. A. P. Liberati, L. M. Trautwein, E. D. Leonel, R. K. T. Marques, and L. C. Almeida "Avaliação estatística de erro de modelos de resistência à punção de lajes lisas de concreto armado" in *An. 59º Cong. Bras. Concr. IBRACON2017*, Bento Gonçalves, 2017.

Author contributions: NLAM: Data curation, formal analysis, investigation, methodology, validation, writing-original draft; CGN: Conceptualization, funding acquisition, supervision, formal analysis, investigation, methodology, project administration, software, writing-review & edition.

Editors: Antonio Carlos dos Santos, Guilherme Aris Parsekian.

APPENDIX

Tables A1, A2 and A3 show the data set of each literature reference used in this study for central, border and edge slab-column connection, respectively. It is also presented the punching shear ultimate loads observed in the experiments and the predicted loads by the ABNT NBR 6118 [35].

Table A1. Data for central column.

Reference	Slabs	f_c (MPa)	d (cm)	ρ (%)	F_{exp} (kN)	F_{teo} (kN)
Carvalho <i>apud</i> Gardner [19]	21	12.8 - 37.4	11.4 - 11.8	1.2 - 7.0	280.2 - 533.8	307.6 - 696.2
Moe <i>apud</i> Gardner [19]	13	20.5 - 35.2	11.4	1.0 - 1.5	311.4 - 432.8	324.7 - 426.9
Marzouk and Hussein [22]	14	30.0 - 80.0	9.0 - 12.0	0.5 - 2.4	178.0 - 645.0	240.9 - 596.1
Melges [7]	1	26.6	12.7	1.7	441.6	416.7
Oliveira [9]	2	60.9 - 62.9	9.3 - 9.7	1.4	270.0 - 335.0	299.6 - 321.4
Gomes and Regan [20]	3	36.5 - 41.1	15.9 - 16.3	1.26	560.0 - 650.0	628.8 - 633.4
Teng et al. <i>apud</i> Paiva [10]	5	36.0 - 43.0	10.3 - 11.1	1.65 - 1.81	423.0 - 649.0	383.7 - 576.4
Borges et al. [36]	9	36.2 - 44.7	13.9 - 16.4	1.28 - 1.58	550.0 - 897.0	571.9 - 931.2
Silva and Gomes [37]	3	39.6 - 40.8	9	1.45	273.0 - 469.0	269.5 - 366.5
Oliveira and Melo <i>apud</i> Carvalho et al. [1]	15	54.0 - 67.0	10.6 - 11.0	1.1	240.0 - 446.0	320.2 - 351.4
Mouro <i>apud</i> Regan and Rezaei-Jarobi [24]	6	29.0 - 38.2	7.9	1.5 - 1.6	77.0 - 132.0	179.5 - 237.6
Ferreira [13]	11	36.1 - 58.0	8.7 - 8.9	0.9 - 1.5	159.5 - 228.0	192.9 - 238.8
Mouro [17]	8	22.0 - 29.0	9.0 - 9.4	1.4 - 1.5	275.0 - 395.0	275.2 - 311.1
Vilhena et al. <i>apud</i> Paiva [10]	4	51.2 - 55.2	6.5	1.2 - 1.4	122.0 - 124.5	147.1 - 252.1
Damasceno [12]	3	41.3 - 42.0	8.9 - 9.8	0.6 - 1.2	172.0 - 194.5	192.0 - 217.3
Moraes [38]	2	39.4 - 39.8	8.7	1.2 - 1.4	224.0 - 241.0	215.0 - 255.4
Hawkins et al. [21]	6	27.0 - 32.0	11.7 - 12.1	0.8 - 1.1	321.0 - 358.0	345.2 - 430.7

Table A2. Data for border column.

Reference	Slabs	f_c (MPa)	d (cm)	ρ (%)	F_{exp} (kN)	F_{teo} (kN)
Narasimhan [39]	3	27.0 - 32.1	12.7	1.0	264.0 - 342.0	217.0 - 229.9
Kinnunen <i>apud</i> Albuquerque [5]	3	23.4 - 26.6	10.2	1.0 - 1.5	128.0 - 169.0	96.5 - 125.6
Zaghlool [28]	2	38.7 - 40.5	11.7 - 12.1	1.4 - 2.0	247.0 - 268.0	196.3 - 204.0
Regan et al. <i>apud</i> Albuquerque [5]	7	27.4 - 50.0	9.8 - 10.1	0.5 - 1.0	114.0 - 192.0	117.1 - 159.6
Takeya [18]	3	34.5 - 45.8	8.5	1.8	122.7 - 125.8	111.1 - 118.6
Brandli et al. <i>apud</i> Albuquerque [5]	2	34.6	16.3 - 16.7	1.1 - 1.2	345.0 - 360.0	314.1 - 387.3
Libório [11]	9	22.0 - 43.9	6.0	1.9	54.1 - 98.4	40.4 - 72.3
Gonçalves [16]	3	42.8 - 46.5	8.5	1.8	110.0 - 117.8	119.3 - 122.7
Mortin and Ghali [23]	2	32.2 - 43.2	12.2	0.7 - 1.0	105.0 - 141.0	118.2 - 146.9
El-Salakawy et al. [40]	2	33.0 - 36.5	10.0	0.6	69.4 - 125.0	63.6 - 111.7
Regan [25]	10	35.4 - 42.7	16.8	0.5 - 0.8	233.0 - 416.0	200.2 - 293.6
Lim and Rangan <i>apud</i> Albuquerque [5]	1	25.0	9.8	0.3	106.0	94.5
Sherif and Dilger [27]	2	28.0 - 84.1	11.4	1.3 - 1.4	185.0 - 245.0	195.5 - 195.8
Afhami et al. <i>apud</i> Albuquerque [5]	2	34.8	11.6	0.5 - 1.0	181.0 - 220.0	158.9 - 162.3
Sudarsana [41]	11	33.9 - 44.0	10.5	0.9 - 1.2	79.8 - 220.0	83.2 - 163.4
Sherif et al. [26]	5	31.0 - 35.6	10.0	1.0 - 1.2	95.0 - 172.0	99.8 - 153.0
Feliciano [15]	4	45.1	15.2	0.75	197.5 - 300.0	254.9 - 295.4
Albuquerque [5]	3	44.8 - 50.1	14.6 - 14.7	1.0 - 1.3	308.0 - 374.0	312.7 - 348.2

Tabela A3. Data for edge column.

Reference	Slabs	f_c (MPa)	d (cm)	ρ (%)	F_{exp} (kN)	F_{teo} (kN)
Narasimhan [39]	1	34.1	15.1	1.0	385.0	147.8
Martinelli [42]	8	41.1 - 47.3	8.5	1.8	60.3 - 66.3	47.0 - 49.3
Sudarsana [41]	4	44.4	10.5	1.1	62.1 - 108.6	74.5 - 84.6

For each slab-column connection, Figures A1, A3 and A5 illustrate the trend of the model error regarding some design parameters, such as: reinforcement geometric ratio (ρ), concrete compressive strength (f_c), slab serviceable thickness (d) and eccentricity (e). In addition, Figures A2, A4 and A6 show the accuracy of the ABNT NBR 6118 [35] prediction model for punching shear failure.

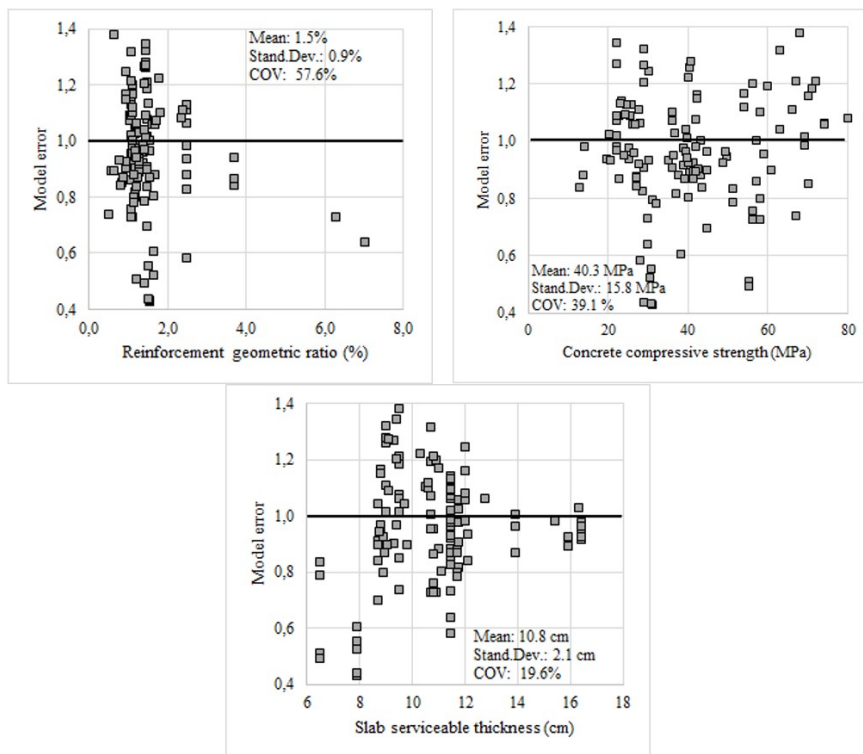


Figure A1. Influence of ρ , f_c and d on the model error for central columns.

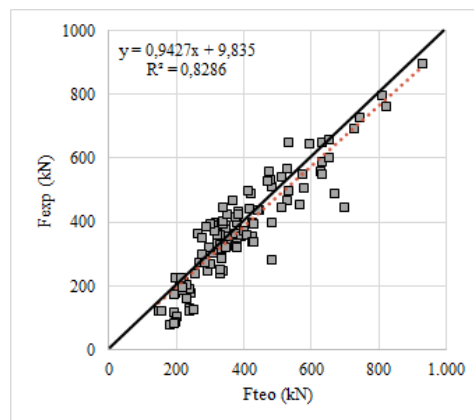


Figure A2. Accuracy of the Brazilian standard punching shear prediction model for central columns.

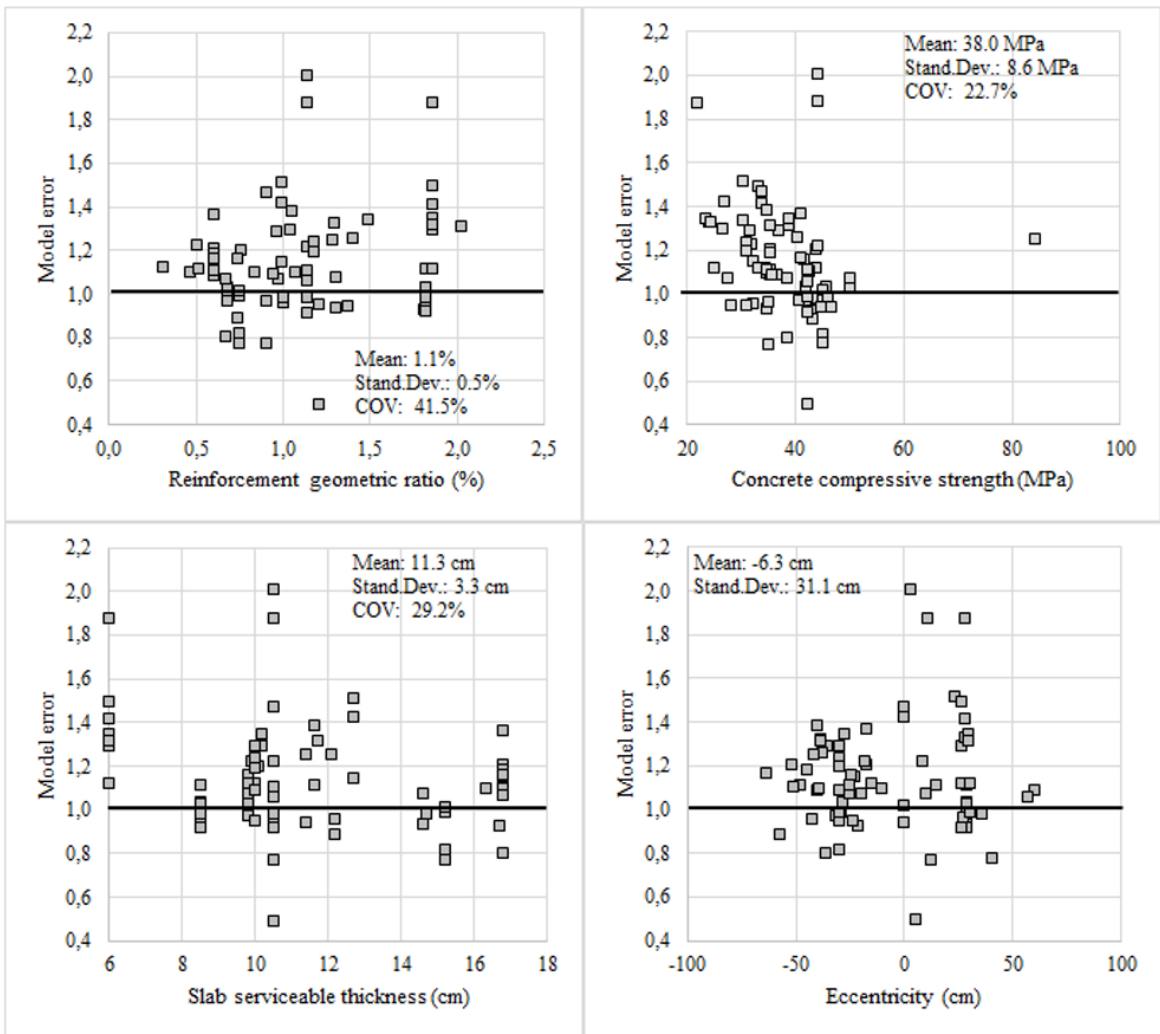


Figure A3. Influence of ρ , f_c , d and e on the model error for border columns.

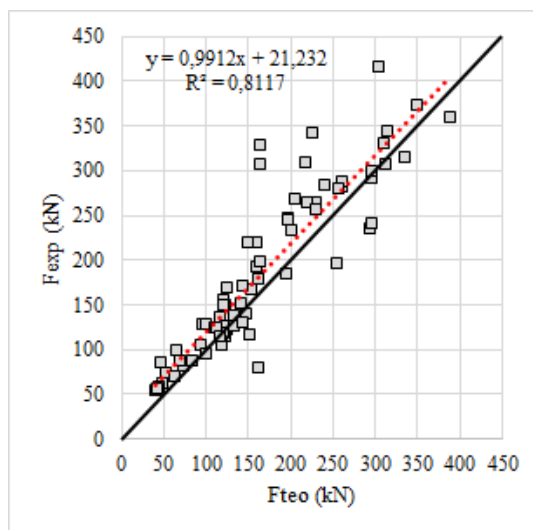


Figure A4. Accuracy of the Brazilian standard punching shear prediction model for border columns.

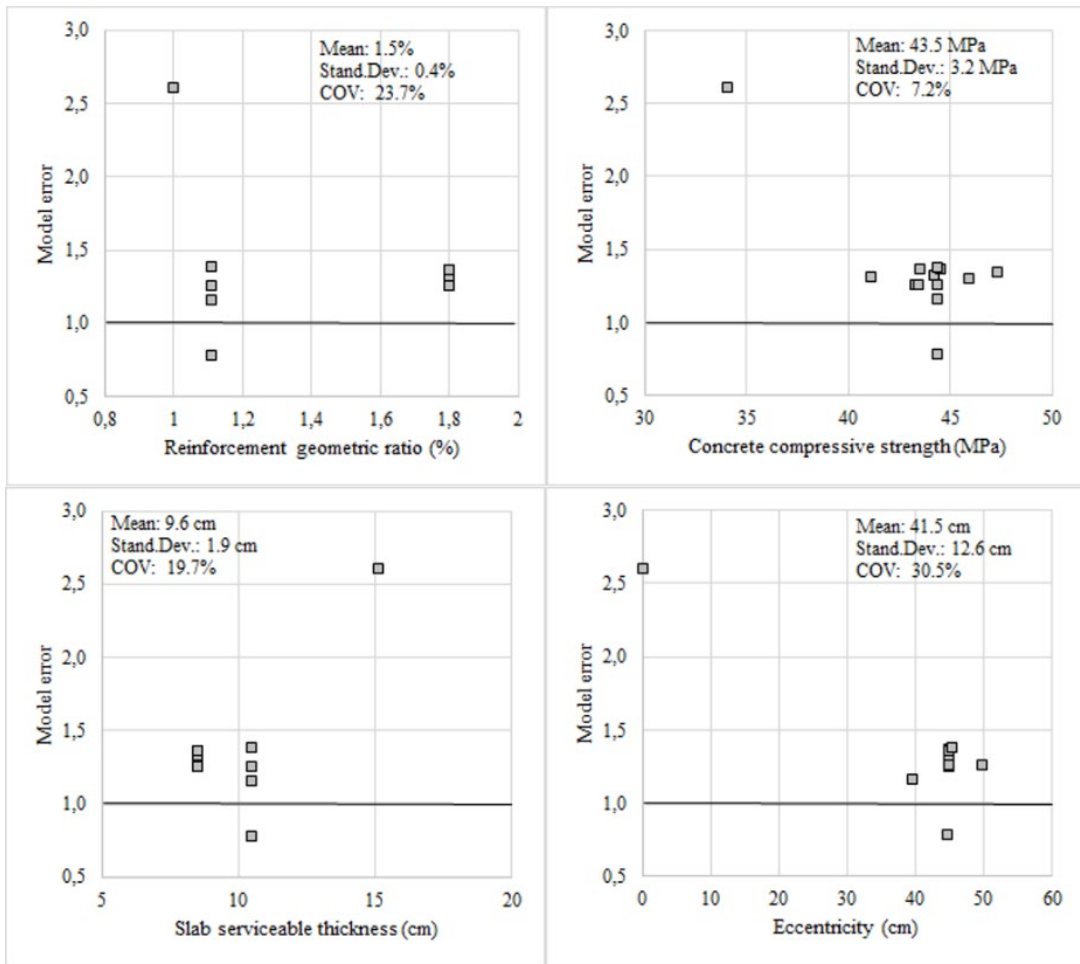


Figure A5. Influence of ρ , f_c , d and e on the model error for edge columns.

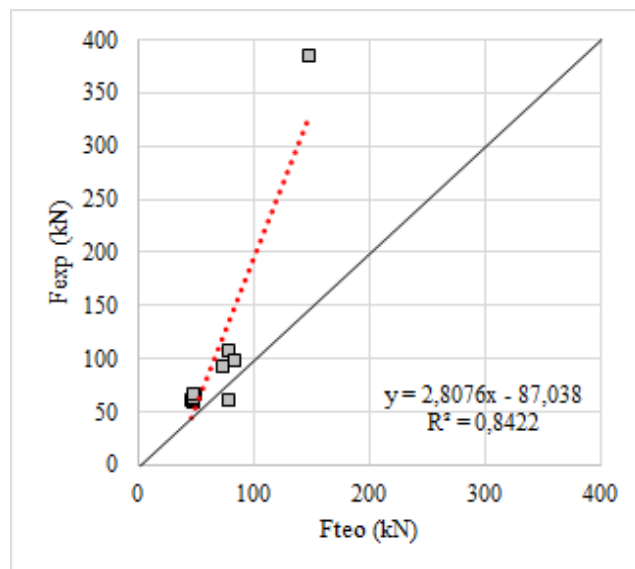


Figure A6. Accuracy of the Brazilian standard punching shear prediction model for edge columns.



ORIGINAL ARTICLE

Optimization of slender reinforced concrete columns subjected to biaxial bending using genetic algorithms

Optimização de pilares esbeltos de concreto armado sujeitos a flexão biaxial utilizando algoritmos genéticos

Susana de Lima Pires^a Maria Cecilia Amorim Teixeira da Silva^a

^aUniversidade Estadual de Campinas – UNICAMP, Faculdade de Engenharia Civil, Arquitetura e Urbanismo, Departamento de Estruturas, Campinas, SP, Brasil

Received 14 September 2020

Accepted 17 March 2021

Abstract: In this paper, a computational tool was developed to optimize the design of slender reinforced concrete columns subjected to biaxial bending considering the material and geometric nonlinearities rigorously. The optimization process utilizes the technique of genetic algorithms to find the best cross-sectional dimension and the best distribution and amount of reinforcement, to minimize the cost of the column subject to certain constraints of strength, stability, feasibility and regulatory. The analysis applies to rectangular cross-section of columns, and constant and symmetrical distribution of reinforcement. The results obtained by the developed software converge properly to an optimal solution or to a solution around the optimum in a significantly shorter time interval in relation to the results obtained when considering all solutions within the previously established domain. The effect of slenderness on the optimal design of reinforced concrete columns was also analyzed. The results showed that the column cost increases as the slenderness ratio increases, and steel becomes the predominant material to establish the equilibrium of the structural element.

Keywords: structural analysis, reinforced concrete design, material nonlinearity, geometric nonlinearity, second order effects.

Resumo: Neste trabalho, foi desenvolvida uma ferramenta computacional para otimizar o dimensionamento de pilares de concreto armado esbeltos sujeitos a flexão oblíqua, considerando-se rigorosamente as não-linearidades física e geométrica. O processo de otimização utiliza a técnica dos algoritmos genéticos para encontrar a melhor seção transversal, a melhor distribuição e a melhor quantidade de armadura, de modo a minimizar o custo do pilar sujeito a certas restrições de resistência, estabilidade, de exequibilidade e normativas. A análise se aplica a pilares de seção transversal retangular constante e com distribuição simétrica de armadura. Os resultados obtidos pelo programa computacional desenvolvido convergem adequadamente para uma solução ótima ou para uma solução em torno da ótima num intervalo de tempo significativamente menor comparativamente aos resultados obtidos quando todas as soluções dentro do domínio previamente estabelecido são considerados. Foi também analisado o efeito da esbeltez no dimensionamento ótimo de pilares de concreto armado. Os resultados mostraram que o custo do pilar aumenta à medida que a esbeltez aumenta, e o aço torna-se o material predominante para estabelecer o equilíbrio do elemento estrutural.

Palavras-chave: análise estrutural, dimensionamento de concreto armado, não linearidade física, não linearidade geométrica, efeitos de segunda ordem.

How to cite: S. L. Pires and M. C. A. T. Silva, "Optimization of slender reinforced concrete columns subjected to biaxial bending using genetic algorithms," *Rev. IBRACON Estrut. Mater.*, vol. 14, no. 6, e14610, 2021, <https://doi.org/10.1590/S1983-41952021000600010>

Corresponding author: Maria Cecilia Amorim Teixeira da Silva. E-mail: mcatds07@gmail.com

Financial support: CAPES (Coordenação de Aperfeiçoamento de Pessoal de Nível Superior) – Finance Code 001.

Conflict of interest: Nothing to declare.



This is an Open Access article distributed under the terms of the Creative Commons Attribution License, which permits unrestricted use, distribution, and reproduction in any medium, provided the original work is properly cited.

1 INTRODUCTION

In an earlier paper, Pires and Silva [1] developed a numerical procedure for the design of slender columns of reinforced concrete subjected to uniaxial bending. In the design of slender columns, displacements arising from second-order effects gradually increase until the column find a deformed position to establish the equilibrium condition. However how to find the steel area of a column, whose internal loads are not known? How to find the second-order internal loads of a column whose steel area is unknown? To answer these questions, the authors developed an iterative process that establishes the smallest area of steel necessary to equilibrate the column, based on a previously chosen reinforcement distribution.

A natural progression for this procedure would be to develop it to design slender columns subjected to biaxial bending. However, there would be nothing new on this subject, as many researchers have studied the nonlinear behavior of slender reinforced concrete columns subjected to uniaxial and biaxial bending [2]–[12].

Therefore, the idea arose to optimize the design of slender columns considering the concrete area, the steel area, and the reinforcement distribution as variables, so that the column is equilibrated in the safest and most economical possible way.

In the search for solutions to optimize reinforced concrete structures, several studies using genetic algorithms (AG) have been found in the current literature, with different approaches: beam optimization [13]–[15], column optimization [16], [17], frame optimization [18]–[22], reservoir optimization [23], seismic retrofitting of reinforced concrete columns [24], precast concrete structures [25], [26], concrete structures with FRP [27], and corrosion-affected reinforced concrete structures [28].

These studies confirm the efficiency of GA for reinforced concrete structures. In particular, studies found on the optimization of reinforced concrete columns, isolated or as frame members, provide answers using, in general, the design solution by simplified methods. The aim of this paper is to expand the use of AG for reinforced concrete columns by introducing a more comprehensive procedure in which material and geometric nonlinearities are strictly considered. This procedure allows the analysis of reinforced concrete columns from the shortest to the slenderest with the same rigor.

In the present study, the results provided by GA are compared with the solutions obtained by the procedure called Total Research, which provides the exact optimal results for the design of reinforced concrete columns. It should be noted that the Total Search procedure, although providing the exact solution, leads to an extremely high computational cost, and for this reason this procedure is used only to validate the results obtained by GA, but it is not economically viable as a computational tool.

In summary, this paper presents the systematization of the optimal design of slender reinforced concrete columns. The optimization process uses the technique of genetic algorithms that allow to find the best dimension of the cross section and the best distribution of the reinforcement so that the cost of the column, subject to certain constraints of strength, stability, feasibility, and regulatory specifications, is minimized. Columns are treated as individuals that are coded according to their characteristics, and are assessed by a cost function that is penalized according to the imposed constraints. The optimal column will correspond, at the end of the procedure, to the individual who best meets the safety criteria and, at the same time, has the lowest cost.

The present analysis covers isolated reinforced concrete columns of rectangular cross section submitted to biaxial bending, considering any type of support, and characteristic compressive concrete strengths between 20 MPa and 50 MPa. Material and geometric nonlinearities are strictly considered.

2 MATERIALS AND METHODS

2.1 Uniaxial constitutive models

The constitutive model for concrete in compression defined by the Brazilian standard NBR 6118 [29] is considered. The concrete stress-strain relationship is given by Equations 1 to 3:

$$\sigma_c = 0.85 f_{cd} \left[1 - \left(1 - \frac{\varepsilon_c}{0.002} \right)^2 \right] \text{ if } \varepsilon_c \leq 0.2\% \quad (1)$$

$$\sigma_c = 0.85 f_{cd} \text{ if } 0.2\% < \varepsilon_c \leq 0.35\% \quad (2)$$

$$\sigma_c = 0 \text{ if } \varepsilon_c > 0.35\% \quad (3)$$

where σ_c = compressive stress of concrete; ε_c = compressive strain of concrete; and f_{cd} = design compressive strength of concrete for concretes from 20 MPa to 50 MPa.

The constitutive model for steel adopted by the Brazilian Standard NBR 6118 [29] applies to tension and compression, and the stress-strain relationship is given by Equations 4 and 5:

$$\sigma_s = E_s \varepsilon_s \text{ if } \varepsilon_s < \varepsilon_{yd} \tag{4}$$

$$\sigma_s = f_{yd} \text{ if } \varepsilon_s \geq \varepsilon_{yd} \tag{5}$$

where σ_s = stress of steel; E_s = elastic modulus of steel; ε_s = strain of steel; f_{yd} = design strength of steel, and ε_{yd} = yield strain of steel.

2.2 Considerations on stability of slender reinforced concrete columns subjected to biaxial bending

The design of slender reinforced concrete columns requires the study of the element's stability, which implies in an analysis of the second order effects.

A bar subjected to biaxial bending caused by an eccentric load F_d , with an eccentricity e_1 , will have its axis deformed. In the case of slender bars, the second order eccentricity (e_2) is added to the transverse displacements. Axial loading and biaxial bending considering second order effects are given by Equations 6 to 9:

$$N_d = F_d \tag{6}$$

$$M_{d1} = F_d e_1 \tag{7}$$

$$M_{d2} = F_d e_2 \tag{8}$$

$$M_d = M_{d1} + M_{d2} \tag{9}$$

In Equations 6 to 9, the numerical values used for the variables correspond to respective vector modules.

When the axial force N_d and the bending moment \mathbf{M}_d (components M_{zd} and M_{yd}) are considered as ultimate values (N_R, M_{Rz}, M_{Ry}), they produce strains and stresses corresponding to the ultimate limit state of the cross section. The relationships between the ultimate values (N_R, M_{Rz}, M_{Ry}) and the stresses in concrete and steel are given by Equations 10 a 12:

$$N_d = N_R = \int_{Ac} \sigma_{cd} dA + \sum_{i=1}^n \sigma_{si} A_{si} \tag{10}$$

$$M_{zd} = M_{Rz} = \int_{Ac} \sigma_{cd} z dA + \sum_{i=1}^n \sigma_{si} z_{si} A_{si} \tag{11}$$

$$M_{yd} = M_{Ry} = \int_{Ac} \sigma_{cd} y dA + \sum_{i=1}^n \sigma_{si} y_{si} A_{si} \tag{12}$$

It is necessary to know the deformed configuration of the column to solve Equations 10 to 12, which implies knowing the curvature of the column axis and the stresses and strains in each column cross section.

2.3 Assumptions and ultimate limit states

The assumptions admitted in this paper are: (1) the plane sections remain plane after the element is strained; (2) the strain in a generic fiber of the cross section is directly proportional to its distance from the neutral axis; (3) there is a perfect bonding between the reinforcement bars and the concrete that surrounds them; (4) the tensile strength of concrete is totally neglected; (5) the parabola-rectangle diagram is adopted to represent the stress-strain relationship of concrete; (6) a perfect elastic-plastic diagram is adopted to represent the stress-strain relationship of steel; (7) the concrete cross section is considered to be non-cracked when calculating the stiffness matrix; (8) the conventional value of 0.35% is taken as the strain limit for shortening concrete in partially compressed sections; concrete strain limits vary from 0.2% to 0.35% under non-uniform compression. In this case, the strain related to the fiber positioned at 3/7 of the total section height from the most compressed edge remains unchanged and equal to 0.2%; (9) the maximum elongation allowed in the tensile reinforcement is 1%.

The small displacements assumption is considered. Thus, the curvature (χ) of the column axis is given by Equation 13:

$$\chi = \frac{d^2w(x)}{dx^2} \tag{13}$$

where w = transverse displacement. The variable x is measured along the non-deformed axis, and the axial load remains constant regardless of column deformations.

The safety of reinforced concrete columns is verified for the following ultimate limit states: (1) the ultimate limit state of loss of equilibrium of the structure; (2) the ultimate limit state related to the load capacity of the structure considering the second order effects.

2.4 Calculation of displacements

A local coordinate system for the bar is adopted to define the displacements (Figure 1a). The bar is subjected to biaxial bending. Internal forces occur in the XZ and XY planes. The axis of the bar is displaced $u_0(x)$ in the x direction. In the XZ plane, the bar undergoes a displacement $w(x)$ and the cross-section undergoes a $\theta_z(x)$ rotation (Figure 1b). In the XY plane, the bar undergoes a displacement $v(x)$ and the cross-section undergoes a $\theta_y(x)$ rotation (Figure 1c). The transverse displacements $w(x)$ and $v(x)$ are positive in the direction of the local axis, and the bending rotations, $\theta_z(x)$ and $\theta_y(x)$, are positive in the clockwise direction.

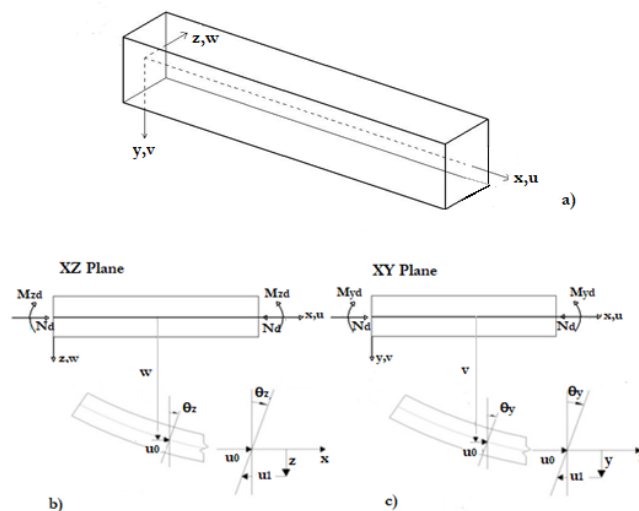


Figure 1. Analyzed bar: a) non-deformed bar and coordinate axes; b) internal loads and displacements in XZ plane; c) internal loads and displacements in XY plane.

The displacement $u(x, y, z)$ in a generic fiber of the cross section, according to Chen and Atsuta [30], is given by Equation 14:

$$u(x, y, z) = u_0(x) - y \left(\frac{dv}{dx} \right) - z \left(\frac{dw}{dx} \right) \tag{14}$$

The longitudinal strain is given by Equation 15:

$$\varepsilon_x = \varepsilon_0 - y\chi_y - z\chi_z \tag{15}$$

The axial strain ε_0 , the χ_y curvature in the XY plane, and χ_z curvature in the XZ plane are given by Equations 16, 17 and 18, respectively:

$$\varepsilon_0 = \frac{du_0}{dx} + \frac{1}{2} \left[\left(\frac{dv}{dx} \right)^2 + \left(\frac{dw}{dx} \right)^2 \right] \tag{16}$$

$$\chi_y = \left(\frac{d^2v}{dx^2} \right) \tag{17}$$

$$\chi_z = \left(\frac{d^2w}{dx^2} \right) \tag{18}$$

In the expression for the longitudinal strain (ε_x), the non-linear relationship is given by the axial strain (ε_0).

In the analysis of slender columns, material and geometric nonlinearities must be considered so that the displacements are calculated accurately. The numerical procedure developed for calculating displacements is based on the Finite Element Method using the Virtual Work Principle. The column axis is discretized into small elements of length L that are connected by their nodes. Each node has an axial displacement, a transverse displacement in the z direction, a transverse displacement in the y direction, a rotation in the XZ plane, and a rotation in the XY plane. The axis displacements of the element (u_0, w, v) are given by Equations 19, 20 and 21, respectively:

$$u_0 = \phi_1 U_1 + \phi_4 U_6 \tag{19}$$

$$w = \phi_2 U_2 + \phi_3 U_3 + \phi_5 U_7 + \phi_6 U_8 \tag{20}$$

$$v = \phi_2 U_4 + \phi_3 U_5 + \phi_5 U_9 + \phi_6 U_{10} \tag{21}$$

The interpolation functions ϕ_i are given by Equations 22 to 27:

$$\phi_1 = 1 - \left(\frac{x}{L} \right) \tag{22}$$

$$\phi_2 = 2 \left(\frac{x}{L} \right)^3 - 3 \left(\frac{x}{L} \right)^2 + 1 \tag{23}$$

$$\phi_3 = L \left[\left(\frac{x}{L} \right)^3 - 2 \left(\frac{x}{L} \right)^2 + \left(\frac{x}{L} \right) \right] \quad (24)$$

$$\phi_4 = \left(\frac{x}{L} \right) \quad (25)$$

$$\phi_5 = -2 \left(\frac{x}{L} \right)^3 + 3 \left(\frac{x}{L} \right)^2 \quad (26)$$

$$\phi_6 = L \left[\left(\frac{x}{L} \right)^3 - \left(\frac{x}{L} \right)^2 \right] \quad (27)$$

The nodal nonlinear forces in each element $\left(F_{in}^{(e)} \right)$ are given by Equations 28 to 37:

$$F_{1n}^{(e)} = \int_0^1 N_d \phi_1' dx \quad (28)$$

$$F_{2n}^{(e)} = \int_0^1 -M_{zd} \phi_2'' dx + \int_0^1 N_d \left(\phi_2' U_2 + \phi_3' U_3 + \phi_5' U_7 + \phi_6' U_8 \right) \phi_2' dx \quad (29)$$

$$F_{3n}^{(e)} = \int_0^1 -M_{zd} \phi_3'' dx + \int_0^1 N_d \left(\phi_2' U_2 + \phi_3' U_3 + \phi_5' U_7 + \phi_6' U_8 \right) \phi_3' dx \quad (30)$$

$$F_{4n}^{(e)} = \int_0^1 -M_{yd} \phi_2'' dx + \int_0^1 N_d \left(\phi_2' U_4 + \phi_3' U_5 + \phi_5' U_9 + \phi_6' U_{10} \right) \phi_2' dx \quad (31)$$

$$F_{5n}^{(e)} = \int_0^1 -M_{yd} \phi_3'' dx + \int_0^1 N_d \left(\phi_2' U_4 + \phi_3' U_5 + \phi_5' U_9 + \phi_6' U_{10} \right) \phi_3' dx \quad (32)$$

$$F_{6n}^{(e)} = \int_0^1 N_d \phi_4' dx \quad (33)$$

$$F_{7n}^{(e)} = \int_0^1 -M_{zd} \phi_5'' dx + \int_0^1 N_d \left(\phi_2' U_2 + \phi_3' U_3 + \phi_5' U_7 + \phi_6' U_8 \right) \phi_5' dx \quad (34)$$

$$F_{8n}^{(e)} = \int_0^1 -M_{zd} \phi_6'' dx + \int_0^1 N_d (\phi_2' U_2 + \phi_3' U_3 + \phi_5' U_7 + \phi_6' U_8) \phi_6' dx \tag{35}$$

$$F_{9n}^{(e)} = \int_0^1 -M_{yd} \phi_5'' dx + \int_0^1 N_d (\phi_2' U_4 + \phi_3' U_5 + \phi_5' U_9 + \phi_6' U_{10}) \phi_5' dx \tag{36}$$

$$F_{10n}^{(e)} = \int_0^1 -M_{yd} \phi_6'' dx + \int_0^1 N_d (\phi_2' U_4 + \phi_3' U_5 + \phi_5' U_9 + \phi_6' U_{10}) \phi_6' dx \tag{37}$$

The Gauss-Legendre quadrature rule is used to solve these equations. The nodal displacements, the six interpolation functions, and the ten equilibrium equations, combined, establish the system of Equation 38:

$$F_n^{(e)} = K^{(e)} U^{(e)} \tag{38}$$

where $F_n^{(e)}$ = load vector; $K^{(e)}$ = stiffness matrix; and $U^{(e)}$ = displacement vector of the e^{th} finite element.

Geometric nonlinearity is included in the last term of Equations 29 to 32 and Equations 34 to 37. The modified Newton-Raphson method with constant stiffness is used to solve the previously established nonlinear equations.

Material nonlinearity is considered when calculating the axial load N_d given by Equation 10, and when calculating the bending moments M_{zd} and M_{yd} obtained by Equations 11 and 12, respectively. The procedure proposed by Campos [31] is used to calculate these internal loads.

The global equation system is made by assembling the respective vectors and matrices of the finite elements that make up the column, and is given by Equation 39:

$$F_n = K U \tag{39}$$

where F_n = global load vector; K = global stiffness matrix; and U = global displacement vector.

2.5 Procedure for the optimal design of the column

The aim of optimization is to select the lowest cost column that meets the criteria established by the Brazilian Standard NBR 6118 [29].

The problem variables are (Figure 2a): width (b); height (h); diameter of the bars in layers Cam01 and Cam03 (dicam13); diameter of the bars in layers Cam02 and Cam04 (dicam24); number of bars in layers Cam01 and Cam03 (ncam13); number of bars in layers Cam02 and Cam04 (ncam24). Minimum and maximum values for the width (b) and height (h) of the column cross-section are established. The lowest value adopted for width and height is equal to 20 cm, and the highest value is equal to 95 cm. The diameters of the bars of the layers Cam01, Cam02, Cam03 and Cam04 can take commercial values between 10 mm and 40 mm. Layers Cam01, Cam02, Cam03 and Cam04 can have up to 9 bars per layer, and layers Cam02 and Cam04 can have no bars. Under the given conditions, the number of combinations of the variables involved results in 1,048,576 (Figure 2b).

Optimization of reinforced concrete column cross sections starts from a set of randomly created cross sections, and is carried out over generations. During the evolutionary process, individuals (cross sections) are coded by a set of bits (binary coding), and represented by chromosomes. Each value assigned to variables b, h, dicam13, dicam24, ncam13 and ncam24 is related to an integer and corresponds to a binary number according to Table 1.

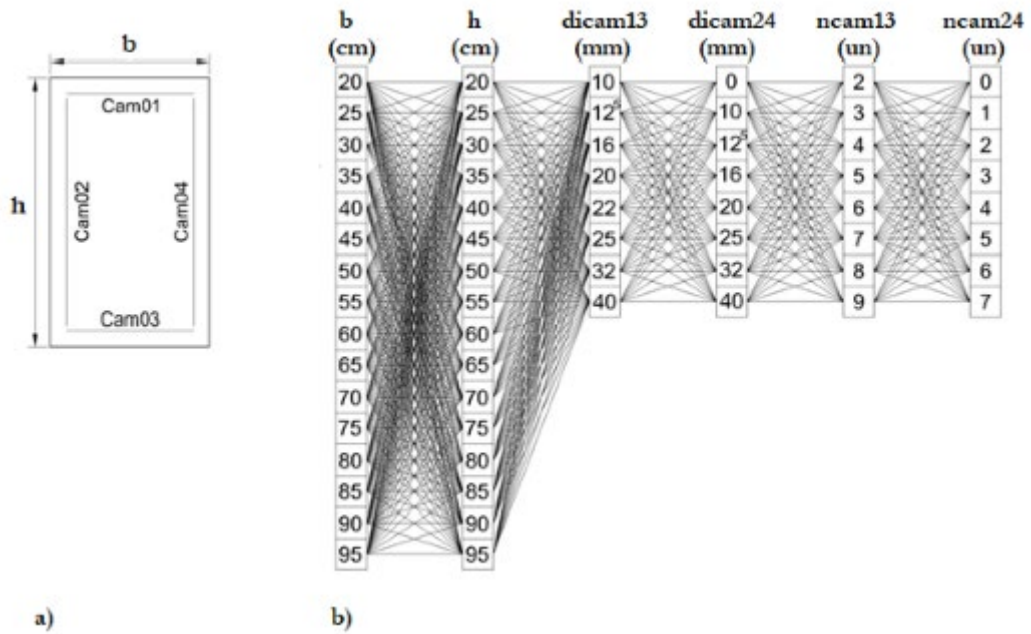


Figure 2. Column cross section: a) representation of variables; b) all combinations of variables.

Chromosome is represented by the following bit sequence: width (b) - 4 bits; height (h) - 4 bits; diameter of the bars of layers 01 and 03 (dicam13) - 3 bits; diameter of the bars of layers 02 and 04 (dicam24) - 3 bits; number of bars in layers 01 and 03 (ncam13) - 3 bits; number of bars in layers 02 and 04 (ncam24) - 3 bits.

Table 2 shows an example of coding the cross section of reinforced concrete columns, and Figure 3 illustrates the resulting chromosome.

Table 1. Relationship between variables and binary coding.

Integer	Binary number				b	dicam13	ncam13	ncam24
					h	dicam24		
					(cm)	(mm)		
0	0	0	0	0	20	10	2	0
1	0	0	0	1	25	12.5	3	1
2	0	0	1	0	30	16	4	2
3	0	0	1	1	35	20	5	3
4	0	1	0	0	40	22	6	4
5	0	1	0	1	45	25	7	5
6	0	1	1	0	50	32	8	6
7	0	1	1	1	55	40	9	7
8	1	0	0	0	60			
9	1	0	0	1	65			
10	1	0	1	0	70			
11	1	0	1	1	75			
12	1	1	0	0	80			
13	1	1	0	1	85			
14	1	1	1	0	90			
15	1	1	1	1	95			

Table 2. Cross section coding example.

Variable	Real number	Coding
b	20 cm	0001
h	80 cm	1100
dicam13	20 mm	011
dicam24	20 mm	100
ncam13	2	000
ncam24	5	101

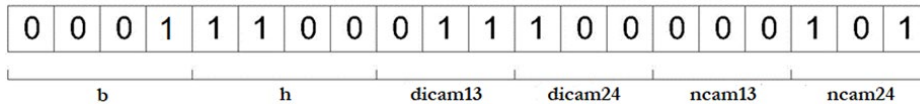


Figure 3. Cross section coding example.

After coding, each individual is evaluated during the evolutionary process by means of a fitness function, $Fa(x)$. This function is used to rank the best solutions, indicating the chances of survival and permanence of good features over generations. The fitness function, $Fa(x)$, is defined by Equation 40:

$$Fa(x) = F(x) \pm P(x) \tag{40}$$

where $F(x)$ = objective function; and $P(x)$ = penalty function.

In order to work with the term *fitness* of the individual, the cost minimization problem is transformed into a fitness maximization problem. The objective function $F(x)$ is defined as the inverse of the cost function $Cost(x)$ in Equation 41:

$$F(x) = \frac{1}{Cost(x)} \tag{41}$$

The cost function $Cost(x)$ is given by Equation 42:

$$Cost(x) = C_c l b h + C_s A_{s\ tot} l + C_f (2h + 2b) l \tag{42}$$

where C_c = cost of concrete per unit volume; C_s = cost of steel per unit volume; C_f = cost of the formwork per unit area; l = length of the column; b and h = dimensions of the column cross section; and $A_{s\ tot}$ = total steel area of the cross section of the column. The values for C_c , C_s and C_f were obtained on the website of the Foundation for the Development of Education [32].

The penalty function $P(x)$ represents the different constraints of the problem, and is given by Equation 43:

$$P(x) = \alpha(t) \left(\sum_{i=1}^r \max(0, g_i(x)) + \sum_{j=1}^m |h_j(x)| \right) \tag{43}$$

where α = coefficient used to control the degree of penalty; t = current generation; r = number of inequality constraints; and m = number of equality constraints.

In this paper, there are no equality constraints $h_j(x)$, and there are seven-inequality constraints $g_i(x)$, namely: the maximum strains of concrete and steel, the stability of the column, the minimum spacing of the reinforcement, the maximum spacing of the reinforcement, the minimum reinforcement rate, and the maximum reinforcement rate.

The magnitude of the coefficient α , in Equation 43, defines the degree of penalty that will be imposed on the individual. The degree of penalty must be sufficient to make the best feasible solution of the generation have the highest fitness value after the penalty. In this paper, the procedure proposed by Nanakorn and Meesomklin [33] is used to adjust the coefficient α .

In the optimization process, whenever an individual violates a constraint, whether strength, stability, or regulatory, that individual reduces its chances of being selected for the next generation. The individuals selected for the next generation are recombined or mutated and will form a new population that, in turn, will be used as input for the next iteration of the optimization algorithm. This procedure is repeated until a solution is found that satisfies the convergence criteria. The developed algorithm was implemented in a computer program called GENETIC ALGORITHM.

A second computer program called TOTAL SEARCH was developed to validate the GENETIC ALGORITHM computer program. The role of TOTAL SEARCH is to obtain the optimal design solution for a given column, using all possible combinations of variables, which in this paper is a total of 1,048,576 individuals (Figure 2b). In the TOTAL SEARCH program, each individual is checked once again for the same constraints used in the GENETIC ALGORITHM program. Among all the individuals, the one that has the lowest cost and satisfies all the constraints is chosen.

The TOTAL SEARCH program provides the exact answer to the problem, but its processing time is significantly longer than the time used by the GENETIC ALGORITHM program. Therefore, the results obtained by the TOTAL SEARCH program are only used as reference values to confirm the efficiency of the GENETIC ALGORITHM program.

A third computer program called COLUMN PROCESSING was developed to check the constraints of the column regarding its strength, stability, and compliance with normative specifications.

The development and details of the TOTAL SEARCH, GENETIC ALGORITHM and COLUMN PROCESSING computer programs are found in Pires [34].

2.6 About developed programs

The development of the GENETIC ALGORITHM program is derived from the LGADOS program developed by Coley [35]. In present paper, all necessary adjustments were inserted for adapting the LGADOS program to the proposed problem.

The analysis of the constraints in the GENETIC ALGORITHM program is done by two approaches. The first approach applies the Death Penalty Method, in which individuals (cross sections of the column) that do not meet one or more constraints are eliminated in the next generation. The second approach considers the inclusion of individuals (cross sections of the column) that have violated one or more constraints. This second approach applies the Penalty Method according to the procedure proposed by Nanakorn and Meesomklin [33].

The options adopted for the development of the GENETIC ALGORITHM program are presented below: selection - roulette; crossing - 1 point (randomly selected point); elitism - yes (one individual); number of generations - 100; stopping criterion - number of generations; population size (N_{POP}) - 60; crossover probability (P_c) - 0.6; mutation probability (P_m) - 0.02. For the Death Penalty Method, linear scaling is adopted, with a scale constant (C) equal to 2. For the Penalty Method, bilinear scaling is adopted, with constants C , ϕ and Z equal to 2, 1 and 5, respectively.

The COLUMN PROCESSING program calculates the ultimate load for a reinforced concrete column subjected to biaxial bending, considering the material and geometric nonlinearities rigorously. This program also checks the constraints imposed on the objective function $F(x)$.

3 RESULTS AND DISCUSSION

3.1 Analysis of the COLUMN PROCESSING computer program

The COLUMN PROCESSING program, before being used as a computational tool to support the optimization programs GENETIC ALGORITHM and TOTAL SEARCH, had its efficiency verified through a comparative analysis. Two experimental studies were used: Kim and Yang [36], and Claeson and Gylltoft [37]. The following variables were considered in this comparative analysis: c is the concrete cover of the column; L is the length of the column; f_c is the

compressive strength of concrete; f_y is the yield strength of steel; $P_{u,a}$ is the ultimate load calculated by COLUMN PROCESSING program; $P_{u,t}$ is the ultimate load of the experimental study. The rate of change of the ultimate load values calculated by the COLUMN PROCESSING program in relation to the experimental ultimate load values, Δ , is given by Equation 44:

$$\Delta = \left(\frac{P_{u,a}}{P_{u,t}} \right) \tag{44}$$

Kim and Yang [36] performed a series of tests on reinforced concrete columns to verify the effects of concrete compressive strength, slenderness, and reinforcement ratio on ultimate load and on the relationship between axial force and bending moment. The authors used different values for concrete compressive strength f_c (25.5 MPa, 63.5 MPa, and 86.2 MPa), reinforcement rate ρ (1.98% and 3.95%), and slenderness ratio λ (10, 60, and 100). In this comparative analysis, two columns (1 and 2) were considered, and only concrete compressive strength equal to 25.5 MPa was used. The rate of change (Δ) of the values of the ultimate loads calculated by the COLUMN PROCESSING program in relation to the experimental ultimate loads obtained by Kim and Yang [36] ranged from 0.89 to 1.09. Table 3 presents the characteristics and results of those analyzed columns.

Table 3. Comparison between COLUMN PROCESSING program results and the experimental results of Kim and Yang [36].

Col.	b (cm)	h (cm)	ρ	L (cm)	f_c (MPa)	f_y (MPa)	$P_{u,t}$ (kN)	$P_{u,a}$ (kN)	Δ
10L4-1	8	8	3.95%	24	25.5	387	109.5	98	0.89
10L4-2	8	8	3.95%	24	25.5	387	109.3		0.90
60L2-1	8	8	1.98%	144	25.5	387	63.7	62	0.97
60L2-2	8	8	1.98%	144	25.5	387	65.7		0.94
100L2-1	8	8	1.98%	237	25.5	387	38.2	38	0.99
100L2-2	8	8	1.98%	237	25.5	387	35.0		1.09
100L4-1	8	8	3.95%	237	25.5	387	49.0	48	0.98
100L4-2	8	8	3.95%	237	25.5	387	47.0		1.02

Claeson and Gylltoft [37] carried out an experimental study to analyze the behavior of reinforced concrete columns. The authors analyzed the effects of slenderness and concrete compressive strength on the ultimate load of the columns. The rate of change (Δ) of the values of the ultimate loads calculated by the COLUMN PROCESSING program in relation to the experimental ultimate loads obtained by Claeson and Gylltoft [37] ranged from 0.95 and 1.07. Table 4 presents the characteristics and results of those analyzed columns.

Table 4. Comparison between COLUMN PROCESSING program results and the experimental results of Claeson and Gylltoft [37].

Col.	b (cm)	h (cm)	L (cm)	dicam13 (mm)	dicam24 (mm)	ncam13	ncam24	c (cm)	f_c (MPa)	f_y (MPa)	$P_{u,t}$ (kN)	$P_{u,a}$ (kN)	Δ
23	12	12	240	12	0	2	0	1.5	43	684	320	305	0.95
24	12	12	240	12	0	2	0	1.5	43	636	288	305	1.06
27	20	20	300	16	0	2	0	1.5	33	636	990	1019	1.03
28	20	20	300	16	0	2	0	1.5	33	636	990	1019	1.03
32	20	20	400	16	0	2	0	1.5	37	636	920	981	1.07

The comparative study showed that there is good agreement between the experimental results and the values obtained by the COLUMN PROCESSING program.

3.2 Analysis of the GENETIC ALGORITHM program

Three columns named P1, P2 and P3 were used to evaluate the effectiveness of the Genetic Algorithm program. Table 5 shows the geometric characteristics of these columns and the characteristics of the materials used.

Table 5. Features of the columns P1, P2 and P3.

Features	Column		
	P1	P2	P3
Concrete cover (cm)	2.5	2.5	2.5
Column height (cm)	300	423	423
f_{ck} (kN/cm ²)	3.3	2.5	2.5
f_{yk} (kN/cm ²)	63.6	50	50
E_s (kN/cm ²)	20700	21000	21000

The structural analysis was performed using FEM. Column P1 is subject to uniaxial bending. Columns P2 and P3 are subject to biaxial bending, with column P3 subject to much larger first-order moments (M_z and M_y) than those applied to column P2. Each column was composed of 10 bars and 11 nodes. Nodes 1 and 11 are the end nodes. Node 1 was constrained in the x, y and z directions, and node 11 was constrained in the y and z directions. The axial force applied in the x direction at nodes 1 and 11 was equal to 1019 kN at column P1, 1230 kN at column P2, and 2000 kN at column P3. The bending moment M_z applied to nodes 1 and 11 of column P1 was equal to 2038 kN.cm. The bending moments M_z and M_y applied to nodes 1 and 11 of column P2 were equal to 1291.5 and 701.1, respectively. The bending moments M_z and M_y applied at nodes 1 and 11 of column P3 were equal to 60000 kN.cm.

Initially, the TOTAL SEARCH program is used to calculate the exact global minimum cost (C_{global}) for each column analyzed.

Next, the GENETIC ALGORITHM program is used according to the following steps: each column is calculated 10 times by applying the Death Penalty Method to the constraint analysis, and the column is again calculated 10 times by applying the Death Penalty Method. The minimum cost values (C_{min}) are obtained. Tables 6, 7 and 8 show the results for columns P1, P2 and P3, respectively. The relative error (E_{rel}) is calculated based on the cost value obtained by the TOTAL SEARCH program, and is given by Equation 45:

$$E_{rel} = \frac{C_{min} - C_{global}}{C_{global}} \quad (45)$$

The results obtained for column P1 show that the relative error (E_{rel}) ranged from 0 to 3%, with seven values converging to the optimal value calculated by the TOTAL SEARCH program, when the Penalty Method was adopted for the constraints analysis. The relative error (E_{rel}) ranged between 0 and 2%, and six values converged to the optimum value, when the Death Penalty Method was used.

The results obtained for column P2 show that the relative error (E_{rel}) ranged from 0 to 4%, with two values converging to the optimal value calculated by the TOTAL SEARCH program, when the Penalty Method was adopted for the constraints analysis. The relative error (E_{rel}) ranged between 0 and 4%, and two values converged to the optimum value, when the Death Penalty Method was used.

The results obtained for column P3 show that the relative error (E_{rel}) ranged from 0 to 5%, with one value converging to the optimal value calculated by the TOTAL SEARCH program, when the Penalty Method was adopted for the constraints analysis. The relative error (E_{rel}) ranged between 0 and 4%, and one value converged to the optimum value, when the Death Penalty Method was used.

In general, it was found that the results obtained by the GENETIC ALGORITHM program converged to the optimal solution or to values close to the optimal solution, taking the values provided by the TOTAL SEARCH program as reference. This finding confirms the efficiency of the GENETIC ALGORITHM program, since the TOTAL SEARCH program provides the exact value of the optimization process. It should also be noted that the processing time spent by the GENETIC ALGORITHM program is significantly lesser than the processing time spent by the TOTAL SEARCH program. The respective processing times spent on the analysis of columns P1, P2 and P3 are shown in Tables 6, 7 and 8.

Table 6. Results obtained for column P1.

TOTAL SEARCH Results - Processing time: 18 minutes							
C_{global}	Width	Height	Diameter		Diameter		Number of bars
(RS)	(cm)	(cm)	[layers 1 and 3]	[layers 2 and 4]	[layers 1 and 3]	[layers 2 and 4]	
			(mm)	(mm)	(un)	(un)	
439,79	40	20	10	0	3	0	
GENETIC ALGORITHM Results (using Penalty Method) - Processing time - 12 seconds							
C_{min}	E_{rel}	Width	Height	Diameter		Diameter	
(RS)		(cm)	(cm)	[layers 1 and 3]	[layers 2 and 4]	[layers 1 and 3]	[layers 2 and 4]
				(mm)	(mm)	(un)	(un)
439.79	0%	40	20	10	10	2	1
447.94	2%	35	25	10	16	3	0
439.79	0%	40	20	10	40	3	0
447.94	2%	35	25	10	10	2	1
453.87	3%	30	30	12.5	0	2	0
439.79	0%	40	20	10	16	3	0
439.79	0%	40	20	10	0	3	0
439.79	0%	40	20	10	20	3	0
439.79	0%	40	20	10	10	3	0
439.79	0%	40	20	10	0	3	0
GENETIC ALGORITHM Results (using Death Penalty Method) - Processing time: 10 seconds							
C_{min}	E_{rel}	Width	Height	Diameter		Diameter	
(RS)		(cm)	(cm)	[layers 1 and 3]	[layers 2 and 4]	[layers 1 and 3]	[layers 2 and 4]
				(mm)	(mm)	(un)	(un)
443.00	1%	40	20	12.5	0	2	0
439.79	0%	40	20	10	12.5	3	0
447.94	2%	35	25	10	0	3	3
439.79	0%	40	20	10	10	3	0
443.00	1%	40	20	12.5	0	2	0
439.79	0%	40	20	10	0	3	0
439.79	0%	40	20	10	0	3	0
439.79	0%	40	20	10	0	3	0
450.66	2%	30	30	10	12.5	3	0
439.79	0%	40	20	10	0	3	0

Finally, it was found that no significant differences were found when comparing the results obtained by the two methods used in the GENETIC ALGORITHM program for the constraints analysis, the Penalty Method and the Death Penalty Method. Both methods showed consistent and satisfactory results.

3.3 The effect of slenderness on the optimal design of reinforced concrete columns

The effect of slenderness ratio (λ) on the optimal design of reinforced concrete columns was also analyzed.

Twelve columns were adopted, based on the characteristics of P2 column. These columns were called P2.i, with i ranging from 1 to 12. Column P2 was selected as a reference because it was subjected to biaxial bending and not very high first-order moments, which allowed the length of the column to be varied until very high values of λ were reached.

Values between 300 cm and 1400 cm were considered for the column length (l), and the smallest dimension (h) of the column cross section was fixed at 25 centimeters in order to induce high values for λ .

The slenderness ratio of columns P2.1 to P2.12 were calculated according to the following criteria of code NBR 6118/2014: columns must have a slenderness ratio less than or equal to 200 ($\lambda \leq 200$); second order local internal

loads on isolated members can be neglected when slenderness ratio is less than the limit value (λ_1). Slenderness ratio (λ) and limit slenderness ratio (λ_1) are obtained by Equations 46 and 47, respectively:

$$\lambda = \frac{l\sqrt{12}}{h} \tag{46}$$

$$\lambda_1 = \frac{25 + \frac{12.5e_1}{h}}{\alpha_b} \quad 35 \leq \lambda_1 \leq 90 \tag{47}$$

where l = column length; h = size of the cross section parallel to the plane of the moment acting on the column; e_1 = smallest value of the first-order eccentricity at the cross section under consideration; and α_b = coefficient that depends on the bending moment distribution in the column.

Table 7. Results obtained for column P2.

TOTAL SEARCH Results - Processing time: 48 minutes							
C_{global} (R\$)	Width (cm)	Height (cm)	Diameter [layers 1 and 3] (mm)	Diameter [layers 2 and 4] (mm)	Number of bars [layers 1 and 3] (un)	Number of bars [layers 2 and 4] (un)	
807.30	30	40	12.5	0	3	0	
GENETIC ALGORITHM Results (using Penalty Method) - Processing time: 21 seconds							
C_{min} (R\$)	E_{rel}	Width (cm)	Height (cm)	Diameter [layers 1 and 3] (mm)	Diameter [layers 2 and 4] (mm)	Number of bars [layers 1 and 3] (un)	Number of bars [layers 2 and 4] (un)
807.30	0%	30	40	12.5	0	3	0
818.61	1%	30	40	10	10	5	0
818.61	1%	30	40	10	0	5	0
837.80	4%	45	30	10	25	4	0
826.78	2%	35	35	16	40	2	0
843.40	4%	40	30	12.5	16	2	1
837.80	4%	45	30	10	0	4	0
822.95	2%	40	30	16	32	2	0
838.97	4%	30	40	10	12.5	4	1
807.30	0%	30	40	12.5	0	3	0
GENETIC ALGORITHM Results (using Death Penalty Method) - Processing time: 18 seconds							
C_{min} (R\$)	E_{rel}	Width (cm)	Height (cm)	Diameter [layers 1 and 3] (mm)	Diameter [layers 2 and 4] (mm)	Number of bars [layers 1 and 3] (un)	Number of bars [layers 2 and 4] (un)
822.44	2%	35	35	10	10	2	3
818.61	1%	30	40	10	40	5	0
822.95	2%	30	40	16	0	2	0
822.95	2%	30	40	16	0	2	0
826.78	2%	35	35	16	0	2	0
837.80	4%	45	30	10	10	2	2
807.30	0%	30	40	12.5	40	3	0
822.95	2%	40	30	16	0	2	0
807.30	0%	30	40	12.5	0	3	0
826.78	2%	35	35	16	0	2	0

Table 8. Results obtained for column P3.

TOTAL SEARCH Results - Processing time: 18 minutes							
C_{global}	Width	Height	Diameter	Diameter	Number of bars	Number of bars	
(R\$)	(cm)	(cm)	[layers 1 and 3]	[layers 2 and 4]	[layers 1 and 3]	[layers 2 and 4]	
			(mm)	(mm)	(un)	(un)	
2779.5	65	95	20	10	5	2	
GENETIC ALGORITHM Results (using Penalty Method) - Processing time: 32 seconds							
C_{min}	E_{rel}	Width	Height	Diameter	Diameter	Number of bars	Number of bars
(R\$)		(cm)	(cm)	[layers 1 and 3]	[layers 2 and 4]	[layers 1 and 3]	[layers 2 and 4]
				(mm)	(mm)	(un)	(un)
2855.32	3%	60	95	20	10	6	3
2929.16	5%	60	95	16	10	9	6
2867.08	3%	60	95	22	12.5	5	2
2820.22	1%	65	95	20	12.5	5	2
2779.50	0%	65	95	20	20	5	2
2796.87	1%	65	95	16	10	8	2
2855.32	3%	60	95	25	10	4	2
2896.04	4%	60	95	25	12.5	4	2
2891.51	4%	60	95	25	10	4	3
2796.87	1%	65	95	16	10	8	2
GENETIC ALGORITHM Results (using Death Penalty Method) - Processing time: 19 seconds							
C_{min}	E_{rel}	Width	Height	Diameter	Diameter	Number of bars	Number of bars
(R\$)		(cm)	(cm)	[layers 1 and 3]	[layers 2 and 4]	[layers 1 and 3]	[layers 2 and 4]
				(mm)	(mm)	(un)	(un)
2796.87	1%	65	95	16	10	8	2
2796.87	1%	65	95	16	10	8	2
2839.42	2%	70	95	22	10	3	2
2861.50	3%	70	95	22	10	4	2
2896.04	4%	60	95	25	12.5	4	2
2796.87	1%	65	95	16	10	8	2
2869.27	3%	65	95	16	10	8	4
2855.32	3%	60	95	20	10	6	3
2881.77	4%	70	95	16	10	7	4
2779.50	0%	65	95	20	10	5	2

The optimal design results shown in Table 9 were obtained by the TOTAL SEARCH program. This computer program was used in this step because it provides the exact solution in the search space.

Figure 4 elaborated from the values in Table 9 shows the relationship between critical slenderness ratio and column cost. In this analysis, the critical slenderness ratio always occurred in the XZ plane, that is, λ_z . The slenderness ratio λ_z ranged from 41.57 to 193.99, and costs ranged from R\$ 546.40 to R\$ 9843.42. These relationships show that the more slender a reinforced concrete column is, the higher its cost.

The classification of the columns according to slenderness used in this work is shown in Table 10, and the results found for slenderness ratios and reinforcement rates for columns P2.1 to P2.12 are shown in Table 11.

Table 9. Optimal design of reinforced concrete columns P2.1 to P2.12.

Column	l (cm)	h (cm)	b (cm)	λ_y	λ_z	Diameter Layers 1 and 3 (mm)	Number of bars 1+3 (un.)	Diameter Layers 2 and 4 (mm)	Number of bars 2+4 (un.)	Column Cost (R\$)
2.1	300	25	40	23.09	41.57	10	10	0	0	546.40
2.2	400	25	45	30.75	55.43	16	16	0	0	767.34
2.3	500	25	50	34.74	69.28	10	10	10	4	972.20
2.4	600	25	55	37.79	83.14	10	10	10	4	1239.78
2.5	700	25	60	40.41	96.99	10	10	10	4	1531.73
2.6	800	25	60	46.19	110.85	10	10	12.5	6	1934.54
2.7	900	25	55	56.69	124.71	16	16	12.5	12	2667.97
2.8	1000	25	55	62.98	138.56	12.5	12.5	16	14	3524.93
2.9	1100	25	55	69.28	152.42	10	10	20	14	4720.39
2.1	1200	25	55	75.58	166.28	10	10	25	12	6125.08
2.11	1300	25	50	90.07	180.13	10	10	32	10	8001.14
2.12	1400	25	50	96.99	193.99	10	10	32	12	9843.42

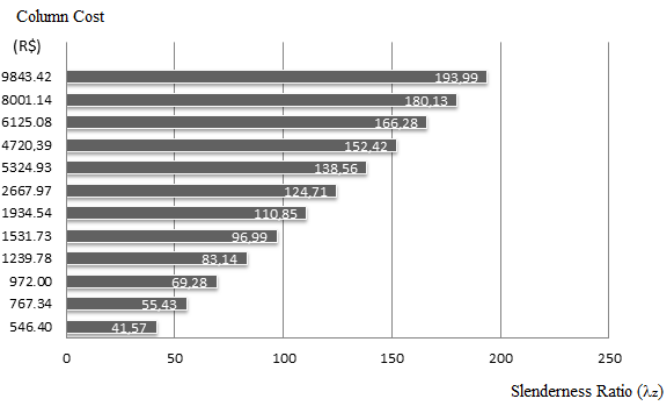


Figure 4. Relationship between the Slenderness Ratio (λ_z) and the Column Cost.

Table 10. Column classification according to slenderness.

λ	Classification	Group
$\lambda \leq \lambda_l$	Short column	1
$\lambda_l < \lambda \leq 90$	Moderately slender column	2
$90 < \lambda \leq 140$	Slender column	3
$140 < \lambda \leq 200$	Very slender column	4

By initially analyzing the complete set of columns from P2.1 to P2.12, it can be seen that as the slenderness ratio increases, the concrete area (A_c) and the steel area (A_s) increase. However, while A_c increases by at most 50% (from 1,000 cm² to 1,500 cm²), A_s increases about 20 times (from 4.71 cm² to 99.65 cm²). This behavior shows that the increased bending due to second order effects caused by the increased slenderness is now absorbed predominantly by the reinforcement.

It is also possible to analyze columns P2.1 to P2.12 according to the slenderness classification shown in Table 10. The columns were divided into three groups: moderately slender columns, with $\lambda_l < \lambda \leq 90$ (P2.1 to P2.4); slender columns, with $90 < \lambda \leq 140$ (P2.5 to P2.8), and very slender columns, with $140 < \lambda \leq 200$ (P2.9 to P2.12). In the moderately slender columns group, the concrete area varied around 37% (from 1,000 to 1,375 cm²), while the reinforcement rate (ρ) varied around 54% (from 0.46% to 0.71%). In the slender columns group, the concrete area

varied around 9% (from 1,375 to 1,500 cm²) while the reinforcement rate varied more than 400% (from 0.42% to 2.40%). In the very slender columns group, the concrete area varied 10% - very close to the variation in the previous group - and the reinforcement rate varied around 130% (from 3.43% to 7.97%).

Table 11. Slenderness ratio (λ), reinforcement rate (ρ), and column classification according to slenderness.

Column	λ_y	λ_z	e_{1y}	e_{1z}	α_b	λ_{1Y}	λ_{1Z}	$\frac{A_{s\ total}}{(cm^2)}$	$\frac{A_c}{(cm^2)}$	ρ	Group
2.1	23.09	41.57	0.57	1.05	1	35	35	4.71	1000	0.47%	2
2.2	30.75	55.43	0.57	1.05	1	35	35	8.04	1125	0.71%	2
2.3	34.74	69.28	0.57	1.05	1	35	35	6.28	1250	0.50%	2
2.4	37.79	83.14	0.57	1.05	1	35	35	6.28	1375	0.46%	2
2.5	40.41	96.99	0.57	1.05	1	35	35	6.28	1500	0.42%	3
2.6	46.19	110.85	0.57	1.05	1	35	35	10.50	1500	0.70%	3
2.7	56.69	124.71	0.57	1.05	1	35	35	22.77	1375	1.66%	3
2.8	62.98	138.56	0.57	1.05	1	35	35	33.06	1375	2.40%	3
2.9	69.28	152.42	0.57	1.05	1	35	35	47.12	1375	3.43%	4
2.1	75.58	166.28	0.57	1.05	1	35	35	62.05	1375	4.51%	4
2.11	90.07	180.13	0.57	1.05	1	35	35	83.57	1250	6.69%	4
2.12	96.99	193.99	0.57	1.05	1	35	35	99.65	1250	7.97%	4

$A_{s\ total}$ -total steel area of cross section; A_c -gross concrete area of cross section; ρ -reinforcement rate ($A_{s\ total}/A_c$).

These results show that in the optimization of moderately slender columns there was an equilibrium between concrete and steel. On the other hand, in the search for the optimal solution for slender and very slender columns, the concrete area oscillated very little, while the steel area played a predominant role. Figure 5 elaborated from the values in Table 11 shows the relationship between the reinforcement rate and the slenderness ratio for columns P2.1 to P2.12.

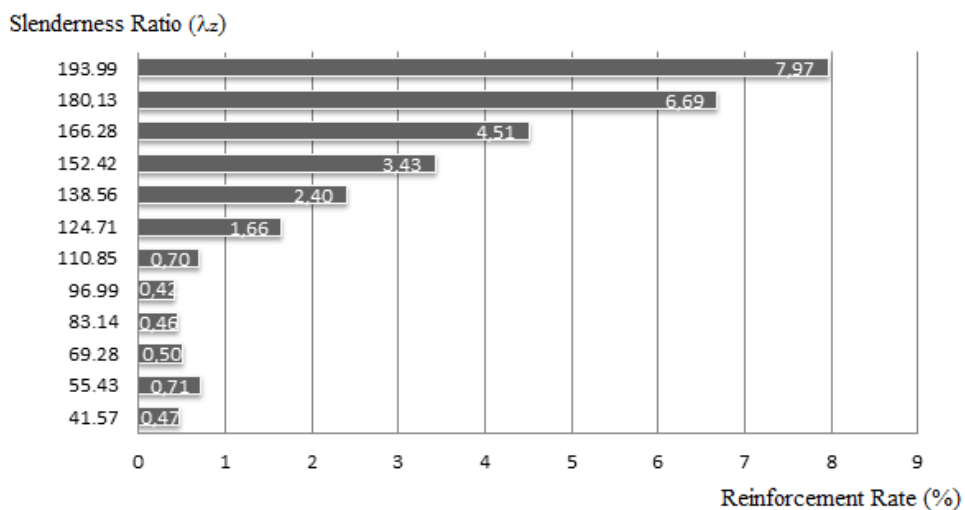


Figure 5. Relationship between Reinforcement Rate and Slenderness Rate (λ_z).

4 CONCLUSIONS

In this paper, a procedure was developed to choose, within a range of possible solutions, the column that best meets the requirements of safety, economy and regulation. From this procedure, a computational tool was developed to optimize the cross section of slender reinforced concrete columns subjected to biaxial bending, strictly considering material and geometric nonlinearities, i.e., simplified methods are not used.

The computational tool composed of the GENETIC ALGORITHM and COLUMN PROCESSING programs provided answers that always converged to an optimal solution or to a solution located in the vicinity of the optimal solution. It is relevant to note that, of the more than one million possible solutions that make up the search space of the problem, the Genetic Algorithm technique allowed a satisfactory answer to be found by exploring only two thousand solutions.

It is also possible to conclude, analyzing each program separately, that:

- the COLUMN PROCESSING program, before being used to support the optimization programs, had its efficiency proven through a comparative study with experimental results obtained in the current literature;
- the efficiency obtained by the GENETIC ALGORITHM program showed that the chosen optimization technique is not limited to a series of random crossings. Rather, the technique uses evolutionary crossings that always result in an efficient solution to the problem;
- the Genetic Algorithm technique and the associated program developed in this study resulted in a robust procedure that works with discrete variables, and proved to be quite adaptable to the proposed problem;
- no significant differences were found when comparing the results obtained by the two methods used in the GENETIC ALGORITHM program for constraint analysis, the Penalty Method and the Death Penalty Method. Both methods showed consistent and satisfactory results.

Finally, the GENETIC ALGORITHM program combined with the COLUMN PROCESSING program proved to be an efficient computational tool, providing safe and economical solutions that guarantee the best cost-benefit ratio for the design.

Regarding the effect of the slenderness coefficient (λ) on the optimal design of reinforced concrete columns, the analysis showed that the more slender a reinforced concrete column is, the higher its cost will be. The analysis also showed that to establish the equilibrium of the structural element, the increase in bending due to second-order effects caused by the increase in slenderness starts to be absorbed predominantly by the reinforcement.

ACKNOWLEDGEMENTS

The authors gratefully acknowledge the financial support received by the Brazilian Grant Agency CAPES (Coordenação de Aperfeiçoamento de Pessoal de Nível Superior) – Finance Code 001.

5 REFERENCES

- [1] S. L. Pires and M. C. A. T. Silva, "A numerical procedure for reinforced concrete columns with a focus on stability analysis," *Comput. Concr.*, vol. 14, no. 6, pp. 657–674, 2014.
- [2] J. K. Kim and S. S. Lee, "The behaviour of reinforced concrete columns subjected to axial force and biaxial bending," *Eng. Struct.*, vol. 22, no. 11, pp. 1518–1528, 2000.
- [3] G. K. Kwak and J. K. Kim, "Ultimate resisting capacity of slender RC columns," *Comput. Struct.*, vol. 82, no. 11-12, pp. 901–915, 2004.
- [4] G. K. Kwak and J. K. Kim, "Nonlinear behavior of slender RC columns (1). Numerical formulation," *Constr. Build. Mater.*, vol. 20, no. 8, pp. 527–537, 2006.
- [5] G. K. Kwak and J. K. Kim, "Nonlinear behavior of slender RC columns (2). Introduction of design formula," *Constr. Build. Mater.*, vol. 20, no. 8, pp. 538–553, 2006.
- [6] T. Majewski, J. Bobinski, and J. Tejchman, "FE analysis of failure behavior of reinforced concrete columns under eccentric compression," *Eng. Struct.*, vol. 30, no. 2, pp. 300–317, 2008.
- [7] H. G. Kwak and J. H. Kwak, "An improved design formula for biaxially loaded slender RC column," *Eng. Struct.*, vol. 32, no. 1, pp. 226–237, 2010.
- [8] J. L. Bonet, P. F. Miguel, M. A. Fernandez, and M. L. Romero, "Biaxial bending moment magnifier method," *Eng. Struct.*, vol. 26, no. 13, pp. 2007–2019, 2004.
- [9] J. L. Bonet, M. L. Romero, P. F. Miguel, and M. A. Fernandez, "A fast stress integration algorithm for reinforced concrete sections with axial loads and biaxial bending," *Comput. Struct.*, vol. 82, no. 2-3, pp. 213–225, 2004.
- [10] J. L. Bonet, M. H. F. M. Barros, and M. L. Romero, "Comparative study of analytical and numerical algorithms for designing reinforced concrete sections under biaxial bending," *Comput. Struct.*, vol. 84, no. 31-32, pp. 2184–2193, 2006.
- [11] J. L. Bonet, M. L. Romero, and P. F. Miguel, "Effective flexural stiffness of slender reinforced concrete columns under axial forces and biaxial bending," *Eng. Struct.*, vol. 33, no. 3, pp. 881–893, 2011.
- [12] L. Pallarés, P. F. Miguel, and M. A. Fernández-Prada, "A numerical method to design reinforced concrete sections subjected to axial forces and biaxial bending based on ultimate strain limits," *Eng. Struct.*, vol. 31, no. 12, pp. 3065–3071, 2009.

- [13] C. A. C. Coello, A. D. Christiansen, and F. S. Hernandez, "A simple genetic algorithm for a design of reinforced concrete beams," *Eng. Comput.*, vol. 13, no. 4, pp. 185–196, 1997.
- [14] V. Govindaraj and J. V. Ramasamy, "Optimum detailed design of reinforced concrete continuous beams using Genetic Algorithms," *Comput. Struc.*, vol. 84, no. 1-2, pp. 34–48, 2005.
- [15] P. G. Bakir and Y. S. Erdogan, "Damage identification in reinforced concrete beams by finite element model updating using parallel and hybrid genetic algorithms," *Int. J. Comput. Methods*, vol. 10, no. 3, 1350010, 2013.
- [16] M. Y. Rafiq and C. Southcombe, "Genetic algorithms in optimal design and detailing of reinforced concrete biaxial columns supported by a declarative approach for capacity checking," *Comput. Struc.*, vol. 69, no. 4, pp. 443–457, 1998.
- [17] V. K. Koumousis and S. J. Arsenis, "Genetic algorithms in optimal detailed design of reinforced concrete members," *Comput. Aided Civ. Infrastruct. Eng.*, vol. 13, no. 1, pp. 43–52, 1998., <http://dx.doi.org/10.1111/0885-9507.00084>.
- [18] S. Rajeev and C. S. Krishnamoorthy, "Genetic algorithm-based methodology for design optimization of reinforced concrete frames," *Comput. Aided Civ. Infrastruct. Eng.*, vol. 13, no. 1, pp. 63–74, 1998., <http://dx.doi.org/10.1111/0885-9507.00086>.
- [19] A. Kaveh and H. Rahami, "Nonlinear analysis and optimal design of structures via force method and genetic algorithm," *Comput. Struc.*, vol. 84, no. 12, pp. 770–778, 2006.
- [20] I. N. Serpik, I. V. Mironenko, and V. I. Averchenkov, "Algorithm for evolutionary optimization of reinforced concrete frames subject to nonlinear material deformation," *Procedia Eng.*, vol. 150, pp. 1311–1316, 2016.
- [21] M. Mangal and J. C. P. Cheng, "Automated optimization of steel reinforcement in RC building frames using building information modeling and hybrid genetic algorithm," *Autom. Construct.*, vol. 90, pp. 39–57, 2018.
- [22] S. Taфраout, N. Bourahla, Y. Bourahla, and A. Mebarki, "Automatic structural design of RC wall-slab buildings using a genetic algorithm with application in BIM environment," *Autom. Construct.*, vol. 106, pp. 102901, 2019.
- [23] A. Stanton and A. A. Javadi, "An automated approach for an optimised least cost solution of reinforced concrete reservoirs using site parameters," *Eng. Struct.*, vol. 60, pp. 32–40, 2014.
- [24] F. Di Trapani, M. Malavisi, G. C. Marano, A. P. Sberna, and R. Greco, "Optimal seismic retrofitting of reinforced concrete buildings by steel-jacketing using a genetic algorithm-based framework," *Eng. Struct.*, vol. 219, pp. 110864, 2020.
- [25] A. T. Albuquerque, M. K. El Debs, and A. M. C. Melo, "A cost optimization-based design of precast concrete floors using genetic algorithms," *Autom. Construct.*, vol. 22, pp. 348–356, 2012.
- [26] Y. Chen et al., "Optimum design for unbonded posttensioned precast split shear wall system using genetic algorithm," *Struct. Des. Tall Spec. Build.*, vol. 28, no. 5, e1582, 2019. <http://dx.doi.org/10.1002/tal.1582>.
- [27] M. Shahnewaz, R. Machial, M. S. Alam, and A. Rteil, "Optimized shear design equation for slender concrete beams reinforced with FRP bars and stirrups using Genetic Algorithm and reliability analysis," *Eng. Struct.*, vol. 107, pp. 151–165, 2016.
- [28] H. Baji, W. Yang, and C.-Q. Li, "An optimum strengthening strategy for corrosion-affected reinforced concrete structures," *ACI Struct. J.*, vol. 114, no. 6, pp. 1591–1602, 2017.
- [29] Associação Brasileira de Normas Técnicas, *Projeto de Estruturas de Concreto – Procedimentos*, NBR-6118, 2014.
- [30] W. F. Chen and T. Atsuta, *Theory of Beam-Columns, vol. 2, Space Behavior and Design*. New York: J. Ross Publishing, 2007.
- [31] A. Campos Fo., *Dimensionamento e Verificação de Seções Poligonais de Concreto Armado Submetidas à Flexão Composta Oblíqua*. Porto Alegre: CPGEC/UFRGS, 2014.
- [32] Fundação para o Desenvolvimento da Educação – FDE. http://www.fde.sp.gov.br/fornecedores/produtos_técnicos (accessed Nov. 10, 2016).
- [33] P. Nanakorn and K. Meesomklin, "An adaptive penalty function in genetic algorithms for structural design optimization," *Comput. Struc.*, vol. 79, no. 29-30, pp. 2527–2539, 2001.
- [34] S. L. Pires, "Otimização por algoritmos genéticos de pilares esbeltos de concreto armado submetidos à flexão oblíqua," Ph.D. dissertation, FEC, UNICAMP, Campinas, SP, 2014.
- [35] D. A. Coley, *An Introduction to Genetic Algorithms for Scientists and Engineers*. Singapore: World Scientific, 1999.
- [36] J. K. Kim and J. K. Yang, "Buckling behaviour of slender high-strength concrete columns," *Eng. Struct.*, vol. 17, no. 1, pp. 39–51, 1995.
- [37] C. Claeson and K. Gylltoft, "Slender high-strength concrete columns subjected to eccentric loading," *J. Struct. Eng.*, vol. 124, no. 3, pp. 233–240, 1998.

Author contributions: SLP: conceptualization, methodology, formal analysis, development of the computational tools, writing; MCATS: conceptualization, methodology, data curation, writing, supervision.

Editors: Mauricio Pina Ferreira, Guilherme Aris Parsekian.



ORIGINAL ARTICLE

Numerical and parametric study of the yield stress limits of reinforcement bars in clay block masonry structures

Estudo numérico e paramétrico sobre o limite da tensão de escoamento da armadura na alvenaria estrutural de blocos cerâmicos

Orieta Soto Izquierdo^a Márcio Roberto Silva Corrêa^b Indara Soto Izquierdo^a Iván Gómez Araújo^c ^aUniversidade Federal do Tocantins – UFT, Curso de Engenharia Civil, Palmas, TO, Brasil^bUniversidade de São Paulo – USP, Departamento de Estruturas, São Carlos, SP, Brasil^cUniversidade Federal da Integração Latino-Americana – UNILA, Departamento de Engenharia Civil e de Infraestrutura, Foz do Iguaçu, PR, BrasilReceived 07 June 2020
Accepted 05 April 2021

Abstract: The Brazilian Standard Structural Masonry considers for the maximum tensile stress (f_t) of the reinforcements embedded in the grout in clay blocks with smooth surfaces several limits of the yield stress for the reinforcement (f_{yk}). This work aims to analyze the limits of the yield stress of reinforcement bars in clay block masonry structures by numerical and parametric analysis in push-out and pull-out tests, varying the type of grout and reinforcement diameter. A numerical study was performed using a 3D-model with the DIANA® software based on the Finite Element Method. The parametric study confirmed that the limits obtained in this research for reinforcement diameter of 8 mm, 10 mm, 12.5 mm and 16 mm are in agreement with the limits specified by the Brazilian Standard, with exception of the 20 mm diameter, which limit was lower than indicated by the Standard. The tensile stress limits of the embedded reinforcement progressively reduce with increasing rebar diameter, being the failure is dominated by the bond strength of the block/grout interface.

Keywords: yield stress, bond strength, block/grout interface, finite element, clay blocks.

Resumo: A norma brasileira de alvenaria estrutural considera para a tensão máxima de tração das armaduras (f_t) embutida no graute em blocos cerâmicos com superfícies lisas vários limites da tensão de escoamento do aço (f_{yk}). Este trabalho teve como principal objetivo analisar os limites da tensão de escoamento das armaduras inseridas na alvenaria estrutural de blocos cerâmicos por meio de análises numéricas e paramétricas em corpos de provas push-out e pull-out, variando o tipo de graute e diâmetro das armaduras. O estudo numérico dos modelos analisados foi feito pelo Método dos Elementos Finitos utilizando o pacote computacional FX+DIANA®. A análise paramétrica confirmou que os limites obtidos nesta pesquisa para armaduras com diâmetros de 8 mm, 10 mm, 12.5 mm e 16 mm estão em concordância com os especificados pela norma brasileira, com exceção da armadura de 20 mm de diâmetro, cujo limite ficou menor que o apontado pela norma. Dessa maneira, a tensão de escoamento da armadura embutida no graute diminui progressivamente com o aumento do diâmetro das barras, sendo a falha dominada pela tensão de aderência da interface que se cria entre as paredes dos blocos cerâmicos e o graute.

Palavras-chave: tensão de escoamento, tensão de aderência, interface bloco/graute, elementos finitos, blocos cerâmicos.

How to cite: O. Soto Izquierdo, M. R. S. Corrêa, I. Soto Izquierdo, and I. G. Araújo, “Numerical and parametric study of the yield stress limits of reinforcement bars in clay block masonry structures,” *Rev. IBRACON Estrut. Mater.*, vol. 14, no. 6, e14611, 2021, <https://doi.org/10.1590/S1983-41952021000600011>

Corresponding author: Orieta Soto Izquierdo. E-mail: orietasi@uft.edu.br

Financial support: The authors would like to thank the Conselho Nacional de Desenvolvimento Científico e Tecnológico-CNPq for the financial support.

Conflict of interest: Nothing to declare.



This is an Open Access article distributed under the terms of the Creative Commons Attribution License, which permits unrestricted use, distribution, and reproduction in any medium, provided the original work is properly cited.

1 INTRODUCTION

Structural masonry is an important structural system that has significantly evolved over the years. Buildings have become increasingly tall, reaching 20 floors. Furthermore, the taller the building, the larger the compression levels and vertical loads that are attributed to wind action and torsion. In structural masonry, compression is usually resisted by filling the vertical holes with grout (liquid concrete with small aggregate), which increases the resistance of the masonry to compression [1].

With respect to traction on the walls, reinforcement bars that are properly coated with grout are generally used to solidify the compound because the resistance of masonry is low. Reinforcements are a solution to increase the tensile strength and thus improve the mechanical behavior of masonry under lateral loading [2].

When a wall is subjected to lateral action, one of its sides is compressed, whereas the other is subjected to traction. Under these conditions, internal tensions are observed on the grout/block interfaces because of the different deformation properties. By analyzing the internal components of the grout/block contact plane, it can be concluded that rupture is caused by slippage near the plane [3].

Soric and Tulin [4] concluded that two types of bond should be considered when evaluating the performance of reinforced masonry: the bond between reinforcing steel and grout, and the bond between the grout and internal faces of the concrete unit. The bond that can be developed between the reinforcement and surrounding grout is a complex phenomenon that is dominated by the interlocking action of the reinforcing bar ribs in the grout mass. However, the bond between the grout and surrounding masonry unit is primarily limited by the adhesion with the interface.

1.1. Justification

Regarding the tension on the walls, because of the low resistance of masonry, reinforcement bars that are properly coated with grout are generally used to solidify the whole structure. International reference standards, such as British BS 5628-2 [5], European EC6-1 [6] and Australian AS 3700 [7], present an indirect limit for the maximum reinforcement diameter embedded in a grouted hole. However, the Brazilian Standard of Structural Masonry ABNT NBR 16868-1 [8] imposes limits directly for the maximum tensile stress (f_s) of the reinforcements and maximum reinforcement rate in a grouted hole.

The Brazilian Standard of Structural Masonry ABNT NBR 16868-1 [8] suggests that in clay blocks with smooth surface the maximum tensile stress of the reinforcement embedded in the grout cannot be larger than the yield stress (f_{yk}) for 10 mm rebar diameters, 75% of its yield stress ($0.75 f_{yk}$) for 12.5 mm rebar diameters and 50% of its yield stress ($0.5 f_{yk}$) for 16 mm or more rebar diameters. This request is relevant for high rise buildings and for buildings in high-intensity seismic zones. Therefore, the present study is mainly to verify the need to establish such limits.

A better understanding of the behavior of structural masonry requires research on the block/grout interface, especially considering that wind loads become substantial for tall buildings causing significant traction on the bracing walls.

Sipp [9] studied the properties that affect the adherence between 5 types of ceramic blocks and two types of grouts. The push-out test was used to evaluate the bond strength mobilized by the combination of these different materials. In addition, the pull-out test was also employed for some block types, seeking a more realistic analysis of the bonding behavior on masonry elements. The results obtained in the push-out test prove that there is a wide variation in the results, depending on the type of block and grout employed. Some of the main characteristics that influenced these results were the shape of the block cells and the shrinkage of the grout. In the case of grout, the use of grout with higher compression resistance was responsible for the reduction in the results of the push test, precisely due to the reduction in the contact area caused by the shrinkage of the filler material.

Guarnieri [10] analyzed the influence of the structural ceramic block/grout adhesion on the mechanical behavior of the assembly in order to determine a value of adhesion tension. The author concluded that the grout/ceramic block adhesion is superior to the mechanical tensile strength of the ceramic block and, therefore, the rupture of the assembly will occur first in the block.

In this regard, Izquierdo et al. [11] studied the behavior of the block/grout interface of concrete and clay block masonry. Their study concluded that there is a good bond between the internal faces of the concrete blocks and grout, enough to prevent infill-slippage, and that the whole tensile strength of the usual reinforcement bars is achieved provided they are properly anchored. Nevertheless, for clay blocks, there is low bond between the interface of the clay blocks and grout, allowing for infill-slippage before the reinforcement bars reach their yield stress. In this way, numerical modeling of masonry structures can effectively be useful for better understanding of the mechanical behavior of masonry elements for scenarios different from those tested in the laboratory [2]. Therefore, this paper aims to

investigate the block/grout interface in clay blocks and verify the limits on the yield stress of the reinforcement by performing experimental and numerical tests, thereby enabling a parametric analysis. This study intends to draw the attention of technologists to the importance of ensuring the homogeneity of masonry by considering the bond to be a study parameter of the grout.

2 EXPERIMENTAL INVESTIGATION

This experimental investigation studied the masonry behavior using push-out specimens to determine the bond strength between the grout and clay unit, and pull-out specimens to study the behavior of the interface of the grout/block/reinforcement set. One type of block material (clay), two types of grout (large and small compressive resistance) and two rebar diameters (12.5 mm and 16 mm) were considered.

These laboratory tests were preceded by a set of material characterization tests. Statistical tests (Student's t test) were applied to evaluate the differences of the experimental results at a 5% significance level, for a better understanding of the results.

A detailed description of the experimental results was presented by Izquierdo et al. [11]. Figure 1 and Figure 2 show the nominal dimensions and test rig of the push-out and pull-out specimens, respectively. The experimental tests were carried out on servo-hydraulic universal machine INSTRON brand, model 8506, and the reading of the data was done with SYSTEM 5000 acquisition system.

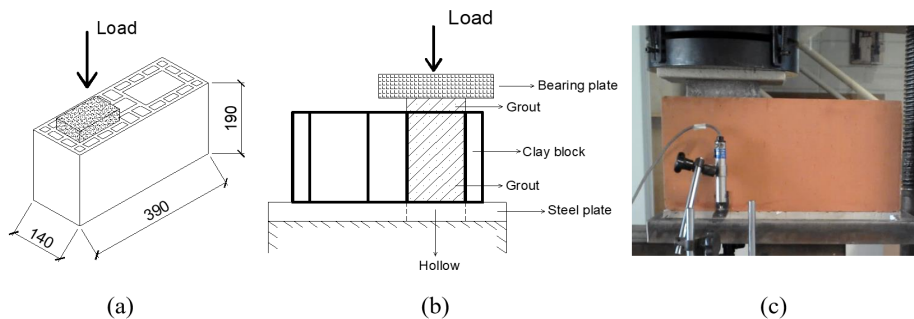


Figure 1. Push-out specimens: (a) Nominal dimensions [in mm], (b) test rig and (c) experimental test (Adapted from Izquierdo et al. [11]).

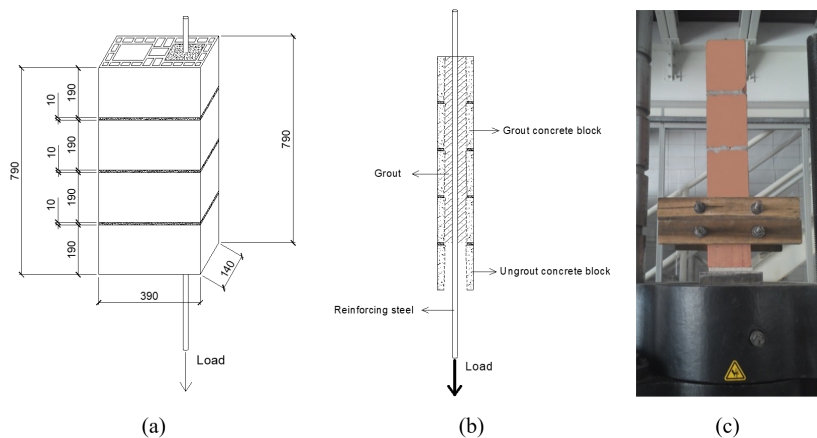


Figure 2. Pull-out specimens: (a) Nominal dimensions [in mm], (b) test rig and (c) experimental test (Adapted from Izquierdo et al. [11]).

Two series were built with six specimens for each series for the push-out test:

- Series CIG14: Clay block and grout G14
- Series CIG30: Clay block and grout G30

Four series were built with six specimens for each series for the push-out test:

- Series CIG14S12: Clay block, grout G14 and rebar diameters 12.5 mm
- Series CIG30S12: Clay block, grout G30 and rebar diameters 12.5 mm
- Series CIG14S16: Clay block, grout G14 and rebar diameters 16 mm
- Series CIG30S16: Clay block, grout G30 and rebar diameters 16 mm

Complementary tests were performed to characterize the masonry: compressive strength testing of cylindrical mortar specimens, cylindrical grout specimens, and units. The specimens were rectified to obtain regular and smooth surfaces.

The mean of the compressive strength for grout G14 and G30 used for filling the clay blocks was 14.18 MPa and 31.43 MPa, respectively. Grout G14 was designed to be weaker than grout G30.

The reinforcement rebars were subjected to tensile strength tests. Three 12.5 mm and 16 mm steel rebar samples were submitted to direct tensile tests. Table 1 shows the results obtained on the reinforcements used in clay blocks. The yield stress was calculated according to ABNT NBR 6892-1 [12].

Table 1. Results of the steel reinforcements Ø 12.5mm and Ø 16 mm used in clay blocks.

Diameter rebar (mm)	Area of reinforcement cross section (mm ²)		Mean Ultimate Load (kN)	Mean Yield Load (kN)	Mean Ultimate Stress (MPa)	Mean Yield Stress (MPa)
12.5	125		93.32	65.55	760.43	534.15
		S.D	1.30	1.94	10.58	15.77
		C.V (%)	1.39	2.95	1.39	2.95
16	200		159.86	117.32	795.05	583.52
		S.D	1.91	3.28	9.52	16.30
		C.V (%)	1.20	2.79	1.20	2.79

S.D: Standard Deviation. C.V: Coefficient of Variation

The bond strength was determined by dividing the maximum load applied by the area of the internal cavity surface of the unit. The average value of this area was 0,072 m². The results of the push-out tests are displayed in Table 2.

Table 2. Results of the push-out tests [11].

Series	Mean Ultimate Load (kN)	S.D	C.V (%)	Bond Strength (MPa)	S.D	C.V (%)
CIG14	11.64	1.32	11.31	0.16	0.02	8.87
CIG30	14.02	1.24	8.87	0.19	0.02	8.87

S.D: Standard Deviation. C.V: Coefficient of Variation

Table 3 shows the maximum stress of the pull-out clay block specimens for the four series. Figure 3 presents the results of the pull-out loads and the reference values of the yield load and the ultimate load, both obtained in the simple tensile test of the rebars, according to Izquierdo et al. [11].

Table 3. Results of the pull-out of clay block specimens [11].

Series	Mean Ultimate Load (kN)	S.D	C.V (%)	Mean Ultimate Stress (MPa)	S.D	C.V (%)
CIG14S12	48.47	1.14	2.36	394.95	9.31	2.36
CIG30S12	59.26	7.42	10.51	482.91	50.75	10.51
CIG14S16	48.96	1.76	3.60	243.49	8.76	3.60
CIG30S16	60.11	5.11	8.50	298.94	25.40	8.50

S.D: Standard Deviation. C.V: Coefficient of Variation

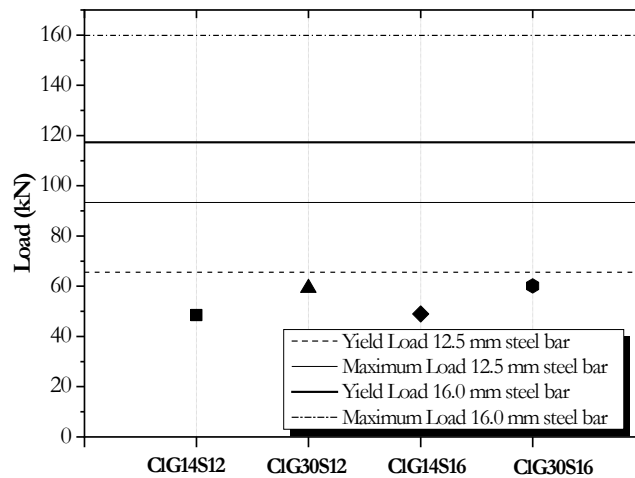


Figure 3. Results of the pull-out of clay block specimens with yield load and maximum load of the reinforcements [11].

The pull-out specimens built with reinforcement of 12.5 mm and 16 mm diameter reached an ultimate load less than the yield load of the referred bar. The maximum load of the specimens with the same type of grout obtained similar values. The Figure 3 shows that the failure of the pull-out specimens was determined by the type of grout.

Izquierdo et al. [11] concluded that the bond load between the grout and clay block was 11.64 kN for grout G14 and 14.02 kN for grout G30, for a single grouting block. These loads multiplied by the number of grouting blocks used in the pull-out specimens (4 blocks) set important limits related to the grout/block bond. These values can be compared with the ultimate loads obtained in the pull-out tests, as shown in Table 4.

Table 4. Load limited by bond and ultimate load of the pull-out tests of clay blocks [11].

Push-out specimens		Pull-out specimens			
Ultimate Load x 4 (kN)		Ultimate Load (kN)			
G14	G30	CIG14S12	CIG14S16	CIG30S12	CIG30S16
46.56	56.12	48.49	48.96	59.26	60.10

The results in Table 4 show that the ultimate loads of pull-out tests were approximately equal to the extrapolated limits of the push-out tests. The statistical analysis showed that these limits are not significantly different. Therefore, the pull-out specimens breached before the reinforcement bars reached its yield strength.

3 NUMERICAL MODEL

The numerical model applied to the study of the block/grout interface in the clay block masonry structures was defined using the Fx + DIANA® software program [13].

The numerical analysis was performed by two steps. In the first step, the validation of the numerical model was carried out based on the experimental results. The second step included a parametric analysis varying the rebar diameters on the pull-out specimens (8 mm, 10 mm and 20 mm).

The simplified micro-model was using in this study. Some researchers adopted micro-modeling approaches to study masonry as they represent its comp lex behavior very well. Mortar and two unit-mortar interfaces are lumped into a zero-thickness joint (modeled using an interface element) between expanded masonry units [2], [14], [15].

The Quasi-Newton iteration method (Secant) and a displacement convergence norm was used in the DIANA® software to solve the three-dimensional finite element model adopted in the push-out and pull-out specimens.

3.1 Finite Element Mesh

The mesh was composed of a HX24L solid element to represent the masonry units, grout and a TP18L solid element to represent the steel reinforcement (Figure 4). A Q24IF interface element was employed to represent the block/grout interface, grout/reinforcement interface and bed joints. The Q24IF element is an interface element between two planes

in a three-dimensional configuration (Figure 5), suitable for three-dimensional models. Each node of this element has three degrees of freedom and the element is based on linear interpolation and Gaussian integration.

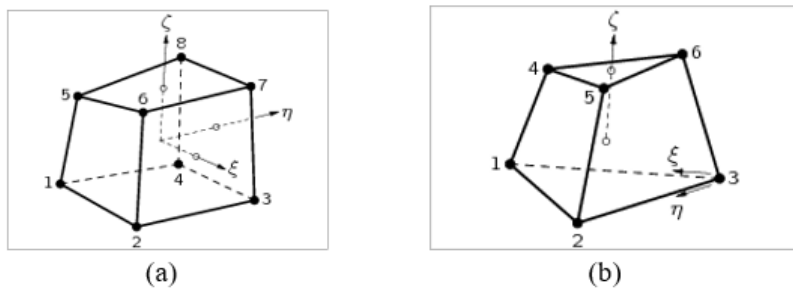


Figure 4. (a) HX24L solid element of the units and grout and (b) TP18L solid element of the steel reinforcement used in the numerical modeling [13].

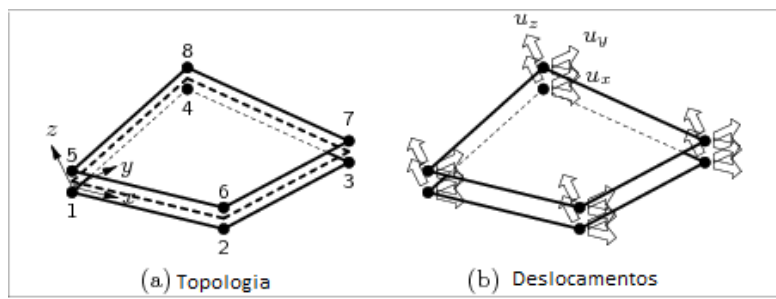


Figure 5. Q24IF interface element [13].

The mesh convergence was done satisfactorily with three different refinement levels to evaluate its influence on the results. Table 5 and Table 6 show the number and size elements of the final mesh of the push-out tests and pull-out test, respectively.

Table 5. Number and size elements of the push-out mesh.

	Clay block	Grout	Block/grout interface
Elements number	1260	462	180
Size of elements (mm)	10x10x40	10x10x40	40x10
Subtotal		1722	180
Total		1902	

Table 6. Number and size elements of the pull-out mesh.

	Clay block	Grout	Reinforcement	Block/grout interface	Grout/reinforcement interface	Bed joints masonry
Elements number	5040	1848	500	720	180	252
Size of elements (mm)	10x10x40	10x10x40	10x10x200	40x10	10x200	10x10
Subtotal		7388			1152	
Total				8540		

3.2 Loading and Boundary Conditions

The push-out specimens consisted of a single clay block with one of its cavities completely grouted. The salient grout from the surface of the block at a distance of 30 mm was loaded in compression through a bearing plate at the top surface, while the block was supported only around the perimeter of the unit shells at the bottom surface. The pull-out specimens were built with four clay blocks in stack bond. The 4 blocks were grouted. The reinforcement rebar was subjected to a tensile load [11].

Similarly to the experimental tests (see Figure 1c and Figure 2c), the boundary conditions used in the push-out and pull-out specimens were restrictions of the displacements in the Z direction at half of the nodes of the bottom block. Two nodes of the symmetry axis were restricted in the X, Y, and Z directions to avoid numerical instability.

In the case of the push-out specimens, vertical displacements were imposed on all nodes of the top of the grout (Figure 6a), and in the case of the pull-out specimens, vertical displacements were imposed on all nodes of the base of the reinforcement rebar (Figure 6b). The boundary conditions and loading were similar in the experimental tests.

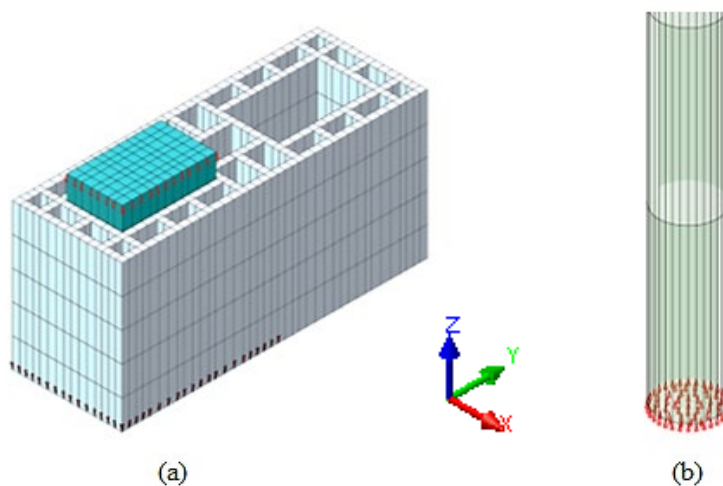


Figure 6. Vertical displacements of the (a) push-out and (b) pull-out specimens.

3.3 Constitutive Models and Mechanical Properties

Total Strain Crack Model was used to characterize the crack distribution and nonlinear behavior of both the units and grout. According to the DIANA® software [13], this model describes the tensile and compressive behavior of the material with one stress-strain relationship in a coordinate system that is fixed upon crack initiation. Exponential and parabolic constitutive laws were used to describe the tensile and compressive behavior of clay masonry units respectively, as shown in Figure 7a and Figure 7b. The shear behavior during cracking was described via a shear retention model defined by a constant, see Figure 7c [16].

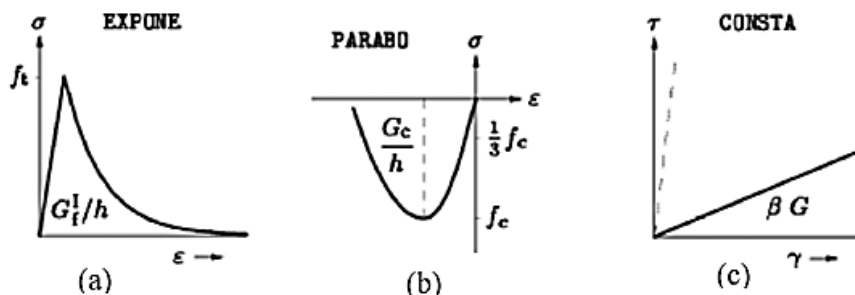


Figure 7. Mechanical behavior of the units used in numerical modeling: (a) tension, (b) compression, and (c) shear [13].

The mechanical properties are presented in Table 7 for masonry units and two types of grout and were determined during the characterization tests as presented by Izquierdo [11]. However, some properties that could not be obtained experimentally were calibrated by adjusting the numerical results with the experimental results. All mechanical properties units were considered in relation to its net area. The calibrated properties (indicated in the Table 7) were obtained according to Haach [16], Izquierdo [17], *fib* [18], Haach et al. [19], Diógenes [20] and Izquierdo [21].

Table 7. Mechanical properties of the Total Strain Crack Model (masonry units and grout).

Parameters	Symbol/Units	Clay block	Grout G14	Grout G30
Elastic modulus (exp)	E (MPa)	9876.43	20521.17	29719.67
Poisson (exp)	ν	0.20	0.20	0.20
Tensile strength (exp)	f_t (MPa)	1.08	1.43	2.35
Fracture energy for Mode I (cal)	G_{II} (MPa·mm)	0.06	0.03	0.06
Compressive strength (exp)	f_c (MPa)	30.92	14.18	31.43
Fracture energy under compression (cal)	G_c (MPa·mm)	5.51	3.19	5.57
Shear retention (cal)	β	0.5	0.5	0.5

Experimental properties (exp). Calibrated properties (cal)

The model used for interface elements indicate that the block/grout interface and bed joints masonry was an interface cap model. This model was proposed by Lourenço and Rots [22], and further enhanced by Van Zijl [23] with modern plasticity concepts. This interface material model, also known as the “Composite Interface model” or “Cracking-Shearing-Crushing Model”, is appropriate to simulate fracture, frictional slip, and crushing along material interfaces, which are possible failure modes of masonry interfaces. The model includes a tension cut-off model to capture Mode I failure, a Coulomb friction envelope to describe Mode II failure and a cap model for compressive failure (Figure 8) [2], [24], [25].

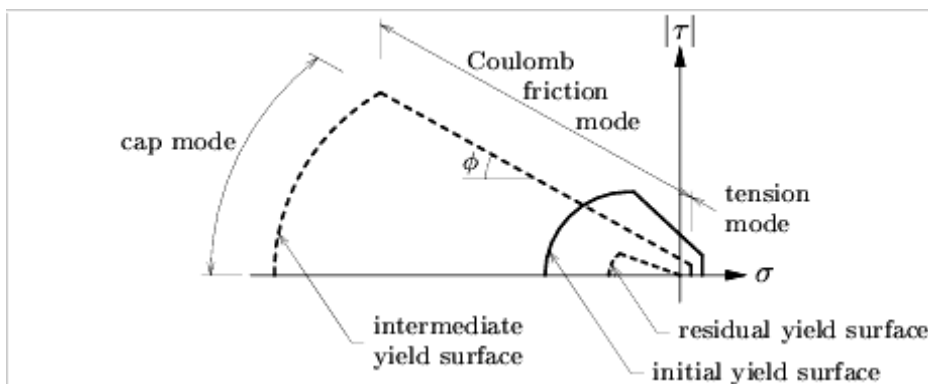


Figure 8. Constitutive model for masonry interfaces [22] adapted from Haach [16].

Table 8 shows the mechanical properties used for the Composite Interface Model of the block/grout interface and bed joints masonry. Most properties were obtained experimentally according to Izquierdo [17] and Oliveira [26]. Other properties (indicated in the Table 8) were obtained by calibrating the numerical and experimental model with similar raw material compositions based on previous work as Haach et al. [19], Oliveira [26], Capuzzo et al. [27] and Rahman and Ueda [28].

The normal stiffness (k_n) was calculated based on the results of the direct tensile tests carried out to characterize the tensile bond strength of the unit-mortar. The shear stiffness (k_i) was obtained through the results of the shear tests carried out on triplet specimens to characterize the shear behavior of clay unit-mortar interface interface [16], [19], [29].

Elasto-plastic behavior was adopted for the reinforcements through the yield criterion of the Von Mises model. These properties were obtained experimentally as presented by Izquierdo et al. [11]. Table 9 shows the mechanical properties used in this model.

Table 8. Mechanical properties of the Composite Interface Model (block/grout interface and the bed joints masonry).

Parameters	Symbol/Units	Block/grout interface	Block/grout interface	Bed joints masonry
Normal stiffness (exp)	k_n (MPa/mm)	1.00	1.00	11.71
Tangential stiffness (exp)	k_t (MPa/mm)	1.76	1.19	11.71
Cohesion (exp)	f_{v0} (MPa)	0.16	0.19	0.20
Friction coefficient (exp)	$\tan \varphi_0$	0.70	0.70	0.250
Dilatancy coefficient (exp)	$\tan \Psi$	1.00×10^{-4}	1.00×10^{-4}	1.723
Residual friction coefficient (exp)	$\tan \varphi_r$	0.39	0.39	0.29
Confining normal stress (exp)	σ_u (MPa)	-1.18	-1.18	-1.37
Exponential degradation coefficient (cal)	δ	1.85	1.85	0
Tensile strength (exp)	f_t (MPa)	0.23	0.23	0.29
Fracture energy for Mode I (exp)	G_{fI} (MPa·mm)	0.02	0.02	0.02
Fracture energy for Mode II (exp)	G_{fII} (MPa·mm)	0.19	0.24	0.22
Cap critical compressive strength (exp)	f_c (MPa)	3.15	3.15	3.05
Shear traction control factor (cal)	C_s	4.00	4.00	4.00
Compressive fracture energy (cal)	G_{fc} (MPa·mm)	1.18	1.18	5.00

Experimental properties (exp). Calibrated properties (cal)

Table 9. Mechanical properties used for the Von Mises model (reinforcement).

Parameters	Symbol/Units	Ø 12.5 mm	Ø 16 mm
Elastic modulus (exp)	E (MPa)	198513.12	200844.39
Poisson (cal)	ν	0.30	0.30
Yield stress (exp)	f_y (MPa)	556.24	588.60

Experimental properties (exp). Calibrated properties (cal)

The grout/reinforcement interface was considered in the linear regime with $k_n = 5$ MPa/mm and $k_t = 100$ MPa/mm.

4 VALIDATION OF THE NUMERICAL MODEL

The calibration of the numerical model was performed based on the comparison between the numerical and experimental results and failure modes.

4.1 Push-Out Tests

Figure 9 shows a comparison between the experimental and numerical behavior of the push-out tests corresponding to the CIG14 series and Figure 10 for the CIG30 series. Figure 11 displays the grout slippage of the numerical and physical models of the CIG14 series.

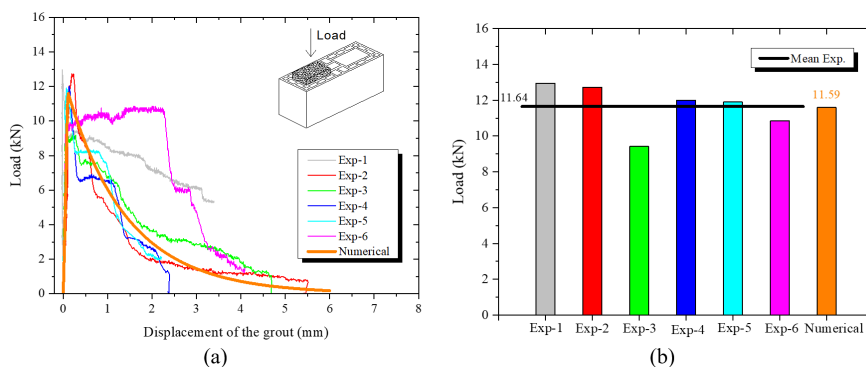


Figure 9. Validation of numerical results of the CIG14 series of push-out tests: (a) force vs displacement diagrams and (b) mean maximum load.

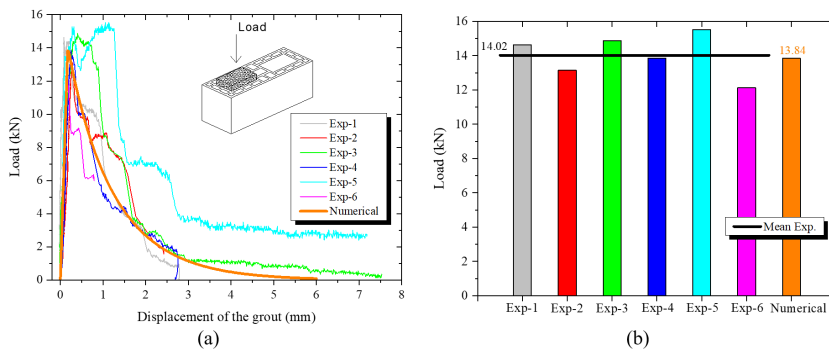


Figure 10. Validation of numerical results of the CIG30 series of push-out tests: (a) force vs displacement diagrams and (b) mean maximum load.

Figures 9 and 10 showed that the numerical model adequately predicts the same response of experimental push-out tests. The maximum difference between both models was less than 2%. Therefore, it can be said that the numerical push-out model was calibrated.

Figure 11 shows that the numerical model characterizes the performance of the physical push-out model.

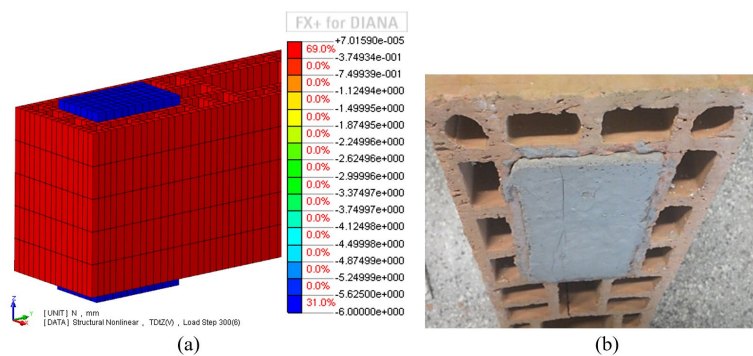


Figure 11. Displacement of the grout according to the CIG14 series (a) numerical model and (b) bottom face of the physical model.

4.2 Pull-Out Tests

Figure 12 to Figure 15 show a comparison of the experimental and numerical behavior of the pull-out tests for the CIG14S12, CIG14S16, CIG30S12 and CIG30S16 series, respectively.

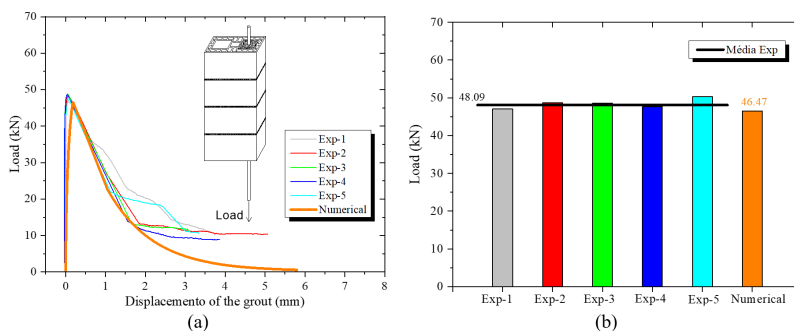


Figure 12. Validation of numerical results of the CIG14S12 series of pull-out tests: (a) force vs displacement diagrams and (b) mean maximum load.

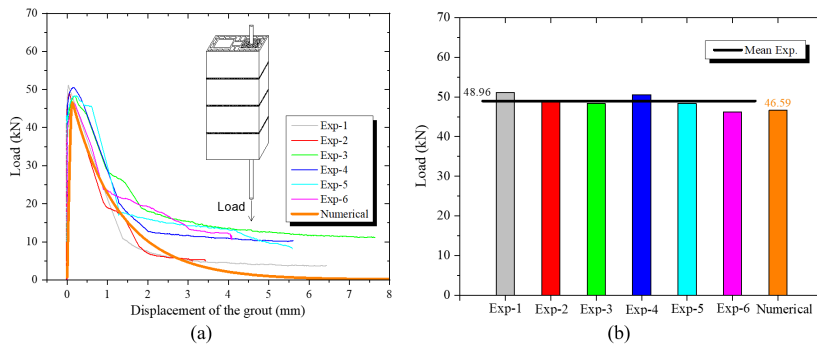


Figure 13. Validation of numerical results of the CIG14S16 series of pull-out tests: (a) force vs displacement diagrams and (b) mean maximum load.

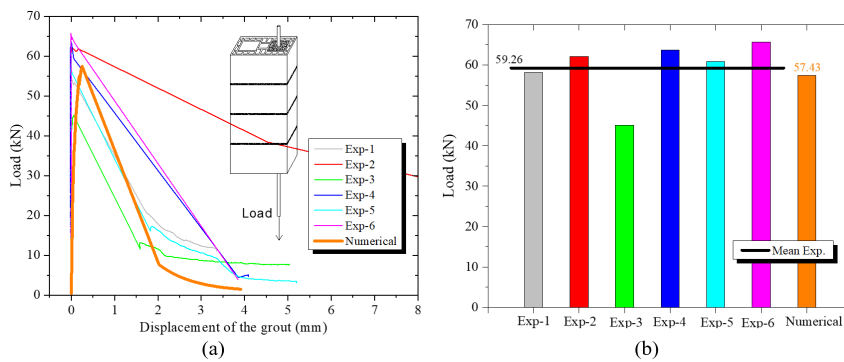


Figure 14. Validation of numerical results of the CIG30S12 series of pull-out tests: (a) force vs displacement diagrams and (b) mean maximum load.

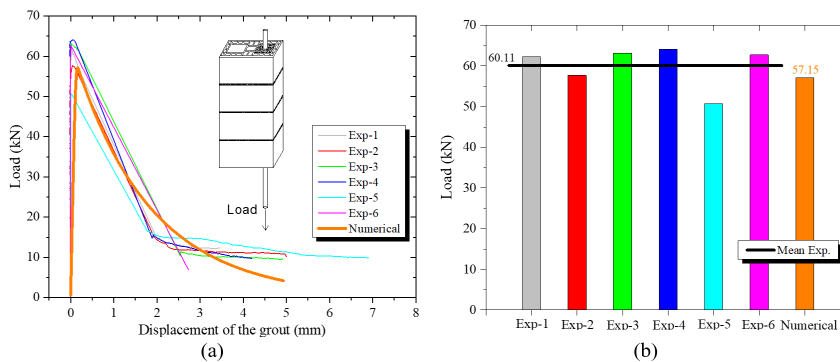


Figure 15. Validation of numerical results of the CIG30S16 series of pull-out tests: (a) force vs displacement diagrams and (b) mean maximum load.

The numerical behavior for the CIG14S12, CIG14S16, CIG30S12 and CIG30S16 curves were similar to the physical model. The maximum difference between experimental and numerical model was less than 6% in all series. Therefore, it can be said that the numerical pull-out model was calibrated.

Grout slippage was observed in all of the tested numerical and experimental series (see Figure 16).

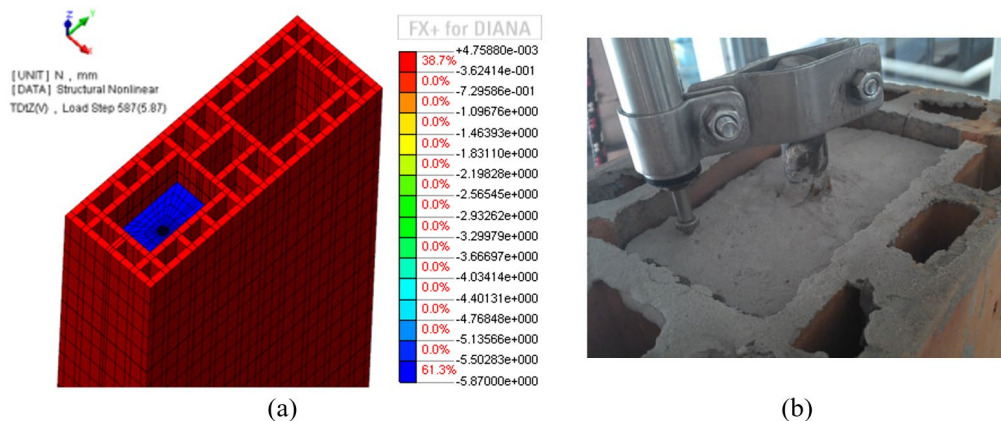


Figure 16. Displacement of the grout according to (a) the numerical model and (b) physical model of the CIG14S12 series.

5 PARAMETRIC ANALYSIS

After the validation of the numerical model, a parametric analysis was performed for the pull-out test varying the rebar diameters of the steel reinforcement (8 mm, 10 mm and 20 mm) and two types of grout (large and small compressive resistance).

Steel rebar samples of the 8 mm, 10 mm and 20 mm diameter were submitted to the direct tensile test described by Kataoka and El Debs [30] under the same test conditions of the reinforcement rebars of this study (12.5 mm and 16 mm). The yield load obtained for the 8 mm steel rebar was 31.01 kN, the 10 mm steel rebar was 44.94 kN and the 20 mm steel rebar was 178.19 kN.

5.1 Rebar Diameters of 10 mm

Figure 17a is the load vs displacement diagram of the numerical model for the series with G14 and G30 grout and rebar diameters of 10 mm. The experimental yield is also highlighted in the Figure 17a.

As shown in Section 2, the bond load between the grout and clay block was 11.64 kN for G14 grout and 14.02 kN for G30 grout, for a single grouting block (see Table 1). These loads, multiplied by the number of grouting blocks used in the pull-out specimens (4 blocks), established important limits related to the grout/block bond. The value for the G14 grout was 46.56 kN and for the grout G30 was 56.12 kN.

Figure 17b is the maximum load for these two series (41.11 kN and 41.26 kN) compared with the values of the load limited by bond obtained experimentally (46.56 kN for G14 and 56.08 kN for G30).

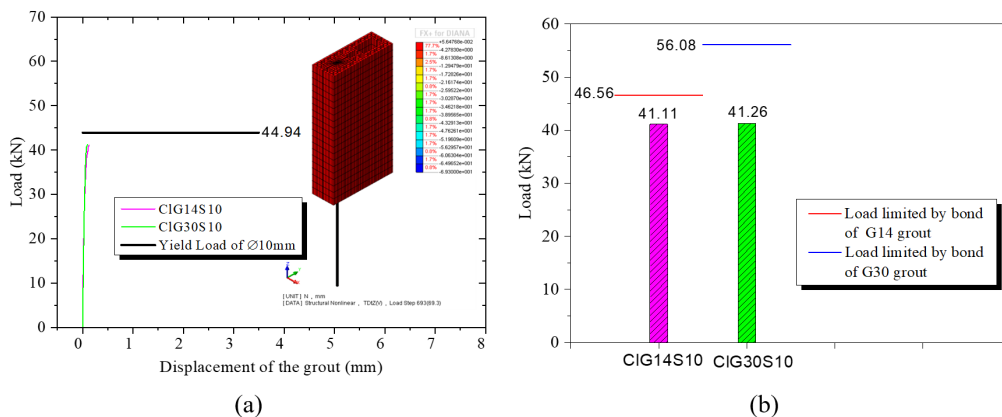


Figure 17. Pull-out tests with rebar diameters of Ø10 mm (a) parametric results (load vs displacement diagrams) and (b) maximum load.

The maximum loads obtained in the numerical model was 41.11 kN and 41.26 kN for CIG14S10 and CIG30S10 series, respectively. These values represent a maximum difference of 9% in relation to experimental yield load of the 10 mm steel rebar (44.94 kN). This difference can be considered low since simplifications and approximations are used in the numerical model. Therefore, both yield loads (experimental and numerical) were considered the same.

The numerical model stopped converging once these values were reached. Figure 17a illustrates that the grout did not slip in relation to the clay block webs for 10 mm of rebar diameters.

Figure 17b shows that the ultimate load numerical (41.11 kN and 41.26 kN) was lower than the load limited by experimental bond for both grouts (46.56 kN and 56.08 kN), respectively. Therefore, this research concluded that the failure for pull-out specimens of 10 mm steel rebars was dominated by the yield load of the reinforcements and not by bond load.

The pull-out test with 8 mm steel rebars was not carried out numerically because the experimental yield load for this reinforcement was 31.01 kN. This value is less than the load limited by experimental bond for both grouts (46.56 kN and 56.08 kN). For that reason, the failure will be due by the yield stress of the steel bar and not by the bond strength of the clay block/grout interface.

5.2 Rebar Diameters of 20 mm

Figure 18 shows the results obtained in the parametric study using rebar diameters of 20 mm.

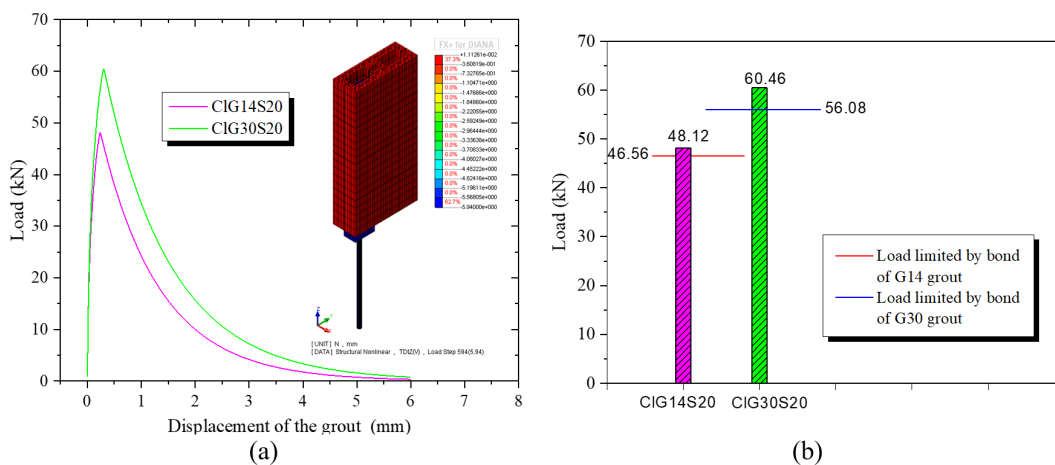


Figure 18. Pull-out tests with rebar diameters of Ø20 mm (a) parametric results (load vs displacement diagrams) and (b) maximum load.

The ultimate numerical load for both series (48.12 kN and 60.46 kN) were similar than their respective experimental load limited by bond (46.56 kN and 56.08 kN). The maximum difference between experimental and numerical load was of about 8%. The other hand, the experimental yield load (179.19 kN) of 20 mm of steel rebar diameter was significantly larger than the numerical load for both series (48.12 kN and 60.46 kN). Therefore, the reinforcement of Ø 20 mm embedded in both series has not reached its yield limit.

Figure 18a shows that the column of the grout inside the clay blocks slipped for both grouts. Therefore, with the use of 20 mm diameter rebar, the effect was the same as the 12.5 mm and 16 mm reinforcement rebars, where the masonry limit state depends on the bond strength of the block/grout interface for the specific grout type.

5.3 Comparative analysis according to Brazilian Standard Structural Masonry ABNT NBR 16868-1 [8]

The parametric study provides a summary of the ultimate stress of the pull-out test of clay blocks based on the yield stress of the steel bar, for several reinforcement diameters, see Table 10.

Table 10. Ultimate stress of the pull-out tests of clay blocks with respect to the yield stress of the steel rebar for different diameters.

Rebar Diameters (mm)	Ultimate Stress	
	G14	G30
Ø 8	100% f_{yk}	100% f_{yk}
Ø 10	100% f_{yk}	100% f_{yk}
Ø 12.5	74% f_{yk}	90% f_{yk}
Ø 16	42% f_{yk}	51% f_{yk}
Ø 20	27% f_{yk}	33% f_{yk}

As previously mentioned, the Brazilian Standard Structural Masonry ABNT NBR 16868-1 [8] imposes limits directly for the maximum tensile stress (f_s) of the reinforcement embedded in the grout in clay blocks with smooth surfaces. These limits are:

- f_{yk} , for steel rebars of Ø10 mm
- 0.75 f_{yk} , for steel rebars of Ø12.5 mm
- 0.50 f_{yk} , for steel rebars of Ø16 mm or more.

The limits obtained in this research (Table 10) are in agreement with the limits specified by the Brazilian Standard for 10 mm, 12.5 mm and 16 mm reinforcement diameter. However, the limits for 20 mm of diameter (27% f_{yk} and 33% f_{yk}) do not coincide with the limit of the Brazilian Standard (50% f_{yk}). This research concluded that these limits reduce progressively with increasing rebar diameter. The other hand, more studies need to be done and the bond stress at the grout/block interface should be considered during the design development to guarantee safety.

6 CONCLUSIONS

In this paper a numerical analysis was performed to analyze the limits of the yield stress of reinforcements in clay block masonry structures. The parametric analysis was carried out by varying the rebar diameter (8 mm, 10 mm, and 20 mm) and type of grout (large and small compressive resistance) in pull-out specimens.

The following conclusions are:

- The numerical analysis showed that the computer models of the push-out and pull-out specimens adequately represented the behavior of the physical models, and thus can be used in parametric analysis.
- The pull-out tests with rebar diameters of 8 mm and 10 mm showed that the reinforcements embedded in the grout reached their yield stress without slippage. This feature demonstrated that the anchorage length used in this work was appropriate. The grout did not slip in relation to the clay block webs.
- The pull-out tests with clay blocks, large and small compressive resistance grout and reinforcement bars with diameters of 12.5 mm, 16 mm and 20 mm showed slippage of the grout's column before the reinforcement rebars achieved their yield stresses. The failure was dominated by the lack of a sufficient bond strength of the clay block/grout interface.
- The limits achieved in this research for 8 mm, 10 mm, 12.5 mm and 16 mm diameters bars are in agreement with the limits specified by the Brazilian Standard Structural Masonry ABNT NBR 16868-1 [8]. However the limit for steel rebars with 20 mm of diameter was less than specified by the standard. The authors of this paper suggest 25% f_{yk} for Ø20 mm as a reference point for future investigations, while a comprehensive research program covering the bond between different clay blocks and grout infills is not performed.
- Two types of bond strengths that occur in the reinforced masonry should be considered during the design: grout/reinforcement bond and block/grout bond.

ACKNOWLEDGEMENTS

The authors would like to thank the Department of Structural Engineering of the School of Engineering of São Carlos at the University of São Paulo for permission to conduct the survey.

CITATIONS

- [1] D. T. Biggs, "Grouting Masonry using Portland Cement-Lime Mortars," in *Proc. Int. Build. Lime Symp.*, Orlando, Florida, Mar. 9-11, 2005.

- [2] V. G. Haach, G. Vasconcelos, and P. B. Lourenço, "Parametrical study of masonry walls subjected to in-plane loading through numerical modeling," *Eng. Struct.*, vol. 33, no. 4, pp. 1377–1389, Apr 2011, <http://dx.doi.org/10.1016/j.engstruct.2011.01.015>.
- [3] L. A. Pereira de Oliveira, "Adhesive strength as a parameter of compatibility between filler grout and structural masonry units," in *5th Int. Semin. Struct. Masonry Dev. Ctries.*, Florianópolis, 1994, pp. 214–227.
- [4] Z. Soric and L. G. Tulin, "Bond stress/deformation in pull-out masonry specimens," *J. Struct. Eng.*, vol. 115, no. 10, pp. 2588–2602, Oct 1889, [http://dx.doi.org/10.1061/\(ASCE\)0733-9445\(1989\)115:10\(2588\)](http://dx.doi.org/10.1061/(ASCE)0733-9445(1989)115:10(2588)).
- [5] British Standard Institution, *Code of Practice for Use of Masonry – Structural Use of Reinforced and Prestressed Masonry*, BSI 5628-2, 1995.
- [6] European Standard. *Eurocode 6: Design of Masonry Structures*, EN 1996-1-1, 2005.
- [7] Standards Association of Australia, *The Australian Masonry Code*, AS3700, 2001.
- [8] Associação Brasileira de Normas Técnicas, *Structural Masonry – Part 1: Design*, NBR 16868-1, 2020 (in Portuguese).
- [9] G. Sipp, "Evaluation of the bonding behavior between ceramic blocks and grouts," M.S. thesis, Fed. Univ. São Carlos, São Carlos, 2019 (in Portuguese). [Online]. Available: <https://repositorio.ufscar.br/handle/ufscar/11749?show=full>
- [10] L. O. Guarnieri, "Influence of grout adhesion/structural clay block on the mechanical strength of the set," M.S. thesis, Mining, Metal. Mater. Eng., Fed. Univ. Rio Grande do Sul, Porto Alegre, 2017 (in Portuguese). [Online]. Available: <https://lume.ufrgs.br/handle/10183/178445>
- [11] O. S. Izquierdo, M. R. S. Corrêa, and I. I. Soto, "Study of the block/grout interface in concrete and clay block masonry structures," *IBRACON Struct. Mater. J.*, vol. 10, no. 4, pp. 924–936, Aug 2017, <http://dx.doi.org/10.1590/s1983-41952017000400009>.
- [12] Associação Brasileira de Normas Técnicas, *Metallic Materials – Tensile Testing Part 1: Method of Test at Room Temperature*, NBR 6892-1, 2013 (in Portuguese).
- [13] TNO DIANA, *DIANA Finite Element Analysis – User's Manual Release 9.6*. Delft, Netherland, 2015. Accessed: June 7, 2020. [Online]. Available: <http://tnodiana.com>
- [14] L. M. F. Oliveira and M. R. S. Corrêa, "Numerical and experimental analysis of the shear capacity of interconnected concrete block walls," *Ambient. Constr.*, vol. 17, no. 3, pp. 25–37, Jul/Sep 2017, <http://dx.doi.org/10.1590/s1678-86212017000300160>.
- [15] N. Kumar and M. Barbato, "New constitutive model for interface elements in finite-element modeling of masonry," *J. Eng. Mech.*, vol. 145, no. 5, 04019022, Feb 2019, [http://dx.doi.org/10.1061/\(ASCE\)EM.1943-7889.0001592](http://dx.doi.org/10.1061/(ASCE)EM.1943-7889.0001592).
- [16] V. G. Haach, "Development of a design method for reinforced masonry subjected to in-plane loading based on experimental and numerical analysis," Ph.D. dissertation, Univ. Minho, Guimaraes, Portugal, 2009. [Online]. Available: www.civil.uminho.pt/masonry
- [17] O. S. Izquierdo, "Study of the block/grout interface in concrete and clay block masonry structures," Ph.D. dissertation, São Carlos Sch., Eng., Univ. São Paulo, São Carlos, 2015 (in Portuguese). [Online]. Available: <https://www.teses.usp.br/teses/disponiveis/18/18134/tde-13052015-165029/pt-br.php>
- [18] Fédération International Du Béton, *Bond of Reinforcement in Concrete* (Bulletin 14). Lausanne: FIB, 2002.
- [19] V. G. Haach, M. A. Ramalho, and M. R. S. Corrêa, "Parametrical study of unreinforced flanged masonry walls subjected to horizontal loading through numerical modeling," *Eng. Struct.*, vol. 56, pp. 207–217, Nov 2013, <http://dx.doi.org/10.1016/j.engstruct.2013.05.009>.
- [20] H. J. Diógenes, "Interface parameters calibration of numerical push-out models applied to connections for adherence," *Cad. Eng. Estrut.*, vol. 17, no. 67, pp. 37–52, 2017. Accessed: June 7, 2020. [Online]. Available: http://cadernos.set.eesc.usp.br/article/view/275/pdf_2
- [21] I. S. Izquierdo, O. S. Izquierdo, M. A. Ramalho, and A. Taliércio, "Sisal fiber reinforced hollow concrete blocks for structural applications: testing and modeling," *Constr. Build. Mater.*, vol. 151, no. 1, pp. 98–112, 2017, <http://dx.doi.org/10.1016/j.conbuildmat.2017.06.072>.
- [22] P. B. Lourenço and J. G. Rots, "Multisurface interface model for analysis of masonry structures," *J. Eng. Mech.*, vol. 123, no. 7, pp. 660–668, Jul 1997, [http://dx.doi.org/10.1061/\(ASCE\)0733-9399\(1997\)123:7\(660\)](http://dx.doi.org/10.1061/(ASCE)0733-9399(1997)123:7(660)).
- [23] G. P. A. G. Van Zijl, "Modeling masonry shear-compression: role of dilatancy highlighted," *J. Eng. Mech.*, vol. 130, no. 11, pp. 1289–1296, Oct 2004, [http://dx.doi.org/10.1061/\(ASCE\)0733-9399\(2004\)130:11\(1289\)](http://dx.doi.org/10.1061/(ASCE)0733-9399(2004)130:11(1289)).
- [24] P. B. Lourenço, "Masonry modeling," in *Encyclopedia of Earthquake Engineering*, M. Beer, I. A. Kougioumtzoglou, E. Patelli and S. K. Au, Eds., Berlin: Springer, 2015. http://dx.doi.org/10.1007/978-3-642-35344-4_153.
- [25] A. H. Al-Zuhairi and A. R. Ahmed, "Behavior of clay masonry prism under vertical load using detailed micro-modeling approach," *J. Assoc. Arab Univ. Basic Appl. Sci.*, vol. 26, no. 1, pp. 67–73, Mar 2019, <http://dx.doi.org/10.33261/jaaru.2019.26.1.009>.
- [26] L. M. F. Oliveira, "Numerical and experimental study of the behaviour of vertical interfaces of interconnected structural masonry walls," Ph.D. dissertation, São Carlos Sch. Eng., Univ. São Paulo, São Carlos, 2014 (in Portuguese). [Online]. Available: <https://teses.usp.br/teses/disponiveis/18/18134/tde-30072014-085747/es.php>

- [27] V. Capuzzo No., M. R. S. Corrêa, and M. A. Ramalho, "Proposal of a test specimen to evaluate the shear strength of vertical interfaces of running bond masonry walls," *Can. J. Civ. Eng.*, vol. 35, no. 6, pp. 567–573, May 2008, <http://dx.doi.org/10.1139/L07-139>.
- [28] A. Rahman and T. Ueda, "Experimental investigation and numerical modeling of peak shear stress of brick masonry mortar joint under compression," *J. Mater. Civ. Eng.*, vol. 26, no. 9, pp. 04014061–13, Sep 2014, [http://dx.doi.org/10.1061/\(ASCE\)MT.1943-5533.0000958](http://dx.doi.org/10.1061/(ASCE)MT.1943-5533.0000958).
- [29] G. Vasconcelos, P. B. Lourenço, and V. G. Haach, "Avaliação experimental da aderência de juntas de alvenaria de blocos de betão," in *An. 7º Cong. Nac. Mecânica Experimental*, Vila Real, Portugal, 2008. (in Portuguese).
- [30] M. N. Kataoka and A. L. H. de Cresce El Debs, "Beam–column composite connections under cyclic loading: an experimental study," *Mater. Struct.*, vol. 48, no. 4, pp. 929–946, Nov 2015, <http://dx.doi.org/10.1617/s11527-013-0204-4>.

Author contributions: OS: conceptualization, supervision, writing, data curation, formal analysis, methodology; MRS: funding acquisition, supervision, formal analysis, methodology, writing; II: data curation, methodology, writing; IG: formal analysis, writing.

Editors: Edgar Bacarji, Guilherme Aris Parsekian.



ORIGINAL ARTICLE

Load transfer on instrumented prestressed ground anchors in sandy soil

Transferência de carga em ancoragens protendidas instrumentadas em solo arenoso

Alex Micael Dantas de Sousa^a Yuri Daniel Jatobá Costa^b Luiz Augusto da Silva Florêncio^c Carina Maria Lins Costa^b ^aUniversidade de São Paulo – USP, Escola de Engenharia de São Carlos, Departamento de Engenharia de Estruturas, São Carlos, SP, Brasil^bUniversidade Federal do Rio Grande do Norte – UFRN, Departamento de Engenharia Civil, Natal, RN, Brasil^cUniversidade Federal do Rio de Janeiro – UFRJ, Departamento de Engenharia Civil, Rio de Janeiro, RJ, Brasil

Received 09 January 2021

Accepted 08 April 2021

Abstract: This study evaluates load variations in instrumented prestressed ground anchors installed in a bored pile retaining wall system in sandy soil. Data were collected from instrumentation assembled in the bonded length of three anchors, which were monitored during pullout tests and during different construction phases of the retaining wall system. Instrumentation consisted of electrical resistance strain gauges positioned in five different sections along the bonded length. Skin friction distributions were obtained from the field load measurements. Results showed that the skin friction followed a non-uniform distribution along the anchor bonded length. The mobilized skin friction concentrated more intensely on the bonded length half closest to the unbonded length, while the other half of the bonded length developed very small skin friction. The contribution of the unbonded length skin friction to the overall anchor capacity was significant and this should be accounted for in the interpretation of routine anchor testing results. Displacements applied to the anchor head were sufficient to mobilize the ultimate skin friction on the unbonded length, but not on the bonded length. Performance of loading-unloading stages on the ground anchor intensified the transfer of load from the unbonded length to the bonded length. Long-term monitoring of the anchor after lock-off revealed that the load at the anchor bonded length followed a tendency to reduce with time and was not significantly influenced by the retaining wall construction phases.

Keywords: ground anchor, load transfer, skin friction, retaining wall, bored pile.

Resumo: O presente estudo avalia as variações de carga em ancoragens protendidas instrumentadas, instaladas em uma estrutura de contenção composta por estacas escavadas em solo arenoso. Os dados foram coletados a partir de instrumentação disposta no trecho ancorado de três ancoragens, monitoradas durante ensaios de arrancamento e durante diferentes etapas construtivas da contenção. As ancoragens foram instrumentadas com extensômetros elétricos de resistência em cinco seções distintas posicionadas ao longo do trecho ancorado. Distribuições de atrito lateral foram obtidas a partir das medições de carga em campo. Os resultados revelaram uma distribuição não uniforme do atrito lateral ao longo do trecho ancorado. O atrito lateral mobilizado concentrou-se mais intensamente na metade do trecho ancorado mais próxima ao trecho livre, ao passo que uma parcela muito pequena de atrito lateral foi mobilizada na outra metade do trecho ancorado. A contribuição do atrito lateral no trecho livre para a capacidade de carga da ancoragem foi significativa, o que deve ser levado em consideração na interpretação dos resultados de ensaios de rotina em tirantes. Os deslocamentos aplicados na cabeça da ancoragem foram suficientes para mobilizar o atrito lateral último no trecho livre, porém não no trecho ancorado. A execução de estágios de carga-descarga na ancoragem contribuiu para intensificar a transferência de carga do trecho livre ao trecho ancorado. O monitoramento de longo-prazo da ancoragem após incorporação do carregamento revelou que a carga no trecho ancorado seguiu uma tendência de redução ao longo do tempo, não tendo sido significativamente influenciada pelas etapas construtivas da contenção.

Corresponding author: Alex Micael Dantas de Sousa. E-mail: alex_dantas@usp.br

Financial support: Conselho Nacional de Desenvolvimento Científico e Tecnológico.

Conflict of interest: Nothing to declare.



This is an Open Access article distributed under the terms of the Creative Commons Attribution License, which permits unrestricted use, distribution, and reproduction in any medium, provided the original work is properly cited.

Palavras-chave: ancoragem, transferência de carga, atrito lateral, estrutura de contenção, estaca escavada.

How to cite: A. M. D. Sousa, Y. D. J. Costa, L. A. S. Florêncio, and C. M. L. Costa, "Load transfer on instrumented prestressed ground anchors in sandy soil," *Rev. IBRACON Estrut. Mater.*, vol. 14, no. 6, e14612, 2021, <https://doi.org/10.1590/S1983-41952021000600012>

1 INTRODUCTION

Prestressed bond-type grouted anchors are structural elements in which the load is transferred to the ground from a steel tendon bonded to grout. The design of ground anchors can be based on field load tests [1], [2], semi-empirical models [3], [4] and numerical models [5], [6]. Most usual solutions for the design of the bonded length of ground anchors consist of semi-empirical methods [3]–[7], [8]. Although practical for routine applications, semi-empirical methods lose accuracy beyond their range of calibration, which can result in uneconomical design projects due to the high safety factors required to balance the uncertainties and errors involved.

A way to boost the growth of more rational semi-empirical methods for prestressed ground anchor design is to encourage studies involving monitoring of ground anchors in the field. However, most publications to date on stabilized slopes and excavations have focused on soil-nailing systems by developing reduced-scale physical models and numerical studies [9], [10]. A limited number of publications on the behavior of prestressed ground anchor in the field is available. Among the scarcely documented investigations, just a few include results from instrumented ground anchors [5], [6], [11]–[13]. Most available studies involve anchors in clayey soils [14]–[16] and rocks [17]–[19], while anchors in granular soils are more unusual.

Additionally, while ground anchor monitoring has typically focused on the total applied load on the anchor head, investigations on load variations along the anchor bonded length have been virtually overlooked. Particularly, improvement of design solutions for ground anchors can be achieved by assessing load and skin friction variations along the anchor's bonded and unbonded lengths in the field [3]–[7], [20], [21].

The purpose of this paper is to evaluate the load-transfer behavior of prestressed ground anchors installed in a retaining wall system composed of spaced bored piles in a sandy soil profile. Data were collected from the instrumented bonded length of three anchors, both during pullout tests and during different construction phases of the retaining wall. The contribution of the anchor unbonded length to the anchor bearing capacity and the variations of load on the anchor bonded length are evaluated. Skin friction values estimated from the field results are compared to values obtained from theoretical methods.

2 BACKGROUND

2.1 Brief description of design methods for ground anchor pullout capacity estimation

Empirical and semi-empirical methods for estimating the ultimate pullout capacity of ground anchors are abundant in the literature. Ostermayer [3] proposed a solution that includes the use of empirical design charts elaborated from the results of approximately 300 field tests in anchors, carried out in Germany. The proposed charts relate the anchor bonded length to the ultimate load capacity or the ultimate skin friction. The grout injection pressure used during the installation of the anchors in the field is not reported.

Bustamante and Doix [22] developed a design method that accounts for the installation process, the grout injection pressure in single or multiple phases, and the volume of injected grout. The anchor ultimate pullout capacity is estimated by considering a coefficient β that accounts for the diameter increase of the bonded length due to grout injection pressure. Values for β are given for different soil types and for single-phase or double-phase grout injection procedures. The ultimate skin friction on the anchor bonded length is estimated from empirical design charts devised for cohesive and cohesionless soils, which take into consideration whether grouting is performed in single or multiple injection stages. However, it is worth mentioning that the anchor failure load was not reached in most experiments used to create the method.

Costa Nunes [7] proposed a formulation similar to that of Bustamante and Doix [22], but assuming that failure at the ground-grout interface is governed by the Mohr-Coulomb failure theory. The ultimate anchor capacity for anchors is given by:

$$T_{max} = \pi \cdot D_e \cdot L_b \cdot [c' + (\gamma \cdot h + p) \cdot \tan'] \quad (1)$$

where: D_e is the average diameter of the ground anchor section; L_b is the anchor bonded length; c' is the soil-grout adhesion; γ is the specific unit weight of the soil at the depth of the anchor bonded length middle span; h is the depth of the anchor bonded length middle span; ϕ' is the internal friction angle of the soil; Δp is the increase in the vertical stress due to the residual injection pressure. Costa Nunes [7] suggests assuming Δp between $5\gamma h$ and $10\gamma h$. The ultimate skin friction is given by the term between brackets in Equation 1.

AASHTO [23] recommends a method for calculating the pullout resistance of anchors in cohesive soils, cohesionless soils and rocks. Proposed values for the ultimate skin friction for cohesionless soils take into consideration soil type, soil compactness and grout injection pressure. It is advised that the presumptive ultimate skin friction values offered by the method are intended for preliminary design or evaluation of the feasibility of straight shaft anchors installed in small diameter boreholes. Therefore, conservative design pullout capacities can result from using these values.

The former version of Brazilian code ABNT NBR 5629 [24] suggests a method for calculating the pullout capacity of anchors embedded in cohesive and cohesionless soils, which is analogous to that proposed by the current version of the Canadian Foundation Engineering Manual [25]. For cohesionless soils, the ultimate skin friction is given by the product of the overburden vertical stress at the middle span of the bonded length and the skin friction coefficient (k_f). Values for k_f are provided according to soil compactness and soil type (silts, fine sands, medium sands, and coarse sands). The effect of grout injection pressure on pullout capacity is disregarded in the method. No specific method for pullout capacity prediction of ground anchors is proposed by the current version of the Brazilian standard ABNT NBR 5629 [26].

2.2 Load transfer evaluation from ground anchor monitoring

Contrary to what is assumed in most proposed design solutions for ground anchors, the mobilized interface skin friction was found to behave non-uniformly along the anchor bonded length [27], [28]. One reason for the non-uniformity is the dependency of the skin friction on the relative displacement (δ) between the grout body and the surrounding soil [27], [29], [30]. The skin friction reaches the peak value (f_{ult}) and then reduces with increasing relative displacements (δ), until reaching the residual value (f_r). As the load applied to the anchor head is increased, the peak skin friction progressively moves from the portion of the bonded anchor length that is closest to the unbonded length towards the bonded length end. According to Barley and Windsor [31], typically, a ground anchor with a bonded length of 6 m needs, at proof load, to displace about 15 to 20 mm at the top end of the bonded length before any load is transferred to its bottom end.

Selection of an appropriate design value for the soil-grout interface skin friction from design manuals and codes is highly subjective [18]. Capturing the load transfer mechanisms that take place in the anchor bonded length in the field is essential for improving design methodologies. However, while the relationship between the applied load and the anchor head displacement can be easily assessed from standard pullout tests, the load distribution along the bonded length requires a more complex apparatus, which makes it difficult to be obtained in ordinary circumstances.

Li et al. [15] presented one of the first studies on the load transfer of ground anchors. Electrical resistance strain gauges were installed along the anchor bonded length. The anchors were used to stabilize a diaphragm retaining wall on a soil profile consisting of silt and clay layers. The anchors were constructed with a length of 30 m (of which 23 m corresponded to the bonded length). It was observed, from the instrumentation, that the load was not distributed linearly along the bonded length, but concentrated more at its beginning. The load was found to be virtually zero between the middle span and the end of the bonded length.

Briaud et al. [16] investigated variations of load in the bonded length of anchors embedded in a clay soil using vibrating wire extensometers. The instrumented anchors had a bonded length of 4.6 m and a total length of 13.8 m. Results revealed a load distribution configuration similar to that identified by Li et al. [15], that is, a higher concentration of load at the beginning of the anchor's bonded length.

Iten and Puzrin [27] used fiber optic sensors to investigate the load-transfer in 8-m long anchors. It was observed that the load followed a non-linear distribution, with a drastic reduction at the last 2 m of the bonded length.

Bryson and Giraldo [18] analyzed instrumented ground anchors constructed for a landslide stabilization system in a shale stratum. Load transfer was studied based on strain gauge measurements along the bonded length of the anchors, which measured 4.6 m. The strain gauge monitoring revealed that some slippage occurred between the tendon and the grout. The slippage increased as the anchor head load increased. Only minor variations in the strain gauge data were observed after the construction period and during the long-term monitoring, suggesting that the anchor bonded length reached equilibrium and that the anchors installed in the shale stratum did not show significant creep susceptibility.

Platzer et al. [32] conducted a study focusing on the compressive behavior of piles and tensile behavior of ground anchors embedded in cohesionless soils and subjected to dynamic loading. The bonded length of the anchors measured 5.1 m and was instrumented with four strain-gauge sections. The authors observed that the dynamic tensile force distribution along the anchors decreases nonlinearly with increasing anchor length. Moreover, the authors identified that the dynamic tensile forces were depleted within a shorter distance in the anchor than the static tensile forces.

3 RETAINING WALL DESCRIPTION AND SUBSOIL CHARACTERISTICS

3.1 Retaining wall description

A schematic of the elevation view of the retaining wall analyzed in this investigation is shown in Figure 1. The retaining wall had a total height of 8.95 m, a length of 56 m and was built with spaced bored piles with 300 mm in diameter and 14.85 m in length. The piles were installed in the ground with a spacing between axes of 350 mm. The characteristic concrete compressive strength of the piles at 28 days was 25 MPa. The pile reinforcement consisted of 11 longitudinal bars with 10 mm in diameter and 12 m in length, enveloped by a coil steel spiral with 5 mm in diameter and 100 mm in spacing. The top of the piles was connected to a head beam with cross section dimensions of 400 mm x 650 mm.

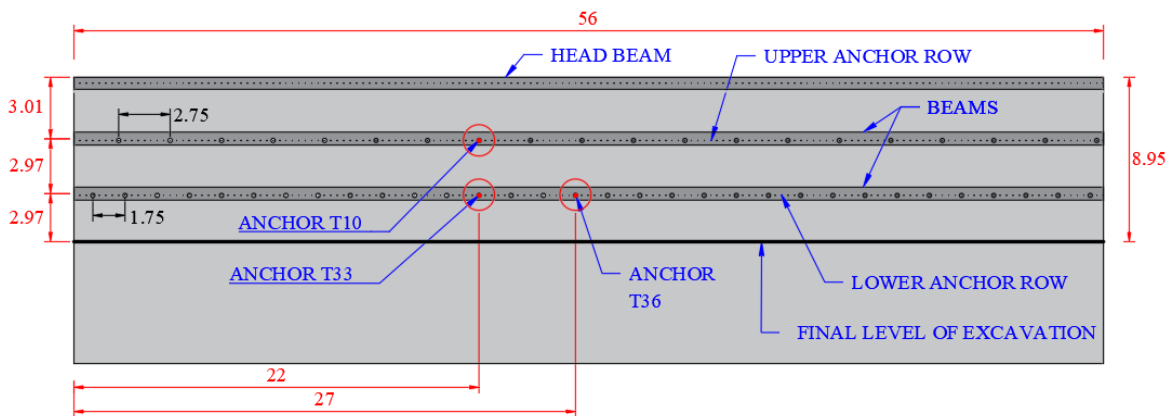


Figure 1 - Schematic showing front elevation view of the instrumented retaining wall (units: m).

The retaining wall was anchored by two rows of ground anchors constructed with steel threaded bar tendons with 32 mm in diameter and installed in a borehole with 100 mm in diameter (D_b). Uniaxial tensile tests were performed on the tendons in order to obtain the elastic modulus. Table 1 lists the mechanical properties of the used bar tendons.

Table 1 - Characteristics of the bar tendons.

Diameter (mm)	32
Yield stress (MPa)	950
Tensile strength (MPa)	1,050
Yield load (KN)	760
Ultimate load (KN)	840
Elastic modulus (MPa)	205,000
Cross-sectional area (mm ²)	804

The horizontal spacing between anchor axes was 2.75 m for the anchors of the upper row and 1.75 m for the anchors of the lower row (Figure 1). Figure 2a shows a cross-section view of the retaining wall, with the position of the anchor rows in relation to the excavation ground surface and the dimensions of the anchor bonded and unbonded lengths. The anchors of the upper row had a bonded length of 8 m and an unbonded length of 6 m, while the anchors of the lower

row had a bonded length of 9 m and an unbonded length of 5 m. A detail of the assembly of the anchor in the bonded length is shown in Figure 2b. Design tensile loads of 192 kN and 260 kN were calculated for the upper and lower rows, respectively. Both rows had the anchor heads connected to a beam with dimensions of 400 mm x 700 mm.

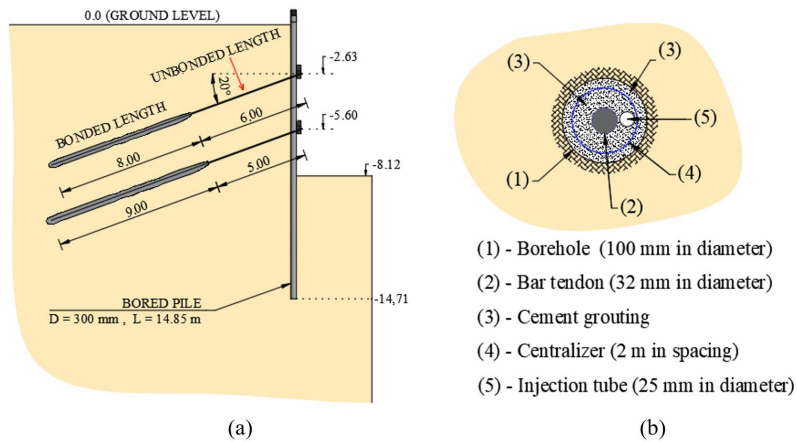


Figure 2 - (a) Schematic showing the cross-section view of the retaining wall system (units: m); (b) detail of the anchor assembly in the bonded length.

Grouting injection was performed in two steps. In the first step, cement grout was injected with a water/cement ratio of approximately 0.5. After the curing of grout in the first injection step, a second injection step with a cement grout with a water/cement ratio of approximately 0.6 was carried out to fill the borehole. Grout was injected in the bonded length with a pressure of 1500 kPa. The unbonded length of the anchor was protected with a PVC debonding sleeve.

Figure 3 shows the building phases of the retaining wall system. Initially, the bored piles were cast in the ground (phase 1). Then, the soil was excavated to a depth of 2.7 m from ground level (phase 2) and the upper row of anchors was installed (phase 3). A new excavation phase was carried out to a depth of 5.65 m (phase 4) and the lower row of anchors was installed (phase 5). The excavation was finished at a depth of 8.12 m (phase 6). The effect of the construction phases on anchor behavior was assessed during the monitoring of the ground anchors. The lateral displacements of the retaining wall were monitored with an inclinometer during the building phases [13], and were less than 0.1% of the excavation height.

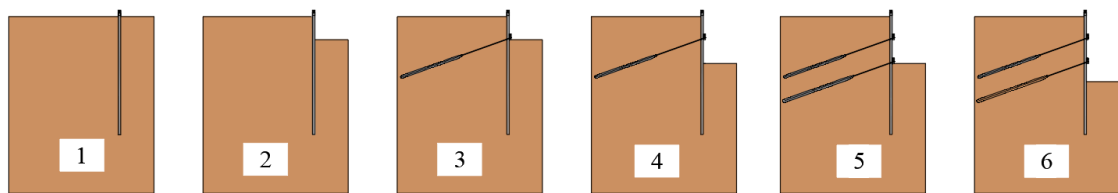


Figure 3 - Retaining wall building phases.

3.2 Subsoil characteristics

The constructed retaining wall is located in the City of Natal, Brazil. Field survey included standard penetration tests (SPT) at two different locations, identified in this study as SP01 and SP02. The tests were performed according to ABNT NBR 6484 [33] and were located near the crest of the excavation, 15.5 m apart from each other. Figure 4a shows the soil stratification at the site and Figure 4b shows the variation of the N_{SPT} blow-count resistance corrected for 60% efficiency (N_{60}) with depth and corresponding mean values. Corrections of the N_{SPT} values were carried out by assuming an efficiency of 72% for the tests, as mentioned by Décourt et al. [34] regarding the Brazilian practice. The soil profile is composed of fine sand and slightly clayey fine sand layers overlying a stiff sandy clay layer, where the tip of the

piles rest. The classification of the soil layers according to the Unified Soil Classification System (USCS) is given in Figure 4a.

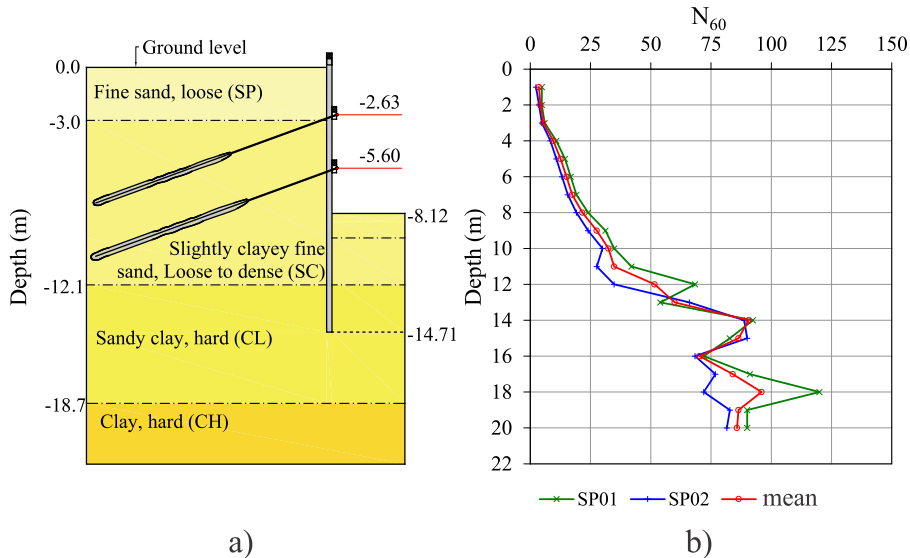


Figure 4 - (a) Subsoil profile (units: m); (b) N_{60} blow-count resistance with depth.

The grain size distribution of the slightly clayey fine sand, where the bonded length of the upper and bottom rows is installed, is shown in Figure 5. The slightly clayey fine sand has an average particle size of 0.22 mm (24.2% of particles are finer than 0.075 mm and more than 99.3% of particles are finer than 2 mm). The specific gravity of this soil is 2.65.

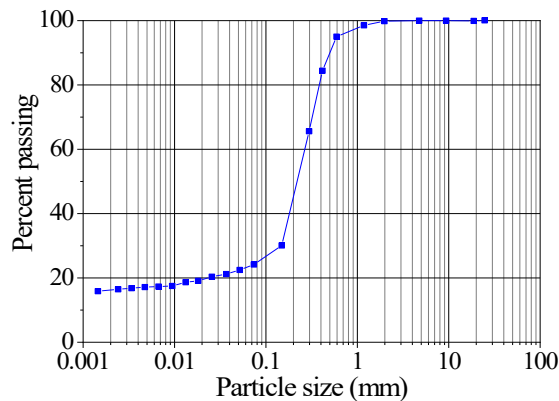


Figure 5 - Grain-size distribution of the slightly clayey fine sand.

Shear strength parameters of the slightly clayey fine sand were obtained from one series of conventional CID triaxial compression tests carried out with confining effective stresses (σ'_3) of 50 kPa, 100 kPa, and 200 kPa. Specimens were prepared with a specific unit weight of 17 kN/m³ to represent field conditions. The results of deviator stress-axial strain behavior for the soil are presented in Figure 6a, and the corresponding p - q diagram is presented in Figure 6b. The peak friction angle (ϕ'_p) of the soil equals 31° and was obtained from the inclination of the K_f line shown in Figure 6b.

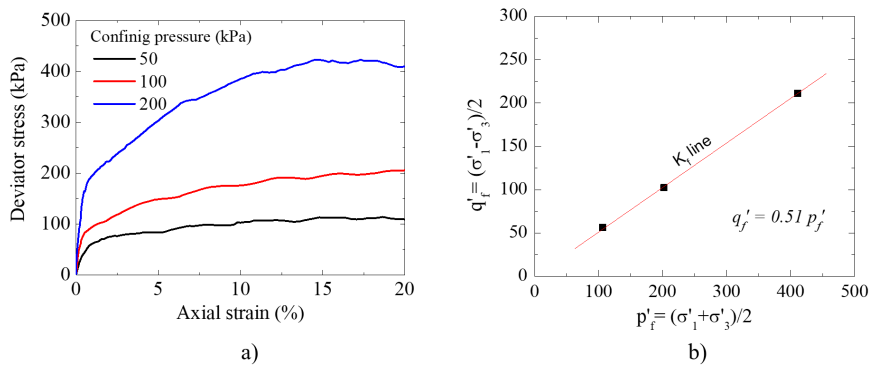


Figure 6 - Results of CID triaxial tests performed on the slightly clayey fine sand: a) Deviator stress v. axial strain relationships for varying confining pressures; b) p - q diagram.

3.3 Ground anchor instrumentation

Three anchors of the retaining wall were instrumented with electrical resistance foil strain gauges to monitor the axial force along the anchor bonded length (labeled as T10, T33 and T36, as shown in Figure 1). Double rosette model strain gauges with a nominal resistance of 120 Ω, connected in a full Wheatstone bridge circuit, were used in the instrumentation of five sections along the bonded length of each anchor. An illustration of the instrumented ground anchors is presented in Figure 7. Table 2 displays the distances of the instrumented sections from the bonded length beginning (L_{se}) in the three ground anchors. The instrumented sections are labeled as SG1 to SG5. The first instrumented section (SG1) of each ground anchor was positioned as close as possible from the beginning of the bonded length. Sections SG1 and SG4 of anchor T10 and section SG2 of anchor T33 presented malfunction after installation of the anchor and were unable to generate data during the tests. Figure 8a shows a stack of bar tendons that were used in the anchors of the retaining wall system. A detail of one instrumented bar tendon is shown in Figure 8b.

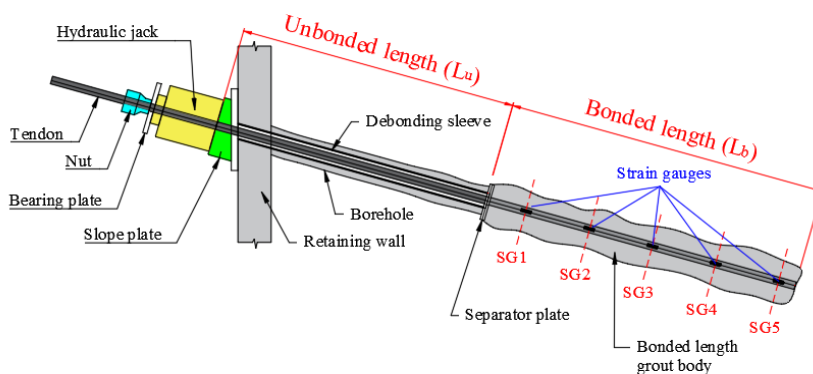


Figure 7 - Instrumented ground anchor.

Table 2 - Positions of the instrumented sections in the anchor bonded length.

Anchor	L_u (m)	L_b (m)	L_{se} (m)				
			SG1	SG2	SG3	SG4	SG5
T10	6.00	9.50	1.65	3.50	5.35	7.20	9.25
T33	5.00	9.25	0.70	1.20	3.35	5.50	9.00
T36	5.00	9.50	0.65	1.20	3.40	5.60	9.25

Note: L_u = anchor unbonded length; L_b = anchor bonded length; L_{se} = distance from the beginning of the bonded length to the instrumented section.

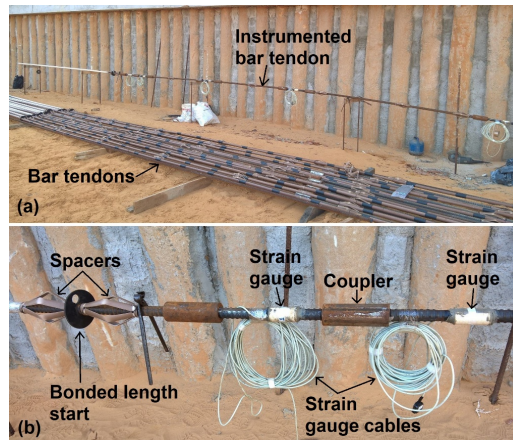


Figure 8 - (a) Bar tendons used in the field; (b) Detail of an instrumented bar tendon.

3.4 Pullout test description

The pullout tests were carried out according to Brazilian code ABNT NBR 5629 [26]. The tensile load was applied by a hydraulic jack with a maximum nominal capacity of 500 kN, connected to a manual pump reacting against the external retaining wall face. The load was applied in cumulative equal increments until stabilization. Displacements of the tendon were recorded at the anchor head using a dial gauge with a resolution of 0.01 mm and a maximum stroke of 50 mm. The dial gauge was fixed in place by a magnetic-articulated base mounted on a steady reference beam. The pullout test apparatus is shown in Figure 9. During the pullout tests and construction phases of the retaining wall, data from the instrumented sections and the load cell were recorded at predetermined time intervals with a data acquisition system with eight channels for strain-gauge-based transducers, manufactured by HBM B.V., model Spider8.

The acceptance tests on anchors T10, T33 and T36 were carried out with a single loading-unloading stage. The acceptance tests started with an initial load (F_0) calculated as $0.1f_{yk}A$ (where f_{yk} is the characteristic tensile strength of the tendon and A is the tendon cross-sectional area). After reaching the maximum load (F_{max}), the anchor was unloaded to F_0 , reloaded to the design load (F_d), and then locked-off.

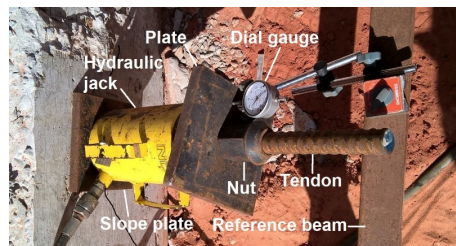


Figure 9 - Pullout test apparatus.

The suitability test on anchor T33 was conducted with four loading-unloading stages. Target loads for the load steps of the suitability test were F_0 , $0.5F_d$, $1F_d$, $1.25F_d$, $1.5F_d$ and $2F_d$. After the conclusion of the test, the anchor was completely unloaded. The pullout tests were conducted at least 15 days after the installation of the ground anchor, allowing enough time for grout curing. Table 3 summarizes the characteristics of the pullout tests performed on the instrumented ground anchors.

Table 3 - Pullout test characteristics.

Ground anchor	Test type	L_u (m)	L_b (m)	h_b (m)	F_d (kN)	F_{max} (kN)
T10	Acceptance	6.00	9.50	6.16	200	360
T33	Acceptance	5.00	9.25	8.95	260	400
T33	Suitability	5.00	9.25	8.95	260	495
T36	Acceptance	5.00	9.50	8.95	260	400

In Table 3, L_u is the anchor unbonded length, L_b is the anchor bonded length, h_b is the depth of the bonded length at its middle span, F_d is the ground anchor design load and F_{max} is the maximum load reached in the test.

4 RESULTS

4.1 Pullout test results

Figure 10a shows the load-displacement curve obtained with the suitability test performed on ground anchor T33. The applied loading-unloading stages allowed separation between elastic (d_e) and plastic (d_p) components of the total displacement measured at the anchor head, as shown in Figure 10b. The anchor unbonded length (L_u) was predicted from Equation 1 [24]:

$$L_u = \frac{\Delta d_e}{\Delta F} EA \tag{1}$$

where: Δd_e is the elastic displacement variation and ΔF is the pullout load variation.

Equation 1 resulted in an unbonded length equal to 5.6 m, which is slightly larger than the unbonded length of 5 m constructed in the field (see Table 3).

Following the procedure described in ABNT NBR 5629 [26], the load reduction due to skin friction along the anchor unbonded length was estimated as the difference between points A and B in the horizontal axis of Figure 10b. Specifically, point B is defined as the intersection between the horizontal axis and a straight line fitted to the elastic displacement curve. A load reduction equal to 60 kN, which corresponds to about 12% of the maximum applied load ($F_{max} = 495$ kN), was obtained according to this procedure.

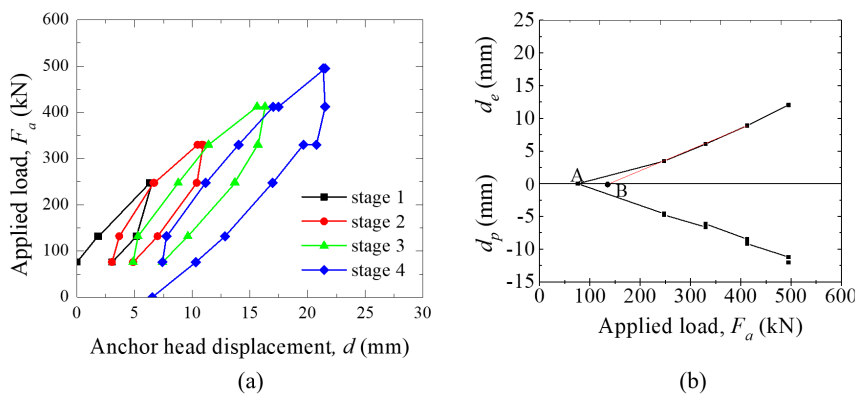


Figure 10 - Suitability test results of anchor T33: (a) Applied load v. anchor head displacement; (b) elastic and plastic displacements.

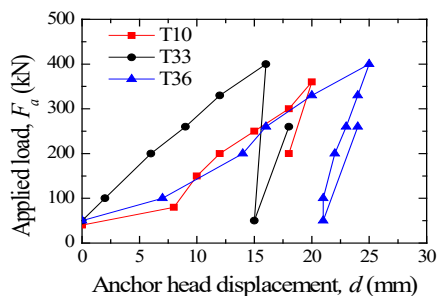


Figure 11 - Acceptance test results of anchors T10, T33 and T36.

Figure 11 shows the load-displacement curves obtained from the acceptance tests on anchors T10, T33 and T36. The head displacement (d) of anchors T10 and T36 was significantly large at the first load increment. This important initial movement of the anchor head might have been a result of soil disturbance during borehole excavation, as well as a consequence of the bentonite-based mud used for stabilizing the borehole during drilling and anchor installation. Significant initial movements in tensile load tests in anchor elements have been reported elsewhere [35], [36]. Due to the previous suitability test, only small displacements developed on anchor T33 during the acceptance test. This increase in the stiffness response of anchor T33 can be attributed to the improvement of the interface shear strength (skin friction) on the bonded length after the previous loading-unloading sequences in the suitability test (Section 3.4). This phenomenon has also been identified by Platzer et al. [32].

4.2 Load distribution on anchor bonded length

Figure 12a, c shows the measured load (F_m) at the instrumented sections of anchors T10 and T36, respectively, as a function of the distance of the instrumented section from the bonded length start normalized by the anchor bonded length (L_{se}/L_b). Figure 12b, d show F_m normalized by the load applied at the anchor head (F_a) as a function of L_{se}/L_b . Data from instrumented sections SG1 and SG4 of anchor T10 and section SG2 of anchor T33 are not included in this analysis because these sections have been damaged during anchor installation, as previously reported.

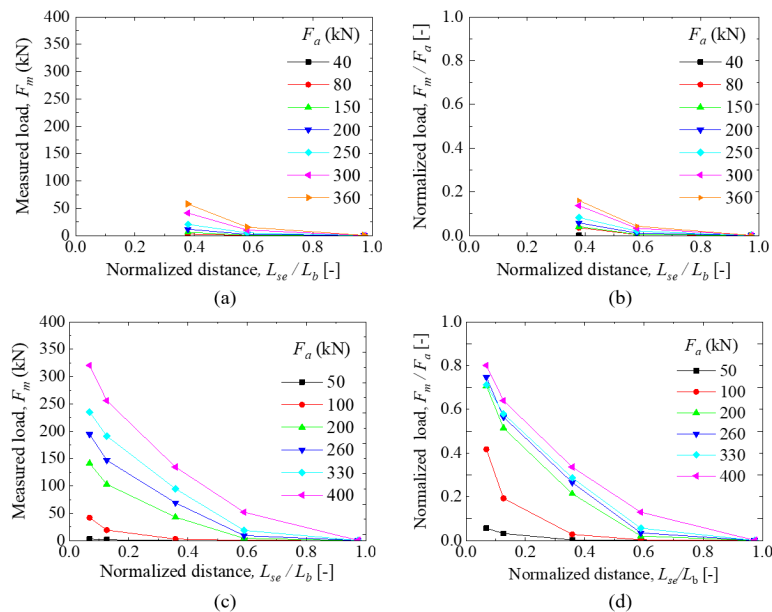


Figure 12 - Load distribution on bonded length of anchors T10 and T36: (a) Anchor T10: measured load v. normalized distance; (b) Anchor T10: normalized load v. normalized distance; (c) Anchor T36: measured load v. normalized distance; (d) Anchor T36: normalized load v. normalized distance.

The experimental results show that the load concentrated more at the beginning of the anchor bonded length and dropped with increasing distance [15], [16], [28]. The degradation of the measured load (F_m) is more significant at higher F_a levels. As the load applied to the anchor head increases, the load at the unbonded length is gradually transferred to the bonded length. In both anchors T10 and T36, the load reaching the farthest half of the bonded length was smaller than 20% of the load applied at the anchor head, while the load reaching the farthest instrumented section (SG5) was negligible.

Figure 13 presents the load distribution on the bonded length of anchor T33. Normalized measured load (F_m/F_a) versus normalized distance (L_{se}/L_b) relationships are shown for all loading stages carried out in the suitability test performed on anchor T33. Similar to anchors T10 and T36, the load concentrates more at the region closest to the beginning of the bonded length [15], [16], [28]. It is also observed that the normalized load becomes very reduced beyond a distance equal to approximately $L_{se}/L_b = 0.4$, which means that most of the load is supported by the first half of the anchor bonded length.

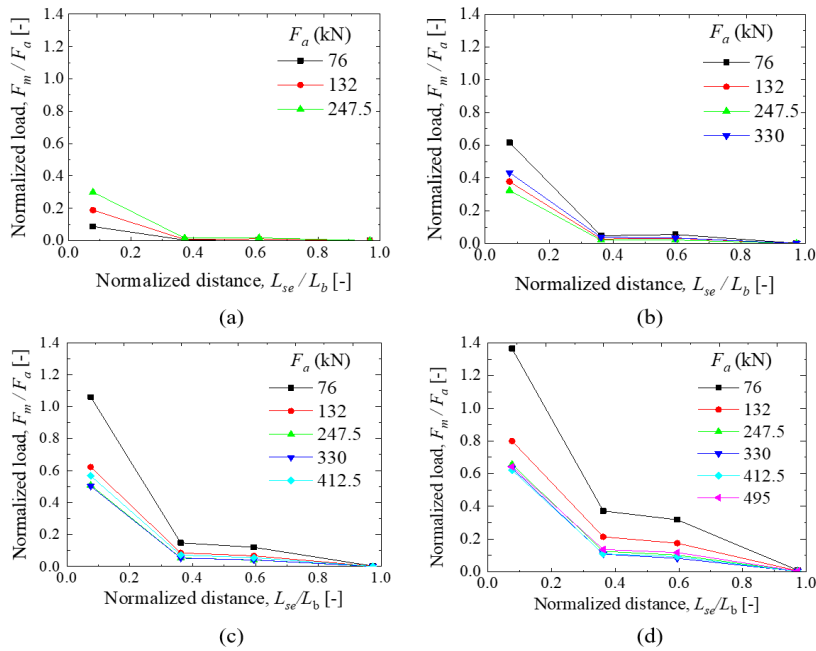


Figure 13 - Load distribution on bonded length of anchor T33 during the suitability test: (a) 1st loading stage; (b) 2nd loading stage; (c) 3rd loading stage; (d) 4th loading stage.

Figure 14 compares the load applied to the anchor head (F_a) with the corresponding measured load (F_m) at section SG1 of anchor T33. The same applied load resulted in a higher measured load in each new stage, as a consequence of the build-up of residual load at the bonded length after unloading to $F_a = 76$ kN in each stage. The load build-up is caused by the recovery of a portion of the elastic elongation of the tendon’s unbonded length after unloading. It can be noted that the residual load increment (ΔF_m) was reduced from stage to stage. Specifically, ΔF_m virtually vanished in stage 4.

Figure 14 also reveals that the measured load at SG1 remained unchanged at the beginning of the loading path of stages 2 to 4, and just increased with the applied load for F_a values higher than 132 kN. This behavior can be attributed to the mobilized skin friction on the anchor’s unbonded length, which is initially high enough to prevent any change in the measured load at SG1, but recedes after some anchor displacement [28]. The average load-transfer rate in the loading phase of each stage can be assessed from the inclination of the dashed lines shown in Figure 14. The average load-transfer rate appeared to remain unchanged between stages. Finally, it is also important to mention that some points of stages 3 and 4 in Figure 14 situate above the 1:1 line, which means that the measured load exceeded the applied load, as a result of residual load build-up.

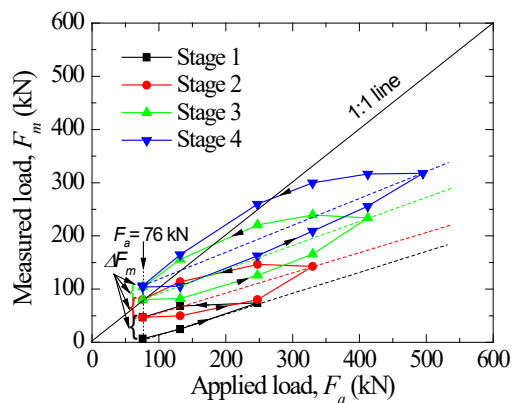


Figure 14 - Measured load at instrumented section SG1 as a function of the applied load at the anchor head.

Figure 15 compares the load distribution obtained from the acceptance tests on the instrumented anchors with results from other experimental investigations [15], [16], [28]. Despite the differences in soils and retaining wall systems, it is noted that the responses of the anchors agree well with the previously published results. All results indicate that more than 50% of the axial load in the bonded length is dissipated within a length L_{se} equal to $0.4 L_b$. However, in some anchors, the load dropped to less than 20% of the applied load within the same length, as shown by the response of anchor T33 and by the results from Briaud et al. [16].

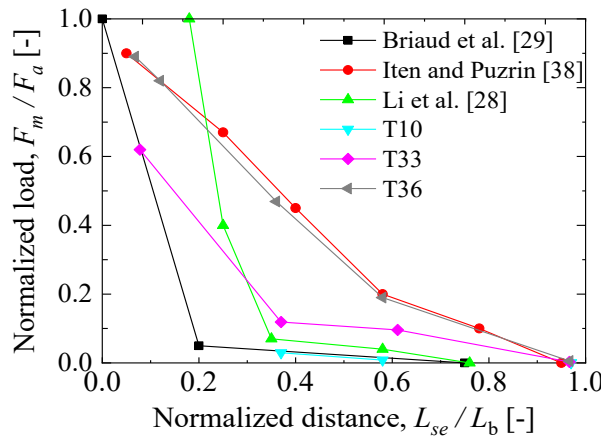


Figure 15 - Load distributions in the bonded length of the instrumented anchors compared with results reported in the literature.

4.3 Skin friction development on unbonded length of anchor T33

Figure 16 shows the skin friction on the unbonded length (f_{su}) as a function of the applied load (F_a), during the loading stages of the suitability test performed on ground anchor T33. Skin friction values were estimated from Equation 2. This analysis assumed that the skin friction develops uniformly along the unbonded length and that the load measured at the first instrumented section of the bonded length (SG1) equals that at the transition section between unbonded and bonded lengths. Also, the coefficient of diameter expansion in the unbonded length, β , was set equal to unity.

$$f_{su} = \frac{(F_a - F_{m(l)})}{\pi \cdot \beta \cdot D_b \cdot L_u} \tag{2}$$

where $F_{m(l)}$ is the load measured at section SG1 (the other parameters were defined previously).

Figure 16 reveals a significant skin friction mobilization on the anchor unbonded length with increasing applied load. The skin friction was found to increase with increasing F_a , but at a reduced rate. Additionally, the skin friction became smaller at each new loading stage for the same applied load. For instance, the calculated skin friction for $F_a = 132$ kN varied from 68.2 kPa in load stage 1 to 16.9 kPa in load stage 4. This behavior took place due to the progressive transfer of stresses from the unbonded length to the bonded length between loading stages. The skin friction reached approximately the same maximum value (f_{max}) in all four loading stages, around 115 kPa, which can be assumed as the unbonded length ultimate skin friction ($f_{ult,u}$).

Figure 16 also reveals the occurrence of negative skin friction for $F_a = 76$ kN in loading stages 3 and 4. As the tensile load decreased after unloading, the anchor unbonded length recovered a portion of the elastic elongation. This rebound caused enough displacement to mobilize residual stresses at the bonded length (at least in the zone comprising the beginning of the bonded length) and reverse the skin friction direction at the unbonded length.

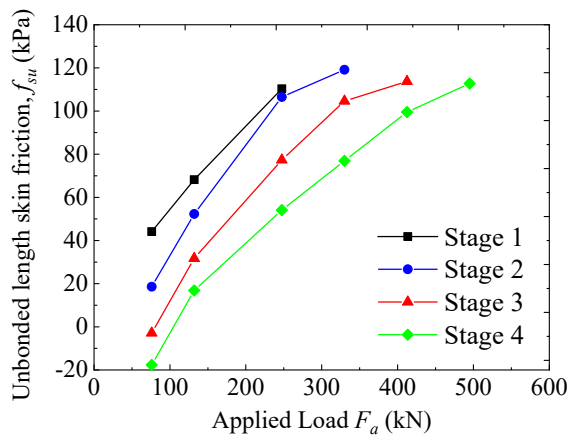


Figure 16 - Calculated skin friction on the unbonded length of ground anchor T33 during loading stages of the suitability test.

4.4 Skin friction development on bonded length of anchor T33

The skin friction on the bonded length (f_{sb}) of anchor T33, between instrumented sections, was estimated using Equation 3. The coefficient of diameter expansion in the bonded length, β , was assumed equal to 1.15 for this analysis.

$$f_{sb} = \frac{(F_{m(i)} - F_{m(i+1)})}{\pi \cdot \beta \cdot D_b \cdot (L_{se(i)} - L_{se(i+1)})} \tag{3}$$

where: $F_{m(i)}$ is the measured load at instrumented section SG_i ; $F_{m(i+1)}$ is the measured load at instrumented section $SG_{(i+1)}$; $L_{se(i)}$ is the distance from the bonded length beginning to instrumented section SG_i ; $L_{se(i+1)}$ is the distance from the bonded length beginning to instrumented section $SG_{(i+1)}$. L_{se} values are listed in Table 2 (Section 3.3).

Figure 17 presents the bonded length skin friction f_{sb} mobilized between sections SG1 and SG2, as a function of the applied load (F_a), during the four loading stages of the suitability test on anchor T33. The mobilized bonded length skin friction increased with F_a according to an increasing rate in loading stages 1 to 3, and according to an approximately constant rate in loading stage 4. In opposition, the skin friction followed a decreasing rate on the anchor's unbonded length, as shown in Figure 16. Also, contrary to what was found for the unbonded length, the skin friction in the bonded length increased after each new loading stage. Results presented in Figure 17 indicate that the ultimate skin friction (f_{ult}) at the bonded length was not reached for load range applied to the anchor head, since a tendency of stabilization of f_{sb} was not observed.

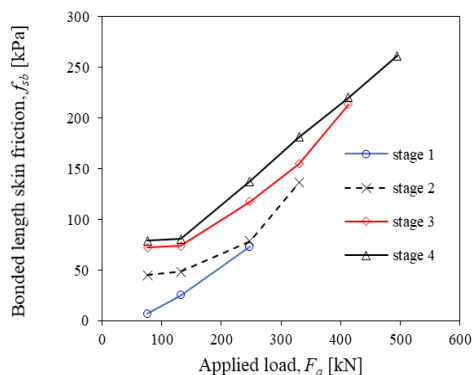


Figure 17 - Skin friction calculated between instrumented sections SG1 and SG2 of anchor T33 as a function of the applied load F_a .

Figure 18a-d shows the mobilized skin friction distribution along the bonded length of anchor T33 in the four loading stages of the suitability test. Mobilized skin friction values on the unbonded length are also included for comparison. Positions shown in Figure 18a-d were calculated from the anchor head to the midpoint between the anchor head and instrumented section SG1, and from the anchor head to the midpoint between each other instrumented section.

The skin friction was larger at the region of the bonded length closest to the transition between unbonded and bonded lengths. However, application of subsequent loading stages promoted a continuing transfer of stresses from the unbonded length to the bonded length, resulting in higher skin friction reaching the initial portion of the bonded length. At the first loading stage, the skin friction mobilized on the unbonded length was larger than that on the bonded length. Eventually, from the second loading stage, the skin friction on the bonded length superseded that on the unbonded length and concentrated almost completely at the initial half of the bonded length.

The important contribution of the anchor unbonded length to the overall pullout capacity of the anchor is clearly shown in Figure 18. It is observed that the unbonded length ultimate skin friction ($f_{ult,u} = 115\text{ kPa}$) was mobilized since the first loading stage (Figure 18a). After $f_{ult,u}$ was reached in the first stage (Figure 18a), the mobilized skin friction in the following stages reduced on the unbonded length and intensified on the bonded length, at the same applied load F_a (Figure 18b,c,d). Ultimately, it is noted from the presented data that carrying out loading-unloading stages on the ground anchor intensified the transfer of load from the unbonded length to the bonded length. Thus, conducting acceptance pullout tests before lock-off, which include the application of loading-unloading stages, is beneficial for improving the bonded length skin friction and reducing the unbonded length skin friction. Such procedure is in line with most design codes and guidelines [25], [26], [37], [38].

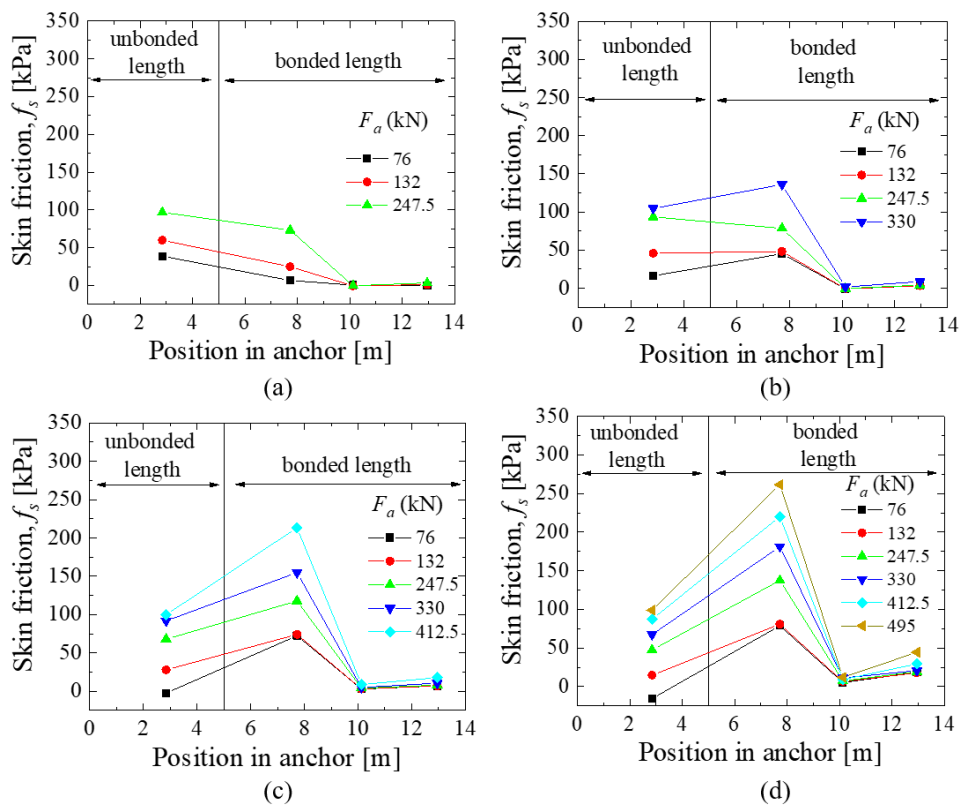


Figure 18 - Skin friction distribution on anchor T33: (a) 1st loading stage; (b) 2nd loading stage; (c) 3rd loading stage; (d) 4th loading stage.

It is important to emphasize that the shear resistance on the unbonded length shown in Figure 18 took place because of the way the anchors were jacked against the retaining wall. In the anchored wall system, the force in the anchor is generated by the active wedge moving towards the excavation, and the portion of the anchor within this zone will not

contribute to the system's stability. Therefore, the contribution of the anchor's unbonded length must not be taken into consideration in the design of anchored retaining walls. Instead, the contribution from the unbonded zone must be accounted for in the interpretation of a conventional pullout test result when the force is applied by jacking against the wall, so as not to overestimate the anchor capacity of the bond zone.

4.5 Comparison between experimental and predicted skin friction

Figure 19 compares the bonded length ultimate skin friction obtained from the field data collected from anchors T33 and T36 ($f_{ult,b,field}$) and with results obtained with the methods of Bustamante and Doix [22], Costa Nunes [7], ABNT NBR 5629 [24], AASHTO [23] and Ostermayer [3] ($f_{ult,b,pred}$). Anchor T10 was excluded from this analysis because its first instrumented section (SG1) was damaged during installation, which prevented obtaining the maximum mobilized skin friction on the bonded length (see Section 3.3). Since stabilization of f_{sb} with the applied load F_a was not achieved for anchor T33, as shown in Figure 17, the field ultimate skin friction was assumed equal to the maximum skin friction ($f_{ult,b,field} = f_{max}$).

Soil parameters were estimated based on the results of the field and laboratory tests (Section 3.3). Specifically, calculations were carried out by assuming that the soil unit weight equals 17 kN/m^3 at the depth of the midpoint of the anchor upper row's bonded length and 18 kN/m^3 at the depth of the midpoint of the anchor lower row's bonded length. Additionally, the soil effective internal friction angle and effective cohesion were assumed equal to 31° and 0 kPa , respectively.

The vertical stress increase due to the residual injection pressure (Δp) in Costa Nunes' [7] approach was considered equal to $5\gamma h$, as recommended by the author. However, it has been observed that this suggestion typically leads to predicted bearing capacity values much higher than those found in the field [20]. Thus, an additional prediction with Costa Nunes' [7] approach was carried out using $\Delta p = 0 \text{ kPa}$.

The diameter increase of the bonded length due to the grouting process injection was assumed equals to $1.15 D_b$ in the methods of Bustamante and Doix [22], Costa Nunes [7], ABNT NBR 5629 [24] and AASHTO [23]. The anchorage coefficient (k_f) required in the method by ABNT NBR 5629 [24] was defined as 1.2, based on soil type.

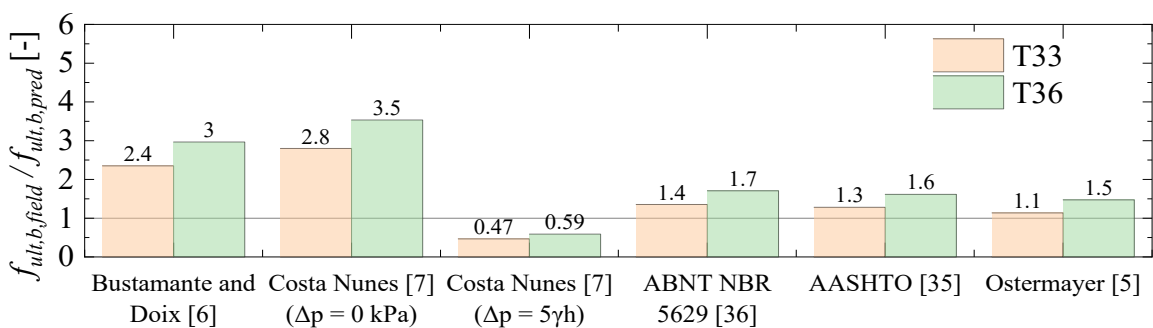


Figure 19 - Comparison between field and predicted ultimate skin friction on bonded length of anchors T33 and T36.

Figure 19 shows that the methods of Bustamante and Doix [22] and Costa Nunes [7] with $\Delta p = 0 \text{ kPa}$ provided over-conservative predictions. On the other hand, slightly conservative predictions were obtained with the methods by AASHTO [25], ABNT NBR 5629 [24] and Ostermayer [3]. On the other hand, predictions with Costa Nunes' [7] method with $\Delta p = 5\gamma h$ overestimated the pullout capacity by more than twice. Porto [20] warns about exaggerated results with this method when the vertical stress increase due to the residual injection pressure is taken into consideration.

All design methods assessed in Figure 19 assume that the skin friction mobilized on the bonded length of a ground anchor follows a uniform distribution [3], [7], [22]–[24]. Although the progressive failure mechanism (i.e., f_{ult} dropping off to the residual value after reaching peak) was not possible to be observed with the field tests, an indication of such behavior can be assessed from the experimental data presented in Figure 18. It may be noted that predictions

for pullout field tests could be improved with design methods that incorporate non-uniform skin friction distributions, in which the skin friction concentrates more at the first half of the anchor bonded length.

4.6 Monitoring of anchor T36 after lock-off

While monitoring of anchors T10 and T33 has been discontinued after lock-off, anchor T36 was continuously tracked for 328 days after lock-off. Figure 20 shows the variation of the load (F_m) measured in the instrumented sections during monitoring of anchor T36 (day 0 is when the anchor was locked-off). It can be observed that minor variations of load took place initially and equilibrium was reached in the long-term. These results are consistent with the findings of [18]. Particularly, the measured load in the bonded length of anchor T36 decreased with time at Sections SG1 to SG4 and increased slightly at section SG5. The most significant load relief took place five days after lock-off and was sharper at section SG1, which recorded a relief of about 11%. In the first minute after lock-off, the measured load at SG1 decreased by 5%. A similar tendency, though less pronounced, occurred at sections SG2 and SG3. The total relief of load at SG1 after 328 days was about 18% (7% of which occurred after the first 5 days). The load relief at SG2 and SG4 was about 7% and 4% after 328 days of installation, respectively. At the same time, the measured load increased slightly at section SG5. Once more, most of the load increase at SG5 occurred immediately after lock-off. No significant changes in the measured load were noticed during or after the third excavation phase of the retaining wall.

The load relief in the anchor bonded length in the long-term can be explained by the viscous behavior of the anchor components (grout, tendon, connections, etc.) and the surrounding soil [15], [39], [40]. A small portion of that load relief was transferred to the zone at the end of the bonded length.

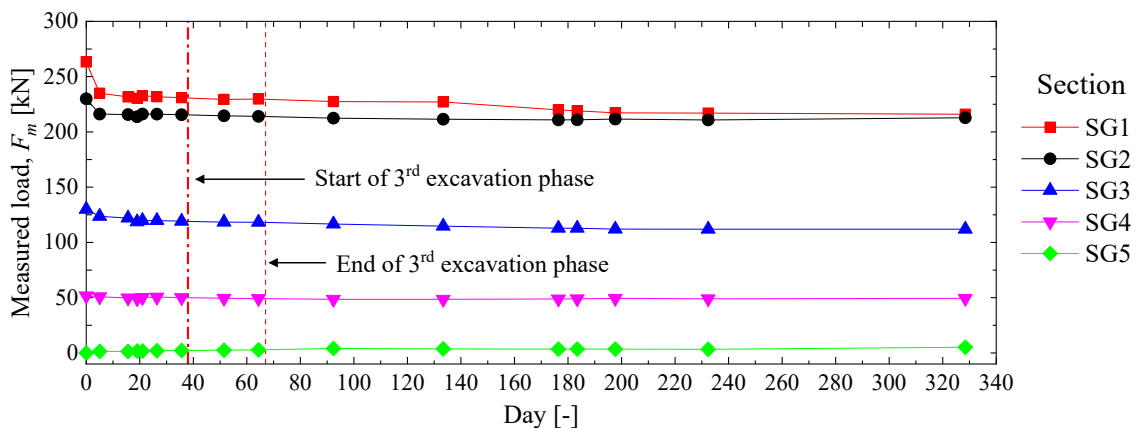


Figure 20 - Load monitoring along time for anchor T36.

5 CONCLUSIONS

This paper addresses the behavior of three instrumented prestressed ground anchors installed in a spaced bored pile retaining wall. The load in the ground anchors was measured with strain gauges installed in five distinct sections along the anchor bonded length. Load variations were monitored during pullout tests performed on the anchors, as well as along the different construction phases of the retaining wall system after locking-off. Skin friction mobilized on the anchor unbonded and bonded lengths were assessed from the data collected in the field. The following conclusions can be drawn from the experimental results obtained in this investigation:

- (1) The measured load followed a non-uniform distribution along the anchor bonded length, being higher at the region closest to the beginning of the bonded length and dropping drastically within the farthest bonded length half. Residual load after anchor unloading was recorded close to the beginning of the anchor bonded length. Eventually, the residual load build-up caused the measured load to exceed the applied load after the anchor was submitted to a number of loading-unloading stages.
- (2) The contribution of the unbonded length skin friction to the overall anchor capacity was found to be significant. The unbonded length skin friction increased at a reduced rate with increasing applied load and decreased with the application of the loading-unloading stages. Displacements applied to the anchor head were sufficient to mobilize

the ultimate skin friction on the unbonded length. Residual stresses in the bonded length caused the development of negative skin friction on the unbonded length after three loading-unloading stages.

- (3) The field test results conducted in the present investigation show that the contribution from the unbonded length must be accounted for in the interpretation of conventional pullout test results so as not to overestimate the anchor capacity of the bonded length.
- (4) The initial portion of the anchor bonded length experienced an increase in the mobilized skin friction after the application of loading-unloading stages on the anchor. The mobilized skin friction concentrated almost completely on the nearest bonded length half, while negligible skin friction was mobilized on the farthest bonded length half. The transfer of load from the unbonded length to the bonded length intensified after the ultimate skin friction on the unbonded length was achieved. Applied load levels were not sufficient to mobilize the ultimate skin friction on the anchor bonded length.
- (5) Long-term monitoring after anchor lock-off revealed that, for the specific case of this project, the load in the anchor bonded length reduced slightly and then stabilized thereafter. The measured load was not significantly influenced by the retaining wall construction phases. Most load reliefs occurred within the first five days after lock-off. A discrete increase in the load with time was found near the end of the bonded length.
- (6) Performance of loading-unloading stages on the ground anchor intensified the transfer of load from the unbonded length to the bonded length. The load transfer became more effective after the ultimate skin friction of the unbonded length was reached. Therefore, the required procedure in the design codes and guidelines for carrying out pullout tests, including loading-unloading stages during anchor installation before lock-off, appears to be well justified.

ACKNOWLEDGEMENTS

The authors gratefully acknowledge the financial support provided by the Brazilian National Council for Scientific and Technological Development (CNPq).

REFERENCES

- [1] S. Yoshida, K. Komura, T. Matsumoto, and T. Yoshida, "Pull-out experiment of two-dimensional model flip-type ground anchors installed in dry sand ground," in *Geotechnics for Sustainable Infrastructure Development* (Lecture Notes in Civil Engineering, 62), P. D. Long and N. T. Dung, Eds., Switzerland: Springer, 2020, pp. 1245–1252.
- [2] A. Parsapajouh, S. Litkouhi, and B. Amini, "A case study on excavation stabilization using ground anchors and high pressure injection," in *Proc. 4th Int. Conf. Grout. Deep Mix.*, New Orleans, Aug. 2012, pp. 1115–1123, <http://dx.doi.org/10.1061/9780784412350.0092>.
- [3] H. Ostermayer, "Construction carrying behaviour and creep characteristics on ground anchors," in *Proc. Conf. Diaphragm Walls and Anchorages*, 1975, pp. 141–151, <http://dx.doi.org/10.1680/dwaa.00056.0023>.
- [4] N. N. Thanh and N. P. Duy, "Full-scale pullout testing of ground anchors to evaluate the applicability of french design practice TA95 for Vietnam," in *CIGOS 2019, Innovation for Sustainable Infrastructure* (Lecture Notes in Civil Engineering 54), C. Ha-Minh, D. Van Dao, F. Benboudjema, S. Derrible, D. V. K. Huynh, and A. M. Tang, Eds., Switzerland: Springer, 2020, pp. 787–792.
- [5] J.-L. Briaud and Y. Lim, "Tieback walls in sand: numerical simulation and design implications," *J. Geotech. Geoenviron. Eng.*, vol. 125, no. 2, pp. 101–110, Feb 1999, [http://dx.doi.org/10.1061/\(ASCE\)1090-0241\(1999\)125:2\(101\)](http://dx.doi.org/10.1061/(ASCE)1090-0241(1999)125:2(101)).
- [6] F. Rashidi and H. Shahir, "Numerical investigation of anchored soldier pile wall performance in the presence of surcharge," *Int. J. Geotech. Eng.*, vol. 13, no. 2, pp. 162–171, Mar 2019, <http://dx.doi.org/10.1080/19386362.2017.1329258>.
- [7] A. J. Costa Nunes, "Ground prestressing: first casagrande lecture," in *VIII CPAMSEF*, Cartagena, Colombia, 1987.
- [8] I. O. Joppert Jr., W. Mallmann, and W. R. Iorio, "Calculation method for estimation of failure load in self-perforating tie-backs of tubular type," in *Sem. Eng. de Fund. Esp. Geotec. SEFE V*, São Paulo, 2004.
- [9] M. Yazdandoust, "Seismic performance of soil-nailed walls using a 1g shaking table," *Can. Geotech. J.*, vol. 55, no. 1, pp. 1–18, 2018, <http://dx.doi.org/10.1139/cgj-2016-0358>.
- [10] G. Zhang, J. Cao, and L. Wang, "Centrifuge model tests of deformation and failure of nailing-reinforced slope under vertical surface loading conditions," *Soil Found.*, vol. 53, no. 1, pp. 117–129, Feb 2013, <http://dx.doi.org/10.1016/j.sandf.2012.12.008>.
- [11] H. Arefizadeh and H. Shahir, "Three-dimensional analysis of anchored wall with concrete bearing pads," *J. Eng. Des. Technol.*, vol. 18, no. 6, pp. 1469–1486, Jan 2020, <http://dx.doi.org/10.1108/JEDT-09-2019-0229>.
- [12] R. Moffat, P. Parra, and M. Carrasco, "Monitoring a 28.5 m high anchored pile wall in gravel using various methods," *Sens. Switz.*, vol. 20, no. 1, pp. 80, Dec 2020, <http://dx.doi.org/10.3390/s20010080>.
- [13] K. Gorska and M. Wyjadłowski, "Analysis of displacement of excavation based on inclinometer measurements," *Stud. Geotech. Mech.*, vol. XXXIV, no. 4, pp. 3–16, 2012, <http://dx.doi.org/10.2478/sgm041201>.

- [14] R. J. Finno and J. F. Roboski, "Three-dimensional responses of a tied-back excavation through clay," *J. Geotech. Geoenviron. Eng.*, vol. 131, no. 3, pp. 273–282, Mar 2005, [http://dx.doi.org/10.1061/\(ASCE\)1090-0241\(2005\)131:3\(273\)](http://dx.doi.org/10.1061/(ASCE)1090-0241(2005)131:3(273)).
- [15] J. C. Li, H. L. Yao, L. P. Shi, and B. I. Shy, "Behavior of ground anchors for Taipei sedimentary soils," in *Proc. 2nd Int. Conf. Case Histories Geotec. Eng.* (Paper No. 6.73), 1988.
- [16] J. L. Briaud, A. Y. Griffin, A. Soto, A. Suroor, and H. Park, *Long-Term Behavior of Ground Anchors and Tieback Walls, Report FHWA_1391-1*. Texas: Department of Transportation, 1998.
- [17] X. Liu, J. Wang, J. Huang, and H. Jiang, "Full-scale pullout tests and analyses of ground anchors in rocks under ultimate load conditions," *Eng. Geol.*, vol. 228, pp. 1–10, Oct 2017, <http://dx.doi.org/10.1016/j.enggeo.2017.07.004>.
- [18] L. S. Bryson and J. R. Giraldo, "Analysis of case study presenting ground anchor load-transfer response in shale stratum," *Can. Geotech. J.*, vol. 57, no. 1, pp. 85–99, Jan 2020, <http://dx.doi.org/10.1139/cgj-2018-0326>.
- [19] B. Benmokrane, M. Chekired, and H. Xu, "Monitoring behavior of grouted anchors using vibrating-wire gauges," *J. Geotech. Eng.*, vol. 121, no. 6, pp. 466–475, 1995, [http://dx.doi.org/10.1061/\(ASCE\)0733-9410\(1995\)121:6\(466\)](http://dx.doi.org/10.1061/(ASCE)0733-9410(1995)121:6(466)).
- [20] T. B. Porto, "Anchors in soils - geotechnical behavior and methodology web for prediction and control," Ph.D. dissertation, Grad. Program Geotech., Univ. Fed. Ouro Preto, Ouro Preto, 2015.
- [21] M. Turner, "Geotechnical design of ground anchors," in *ICE Manual of Geotechnical Engineering Volume II - Geotechnical Design, Construction and Verification*, J. Burland, T. Chapman, H. Skinner and M. Brown, Eds., ICE Publishing, 2012, pp. 1011.
- [22] M. Bustamante and B. Doix, "Une méthode pour le calcul des tirants et des micropieux injectés," *Bull. Liaison des Lab. Ponts Chaussées*, no. 140, pp. 75–92, 1985.
- [23] American Association of State Highway and Transportation Officials, *AASHTO LRFD Bridge Design Specifications*, 8th ed., 2017.
- [24] Associação Brasileira de Normas Técnicas, *Procedure of Ties Anchored in Soil*, ABNT NBR 5629, 2006.
- [25] Canadian Geotechnical Society, *Canadian Foundation Engineering Manual*. Ottawa: CGS, 2006.
- [26] Associação Brasileira de Normas Técnicas, *Ties Anchored in Soil – Design and Execution*, ABNT NBR 5629:2018, 2018.
- [27] M. Iten and A. M. Puzrin, "Monitoring of stress distribution along a ground anchor using BOTDA," *Sensors Smart Struct. Technol. Civil, Mech. Aerosp. Syst.*, vol. 7647, pp. 1–15, 2010, <http://dx.doi.org/10.1117/12.847499>.
- [28] N.-K. Kim, "Performance of tension and compression anchors in weathered soil," *J. Geotech. Geoenviron. Eng.*, vol. 129, no. 12, pp. 1138–1150, Dec 2003, [http://dx.doi.org/10.1061/\(ASCE\)1090-0241\(2003\)129:12\(1138\)](http://dx.doi.org/10.1061/(ASCE)1090-0241(2003)129:12(1138)).
- [29] N. Moraci and P. Recalcati, "Factors affecting the pullout behaviour of extruded geogrids embedded in a compacted granular soil," *Geotext. Geomembr.*, vol. 24, no. 4, pp. 220–242, Aug 2006, <http://dx.doi.org/10.1016/j.geotextmem.2006.03.001>.
- [30] K. Fujita, K. Ueda, and M. Kusabuka, "A method to predict the load-displacement relationship of ground anchors," *Rev. Fr. Geotechnique*, vol. 1, no. 3, pp. 58–62, Oct 1978, <http://dx.doi.org/10.1051/geotech/1978003058>.
- [31] A. D. Barley and C. R. Windsor, "Recent advances in ground anchor and ground reinforcement technology with reference to the development of the art," in *Proc. Int. Conf. Geotech. Geol. Eng.*, 2000.
- [32] K. M. Platzer, C. Wendeler, R. Brändle, and M. Stolz, "Experimental investigation of forces along anchors subjected to dynamic loading under tension and compression in field tests," *Can. Geotech. J.*, vol. 57, no. 5, pp. 770–782, May 2020, <http://dx.doi.org/10.1139/cgj-2018-0144>.
- [33] Associação Brasileira de Normas Técnicas, *Soil - Standard Penetration Test - SPT - Soil Sampling and Classification - Test Method*, ABNT NBR 6484:2001, 2001.
- [34] L. Décourt, A. Belincanta, and A. Quaresma Fo., "Brazilian experience on SPT," in *Suppl. Contrib. Braz. Soc. Soil Mech., XII ICSMFE*, 1989, pp. 49–54.
- [35] A. B. Cerato and R. Victor, "Effects of long-term dynamic loading and fluctuating water table on helical anchor performance for small wind tower foundations," *J. Perform. Constr. Facil.*, vol. 23, no. 4, pp. 251–261, Aug 2009., [http://dx.doi.org/10.1061/\(ASCE\)CF.1943-5509.0000013](http://dx.doi.org/10.1061/(ASCE)CF.1943-5509.0000013).
- [36] J. A. Schiavon, C. H. C. Tsuha, A. Neel, and L. Thorel, "Centrifuge modelling of a helical anchor under different cyclic loading conditions in sand," *Int. J. Phys. Model. Geotech.*, vol. 19, no. 2, pp. 72–88, Mar 2019, <http://dx.doi.org/10.1680/jphmg.17.00054>.
- [37] British Standards Institution, *Code of Practice for Grouted Anchors*, BSI 8081:2015, 2015.
- [38] A. R. Gaba, B. Simpson, W. Powrie, and D. R. Beadman, *Embedded Retaining Walls: Guidance for Economic Design* (CIRIA Report, C580). London: GB. Constr. Ind. Res. Inf. Assoc., 2003.
- [39] A. Correia, A. G. Guerra, and N. C. Pinto, "Behavior of three retaining wall structures of Berlin type," *Geotec. Rev. Soc. Port. Geotec.*, vol. 1, no. 81, pp. 65–78, 1996.
- [40] S. W. Choi, J. Lee, J. M. Kim, and H. S. Park, "Design and application of a field sensing system for ground anchors in slopes," *Sensors*, vol. 13, no. 3, pp. 3739–3752, 2013, <http://dx.doi.org/10.3390/s130303739>. PMID:23507820.
- [41] M. H. Baziar, A. Ghadamgahi, and A. J. Brennan, "Numerical analysis of collapse in a deep excavation supported by ground anchors," *Proc. Inst. Civ. Eng. Geotech. Eng.*, pp. 1–45, 2020, <http://dx.doi.org/10.1680/jgeen.19.00122>.

- [42] A. Ahmadi and M. M. Ahmadi, "Three-dimensional numerical analysis of corner effect of an excavation supported by ground anchors," *Int. J. Geotech. Eng.*, pp. 1–13, Oct. 2019, <http://dx.doi.org/10.1080/19386362.2019.1682349>.
- [43] N. K. Kim, J. S. Park, and S. K. Kim, "Numerical simulation of ground anchors," *Comput. Geotech.*, vol. 34, no. 6, pp. 498–507, Nov 2007, <http://dx.doi.org/10.1016/j.compgeo.2006.09.002>.
- [44] H. Y. Xu, L. Z. Chen, and J. L. Deng, "Uplift tests of jet mixing anchor pile," *Soil Found.*, vol. 54, no. 2, pp. 168–175, Apr 2014, <http://dx.doi.org/10.1016/j.sandf.2014.02.008>.
- [45] B. V. S. Viswanadham and V. M. Rotte, "Effect of facing type on the behaviour of soil-nailed slopes: centrifuge and numerical study," *Discovery*, vol. 46, no. 215, pp. 214–223, 2015. Accessed: Dec. 07, 2020. [Online]. Available: www.discoveryjournals.com
- [46] W. B. Wei and Y. M. Cheng, "Soil nailed slope by strength reduction and limit equilibrium methods," *Comput. Geotech.*, vol. 37, no. 5, pp. 602–618, Jul 2010, <http://dx.doi.org/10.1016/j.compgeo.2010.03.008>.
- [47] D. P. Deng, L. Li, and L. H. Zhao, "Limit equilibrium analysis for stability of soil nailed slope and optimum design of soil nailing parameters," *J. Cent. South Univ.*, vol. 24, no. 11, pp. 2496–2503, Nov 2017, <http://dx.doi.org/10.1007/s11771-017-3662-y>.
- [48] S. Rawat and A. K. Gupta, "Analysis of a nailed soil slope using limit equilibrium and finite element methods," *Int. J. Geosynth. Gr. Eng.*, vol. 2, no. 4, pp. 1–23, Dec 2016, <http://dx.doi.org/10.1007/s40891-016-0076-0>.
- [49] S. K. Razavi and M. Hajjalilue Bonab, "Study of soil nailed wall under service loading condition," *Proc. Inst. Civ. Eng. Geotech. Eng.*, vol. 170, no. 2, pp. 161–174, Apr 2017, <http://dx.doi.org/10.1680/jgeen.16.00006>.
- [50] G. Zhang, J. Cao, and L. Wang, "Failure behavior and mechanism of slopes reinforced using soil nail wall under various loading conditions," *Soil Found.*, vol. 54, no. 6, pp. 1175–1187, Dec 2014, <http://dx.doi.org/10.1016/j.sandf.2014.11.011>.
- [51] P. J. Sabatini, D. G. Pass, and R. C. Bachus, *Ground Anchors and Anchored Systems*, 4th ed. (Geotechnical Engineering Circular). Washington: Assoc. Drilled Shaft Contract. (U.S.), GeoSyntec Consult., Fed. Highw. Adm., Off. Bridge Technol., 1999.
- [52] R. I. Woods and K. Barkhordari, "The influence of bond stress distribution on ground anchor design," in *Gr. Anchorages Anchored Struct. Proc. Conf. London*, 1997, pp. 55–64.

Author contributions: AMDS: methodology, validation, formal analysis, data curation, investigation, manuscript writing, editing and review; YDJC: conceptualization, formal analysis, resources, supervision, manuscript writing and review; LASF: experimental analyses; CMLC: supervision and manuscript review.

Editors: David Oliveira, Guilherme Aris Parsekian.



ERRATUM

Erratum

In the article “**Ultrasonic measurement and elastic properties of the PbO-SrO-B₂O₃ glass system**”, DOI number <https://doi.org/10.1590/S1983-41952020000400015>, published in IBRACON Structures and Materials Journal ISSN 1983-4195, v.13, n.4, e13415, 2020, on page 1-7:

2 CHARACTERIZATION TECHNIQUES

2.2 Density and molar volume

Where it reads:

$$\rho = \rho_H \left(\frac{m_a}{m_d} \right) \quad (\text{Eq. 1.0})$$

“Where, ρ is the density, ρ_H is the density of the water, m_a and m_d are the mass of the sample in the air and the mass of the submerged sample, respectively.”

It should be read:

$$\rho = \rho_H \left(\frac{m_a}{m_d} \right) \text{ or } \rho = \rho_H \left(\frac{m_a}{m_2 - (m_3 - m_1)} \right) \quad (\text{Eq. 1.0})$$

Where ρ is the density, ρ_H is the density of the water, m_a is the mass of the sample in the air, m_d is the mass of the submerged sample, m_1 is the solid sample mass, m_2 is the pycnometer mass totally filled with distilled water, and m_3 is the pycnometer mass + remaining distilled water + solid sample mass.”

2.3 Ultrasonic measurements

Where it reads:

$$V_{ms} = \left[\frac{1}{3} \left(\frac{2}{V_S^3} \left(\frac{1}{V_L^3} \right) \right) \right]^3 \quad (\text{Eq.1.3})$$

It should be read:

$$V_{ms} = \left[\frac{1}{3} \left(\frac{2}{V_S^3} + \frac{1}{V_L^3} \right) \right]^{-1/3} \quad (\text{Eq. 1.3})$$



3 RESULTS AND DISCUSSION

3.2 Ultrasonic study

Where it reads:

$$“ V_L^2 = \sqrt{\frac{k}{\rho}} \tag{Eq. 1.4}”$$

Having k as volumetric modulus of elasticity,
It should be read:

$$“ V_L = \sqrt{\frac{L}{\rho}} \tag{Eq. 1.4}”$$

Having L longitudinal module,
Where it reads:

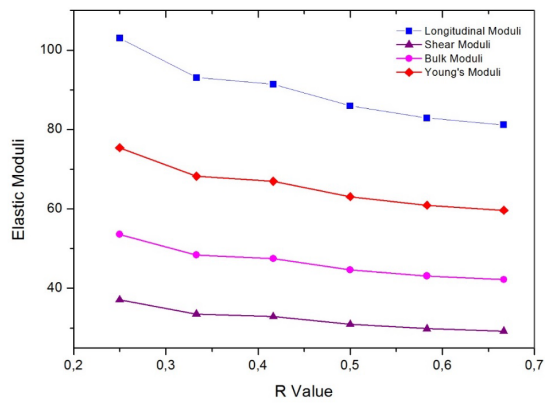


Figure 2. Variation of elastic modules for the BPS glass system. Source: the autors (2018).

It should be read:

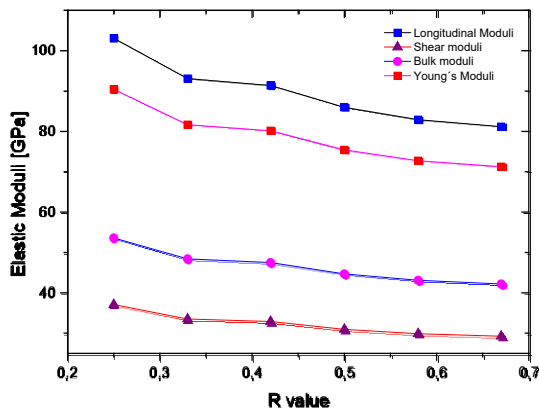


Figure 2. Variation of elastic modules for the BPS glass system. Source: the autors (2018).

Where it reads:

Table 2 Longitudinal Velocity (V_L), Transverse velocity (V_s), Average sound velocity (V_{ms}), Longitudinal Module (L), Transversal Modulus (G), Bulk Module (K) e Young's Module (E).

Glasses	V_L (m/s)	V_s (m/s)	V_{ms} (m/s)	L (10^{10} N/m ²)	G (10^{10} N/m ²)	K (GPa)	E
BPS-1	4918,67	2951,202	3264,75	103,06	37,10	53,59	75,42
BPS-2	4626,00	2775,6	3070,49	93,09	33,51	48,41	68,24
BPS-3	4541,33	2724,798	3014,29	91,36	32,89	47,51	66,99
BPS-4	4361,00	2616,6	2894,60	85,96	30,95	44,69	63,12
BPS-5	4209,00	2525,4	2793,71	82,91	29,85	43,11	60,92
BPS-6	4104,00	2462,4	2724,01	81,18	29,23	42,21	59,68

It should be read:

Table 2 Longitudinal Velocity (V_L), Transverse velocity (V_s), Average sound velocity (V_{ms}), Longitudinal Module (L), Transversal Modulus (G), Bulk Module (K) e Young's Module (E).

Glasses	V_L (m/s)	V_s (m/s)	V_{ms} (m/s)	L (GPa)	G (GPa)	K (GPa)	E (GPa)
BPS-1	4918,67	2951,202	3264,75	103,06	37,10	53,59	90,44
BPS-2	4626,00	2775,6	3070,49	93,09	33,51	48,41	81,69
BPS-3	4541,33	2724,798	3014,29	91,36	32,89	47,51	80,17
BPS-4	4361,00	2616,6	2894,60	85,96	30,95	44,69	75,43
BPS-5	4209,00	2525,4	2793,71	82,91	29,85	43,11	72,75
BPS-6	4104,00	2462,4	2724,01	81,18	29,23	42,21	71,26

Where it reads:

Table 3 Debye Temperature (θ_d), Poisson Coefficient (σ), Acoustic Impedance (Z) and Coefficient of Thermal Expansion (A).

Glasses	θ_d	σ	Z (10^{-7} kg / m ² .s)	A
BPS-1	411,7409	0,21879	2,09	114099,81
BPS-2	382,5736	0,21878	2,01	107309,87
BPS-3	371,1051	0,21874	2,01	105345,53
BPS-4	352,6334	0,21869	1,97	101161,87
BPS-5	338,7643	0,21872	1,96	97635,47
BPS-6	328,3990	0,21867	1,98	95199,47

It should be read:

Table 3 Debye Temperature (θ_d), Poisson Coefficient (σ), Acoustic Impedance (Z) and Coefficient of Thermal Expansion (A).

Glasses	θ_d K	σ	Z (10^7 kg / m ² .s)	A 10^{-6} K ⁻¹
BPS-1	411,7409	0,21879	2,09	11,41
BPS-2	382,5736	0,21878	2,01	10,73
BPS-3	371,1051	0,21874	2,01	10,53
BPS-4	352,6334	0,21869	1,97	10,12
BPS-5	338,7643	0,21872	1,96	9,76
BPS-6	328,3990	0,21867	1,98	9,52

3.3 FTIR infrared spectroscopy

Where it reads:

The spectrum in region (I) has bands close to 2300-2350 cm^{-1} , the vibrations of different C-O bonds or ambient CO_2 concentrations in the Infrared [14] are attributed, these are not part of the glass structures.

It should be read:

The spectrum in region (I) has bands close to 2300-2350 cm^{-1} , the vibrations of different C=O bonds of ambient CO_2 concentrations in the Infrared [14] are attributed, these are not part of the glass structures.

ACKNOWLEDGEMENTS

To Prof. Salmon Landi Jr. for contributing the information that resulted this errata document.